Lecture Notes in Applied and Computational Mechanics Vol. 44

Raouf A. Ibrahim
Vladimir I. Babitsky
Masaaki Okuma (Eds.)

Vibro-Impact Dynamics of Ocean Systems and Related Problems

Springer

Lecture Notes in Applied and Computational Mechanics

Volume 44

Lecture Notes in Applied and Computational Mechanics

Edited by F. Pfeiffer and P. Wriggers

Further volumes of this series found on our homepage: springer.com

Vol. 44: Ibrahim R.A., Babitsky, V.I., Okuma, M. (Eds.)
Vibro-Impact Dynamics of Ocean Systems and Related Problems
300 p. 2009 [978-3-642-00628-9]

Vol. 43: Ibrahim, R.A.
Vibro-Impact Dynamics
320 p. 2009 [978-3-642-00274-8]

Vol. 42: Hashiguchi, K.
Elastoplasticity Theory
432 p. 2009 [978-3-642-00272-4]

Vol. 41: Browand, F., Ross, J., McCallen, R. (Eds.)
Aerodynamics of Heavy Vehicles II: Trucks, Buses, and Trains
486 p. 2009 [978-3-540-85069-4]

Vol. 40: Pfeiffer, F.
Mechanical System Dynamics
578 p. 2008 [978-3-540-79435-6]

Vol. 39: Lucchesi, M., Padovani, C., Pasquinelli, G., Zani, N.
Masonry Constructions: Mechanical Models and Numerical Applications
176 p. 2008 [978-3-540-79110-2

Vol. 38: Marynowski, K.
Dynamics of the Axially Moving Orthotropic Web
140 p. 2008 [978-3-540-78988-8]

Vol. 37: Chaudhary, H.; Saha, S.K.
Dynamics and Balancing of Multibody Systems
200 p. 2008 [978-3-540-78178-3]

Vol. 36: Leine, R.I., van de Wouw, N.
Stability and Convergence of Mechanical Systems with Unilateral Constraints
250 p. 2008 [978-3-540-76974-3]

Vol. 35: Acary, V., Brogliato, B.
Numerical Methods for Nonsmooth Dynamical Systems: Applications in Mechanics and Electronics
545 p. 2008 [978-3-540-75391-9]

Vol. 34: Flores, P.; Ambrósio, J.; Pimenta Claro, J.C.; Lankarani Hamid M.
Kinematics and Dynamics of Multibody Systems with Imperfect Joints: Models and Case Studies
186 p. 2008 [978-3-540-74359-0]

Vol. 33: Nies ony, A.; Macha, E.
Spectral Method in Multiaxial Random Fatigue
146 p. 2007 [978-3-540-73822-0]

Vol. 32: Bardzokas, D.I.; Filshtinsky, M.L.; Filshtinsky, L.A. (Eds.)
Mathematical Methods in Electro-Magneto-Elasticity
530 p. 2007 [978-3-540-71030-1]

Vol. 31: Lehmann, L. (Ed.)
Wave Propagation in Infinite Domains
186 p. 2007 [978-3-540-71108-7]

Vol. 30: Stupkiewicz, S. (Ed.)
Micromechanics of Contact and Interphase Layers
206 p. 2006 [978-3-540-49716-5]

Vol. 29: Schanz, M.; Steinbach, O. (Eds.)
Boundary Element Analysis
571 p. 2006 [978-3-540-47465-4]

Vol. 28: Helmig, R.; Mielke, A.; Wohlmuth, B.I. (Eds.)
Multifield Problems in Solid and Fluid Mechanics
571 p. 2006 [978-3-540-34959-4]

Vol. 27: Wriggers P., Nackenhorst U. (Eds.)
Analysis and Simulation of Contact Problems
395 p. 2006 [978-3-540-31760-9]

Vol. 26: Nowacki, J.P.
Static and Dynamic Coupled Fields in Bodies with Piezoeffects or Polarization Gradient
209 p. 2006 [978-3-540-31668-8]

Vol. 25: Chen C.-N.
Discrete Element Analysis Methods of Generic Differential Quadratures
282 p. 2006 [978-3-540-28947-0]

Vol. 24: Schenk, C.A., Schuëller. G
Uncertainty Assessment of Large Finite Element Systems
165 p. 2006 [978-3-540-25343-3]

Vol. 23: Frémond M., Maceri F. (Eds.)
Mechanical Modelling and Computational Issues in Civil Engineering
400 p. 2005 [978-3-540-25567-3]

Vol. 22: Chang C.H.
Mechanics of Elastic Structures with Inclined Members: Analysis of Vibration, Buckling and Bending of X-Braced Frames and Conical Shells
190 p. 2004 [978-3-540-24384-7]

Vibro-Impact Dynamics of Ocean Systems and Related Problems

Raouf A. Ibrahim, Vladimir I. Babitsky,
Masaaki Okuma (Eds.)

Springer

Raouf A. Ibrahim
Department of Mechanical Engineering
Wayne State University
5050 Anthony Wayne Dr.
Room 2119 Engineering Bldg
Detroit, MI 48202
USA
E-Mail: ibrahim@eng.wayne.edu

Prof. Vladimir I. Babitsky
Loughborough University
Department of Mechanical Engineering
Loughborough, Leicestershire LE11 3TU
UK
E-Mail: V.I.Babitsky@lboro.ac.uk

Prof. Masaaki Okuma
Department of Mechanical and
Aerospace Engineering,
Graduate School of Science and Engineering,
Tokyo Institute of Technology
2-12-1-I3-15, O-okayama
Meguro-ku, Tokyo, 152-8552
Japan
E-Mail: mokuma@mech.titech.ac.jp

ISBN: 978-3-642-00628-9 e-ISBN: 978-3-642-00629-6

DOI 10.1007/978-3-642-00629-6

Lecture Notes in Applied and Computational Mechanics ISSN 1613-7736
e-ISSN 1860-0816

Library of Congress Control Number: 2009921826

Typeset & Cover Design: Scientific Publishing Services Pvt. Ltd., Chennai, India.

Printed on acid-free paper

9 8 7 6 5 4 3 2 1 0

springer.com

Preface

Vibro-impact systems involve multiple impact interactions and are encountered in many engineering applications such as impact of floating ice with ships, slamming of ocean waves on off-shore structures, ships colliding against fenders, percussion machines, loosely fitting joints, gear-pair systems with backlash, collision of human vocal folds, automotive braking systems and fatigue fracture. The analytical modeling of such systems is usually described by equations with strong nonlinearities. Thus they require special mathematical treatment. The analysis of vibro-impact systems involves the development of mathematical models with discontinuities. Such systems exhibit complex types of resonance, bifurcations, chaos and coexistence of different attractors. Of particular interest is the problem of grazing impact bifurcation which takes place at the verge of zero impact velocity. This problem has recently attracted intensive research activities among physicists, engineers, and mathematicians. Under random excitation, the so-called "path integral" is introduced as an effective tool for evaluating the response of vibro-impact systems in terms of probability density at each time instant, for evaluating moments of various orders, energy response probability density function, and first-passage time of strong nonlinear systems.

The aim of this International Symposium on Dynamics of Vibro-Impact Systems is to provide a forum for the discussion of recent developments in the theory and industrial applications of vibro-impact ocean systems. A special effort has been made to invite active researchers from engineering, science, and applied mathematics communities. This symposium has indeed updated engineers with recent analytical developments of vibro-impact dynamics and at the same time allowed engineers and industrial practitioners to alert mathematicians with their unresolved issues. The symposium was held in Troy, Michigan, during the period October 1-3, 2008. It included 28 presentations grouped as follows:

- The first group comprises of nine papers dealing with the interaction of ocean systems with slamming waves and floating ice. It also covers related topics such as sloshing-slamming dynamics, and non-smooth dynamics associated with offshore structures. Moreover, it includes control issues pertaining to marine surface vessels.
- The second group consists of fifteen papers treats the interaction of impact systems with friction and their control, Hertzian contact dynamics, parameter variation in vibro-impact oscillators, random excitation of vibro-impact

systems, vibro-impact dampers, oscillators with a bouncing ball, limiting phase trajectory corresponding to energy exchange between the oscillator and external source, frequency-energy distribution in oscillators with impacts, and discontinuity mapping.

- The third group is covered in four papers and addresses some industrial applications such as hand-held percussion machines, rub-impact dynamics of rotating machinery, impact fatigue in joint structures.

The organizers would like to express their gratitude to Dr. Kelly Cooper, of the USA Office of Naval Research, for sponsoring this Symposium.

Raouf A. Ibrahim
Vladimir I. Babitsky
Masaaki Okuma

Contents

Nonlinear Dynamics of an Impact Object on an Oscillating Plate

Scott E. Anderson, Suttipong Paksuttipol, and Dale G. Karr

Abstract. The dynamical problem of a ball bouncing on an oscillating surface has been widely studied theoretically and experimentally, and has been frequently used as an example to show the evolution of a chaotic system. This system has also been used to model several engineering problems, including the generation and control of noise in machinery such as jackhammers and mechanical linkages with free play, the transportation and separation of granular solids such as rice, and the transportation of components in automatic assembly devices which commonly employ oscillating tracks. Within the paper, the system and assumptions used for one-dimensional simulations are first described. We then address the development of an iterative nondimensional solution, and present analyses of the behavior of the system. The simulations are studied in relation to the effects of grazing impacts and the resulting dynamics structure of the system's response.

1 Introduction

Since introduced by Enrico Fermi in 1949 [1], the dynamic problem of a ball bouncing between a fixed and oscillating plate, and the more common version of a ball subject to gravity bouncing on a vertically oscillating plate, has been widely studied both analytically and experimentally [2-9]. In addition to demonstrating the properties of the Smale horseshoe and the period doubling route to chaos, this dynamic system has been used to model many engineering problems such as controlling of noise in machinery, transporting granular solids and transporting components in automatic assembly devices which employ oscillating tracks [10].

In 1999, professor Ciro Cattuto, Fabio Marchesoni and Franco Nori, working with the physics department at the University of Michigan, carried out computer simulations designed to describe the behavior of granular matter inside a vertically shaken container [11]. The simulations involved a large number of balls bouncing on a vertically oscillating table, allowing the balls to interact with each other. During a simulation, the velocity and height of the balls were recorded every cycle, in

Scott E. Anderson
Prevention Department Sector Lower Mississippi River, 2 Auction Ave. Memphis, TN 38105, U.S.A.

Suttipong Paksuttipol and Dale G. Karr
The University of Michigan, Department of Naval Architecture and Marine Engineering, NA&ME Building, 2600 Draper Dr, Ann Arbor, MI 48109-2145, U.S.A.

R.A. Ibrahim et al. (Eds.): Vibro-Impact Dynamics of Ocean Systems, LNACM 44, pp. 1–14.
springerlink.com

a stroboscopic fashion, for several hundred cycles of the plate. A sample of the results is shown in Figure 1.1.

The horizontal axis represents the height of the balls above an established datum, while the vertical axis shows each ball's velocity with respect to the datum. Instead of showing a uniform distribution of points, this point displays a characteristic "finger-like" structure. The purpose of this paper is to use the simulation of a single ball bouncing on an oscillating plate to explore the source of the "finger-like" structure.

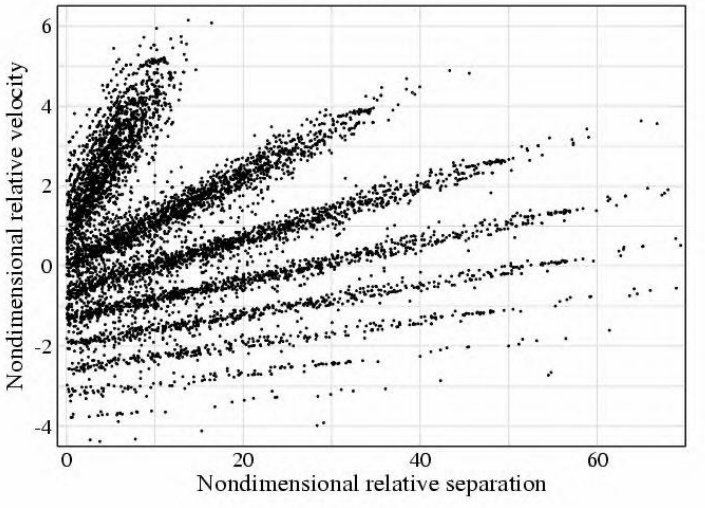

Fig. 1.1 Results of simulation involving multiple balls bouncing on an oscillating plate

2 System and Assumptions

The system consists of a ball with finite restitution ($0 \leq \alpha < 1$) that is free to bounce on a table moving sinusoidally in the vertical with amplitude A and frequency ω.

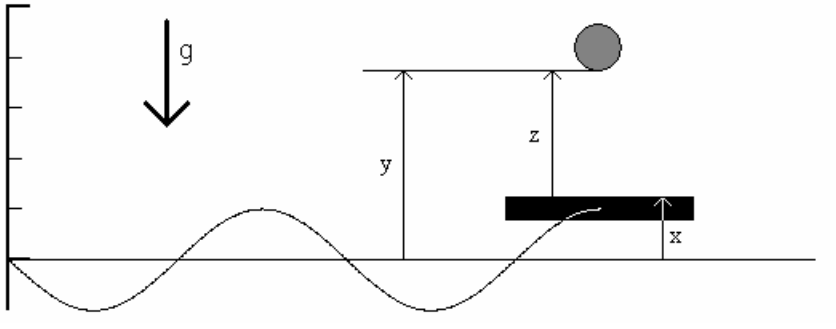

Fig. 2.1 Diagram of variables describing the system

The first assumption is that the mass of the table is much greater than that of the ball. Besides, it is assumed that the collision between the ball and the plate is instantaneous, and completely described by the coefficient of restitution. This coefficient is defined as the ratio of the relative velocity of separation after impact to the relative velocity of approach before the impact, or,

$$\alpha = \frac{-\dot{z}_+}{\dot{z}_-} \tag{2.1}$$

An assumption conspicuously absent is the Chirikov "High Bounce" approximation [2]. The high bounce approximation states that the amplitude of the table is negligible compared with the height of the bounce [12,13]. This assumption allows the duration of each bounce, and the velocity of the ball at each bounce to be determined explicitly, rather than by solving the equations of motion. While this assumption cuts computing requirements drastically and allows for the rapid construction of complex charts such as the bifurcation diagram [10], it also eliminates the possibility of observing "chattering" or "sticking" phenomenon, which can lead to periodic solutions not predicted by the high bounce analysis [14]. Although some of the programs created for this paper are capable of incorporating chattering and sticking phenomena, the long duration simulations where this becomes an important factor are not needed for the analysis at hand. However, for the purposes of determining the source of the finger structure noted in Figure 1.1, the flight path of the ball must be determined iteratively, so the high bounce assumption would decrease accuracy without decreasing computational demands.

Further analysis details of the approach described here can also be found in the thesis by Anderson [15]. Additionally, more recent related studies of random impact vibration dynamics can be found in [16].

3 Equations of Motions

The relative separation between the ball and the plate is given by

$$z = y - x \tag{3.1}$$

and the motion of the table is defined by

$$x = -A\sin(\omega t) \tag{3.2}$$

where A and ω are the amplitude and frequency of the plate motion respectively. There are three different time variables used in this system: t is the time from the beginning of the simulation, t_o is the phase shift or point in the cycle of the plate when impact occurs, and $\bar{t}$ is the free flight time of the ball, $t = t_o + \bar{t}$.

Solving $\ddot{y} = -g$ for free flight and substituting equation (1) and (2) into the solution for y yields:

$$z = -\tfrac{1}{2} g\bar{t}^2 + \dot{y}_o\bar{t} - A\sin\omega t_o + A\sin\left(\omega t_o + \omega\bar{t}\right) \tag{3.3}$$

3.1 Nondimensional Equations of Motion

We now introduce the nondimensional quantities:

nondimensional separation: $\bar{z} \equiv \dfrac{z}{A}$ (3.4)

nondimensional initial velocity: $v \equiv \dfrac{2\omega}{g}\dot{y}_o$ (3.5)

nondimensional forcing amplitude: $\gamma \equiv \dfrac{2A\omega^2(1+\alpha)}{g}$ (3.6)

which leads to :

$$\frac{g}{A} = \frac{2\omega^2(1+\alpha)}{\gamma} \quad \text{and} \quad \frac{\dot{y}_o}{A} = \frac{vg}{2\omega A} = \frac{v\omega(1+\alpha)}{\gamma} \tag{3.7, 3.8}$$

Also, introduce the nondimensional time:

$$\begin{aligned} \bar{\phi} &= \omega\bar{t} \\ \phi &= \omega t \\ \phi_o &= \omega t_o \end{aligned} \tag{3.9}$$

The final forms of the equations of nondimensional relative motion are the following:

$$\bar{z} = -\frac{(1+\alpha)}{\gamma}\bar{\phi}^2 + \bar{z}_o'\bar{\phi} - \bar{\phi}\cos\phi_o - \sin\phi_o + \sin(\phi_o + \bar{\phi}) \tag{3.10}$$

and

$$\frac{d\bar{z}}{d\bar{\phi}} = \bar{z}' = -\frac{2(1+\alpha)}{\gamma}\bar{\phi} + \bar{z}_o' - \cos\phi_o + \cos(\phi_o + \bar{\phi}) \tag{3.11}$$

In equations (3.10) and (3.11), we use the nondimensional initial velocity defined by:

$$\bar{z}'(\bar{\phi} = 0) = \frac{v(1+\alpha)}{\gamma} + \cos\phi_o = \bar{z}_o' \tag{3.12}$$

3.2 Establishing an Upper Bound

During the analysis of equations (3.10) and (3.11), it is convenient to calculate the lowest initial nondimensional relative velocity for which the next bounce will

have a smaller initial velocity. This requires that $\alpha < 1$, and establishes the upper bound of $\bar{z}_o'(\alpha, \gamma)$.

Energy considerations are used to establish the bound, and the subscripts 0, 1, and 2 reference the values when the ball initially leaves the plate, when contact is made at the end of the first bounce, and the instant the ball leaves the plate on the second bounce, respectively.

Establishing the potential and kinetic energy respectively of the ball at $\bar{t} = 0$, we have

$$\begin{aligned} KE_o &= \tfrac{1}{2} m \dot{y}_o^{\,2} \\ PE_o &= mgx_o \end{aligned} \tag{3.13}$$

Just before the next impact, $E_{o,total} = E_{1,total}$ therefore:

$$\dot{y}_1 = \pm\sqrt{\dot{y}_o^2 + 2g(x_o - x_1)} \tag{3.14}$$

Now note that we wish to find conditions such that $\dot{z}_2 < \dot{z}_o$ and recall $\dot{z}_i = \dot{y}_i - \dot{x}_i$; thus we seek conditions:

$$\dot{y}_2 - \dot{y}_o < \dot{x}_2 - \dot{x}_o = \dot{x}_1 - \dot{x}_o \tag{3.15}$$

Accounting for the energy loss at the bounce and solving for $\dot{y}_2$

$$\dot{y}_2 = (1+\alpha)\dot{x}_1 - \alpha\dot{y}_1 \tag{3.16}$$

Substituting equation (3.16) into equation (3.15) yields:

$$\alpha\dot{y}_1 + \dot{y}_o > \alpha\dot{x}_1 + \dot{x}_o \tag{3.17}$$

From equation (3.14),

$$\dot{y}_o - \dot{x}_o - \alpha\dot{x}_1 > \alpha\sqrt{\dot{y}_o^2 + 2g(x_o - x_1)} \tag{3.18}$$

Squaring both sides yields the condition:

$$\dot{y}_o > \frac{(\dot{x}_o + \alpha\dot{x}_1) \pm \sqrt{(\dot{x}_0 + \alpha\dot{x}_1)^2 - (1-\alpha^2)\left[(\dot{x}_0 + \alpha\dot{x}_1)^2 - 2g\alpha^2(x_o - x_1)\right]}}{(1-\alpha^2)} \tag{3.19}$$

Converting back to the relative velocity between the plate and the ball, and choosing values for equation (3.19) that will give the largest possible $\dot{z}_o$, we find:

$$\dot{z}_o > \frac{\overbrace{\dot{x}_o\alpha^2 + \dot{x}_1\alpha}^{\max} \pm \sqrt{\overbrace{\left(\dot{x}_o + \alpha\dot{x}_1\right)}^{\max\ 2} - \left(1-\alpha^2\right)\left[\overbrace{\left(\dot{x}_o + \alpha\dot{x}_1\right)}^{\min\ 2} - 2g\alpha^2\overbrace{\left(x_o - x_1\right)}^{\max}\right]}}{\left(1-\alpha^2\right)} \tag{3.20}$$

In equation (3.20), we indicate the choice for x and $\dot{x}$ that will give the largest possible $\dot{z}_0$. Recall that the motions and velocities of the plate are limited to $-A \le x \le A$ and $-A\omega \le \dot{x} \le A\omega$ respectively. Substituting accordingly into the above equation yields:

$$\dot{z}_o > \frac{A\omega\alpha + A\omega\sqrt{1 + \frac{(1-\alpha)(4g\alpha^2 A)}{(1+\alpha)(A\omega)^2}}}{(1-\alpha)} \tag{3.21}$$

Converting back to the nondimensional relative velocity leads to the upper bound of:

$$\bar{z}'_{o,\max} > \frac{\alpha + \sqrt{1 + \frac{8\alpha^2}{\gamma}(1-\alpha)}}{(1-\alpha)} \tag{3.22}$$

A quick check shows that as the restitution of the ball approaches unity ($\alpha \to 1$), the system becomes unbounded and $\bar{z}'_{o,\max}$ goes to infinity for the conservative system.

4 Visualization and Evaluation of Response

Two types of visualization tools were created for this paper, impact maps and stroboscopic samples. For simplification, the terms "nondimensional" and "relative" will be dropped for the remainder of this paper, with the understanding that all displacements and velocities are nondimensional and relative and that time is nondimensional.

4.1 Impact Maps

Starting with an arbitrary set of initial conditions for bounce N, $\left(\bar{z}'_{o,N}, \phi_{o,N}\right)$, an impact map is created by solving equations (3.10) and (3.11) until the ball returns to the plate at $\left(\bar{z}'_N, \phi_N\right)$. The initial velocity of the N+1 bounce,

$\bar{z}'_{o,N+1} = -\alpha\ \bar{z}'_N$, and phase of the periodic forcing are then plotted. Note that in the figure, each point along the lines represent the unique initial conditions for bounce (N+1) resulting from a single set of initial conditions from the previous bounce (N). This process can also be carried out in reverse form to provide the initial conditions for the (N-1) bounce given the initial conditions for bounce (N). In order to avoid stretching the results out over several cycles of the plate oscillation, it is convenient to fold the time axis into one period of the plate, which has the topology of a circle, and gives the entire plot the topology of a cylinder with the initial velocity plotted on the vertical axis. The folded time axis $(0 \le \phi \le 2\pi)$ along with the upper bound ($\bar{z}'_{o,\max}$) form a reduced phase space available for the system behavior. This reduced phase space is referred to in literature as the impact map [7], phase portrait [14], state space [3], or the phase cylinder [3]. For the remainder of this paper the term "impact map" will be used to describe the reduced phase space. The results from this process for the time axis are plotted in reduced phase space in Figure 4.1.

Figure 4.2 shows the behavior of the system for lines of initial conditions that contain grazing points. The inset chart shows (A-1, B-1) and three horizontal lines representing three sets of balls that have constant initial velocities but

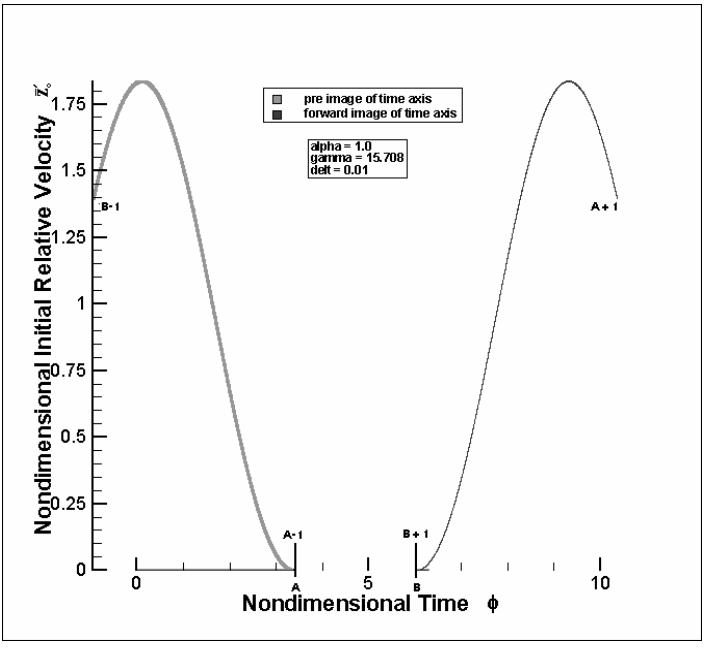

Fig. 4.1 The unreduced phase space showing the pre and forward images of the time axis ("grazing points")

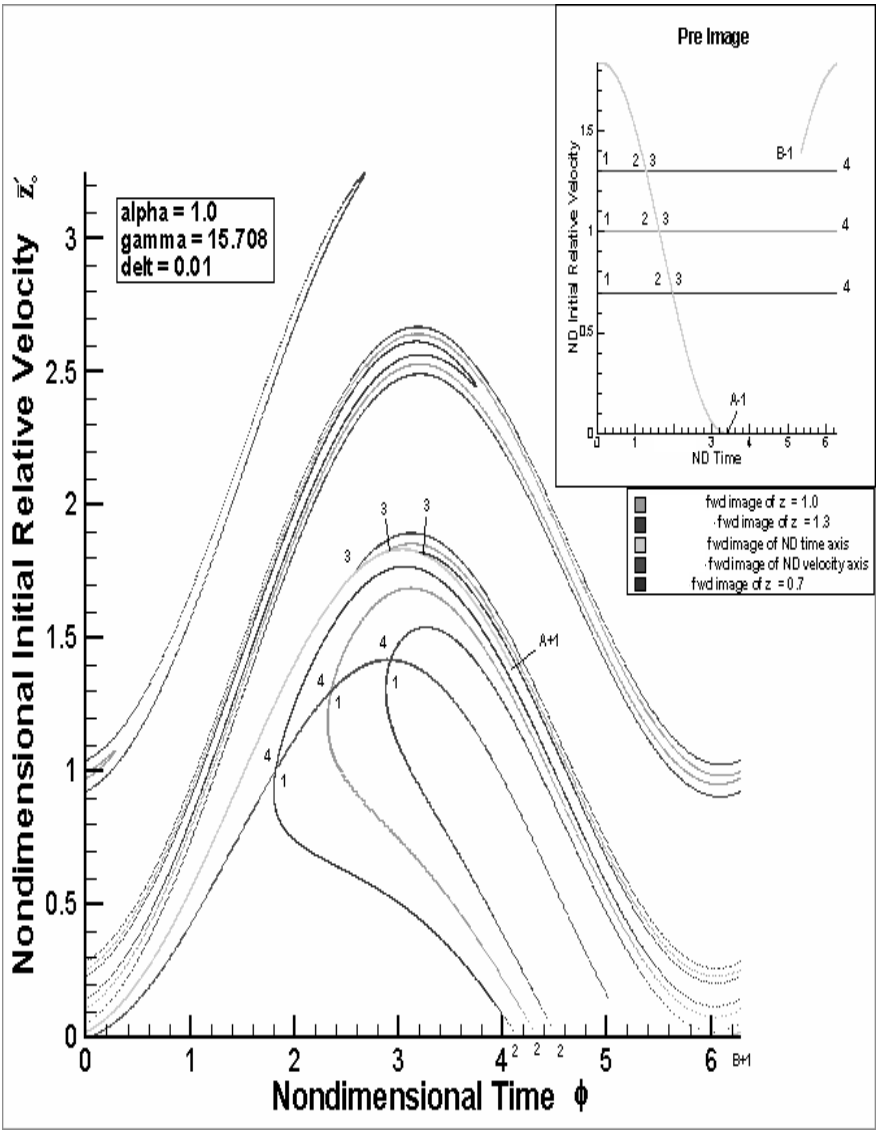

Fig. 4.2 Impact map showing the forward mapping with grazing points

progressively later bounce times. The main chart shows the forward image of the initial velocity axis along with (A+1, B+1) and the forward images of the horizontal lines with numbers inserted to show the progressions of the mapping. Notice that the forward images of the horizontal lines start under the image of the velocity

axis and proceed down until they reach (A, B), at this point, the balls just miss the oscillating surface and so map very near (A+1, B+1). As expected, the forward images of the horizontal lines end at the forward image of the velocity axis, where they started.

In another example, to gain a better concept of the twisting, stretching, and contracting properties of the impact map, the boundary lines of a box containing the reduced phase space will be mapped backwards and forwards. Figures 4.3 and 4.4 show how the points contained in the reduced phase space, defined by the two axes and an upper bound, map forward.

Figure 4.3 shows the boundaries or limits of the initial states, along with the pre image of the initial velocity axis ($\overline{z}_o'$) and the time axis (ϕ). These two pre images divide the area into ten sections, labeled V1 through V10. Numbers and letters have been added to the plot to help clarify the forward mapping, and the "i" terms help clarify the discontinuities.

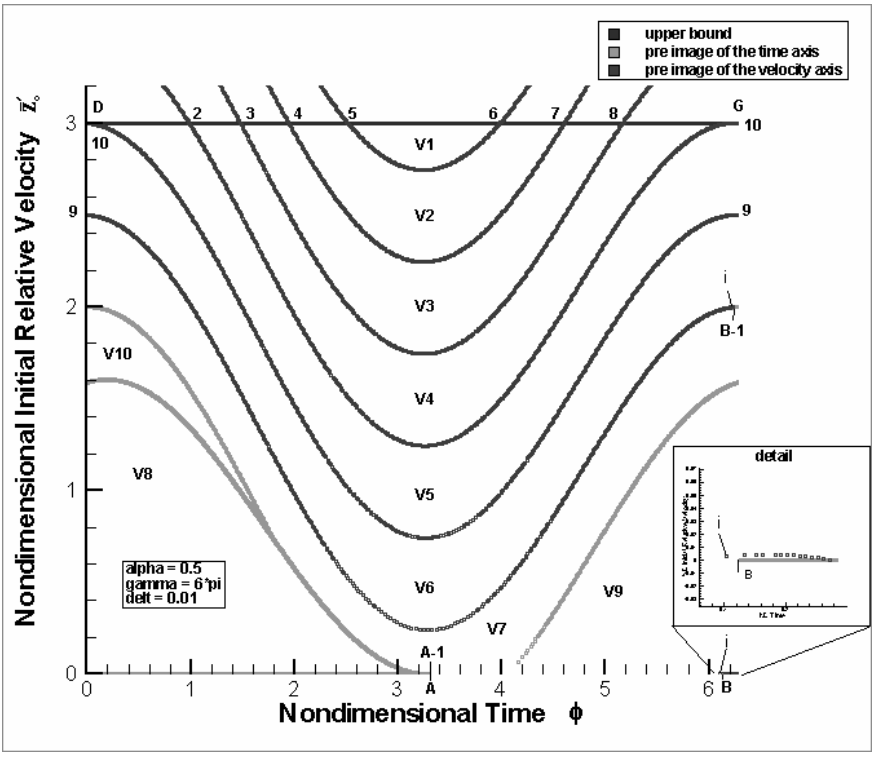

Fig. 4.3 Impact map showing the upper bound and the pre images of the time and velocity axes

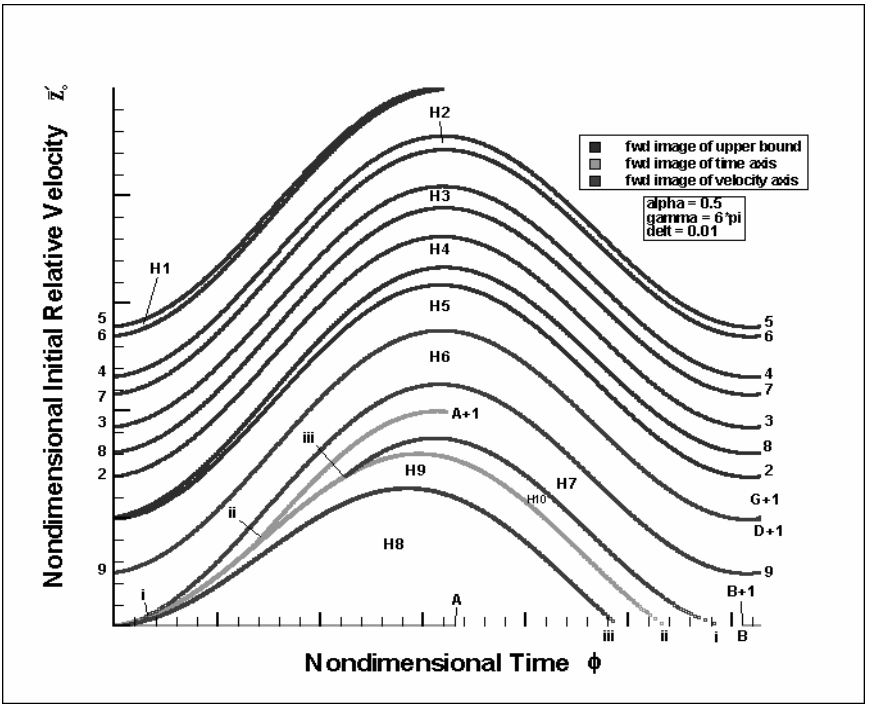

Fig. 4.4 Impact map showing the forward image of the upper bound, the time and velocity axes

Figure 4.4 shows the forward images of the upper bound, the time axis (ϕ) and the initial velocity axis ($\bar{z}'_o$). The sections labeled H1 through H10 represent the forward images of the areas with the corresponding V numbers from Figure 4.3.

To illustrate the dynamics of the mapping process, examine the mapping of the area V2 to H2. The curved lines 5-6 and 4-7 forming the upper and lower boundaries of V2 area compressed and rotated to form small portions of the initial velocity axis. Meanwhile, the segments of the upper boundary 4-5 and 6-7 are stretched completely across the impact map, with curve 6-7 being inverted. Due to the imperfect elasticity of the impact, the transformation of V to H is not an area conserving process [14].

Figure 4.5 shows the data points from a set of uniformly distributed pre-images with the maximum impact velocity ($\bar{z}'_{o,\max}$) that is equal 3. The figure then shows the data points overlaid on Figure 4.4. This clearly verifies that all of the points from the original box map forward into the labeled areas in Figure 4.4.

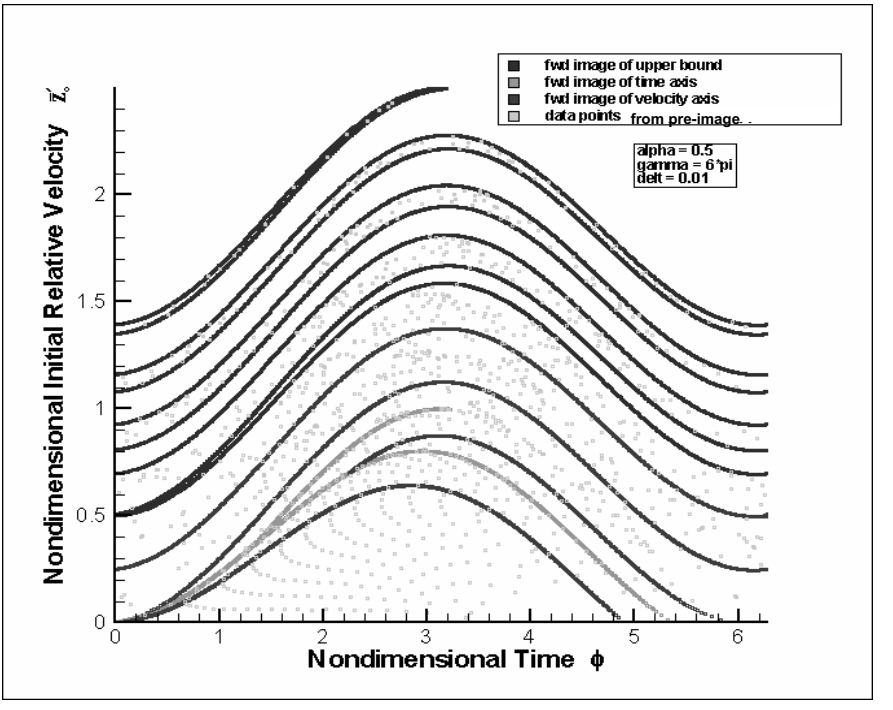

Fig. 4.5 Impact map of figure 4.4 overlaid with pre-image results

4.2 Poincare' Maps

To further study the behavior of this system, the bouncing ball simulation is modified to create a stroboscopic sample, also called a Poincare' plot, which reduces the dimension of the phase space by removing the time variable. In this simulation, a ball with an arbitrary initial velocity and phase shift is followed through one complete bounce. The velocity ($\bar{z}'$) and separation ($\bar{z}$) are recorded each time the oscillating plate completes a cycle ($\phi = n2\pi \quad n = 1,2,3...$).

Carrying this evaluation out for points shown in Figure 4.5 leads to the stroboscopic sample shown in Figure 4.6. This plot shows the distinctive finger structure observed by Cattuto, Marchesoni, and Nori in their multiple ball experiments [11], although the number of fingers and orientations are different. Each finger represents the heights and velocities available for the system behavior at the end of each successive cycle of the plate, starting with the first cycle in the upper left corner of the plot. Taking the stroboscopic sample of the upper boundary line, the time axis (ϕ) and the initial velocity axis ($\bar{z}_o'$) leads to the boundaries for the stroboscopic sample shown in Figure 4.6. The boundaries of each finger are very clear, and one can see that the grazing points also cause discontinuity in the finger structure.

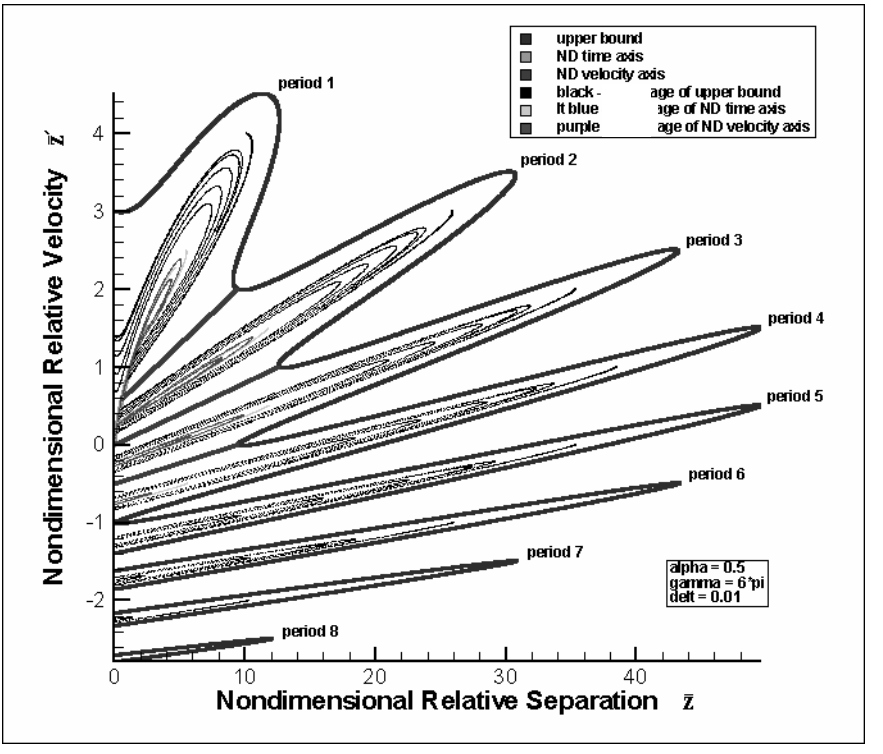

Fig. 4.6 Stroboscopic sample of the boundaries of the reduced phase space and the forward image of those boundaries

Figure 4.6 also reflects the conservative nature of the upper bound equation in that the first forward mapping occupies much less of the area of the fingers than is available.

5 Conclusion

This approach is now applied in the analysis for the purpose of describing the results obtained by Cattuto, Marchesoni, and Nori. Repeatedly mapping a uniformly distributed set of initial conditions using their parameters leads to a pattern contained in the reduced phase space as shown in figure 5.1. The figure shows two sets of uniform initial conditions, one with a high upper bound and the second with a low bound.

When the stroboscopic samples of the same orbits and points from Figure 5.1 are taken, the results, shown in Figure 5.2, are strikingly similar to Figure 1.1 in relative position and size of the finger-like structure.

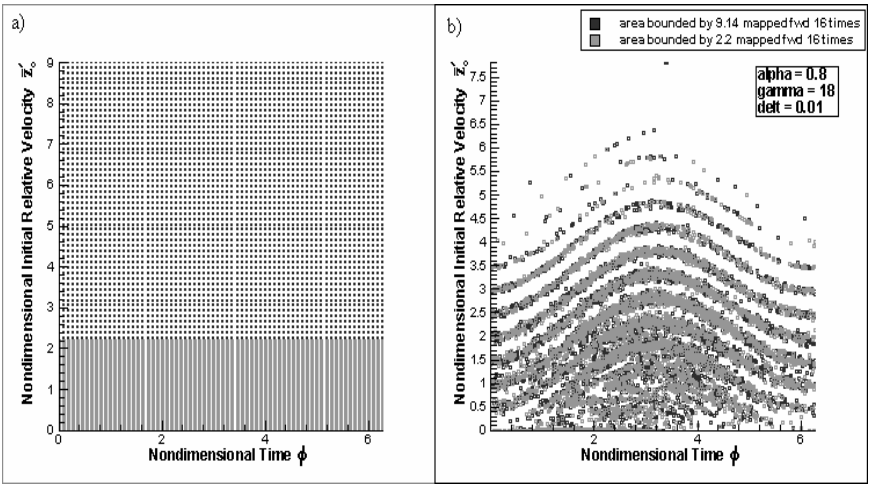

Fig. 5.1 a) Impact map showing two sets of uniform initial conditions, one with an upper bound at $\bar{z}'_o = 9.14$ and the other with an upper bound at $\bar{z}'_o = 2.2$ b) Impact map showing the structure of the two sets of initial conditions

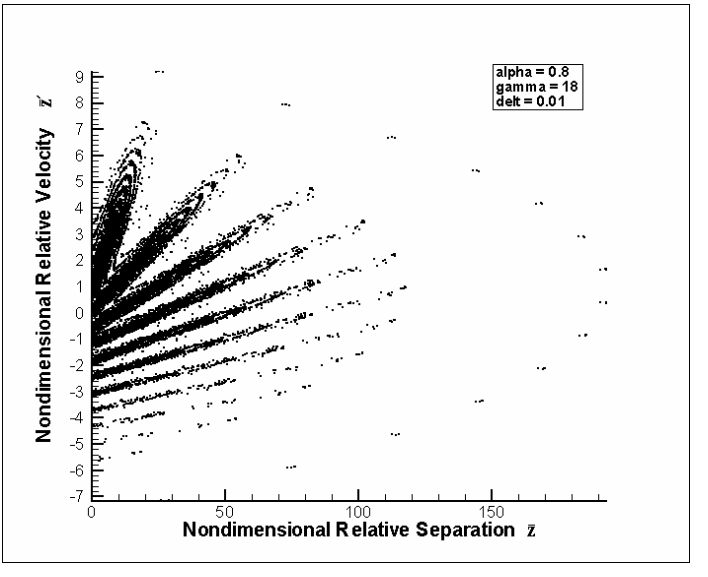

Fig. 5.2 Stroboscopic sample of the steady state pattern of initial conditions

We note in closing that the various stroboscopic samples created for this paper show that the finger structure observed by Cattuto, Marchesoni, and Nori is a property of the bouncing ball dynamic system. The size, number, shape, and orientation

of the fingers change based on the coefficient of restitution, the amplitude of the plate motions and the frequency of the plate oscillations, while the addition of interacting balls tends to blur the boundaries and pattern in the fingers.

These observations lead to practical applications for engineering problems modeled by the bouncing ball system. Given the basic parameters of the system, the bounds of the overall system behavior can be determined even though the exact behavior at any given time is unpredictable. Parameters relating to the expected amplitude of a bound, the velocity of the impact object, or the expected flight time of the object can be determined which provides designers with valuable tools for design and optimization.

References

[1] Fermi, E.: On the origin of the cosmic radiation. Phys.Rev. 75, 1169–1174 (1949)
[2] Chirikov, B.V.: A universal instability of many dimensional oscillator systems. Phys. Rep. 52, 265–379 (1979)
[3] Holmes, P.J.: The dynamics of repeat impacts with a sinusoidally vibrating table. J. Sound Vib. 84, 173–189 (1982)
[4] Pieranski, P.: Direct evidence for the suppression of period doubling in the bouncing-ball model. Phys. Rev. A 37, 1782–1785 (1988)
[5] Tufillaro, N.B., Albano, A.M.: Chaotic dynamics of a bouncing ball. Am. J. Phys. 54, 939–944 (1986)
[6] Everson, R.M.: Chaotic dynamics of a bouncing ball. Physica D 19, 355–383 (1986)
[7] Mello, T.M., Tufillaro, N.B.: Strange attractors of a bouncing ball. Am. J. Phys. 55, 316–320 (1987)
[8] Wiesenfeld, K., Tufillaro, N.B.: Suppression of period doubling in the dynamics of a bouncing ball. Physica D 26, 321–325 (1987)
[9] Luna-Acosta, G.A.: Regular and chaotic dynamics of the damped Fermi accelerator. Phys. Rev. A 42, 7155–7162 (1990)
[10] Tufillaro, N.B.: Braid analysis of a bouncing ball. Phys. Rev. E 50, 4509–4522 (1994)
[11] Cattuto, C., Marchesoni, F., Nori, F.: Shaken granular natter: fluctuations and self-organization in phase space (Unpublished)
[12] Vincent, T.L., Mees, A.I.: Controlling a bouncing ball. International J. of Bifurcation and Chaos 10, 579–592 (2000)
[13] Wood, L.A., Byrne, K.P.: Analysis of a random repeated impact process. J. Sound Vib. 78, 329–345 (1981)
[14] Luck, J.M., Mehta, A.: Bouncing ball with finite restitution: Chattering, locking and chaos. Phys. Rev. E 48, 3988–3997 (1993)
[15] Anderson, S.E.: Nonlinear Dynamics of an Impact Object on an Oscillating Plate. Masters Degree Thesis, Department of Naval Architecture and Marine Engineering, University of Michigan (2001)
[16] Giusepponi, S., Marchesoni, F., Borromeo, M.: Randomness in the bouncing ball dynamics. Physica A 351, 142–158 (2005)

Elastic Identification of Composite Materials from Vibration Test Data of Thin and Thick Plates

Emmanuel Ayorinde

In many applications, composite materials are preferred to monolithics because of significant advantages such as higher specific strength and specific stiffness, better resistance to fatigue and impact damages and to corrosion, as well as greater liberty for multifunctional design whereby the design serves many purposes at once. These advantages account for the widespread use of composites in the marine, aerospace and consumer goods areas. Established standards by various testing organizations for elastic identification of materials are destructive and are relatively costly and time-consuming. Besides this, in modern industry, net and near-net production methods are becoming more necessary as increasing effort is made to avoid waste. This has made nondestructive testing methods to gain more importance. Vibration test methods are among the simplest and most indicative available. This paper describes the basic approach of this strategy, and recent further work in the use of vibration test data to predict elastic constants of these materials.

Emmanuel Ayorinde
Mechanical Engineering Department
Wayne State University
Detroit, Michigan 48202

R.A. Ibrahim et al. (Eds.): Vibro-Impact Dynamics of Ocean Systems, LNACM 44, p. 15.
springerlink.com

Foundations for Design of Vibro-Safe Hand-Held Percussion Machines

V.I. Babitsky, I.J. Sokolov, and N.A. Halliwell

Abstract. An approach to analysis and synthesis of dynamical and engineering structures of a hand-held percussion machines with a vibration-free handle/casing is presented. This is based on consideration of the optimal dynamic conversion of operator's feed force into sequence of impact impulses of the tool against the material being treated. The optimal dynamical cycle in percussion machine was found as an equivalent problem of optimal control [1]. The search for the optimal engineering structure of the vibration free percussion machine was fulfilled for a heavy hydraulic breaker. The key element of the proposed engineering design, which realises the synthesised structure is a mechanism with zero differential stiffness. A hydro-pneumatic unit with zero stiffness was developed and tested. Theoretical recommendations have been applied to development of a commercial hydraulic breaker to provide a significant reduction in vibration transmitted to operator.

1 Introduction

Hand-held percussion machines are used widely throughout industry. Due to a direct tactile control of the machine by the operator the latter is exposed permanently to harmful vibration which leads to a variety of disorders. The current design and development of the hand-held percussion machines have been mainly heuristic due to the complexity of their dynamic behavior. Existing theoretical works limited their analysis to some special models reflecting mainly individual structure of machine units but did not allow understanding of the common dynamical characteristics of the machine as a whole. Such situation makes comparative analysis of machines, choice of their optimal design concepts and estimation of improvement potential difficult.

In [1] the formulation of a general approach to analysis and synthesis of hand held percussion machines using methods of nonlinear dynamics and optimal control was presented. The optimal dynamic conversion of energy in hand-held percussion machines revealed the general relations between the character of excitation of vibro-impact process in machine as well as the main factors of

V.I. Babitsky
Wolfson School of Mechanical & Manufacturing Engineering, Loughborough University, LE11 3TU, UK
v.i.babitsky@lboro.ac.uk

R.A. Ibrahim et al. (Eds.): Vibro-Impact Dynamics of Ocean Systems, LNACM 44, pp. 17–27.
springerlink.com

machine-operator interaction and machine output. The optimal machine was presented as a *discrete converter* transforming the operator efforts into a sequence of impact impulses. The generation of impulses with a minimum influence on the operator was formulated as an equivalent *optimal control*. Such a control has been found as a solution of mathematical *problem of moments* in the proper normed linear space (see Fig. 1):

$$\frac{t_1}{T} = \frac{1}{1+R}\left(1-\sqrt{1-\frac{1-R^2}{2}}\right), \qquad U_0 = \frac{M_1(1+R)^2 v_0}{2T\left(\sqrt{1-0.5(1-R^2)}-0.5(1-R)\right)}, \tag{1}$$

where $R = -v_+/v_0$ indicates the change of the absolute velocity of the striker (Item 1 in Fig. 1,a) during impact, v_+ is its upward velocity after impact and M_1 is the mass of the striker. Hereafter positive values of the force applied to the striker and positive displacements correspond to the upward direction along the machine axis.

The force of excitation *u(t)* is applied to both the striker and the casing (Item 2 in Fig. 1,a). If the friction between these two bodies and the friction between the tool (Item 3 in Fig. 1,a) and the casing are negligibly small, the excitation force *u(t)* is the only source of the casing vibration. The optimal excitation was found for a system without friction. In what follows we refer to the media being treated (Item 4 in Fig. 1,a) as *ground*; in all figures constant forces are shown with solid line arrows, alternating forces are shown with dashed line arrows and the sequence of impact impulses is shown with dotted line arrows.

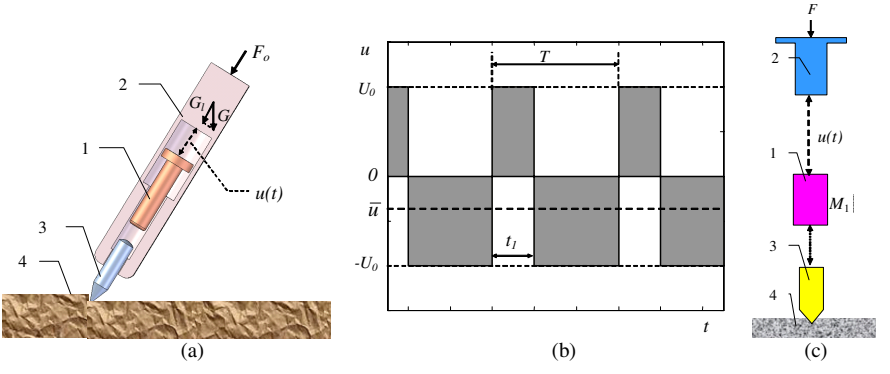

Fig. 1 Optimal excitation with minimum amplitude

The force of excitation *u(t)* has a constant component $\bar{u}$ and an alternating component $\tilde{u}$ given by equations [1]:

$$\bar{u} = -M_1 f(1+R)v_0, \qquad \tilde{u}(t) = u(t) - \bar{u} \tag{2}$$

Here $f=1/T$ is the frequency of impacts. The constant component $\bar{u}$ depends only on the parameters M_1, R, of the system and the parameters T, v_0 of the

regime. This component remains the same for any other excitation that provides the same parameters T, v_0 of the vibro-impact regime with a single impact per period [1]. As a result, for the system with parameters M_1 and R the desired vibro-impact regime of operation with parameters T and v_0 is available only if the operator is able to apply a constant feed force F_o that together with the longitudinal component G_l of the casing weight G balances the constant component $\overline{u}$ of the excitation force, i.e.

$$\left|\overline{u}\right| = G_l + F_0 = F\ . \tag{3}$$

Here F is the full feed force. For simplicity we will not distinguish the operator's feed force from the full feed force. However, it is important to note that the latter force includes the casing weight component that depends on the breaker orientation. In what follows when the short term *feed force* is used it refers to the full feed force. According to (2), for any excitation that provides a vibro-impact regime with impact velocity v_0 and single impact during a period T the full feed force can be found as

$$F = \frac{M_1(1+R)v_0}{T} = M_1(1+R)v_0 f \tag{4}$$

For the optimal excitation shown in Fig. 1,b:

$$F = \left(1 - \frac{2t_1}{T}\right)U_0 \tag{5}$$

The equivalent structure of such a system with negligibly small friction is shown in Fig. 1,c. For this system a reduction in harmful vibration transmitted to the operator can only be achieved by increasing the casing mass or by adding extra inertial bodies. Increasing the mass of the casing is a very straightforward solution with obvious disadvantages. In this paper other means of improving the design of hand-held percussion machines are investigated. The aim is to reduce significantly the operator's exposure to the hazardous vibration for a prescribed intensity of the vibro-impact working process and without increasing the machine's mass. In this way the first approach is to change the design so that the reaction force of the alternating component of the excitation is applied not to the casing, but to the ground. This can dramatically reduce vibration of the casing and is analysed thoroughly in the next section.

2 Optimal Solution for Three-Body System

Let us split the excitation force into two components $u(t) = u_c + u_p(t)$, as Fig. 2,a,b shows. The advantage of this splitting is that the alternating (pulsating) component $u_p(t)$ of the excitation force applied to the striker is now unidirectional and upward. As a result, this component can be applied between the striker 1 and the tool 3. In this case the unidirectional downward counterforce of this

component of the excitation force is applied directly to the ground 4 (via the tool 3) as Fig. 2,c shows. The constant component u_c can be applied between the striker 2 and the casing 3. The only force applied to the casing now is the constant component of the excitation force. This component can be balanced by the constant feed force F_1. As a result this mechanical system can theoretically have a strong vibro-impact process on the one (lower) side and total absence of vibration on the other (upper) side. This is the optimal three-body system with minimal emission of harmful vibration. To the authors' knowledge this structure has not found wide industrial application. The only example found is described in [2,3]. This can possibly be explained by the fact that such a design has the serious disadvantage intrinsic to the scheme. The operator's feed force needed is $F_1=U_0$ which is higher than the feed force F for the traditional system (Fig. 1) where

$$\frac{F_1}{F} = \frac{1}{1-2t_1/T} > 1 \tag{6}$$

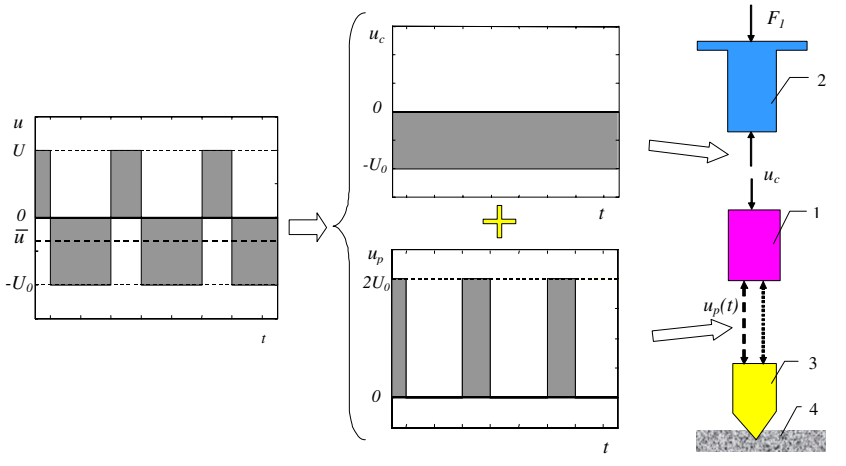

Fig. 2 Splitting excitation force into two components

As was mentioned above, the optimal excitation with minimal amplitude (1) is optimal again in the new system as in this case it minimises the feed force. However, if, for example, $t_1/T=1/3$ the feed force needed for a vibration-free tool is three times as much as for the initial design (Fig. 1).

In what follows we show that the introduction of an extra inertial body allows for a further theoretical solution of the problem of low vibration emission without the necessity for increasing the operator's feed force.

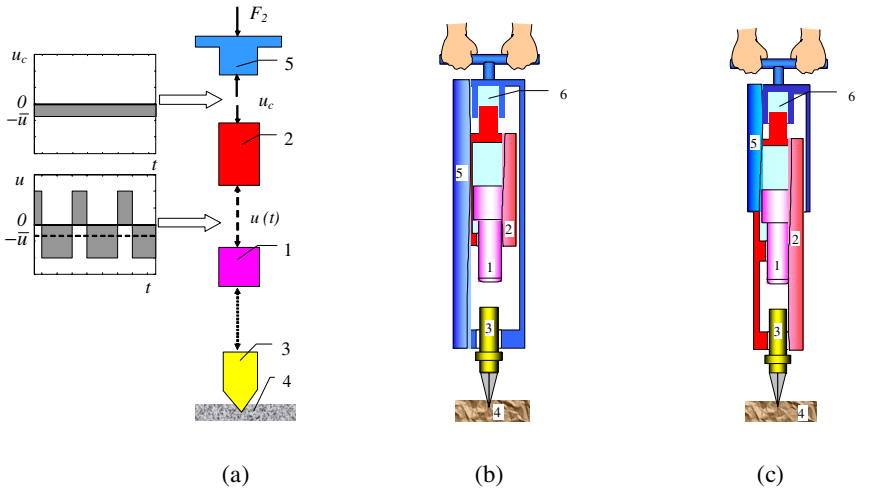

(a) (b) (c)

Fig. 3 Four-body system

3 Optimal Solution for Four-Body System

In the system shown in **Fig. 3**,a the striker 1 is subjected again to a sequence of upward impact impulses. These impulses are balanced by the excitation force *u(t)* with the constant downward component $\overline{u}$. Inevitably, the excitation force *u(t)* has an alternating component to provide the periodic vibro-impact motion of the striker. The excitation force *u(t)* is applied between the striker 1 and the inertial body 2. Unlike the striker, the latter body can be balanced on average by a downward constant force $u_c = \overline{u}$, but it still vibrates. The inertia force resulting from this vibration balances the alternating component of the excitation force. For this reason hereafter we conventionally refer to this body as a 'balance body'. The constant force is applied in this system between the balance body 2 and the body 5. The latter can be balanced by a constant feed force F_2 and can carry a vibration-free handle. This is the optimal four-body system with minimum emission of harmful vibration and minimum operator's feed force $F_2 = F = |\overline{u}|$. This scheme can be developed into two designs shown in Fig. 3,b and Fig. 3,c. Each of these modifications has both advantages and disadvantages. The main advantage of the former design is that the tool 3 is the only external part that vibrates in a steady-state regime, while the whole casing 5 does not vibrate. However, this design needs more complex arrangements to provide the alternating excitation force between bodies 1 and 2, both moving inside the motionless casing. The latter design is simpler; although only the handle 5 is free of vibration, while two other external parts (the casing 2 and the tool 3) vibrate.

Fig. 4,a shows an aggregated Mathlab-Simulink model used for the computer simulation of the system under review [4]. This is a multi-body mechanical system with nonlinear (impact) interaction of moving parts. Linear differential equations

were used to describe the continuous motion of free bodies between impacts or without impacts. Computational difficulties related to discontinuity of some variables during impacts were avoided by using the Kelvin-Voigt model of a viscous-elastic contact interaction of colliding bodies as introduced in [5,6].

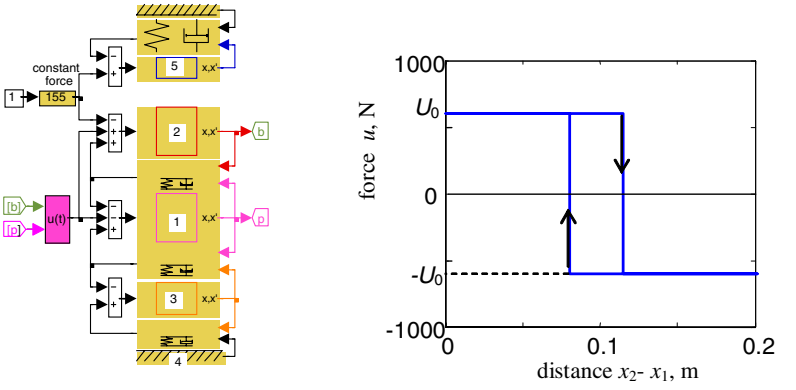

(a) (b)

Fig. 4 Model of four-body system

In the self-sustained system the excitation force *u(t)* was controlled by the relative position x_2-x_1 of the striker 1 and the balance body 2. The simplest relay law of control with U_0=600N was used as shown in Fig. 4,b. Such excitation is a good approximation to the one used in real hydraulic and pneumatic percussion machines.

Fig. 5,a presents an example of the resulting transient process and the stable steady-state regime of vibration of the four-body system; curve numbers correspond to the numbers of the bodies in Fig. 3. Fig. 5,b shows the steady-state regime in more detail (upper diagram) along with the excitation force *u* and the impact instants (lower diagram). Impact instants are shown with the dotted line.

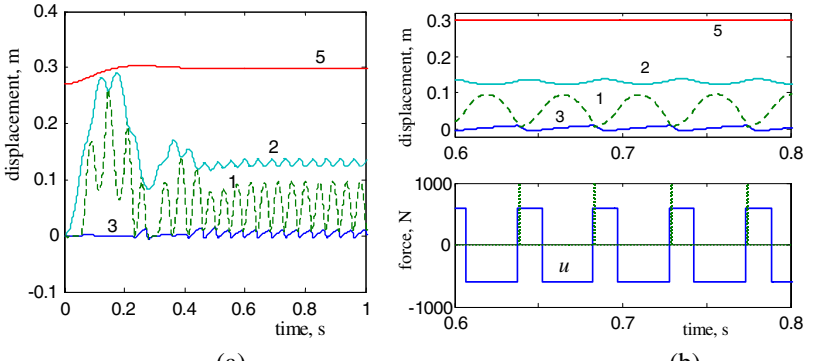

(a) (b)

Fig. 5 Transient process and steady-state regime of four-body system

These results were obtained for the following parameters: M_1=1.2kg, M_2=5kg, M_3=3.5kg, M_5=10kg, R_{12}=0.25, R_{24}=0.15, F_2=155N. The simulation has shown that the desired stable periodic regimes of vibration with single impact during a period of vibration can be obtained in a four-body system with a vibration-free handle. It is important that these regimes have low sensitivity to parameter deviations of the system.

4 Zero-Stiffness Suspension

Both designs shown in Fig. 3,b and Fig. 3,c feature some ideal element 6 that provides a constant force of interaction between the bodies 2 and 5. The structure in Fig. 3,c is in fact a very particular case of the common one of a percussion machine with the vibro-isolated handle. The main advantage of the new system - vibration-free handle/casing - is a result of the fact that the new ideal suspension ensures constant force and hence it has zero differential stiffness in contrast to a common design with a spring-suspended handle [7].

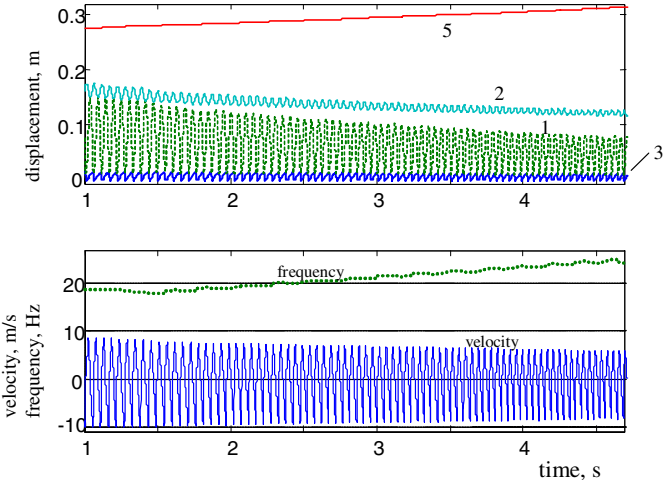

Fig. 6 Feed force variation: effect on vibro-impact regime

A question arises that as the operator cannot control the feed force, any inaccuracy in the zero-stiffness suspension constant force may destroy the necessary vibro-impact regime. Computer simulations have shown, however, that the vibro-impact regime has a very low sensitivity to the feed force. Fig. 6 demonstrates how the vibro-impact regime of the system shown in Fig. 4,a changes with variation of the operator's feed force. These results were obtained for the same parameters M_1, M_2, M_3, M_5, R_{12}, R_{24} as above, but the force F_2 gradually rising from 110N to 185N. The upper graph shows the displacements of the four bodies; the curve numbers correspond to the numbers of the bodies in

Fig. 3. The lower diagram shows the velocity of the striker and the frequency of self-excited vibration. Frequency is shown with a dotted line. It can be seen that the frequency of vibration rises and the impact velocity drops slightly with an increase in the feed force. The system demonstrates low sensitivity to variation of the feed force and the vibration remains stable when this force changes within a wide range.

It is important for this structure that although the amplitude of the balance body 2 vibration rises with a decrease in its mass, this does not affect the handle 5. The zero-stiffness suspension has a great potential for reduction of both the harmful vibration and the total mass of heavy-duty hand-held percussion tools.

The most natural and simplest zero-stiffness suspension can be achieved with a pneumatic or a hydraulic cylinder fed by a source of constant pressure (Fig. 7,a). This type of zero-stiffness suspension can be introduced naturally into pneumatic and hydraulic machines that are very common in manufacturing and construction. Solutions can be found for using such elements in suspension of electric machines as well.

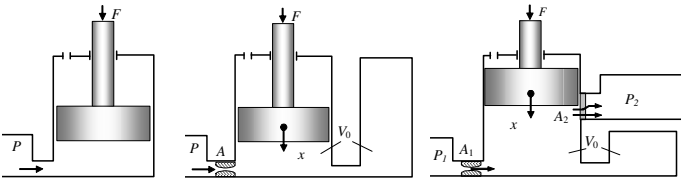

Fig. 7 Zero-stiffness suspension

In the zero-stiffness suspension the friction (damping) is the main reason of the vibration transmission from the machine to the operator. If a source of constant pressure is available some noticeable leakage through the gap between a piston and a cylinder is admissible. Hence there is no need to make this gap very small and as a result very low friction can be achieved. In this case a pneumatic cylinder can be very close to an ideal zero-stiffness element. However, an ideal source of constant pressure is not always available. In practice a pressure supply can have noticeable pulsations that can reduce all advantages of zero differential stiffness.

A possible solution for this case is shown in Fig. 7,b which allows for filtering of the high-frequency pressure pulsations. These pulsations can be suppressed significantly by increasing the volume V_0 of compressed air under the piston. However, in this case a pneumatic cylinder cannot be considered as an ideal zero-stiffness element. In fact it is more similar to the preloaded spring often used in common spring suspension. For high-frequency vibration the air volume below the piston can be considered as isolated from external pressure supply and adiabatic law can be applied: $PV^{\gamma} = P_0 V_0^{\gamma}$, where P is pressure, V is volume, γ=1.44 for air. The differential (dynamic) stiffness is calculated as

$$c_d = \frac{dF}{dx} = S\frac{dP}{dV}\frac{dV}{dx}\bigg|_{V=V_0} = \frac{S^2\gamma P_0}{V_0} \tag{7}$$

Here S is the piston area; P_0 is the average pressure; V_0 is total volume of air below the piston in the working position. Dynamic stiffness is inversely proportional to volume V_0 and can be made as low as needed increasing this volume. Also in this case the value of the gap between the cylinder and the piston is more important. If the effective area of the gap is comparable with the effective area A of the inlet orifice it affects the average pressure P_0 in the cylinder.

In hydraulic tools the scheme shown in Fig. 7,a can be applied without any alterations if a source of constant hydraulic pressure is available. Otherwise, in the case of a pulsating pressure source the scheme shown in Fig. 7,b can be used with an added gas accumulator as Fig. 7,c shows.

For example, hydraulic breakers are often used with a simple constant flow power pack. Reciprocating motion of the striking piston driven by the constant flow of hydraulic fluid results in high pulsations of pressure. Such breakers have a built-in gas accumulator designed to smooth the pressure pulsations. However, the remaining pulsations are still too high for this source of pressure to be used in the zero-stiffness suspension.

A possible solution is shown in Fig. 8,a which allows for filtering the high-frequency pressure pulsations. These pulsations can be suppressed significantly by increasing the volume of compressed air in the additional gas accumulator. Fig. 8,b shows an example of pressure diagrams in the main and additional gas accumulators.

In order to make a simple comparison between the hydraulic and pneumatic systems the expression (7) for dynamic stiffness can be rewritten in the following form:

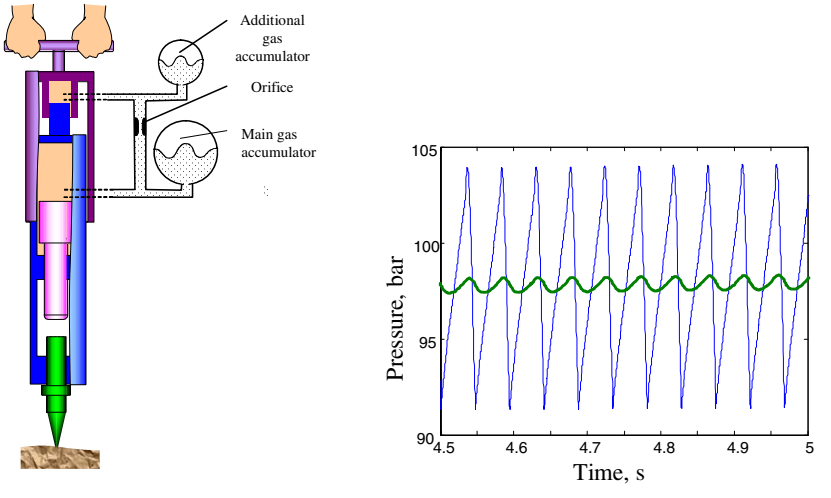

Fig. 8 Combination of gas accumulators in hydraulic breaker with hydro-pneumatic suspension

Fig. 9 New HM25LV hand-held commercial breaker

$$c_d = \gamma F^2 \frac{1}{P_0 V_0}, \tag{8}$$

where $F=P_0S$ is the feed force. This shows that for the prescribed feed force F the same low value of dynamic stiffness c_d can be achieved in a hydraulic system with a smaller volume V_0 of compressed air than in a pneumatic system. This is because the working pressure P_0 in hydraulic systems is usually much higher than in pneumatic systems.

As dynamic stiffness can easily be reduced when using hydraulic or pneumatic devices, more attention should be paid to friction (damping) that becomes the governing factor in transmission of vibration. Traditional bellows and modern rubber-metal analogues can be considered as a substitute to cylinders in some cases with the aim of reducing friction in the zero-stiffness suspension.

The solution shown in Fig. 7,c has been patented by JCB [8]. It was successfully tested on a modified commercially available heavy-duty hand-held hydraulic breaker HM25. Experiments have shown that more than a twofold increase in suppression of vertical vibration in the experimental model can be achieved compared to the original breaker with spring-suspended handles. These experiments have also shown that an operator does not have any serious difficulties while operating a breaker with zero-stiffness suspension, although the feel is slightly different as compared to operating a breaker with spring-suspended handles. The new commercial model HM25LV (Fig. 9) incorporating this solution was released recently by JCB. Despite being more powerful than predecessor HM25, this breaker has much lower hand and arm vibration (HAV) levels than competing models. Operators can safely use this machine for a full eight-hour day without exceeding new EU strict recommended levels for HAV exposure.

5 Conclusions

It is possible to design a hand-held percussion machine with an intensive vibro-impact process on one side and a vibration-free handle on the other side. The

simplest three-body system with one vibration-free body needs a higher operator's feed force than conventional machines. In the four-body system, however, this can be achieved without an increase in the feed force. The feasibility of this solution was proved by computer simulations and verified experimentally. This approach has great potential in reducing vibration transmitted to the operator. In practice, this reduction is limited only by friction in the zero-stiffness suspension of the handle.

Acknowledgements. Authors thank the management and employees of JCB for support of this project and fruitful collaboration.

References

1. Babitsky, V.I.: Hand-Held Percussion Machine As Discrete Non-Linear Converter. Journal of Sound and Vibration 214, 165–182 (1998); erratum 222(5), (1999)
2. Atlas Copco manual. Atlas Copco, 4th edn., pp. 185–186 (1982)
3. Anderson, S.: RDR-36 - a new chipping hammer with unique design. Atlas Copco, Stockholm (1976)
4. Sokolov, I.J., Babitsky, V.I., Halliwell, N.A.: Hand-Held Percussion Machines with Low Emission of Hazardous Vibration. Journal of Sound and Vibration 306, 59–73 (2007)
5. Babitsky, V.I.: Theory of Vibro-Impact Systems and Applications, Appendix I: Simulation of impact on viscoelastic limiter. Springer, Berlin (1998)
6. Babitsky, V.I., Veprik, A.M.: Universal Bumpered Vibration Isolator for Severe Environment. Journal of Sound and Vibration 218, 269–292 (1998)
7. Alabuzhev, P., Gritchin, A., Kim, L., Migirenko, G., Chon, V., Stepanov, P.: Vibration Protecting and Measuring Systems with Quasi-Zero Stiffness. Hemisphere Publishing Co., New York (1989)
8. Malkin, A.A., Sokolov, I., Babitsky, V.: Percussion Power Tool Apparatus with Shock Absorbing Piston Arrangement. UK Patent GB2421466

Ship Roll Motion under Stochastic Agencies Using Path Integral Method

G. Cottone, M. Di Paola, R. Ibrahim, A. Pirrotta, and R. Santoro

Abstract. The response of ship roll oscillation under random ice impulsive loads modeled by Poisson arrival process is very important in studying the safety of ships navigation in cold regions. Under both external and parametric random excitations the evolution of the probability density function of roll motion is evaluated using the path integral (PI) approach. The PI method relies on the Chapman-Kolmogorov equation, which governs the response transition probability density functions at two close intervals of time. Once the response probability density function at an early close time is specified, its value at later close time can be evaluated. The PI method is first demonstrated via simple dynamical models and then applied for ship roll dynamics under random impulsive white noise excitation.

Introduction

Ice loads acting on ocean systems are random in nature and have non-smooth characteristics when they are of impact type. In full-scale experiments, measurements of ice local and global loads revealed randomness in the ice forces and pressures [1, 2]. In some cases, ice loads are of impact type and have been assumed as a Poisson arrival process of loading events. Thus, one must deal with probabilistic approaches when studying ships' stochastic stability, response, and reliability. The treatment of dynamical systems under Poisson random processes has been considered in references [3-5].

For systems under normal or non-normal white noise, the response statistics may be obtained by solving the Fokker-Plank Kolmogorov (FPK) equation or the kolmogorov-Feller equation. However, exact solutions of the partial differential equations governing the evolution of the response probability density function (*pdf*) is known only for very few cases [6-8]. Alternatively, several approximate solutions techniques have been developed including variational methods based on eigenfunction expansion of the transition *pdf* [9], finite element method [10], and

G. Cottone, M. Di Paola, A. Pirrotta, and R. Santoro
Dipartimento di Ingegneria Strutturale e Geotecnica,Viale delle Scienze, I-90128, Palermo, Italy

R. Ibrahim
Wayne State University, Department of Mechanical Engineering, Detroit, MI 48202, USA

R.A. Ibrahim et al. (Eds.): Vibro-Impact Dynamics of Ocean Systems, LNACM 44, pp. 29–40.
springerlink.com

the path integration approach [3]. The PI approach is an effective tool for evaluating the response in terms of probability density at each time instant, for evaluating moments of various orders, energy response *pdf*, first passage time of strong nonlinear systems. This approach is based on rewriting the FPK equation in integral form in which the kernel is the transition probability density function. Thus one can evaluate the response *pdf* at time $(t+\tau)$ when its value at an early close time instant (t) is already specified. The crucial point is to define the kernel according to the system under investigation. In the case of normal white noise, if τ is small, even if the system is nonlinear, the transition *pdf* is almost Gaussian (short-time Gaussian approximation). It follows that the kernel of the integral form is Gaussian and this simplifies the analysis [11]. The accuracy of this method is was validated using Monte Carlo simulation and the exact solution when the latter is available. Recently, Di Paola and Santoro [12] have studied the case of Poisson white noise by evaluating the conditional probability density function (*cpdf*) in order to apply the PI method also for these systems. However, the case of Gaussian white noise acting simultaneously with Poisson white noise has not yet been considered in the literature and the present work is an attempt to extend the PI method for this case. In particular, the method will be utilized to examine the ship roll oscillation under parametric normal white noise acting simultaneously with additive Poisson white noise.

1 Path Integral Method

This section provides the general features of the PI method by adopting a simple nonlinear system driven by a white noise described by the one-dimensional equation:

$$\begin{cases} \dot{\mathrm{X}}(t) = -\alpha \mathrm{X}(t) + f(\mathrm{X},t) + W(t) \\ \mathrm{X}(0) = \mathrm{X}_0 \end{cases} \tag{1}$$

where $f(\mathrm{X},t)$ is a deterministic nonlinear function of the response X(t) and time t, α is a positive parameter and *W(t)* is a white noise and X_0 is the initial condition that may be either deterministic or random (Gaussian or non-Gaussian).

The starting point of the PI method is the Chapman-Kolmogorov equation that holds true, because of the Markovian property of the response:

$$\mathrm{p}_{\mathrm{X}}(x,t+\tau) = \int_D \mathrm{p}_{\mathrm{X}}(x,t+\tau|\bar{x},t)\mathrm{p}_{\mathrm{X}}(\bar{x},t)\mathrm{d}\bar{x} \tag{2}$$

The numerical implementation of the PI method requires selecting a computational domain D. It is convenient to select a symmetrical computational domain with a given maximum size $x_{\max} = |x_1|$, i.e., $-x_1 \le x \le x_1$. The size of the domain is identified by, first, running a Monte Carlo simulation with a low number of samples. Then, dividing the domain in a discrete number of intervals, n_x, for each

grid point, the path integral from equation (2) can be evaluated. One has to evaluate the kernel in equation (2), which requires the conditional joint *pdf*. From the entire set of trajectories of the response process $\mathrm{X}(\mathrm{t})$, one has to select those deterministic values at time t, i.e., $\bar{x}$, hereafter denoted as $\overline{\mathrm{X}}(\rho)$ (see Fig.1), by solving of the following differential equation:

$$\begin{cases} \dot{\overline{\mathrm{X}}}(\rho) = -\alpha \overline{\mathrm{X}}(\rho) + f(\overline{\mathrm{X}}, \rho) + W(t+\rho) \\ \overline{\mathrm{X}}(0) = \bar{x} \end{cases} \tag{3}$$

where $\bar{x}$ is a deterministic initial condition and $0 \le \rho \le \tau$. Note that the *cpdf* of equation (1) coincides with the unconditional PDF of equation (3) evaluated at τ, i.e.,

$$\mathrm{p}_{\mathrm{X}}(x, t+\tau \,|\, \bar{x}, t) = \mathrm{p}_{\overline{\mathrm{X}}}(x, \tau) \tag{4}$$

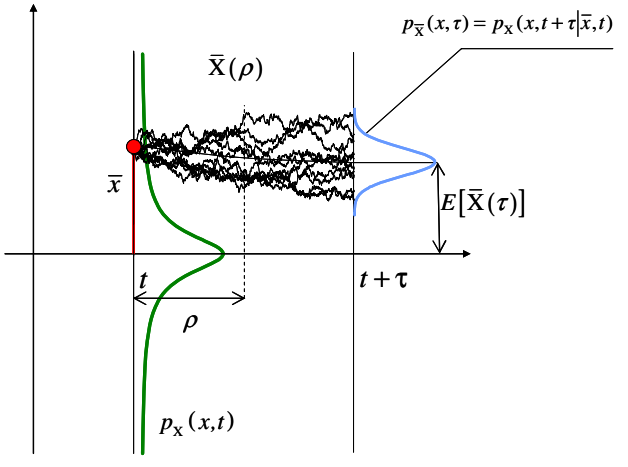

Fig. 1 Sample functions of the process $\overline{\mathrm{X}}(\rho)$ and conditional pdf

Fig.1 demostrates the significance of the *cpdf* of the stochastic process $\overline{\mathrm{X}}(\rho)$ evaluated in $\rho = \tau$. These are the general features of the PI method. To this end the problem is to specify the kernel, which is dependent on the system and excitation characteristics.

1.1 Systems under Poisson White Noise

Sample functions of Poisson white noise process $W_{\mathrm{P}}(t)$ in equation (1) may be written in the form

$$W_{\mathrm{P}}(t) = \sum_{i=1}^{N(t)} R_i \delta(t - T_i) \tag{5}$$

where $\delta(\bullet)$ is the Dirac's Delta function, R_i is the *i-th* realization of the random variable *R* with assigned probability density function $p_R(r)$. T_i is the *i-th* realization of the random variable *T* independent of R and distributed in time according to the Poisson law and *N*(*t*) is the so-called *counting process* giving the total number of impulse occurrences in $[0, t)$. The whole process defined by equation (5) is fully described by the cumulants:

$$K_n[W_P(t_1)W_P(t_2)...W_P(t_n)] = \lambda E\left[\mathrm{R}^n\right]\delta(t_1 - t_2)...\delta(t_1 - t_n) \tag{6}$$

where λ is the mean number of impulse occurrences per unit time.

Replacing $W(t)$ by $W_{\mathrm{P}}(t)$ in equation (1) one can describe the evolution of the system response *pdf* by the Kolmogorov-Feller equation

$$\frac{\partial p_{\mathrm{X}}(x,t)}{\partial t} = -\frac{\partial}{\partial x}(\beta(x,t)p_{\mathrm{X}}(x,t)) - \lambda p_{\mathrm{X}}(x,t) + \lambda \int_{-\infty}^{+\infty} p_{\mathrm{R}}(r-y)p_{\mathrm{X}}(y)\mathrm{d}y \tag{7}$$

where $p_{\mathrm{X}}(x,t)$ and $p_{\mathrm{R}}(r)$ are the unconditional *pdf* of the response process *X(t)* and of the random variable *R*, respectively, and $\beta(x,t) = -\alpha x(t) + f(x,t)$.

The *cpdf* $p_{\mathrm{X}}(x, t+\tau \,|\, \overline{x}, t)$ may be obtained by evaluating the unconditional *pdf* in τ of the following differential equation:

$$\begin{cases} \dot{\overline{\mathrm{X}}}(\rho) = -\alpha\overline{\mathrm{X}}(\rho) + f(\overline{\mathrm{X}}, \rho) + W_{\mathrm{P}}(t+\rho); \quad 0 \le \rho \le \tau \\ \overline{\mathrm{X}}(0) = \overline{x} \end{cases} \tag{8}$$

Considering τ to be small, there are two possible different situations in the interval $(t \div t+\tau)$. The first does not contain any spikes and this happens in mean $1 - \lambda(t)\tau$ times. The second contains one spike whose amplitude possesses the distribution of *R*. This situation happens $\lambda(t)\tau$ times. Since the time interval τ is small an approximation of $\overline{X}(t)$, when no spikes occur, is given by solving equation (1), in which we set $W(t) = W_P(t) = 0$, as:

$$\overline{\mathrm{X}}(\tau) = \overline{x} - \alpha\overline{x}\tau + f(\overline{x}, t)\tau = y(\overline{x}, t, \tau) \tag{9}$$

The function $y(\overline{x}, t, \tau)$ will be denoted as $y(\overline{x})$. When one spike occurs, $\overline{X}(\tau)$ may be evaluated in the approximate form

$$\overline{X}(\tau) = y(\overline{x}) + R \tag{10}$$

Equation (10) remains valid when τ is small, but if τ is not small the location of the spikes within the interval τ will influence the value $\bar{X}(\tau)$.

Equation (9) is deterministic over the time increment $1-\lambda(t)\tau$ and thus the entire sample functions of the response process gives a contribution in the *pdf* of $\bar{X}(\rho)$ in the form $(1-\lambda(t)\tau)\delta(x-y(\bar{x}))$.

In the remaining $\lambda(t)\tau$ sample functions in which a spike occurs one may inspect equation (10), which reveals that $\bar{X}(\tau)$ is a random variable composed of a deterministic plus a random variable with a given *pdf*. It follows that the *pdf* of $\bar{X}(\rho)$ in τ is $p_R(x-y(\bar{x}))$, and this occurs over the time increment $\lambda(t)\tau$. The resulting *cpdf* is

$$p_X(x,t+\tau\,|\,\bar{x},t)=(1-\lambda(t)\tau)\delta(x-y(\bar{x}))+\lambda(t)\tau p_R(x-y(\bar{x})) \tag{11}$$

Substituting equation (11) into equation (2), gives

$$p_X(x,t+\tau)=(1-\lambda(t)\tau)\int_{-\infty}^{+\infty}\delta(x-y(\bar{x}))\,p_X(\bar{x},t)d\bar{x}$$

$$+\lambda(t)\tau\int_{-\infty}^{+\infty}p_R(x-y(\bar{x}))p_X(\bar{x},t)d\bar{x} \tag{12}$$

Since $\bar{x}$ and $y(\bar{x})$ are nonlinear the following relationship holds

$$p_{\mathrm{X}}(\bar{x},t)\mathrm{d}\bar{x}=p_{\mathrm{Y}}(y(\bar{x}),t)\mathrm{d}y(\bar{x}) \tag{13}$$

In this case, equation (12) may be rewritten in the form

$$p_{\mathrm{X}}(x,t+\tau)=(1-\lambda(t)\tau)p_{\mathrm{Y}}(x,t)+\lambda(t)\tau\int_{-\infty}^{+\infty}p_{\mathrm{R}}(x-y)p_{\mathrm{Y}}(y,t)\mathrm{d}y \tag{14}$$

where according to equation (9), one can write

$$p_{\mathrm{Y}}(y,t)=p_{\mathrm{X}}(x=\frac{g(y),t)}{|y'(x)|} \tag{15}$$

where $g(y)$ is the inverse relationship obtained from equation (9). Equation (14) represents an extension of the PI method to a Poisson white noise input.

Equation (14) is a simple integral equation while the Kolmogorov-Feller equation represented by equation (7) is an integro-differential equation. In order to study the ship roll motion another version of the PI method is necessary for the case of combined normal and Poisson white noise.

1.2 Systems under Normal and Poisson White Noise Excitations

The *cpdf* of the response of systems driven simultaneously by Gaussian white noise $W_0(t)$ and Poisson white noise $W_p(t)$, is not available, and hence the PI method may not be implemented. The normal white noise, $W_0(t)$, is characterized by the correlation function:

$$E[W_0(t_1)W_0(t_2)] = q(t_1)\delta(t_1 - t_2) = q(t_2)\delta(t_1 - t_2) \tag{16}$$

where $E[\bullet]$ denotes the ensemble average, $q(t)$ is the strength of the normal white noise (if $W_0(t)$ is stationary then $q(t)=q$) .

Note that we don't have either an equation governing the evolution of response *pdf* or an analytical expression for the kernel in (2). However, the *cpdf* $p_X(x, t+\tau|\overline{x}, t)$ may be obtained by evaluating the unconditional *pdf* in τ of the following differential equation:

$$\begin{cases} \dot{\overline{X}}(\rho) = -\alpha\overline{X}(\rho) + f(\overline{X},\rho) + W_0(t+\rho) + W_p(t+\rho) \\ \overline{X}(0) = \overline{x} \end{cases} \tag{17}$$

Again considering τ to be small, there are two different situations over the interval τ. The first does not have spikes in the presence of the Gaussian white noise, and this happens over the time increment $1-\lambda(t)\tau$. The second case does have one spike whose amplitude possesses the distribution of *R*, simultaneously with the Gaussian one. The latter situation happens over the time increment $\lambda(t)\tau$.

For the first case where no spikes occur, one has to solve equation (17) under Gaussian white noise and setting $W_p(t+\rho) = 0$. Furthermore, if τ is small, the so called short time Gaussian approximation may be used, i.e., $p_{\overline{X}}(x,\tau)$ follows a Gaussian distribution. Then in the *pdf* of whole sample functions of the response may take the following function

$$p_{\overline{X}(\rho)}|_{(1-\lambda\tau)} = (1-\lambda\tau)\frac{1}{\sqrt{2\pi q(t)\tau}}\exp\left(-\frac{(x-\overline{x}-(-\alpha\overline{x}+f(\overline{x},t))\tau)^2}{2q(t)\tau}\right) \tag{18}$$

In the remaining time increment $\lambda(t)\tau$ a spike occurs with a Gaussian white noise, and one has to consider the *pdf* of a sum of two random variables, one is Gaussian and the other is the random variable R with an assigned *pdf*. It follows that in the whole sample function, in which the spike occurs with the Gaussian white noise, one has a *pdf* of $\overline{X}(\rho)$ in τ given by the convolution integral

$$p_{\overline{X}(\rho)}|_{\lambda\tau} = (\lambda\tau)\int_{-\infty}^{\infty}\frac{1}{\sqrt{2\pi q(t)\tau}}\exp\left(-\frac{(\xi-\overline{x}-(-\alpha\overline{x}+f(\overline{x},t))\tau)^2}{2q(t)\tau}\right)p_R(x-\xi)\,d\xi \tag{19}$$

The resulting *cpdf* is given by

$$p_X(x,t+\tau\,|\,\overline{x},t)=(1-\lambda\tau)\frac{1}{\sqrt{2\pi q(t)\tau}}\exp\left(-\frac{(x-\overline{x}-(-\alpha\overline{x}+f(\overline{x},t))\tau)^2}{2q(t)\tau}\right)+$$

$$(\lambda\tau)\int_{-\infty}^{\infty}\frac{1}{\sqrt{2\pi q(t)\tau}}\exp\left(-\frac{(\xi-\overline{x}-(-\alpha\overline{x}+f(\overline{x},t))\tau)^2}{2q(t)\tau}\right)p_R(x-\xi)\,d\xi \qquad (20)$$

Substituting equation (20) into equation (2) yields the PI solution extended to the case of combined case of Gaussian and Poisson white noises. The expression given by equation (20) is applied to the system (17) with $\alpha=1$, and $f(\mathrm{X},t)=-1/2\,\mathrm{X}(t)|\mathrm{X}(t)|$. The Gaussian noise $W_0(t)$ is assumed to have unit intensity, $q=1$, while the Poisson noise $W_P(t)$ possesses a unitary mean rate arrival λ, and $p_R(x)$ is Gaussian distributed with mean $\mu_R=1.5$ and variance $\sigma_R^2=2.25$. The initial condition X_0 is a standard Gaussian distribution. In order to use the short time Gaussian approximation the time interval is selected to be $\tau=0.1$. To validate the proposed method, Monte Carlo (MC) simulation of equation (1) has been performed using Euler's integration scheme with 5000 samples and increment of time 0.005 sec. Fig. 2(a) shows a three-dimensional representation of the time evolution of the response *pdf* with initial Gaussian *pdf*. It is seen that as the time increases the response *pdf* evolves to a bimodal representation with two peaks around the zero mean value. The results are validated by MC simulation and Fig. 2(b) shows a comparison of the stationary response *pdf* as generated from MC simulation and PI solution.

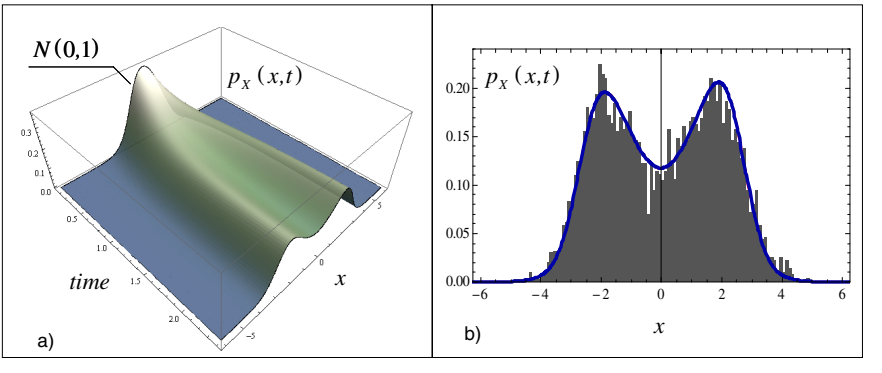

Fig. 2 Response probability density function: a) Time evolution of the response *pdf* as obtained by PI solution; b) Monte Carlo validation for the stationary state

2 Ship Roll Motion under Stochastic Agencies

The study of ship dynamics in following sea waves was first reported by Froude [13] who observed that ships have undesirable roll characteristics when the

frequency of small free oscillations in pitch is twice the frequency of a small free oscillation in roll. It was Paulling and Rosenberg [14] who formulated the analytical modeling of the coupled roll-pitch motion. This coupled motion is described by two nonlinear differential equations. If the nonlinear effect of roll is neglected, the pitch equation of motion is reduced to a linear differential equation, which is free from roll motion terms. When the pitch equation is solved, its response appears as a coefficient to the restoring moment of roll motion, and the roll equation of motion is reduced to Mathieu's equation. These studies did not take into account the nonlinear effects of drag and restoring moments. The nonlinear damping moment is proportional to the product of the roll velocity times its absolute value and acts in a direction opposite to the velocity. This is usually represented by the expression, $a\dot{\phi}\left|\dot{\phi}\right|$, where a is a constant determined experimentally. Based on these considerations the roll dynamics of a ship subjected to simultaneous impulse excitation, $W_{\mathrm{P}}(t)$, and parametric random excitation, W_0, is described by the equation of motion [15]:

$$\begin{aligned} &\ddot{\phi}+2\tilde{\zeta}\omega_n\dot{\phi}+a\dot{\phi}\left|\dot{\phi}\right|+\omega_n^2\phi-\bar{\delta}\phi^3+W_0(t)\phi=W_{\mathrm{P}}(t) \\ &\phi(0)=\phi_0 \quad ; \quad \dot{\phi}(0)=\dot{\phi}_0 \end{aligned} \tag{21}$$

Where ϕ is the ship roll angle, ω_n is the natural frequency of the ship roll oscillation, $\tilde{\zeta}$ is a linear damping factor, the third term represents nonlinear damping, and the cubic term is due to the restoring moment together with the linear term. In particular $W_0(t)$ represents the pitch angle which is assumed to be random stationary process and the right-hand side is the sea wave moment acting on the ship and is represented by the Poisson random process given by equation (5). Note that at the roll angle $\phi_{\mathrm{c}}=\pm\omega_{\mathrm{n}}/\sqrt{\bar{\delta}}$, the ship experiences capsizing. If we consider $W_0(t)$ as a normal white noise, the ship roll dynamics is captured by the solution of a single oscillator under parametric normal white noise acting simultaneously with an external Poisson white noise. Equation (21) may be rewritten in terms of state variables as follows

$$\dot{\mathbf{Z}}(t)=\mathbf{D}\mathbf{Z}(t)+\mathbf{f}(\mathbf{Z},t)+\mathbf{L}W_{\mathrm{P}}(t) \tag{22}$$

Where $$\mathbf{Z}(t)=\begin{bmatrix}Z_1(t)\\Z_2(t)\end{bmatrix}=\begin{bmatrix}\phi(t)\\\dot{\phi}(t)\end{bmatrix};\quad \mathbf{D}=\begin{bmatrix}0 & 1\\-\omega_n^2 & -2\tilde{\zeta}\omega_n\end{bmatrix}$$

$$\mathbf{f}(\mathbf{Z}(t),t)=\begin{bmatrix}0\\-aZ_2\left|Z_2\right|+\delta Z_1^3-Z_1W_0(t)\end{bmatrix};\quad \mathbf{L}=\begin{bmatrix}0\\1\end{bmatrix}$$

For this case the Chapman Kolmogorov equation is given in the form:

$$\mathrm{p}_{\mathbf{Z}}(z_1,z_2,t+\tau)=\int_{-\infty}^{+\infty}\int_{-\infty}^{+\infty}\mathrm{p}_{\mathbf{Z}}(z_1,z_2,t+\tau\left|\bar{z}_1,\bar{z}_2,t\right.)\mathrm{p}_{\mathbf{Z}}(\bar{z}_1,\bar{z}_2,t)\mathrm{d}\bar{z}_1\mathrm{d}\bar{z}_2 \tag{23}$$

The conditional *pdf* in equation (23) may be derived by considering the *pdf* of the response over the time interval τ of the following system

$$\begin{cases} \dot{\bar{\mathbf{Z}}}(\rho) = \mathbf{D}\bar{\mathbf{Z}}(\rho) + \mathbf{f}\left(\bar{\mathbf{Z}}, \rho\right) + \mathbf{L}W\left(t+\rho\right) \\ \bar{\mathbf{Z}}(0) = \bar{\mathbf{z}} \end{cases} \tag{24}$$

Where the initial conditions are the considered deterministic, $\bar{\mathbf{z}}^T = \left[\bar{z}_1, \bar{z}_2\right]$. Equations (24) may be rewritten in the state vector form

$$\begin{aligned} &\dot{\bar{Z}}_1(\rho) = \bar{Z}_2(\rho) \\ &\dot{\bar{Z}}_2(\rho) = -2\tilde{\zeta}\omega_n \bar{Z}_2(\rho) - \omega_n^2 \bar{Z}_1(\rho) - a\bar{Z}_2(\rho)\left|\bar{Z}_2(\rho)\right| + \delta\bar{Z}_1(\rho)^3 - \\ &\qquad \bar{Z}_1 W_0(t+\rho) + W_p(t+\rho) \\ &\bar{Z}_1(0) = \bar{z}_1;\ \bar{Z}_2(0) = \bar{z}_2 \end{aligned} \tag{25}$$

For small τ, equations (25) yield the following statistics

$$E\left[\bar{Z}_1(\tau)\right] = \bar{z}_1 + \bar{z}_2\tau = y_1(\bar{z}_1, \bar{z}_2);\quad \sigma^2_{\bar{Z}_1}(\tau) = 0 \tag{26}$$

$$p_{\bar{Z}_1}(z_1, \bar{z}_1, \bar{z}_2; \tau) = \delta(z_1 - y_1(\bar{z}_1, \bar{z}_2)) \tag{27}$$

Again, for small τ there are two different situations over time interval τ. The first does not contain spikes in the presence of the normal white noise, and this happens over the time increment $1-\lambda(t)\tau$. The second includes one spike which occurs simultaneously with the normal white noise over the time increment $\lambda(t)\tau$. In the first case we set $W_{\mathrm{p}}(t) = 0$

$$\begin{aligned} &E\left[\bar{Z}_2(\tau)\right] = \bar{z}_2 - \left(2\tilde{\zeta}\omega_n \bar{z}_2 + \omega_n^2 \bar{z}_1 + a\bar{z}_2\left|\bar{z}_2\right| - \delta\bar{z}_1^3\right)\tau = y_2\left(\bar{z}_1, \bar{z}_2\right) \\ &\sigma^2_{\bar{Z}_2}(\tau) = \mathrm{E}\left[\bar{Z}_2^2(\tau)\right] - \left(\mathrm{E}\left[\bar{Z}_2(\tau)\right]\right)^2 = \bar{z}_1^2 q\tau \end{aligned} \tag{28}$$

Since $\bar{Z}_1$ is deterministic, the two processes $\bar{Z}_1$ and $\bar{Z}_2$ are independent. In the absence of spikes the contribution for the whole conditional *pdf* in equation (23) is given in the form

$$\mathrm{p}_{\mathbf{Z}}(z_1, z_2, t+\tau\left|\bar{z}_1, \bar{z}_2, t\right)_{\text{no spikes}} = (1-\lambda\tau)\frac{\delta\left(z_1 - \left(\bar{z}_1 + \bar{z}_2\tau\right)\right)}{\sqrt{2\pi\bar{z}_1^2 q\tau}} \exp\left(-\frac{\left(z_2 - y_2\left(\bar{z}_1, \bar{z}_2\right)\right)^2}{2\bar{z}_1^2 q\tau}\right) \tag{29}$$

The other contribution is given by the convolution integral of both excitations:

$$\begin{aligned} &\mathrm{p}_{\mathbf{Z}}(z_1, z_2, t+\tau\left|\bar{z}_1, \bar{z}_2, t\right)_{\text{one spike}} = \\ &\frac{\lambda\tau\delta\left(z_1 - \left(\bar{z}_1 + \bar{z}_2\tau\right)\right)}{\sqrt{2\pi\bar{z}_1^2 q\tau}} \int_{-\infty}^{+\infty} exp\left(-\frac{(\xi - y_2(\bar{z}_1, \bar{z}_2))^2}{2\bar{z}_1^2 q\tau}\right) p_R(z_2 - \xi)d\xi \end{aligned} \tag{30}$$

The *cpdf* of the kernel of equation (23) is

$$p_{\mathbf{Z}}(z_1,z_2,t+\tau|\bar{z}_1,\bar{z}_2,t)=\delta\left(z_1-(\bar{z}_1+\bar{z}_2\tau)\right)\left[\frac{(1-\lambda\tau)}{\sqrt{2\pi\bar{z}_1^2 q\tau}}\exp\left(-\frac{\left(z_2-y_2(\bar{z}_1,\bar{z}_2)\right)^2}{2\bar{z}_1^2 q\tau}\right)+\right.$$

$$\left.\frac{\lambda\tau}{\sqrt{2\pi\bar{z}_1^2 q\tau}}\int_{-\infty}^{+\infty} exp\left(-\frac{(\xi-y_2(\bar{z}_1,\bar{z}_2))^2}{2\bar{z}_1^2 q\tau}\right)p_R(z_2-\xi)d\xi\right] \qquad (31)$$

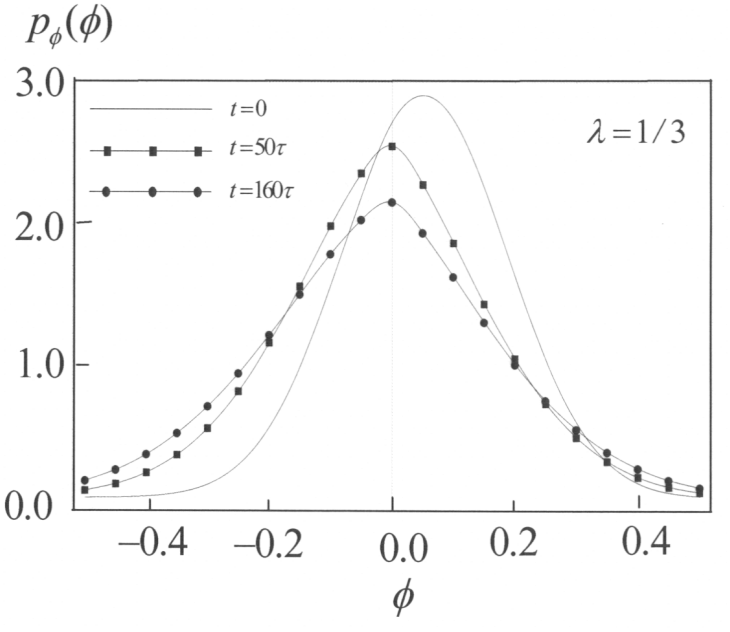

Fig. 3 Response *pdf* at discrete time intervals

The ship roll response *pdf* is determined for $\zeta=0.1$, $\omega=1$, $a=0.005$, and $\delta=0.006$. The external Poisson white noise $W_P(t)$ has a jump Gaussian distribution $p_R(x)$ with zero mean and standard deviation $\sigma_R=0.07$, and the mean rate arrival $\lambda=1/3$. The parametric normal white noise $W_0(t)$ is assumed to possess an intensity parameter $q=0.05$. The initial condition $p_{\phi\dot{\phi}}(\phi,\dot{\phi};0)$ is assumed to be a bivariate normal distribution with vector mean $(0.05,0.025)$ and covariance matrix $\Sigma=\begin{pmatrix}0.133^2 & 0\\ 0 & 0.133^2\end{pmatrix}$. Integrals have been performed numerically on a grid of $\Delta\phi=\Delta\dot{\phi}=0.01$ and time step $\tau=0.1$sec.

Fig. 3 shows the evolution of the response *pdf* at various time instants starting from the initial condition. It is seen that the ship response *pdf* is essentially

non-Gaussian and the mean value is shifted with time towards the zero value. The influence of the mean rate arrival is evaluated by considering different values of $\lambda = 1/3, 1, 3$. The results are shown in Fig. 4 and reveal that as the mean rate arrival of ice impacts increases the response *pdf* is found to be spread and the extreme ship roll angle is extended towards a dangerous value of the capsizing roll angle. Furthermore, as the mean rate arrival increases, the peak of the response *pdf* is reduced. In other words, the probability of the ship response to reach the capsizing angle increases as the mean rate arrival increases.

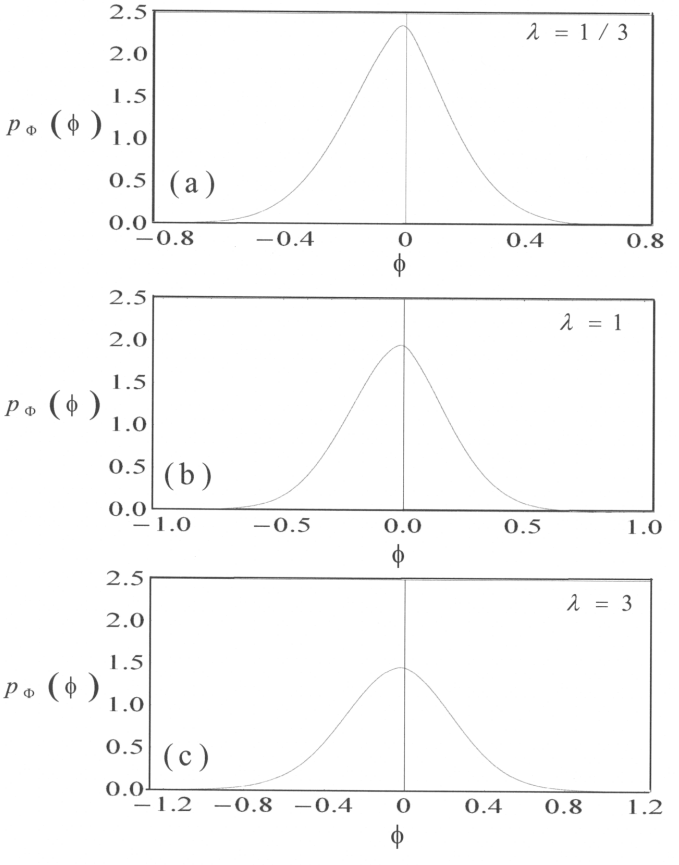

Fig. 4 Response *pdf* of ship roll angle for three different values of the mean rate arrival parameter $\lambda = 1/3, 1,$ and 3

3 Conclusions

The method of path integral has been implemented to the problem of ship roll oscillations subjected to simultaneous white noise parametric excitation and addition pulse excitation. The additive excitation simulates the pulse of random events of

floating ice impact to the ship. It has been found that the evolution of the ship response probability density function is essentially non-Gaussian and the mean value is shifted with time towards a zero value. As the mean rate arrival of ice impacts increases the response *pdf* is found to be spread and the extreme ship roll angle is extended towards a dangerous value of the capsizing roll angle.

Acknowledgement. The third author was supported by a grant from the Office of Naval Research under Award No: N00014-05-1-0040. Dr. Kelly B. Cooper is the Program Director.

References

[1] Timco, G.W., Johnston, M.: Ice loads on the caisson structures in the Canadian Beaufort Sea. Cold Regions Science and Technology 38, 185–209 (2004)
[2] Meyerhoff, W.K., Schlachter, G.: An approach for the determination of hull-girder loads in a seaway including hydrodynamic impacts. Ocean Engineering 7(2), 305–326 (1980)
[3] Köylüoğlu, H.U., Nielsen, S.R.K., Iwankiewicz, R.: Response and reliability of Poisson-driven systems by path integration. ASCE Journal of Engineering Mechanics 121(1), 117–130 (1995)
[4] Di Paola, M., Pirrotta, A.: Nonlinear systems under impulsive parametric input. International Journal of Nonlinear Mechanics 34, 843–851 (1999)
[5] Proppe, C.: Exact stationary probability density functions for nonlinear systems under Poisson white noise excitation. International Journal of Nonlinear Mechanics 38, 557–564 (2003)
[6] Caughey, T.K., Dienes, J.K.: Analysis of Nonlinear First-Order system with a White Noise Input. Journal of Applied Physics 32(11), 2476–2483 (1961)
[7] Dimentberg, M.F.: An Exact Solution to a Certain Nonlinear Random Vibration Problem. International Journal of Non-linear Mechanics 17(4), 231–236 (1982)
[8] Vasta, M.: Exact stationary solution for a class of nonlinear systems driven by a non-normal delta-correlated processes. Int. J. Nonlin. Mech. 30(4), 407–418 (1995)
[9] Atkinson, J.D.: Eigenfunction expansions for randomly excited nonlinear systems. J. Sound & Vib. 30, 153–172 (1973)
[10] Spencer, B.F., Bergman, L.A.: On the numerical solution of the Fokker- Planck equation for nonlinear stochastic systems. Nonlin. Dyn. 4, 357–372 (1993)
[11] Barone, G., Navarra, G., Pirrotta, A.: Probabilistic response of linear structures equipped with nonlinear damper devices (PIS method). Probab. Eng. Mech. 23(2-3), 125–133 (2008)
[12] Di Paola, M., Santoro, R.: Nonlinear systems under Poisson white noise handled by path integral solution. J. Vib. & Control 14(1-2), 35–49 (2008)
[13] Froude, W.F.: Remarks on Mr. Scott Russell's paper on rolling. Trans. Inst. Naval. Res. 4, 232–275 (1863)
[14] Paulling, J.R., Rosenberg, R.M.: On unstable ship motions resulting from nonlinear coupling. J. Ship. Res. 2, 36–46 (1959)
[15] Ibrahim, R.A.: Noise-Induced Transition in Ships Roll Oscillation. Adv. Studies Theor. Phys. 2(2), 51–69 (2008)

Control of Instabilities Induced by Low-Velocity Collisions in a Vibro-Impacting System with Friction

Harry Dankowicz and Fredrik Svahn

Abstract. The onset of low-velocity collisions in vibro-impacting systems induces instabilities in the system dynamics that, when not checked, may result in sudden, and unanticipated discontinuous transitions between distinct steady-state responses. This paper illustrates this phenomenology in an example system that includes dry friction. Here, the instability is associated with the zero-velocity contact of an oscillatory unilateral constraint and a stationary mass suspended through a preloaded spring. The analysis summarizes observations on the passive response of the mass under variations in the oscillation amplitude of the constraint. A control strategy is subsequently shown to successfully suppress the instability. The paper concludes with suggestions for applications of this phenomenology as well as a description of similar observation in mechanical systems with or without friction and with rigid as well as compliant contact.

1 Introduction

The onset of low-velocity collisions in vibro-impacting systems induces instabilities in the system dynamics that, when not checked, may result in sudden, and unanticipated discontinuous transitions between distinct steady-state responses. Typically, the loss of structural stability can be directly traced to a condition of zero-velocity–*grazing*–contact between parts of the system undergoing periodic recurrent motion. The emphasis of this paper is the study of the bifurcation behavior past such a point of grazing contact in an example vibro-impacting system with friction and active means of regulating this behavior.

Harry Dankowicz
Department of Mechanical Science and Engineering,
University of Illinois at Urbana Champaign, Urbana, 61801, Illinois, USA
danko@illinois.edu

Fredrik Svahn
KTH Vehicle Dynamics, Royal Institute of Technology, SE-100 44 Stockholm, Sweden
fsvahn@kth.se

R.A. Ibrahim et al. (Eds.): Vibro-Impact Dynamics of Ocean Systems, LNACM 44, pp. 41–52.
springerlink.com

The sudden grazing-induced disappearance of a local attractor in favor of a separate and typically more violent response of the mechanism may be thought of as a means for energy transfer between different degrees of freedom of a mechanism. From a practical point of view, a mechanism designed to exhibit such a non-persistent grazing bifurcation scenario might thus be used to sense relatively small variations in system parameters, as well as a means of dissipating excess energy through its directed transfer throughout the mechanism. Impact- and friction-like discontinuities could thus be intentionally deployed in a given engineered mechanism to exploit the beneficial aspects of grazing-induced instabilities.

This paper presents a family of control strategies aiming to regulate the onset of low-velocity collisions in vibro-impacting systems and to suppress energy loss associated with transitions to high-contact-velocity oscillations. The proposed strategies are shown to successfully differentiate between supercritical bifurcation scenarios, in which a stable periodic oscillation persists to the limit of zero contact velocity, and subcritical grazing bifurcation scenarios, in which no stable oscillations can be found in this limit. Examples of successful control design are presented for systems with or without friction and discussed in the context of an example system with compliant contact.

2 The Mechanical Model

Of concern in this work is the nonlinear response of a single-degree-of-freedom, piecewise-smooth dynamical system modeling an idealized vibro-impacting mechanism in the presence of dry Coulomb friction (cf. [9]). As shown in Fig. 1, consider an object of mass m resting against a rough horizontal surface and interacting with a linear restoring spring of stiffness k and a harmonically oscillating unilateral constraint, such that the onset of contact is modeled as an instaneous impact with kinematic coefficient of restitution e.

In the absence of collisions, the frictional contact with the horizontal surface results in the existence of a set of relative equilibria, for which the displacement q of the object attains constant values in the interval $\left[-F_f/k, F_f/k\right]$, where F_f is the maximum tangential friction force. In the three-dimensional state space with coordinates given by $(q, \dot{q}, \omega t \mod 2\pi)$, where ω is the angular frequency of the oscillating

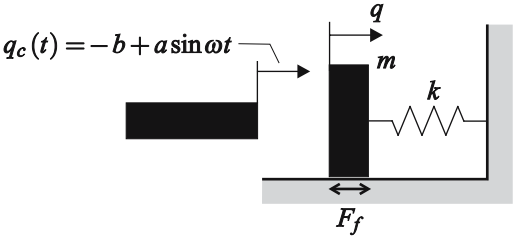

Fig. 1 An example vibro-impacting system with friction

constraint, these relative equilibria correspond to straight-line trajectories parallel to the phase axis and contained within the set $\mathscr{S}_0 \subset \mathscr{S} \stackrel{def}{=} \{\dot{q} = 0\}$ shown in Fig. 2.

With the introduction of the oscillating constraint, only that part of state space with $q \geq a \sin \omega t - b$, where $a, b > 0$, is accessible to the system dynamics. Denote by $\mathscr{I}$ the boundary of this region. It follows that as long as $\mathscr{I}$ does not intersect the right boundary of $\mathscr{S}_0$ (upper panel of Fig. 2), a subset of $\mathscr{S}_0$ persists as an invariant set of the system dynamics. In contrast, if $\mathscr{I}$ intersects the right boundary of $\mathscr{S}_0$ transversally (bottom panel of Fig. 2), any steady-state system response must

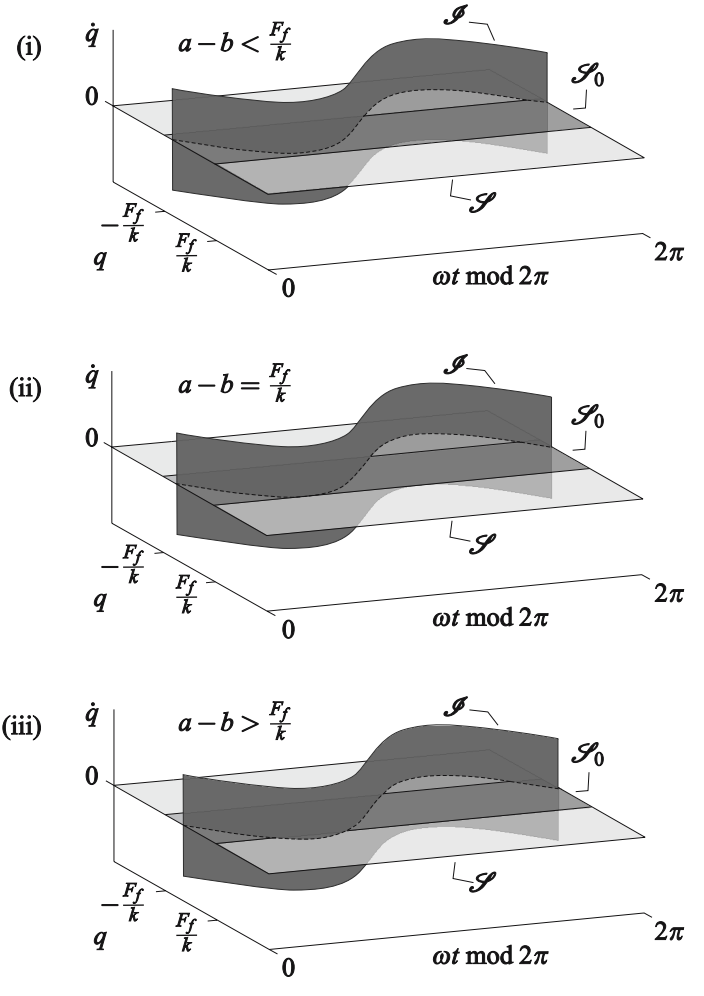

Fig. 2 State-space structure (i) prior to grazing, (ii) at grazing, and (iii) subsequent to grazing. Here, $\mathscr{S}$ denotes the *switching surface* separating motions with opposing directions of the friction force. In the absence of collisions, the invariant subset $\mathscr{S}_0$ consists of straigh-line trajectories parallel to the phase axis and representing equilibrium positions of the object

include impacts and phases of relative slip of the object against the surface. The critical transition (middle panel of Fig. 2) corresponds to a singular condition in which a single relative equilibrium trajectory on $\mathscr{S}_0$ intersects $\mathscr{I}$ at a point of tangential, or *grazing*, contact.

For trajectories in the vicinity of the grazing trajectory, collisions between the object and the oscillating constraint occur with low relative velocity. The objective of this effort is to establish conditions on the system parameters under which low-contact-velocity oscillations can be maintained at **and beyond** grazing and the extent to which feedback control can be employed to sustain such motions (cf. [7]).

3 Equations of Motion

In the absence of collisions with the unilateral constraint, the dynamics of the object is governed by the piecewise-smooth dynamical system

$$m\ddot{q}+kq=F \tag{1}$$

where

$$F=\begin{cases} -F_f & \text{when } \dot{q}>0 \text{ or when } \dot{q}=0 \text{ and } q>\frac{F_f}{k} \\ F_f & \text{when } \dot{q}<0 \text{ or when } \dot{q}=0 \text{ and } q<-\frac{F_f}{k} \\ kq & \text{when } \dot{q}=0 \text{ and } |q|\leq\frac{F_f}{k} \end{cases}. \tag{2}$$

Here, the assumptions of Amonton-Coulomb friction imply that the friction force remains constant (and equal in magnitude to F_f) and opposite to the motion of the object during sliding, and adjusts instantaneously (as long as the magnitude remains bounded by F_f) so as to ensure persistent rest during stick.

As before, let

$$q_c(t)=-b+a\sin\omega t \tag{3}$$

for $a,b,\omega>0$ describe the position of the unilateral constraint. Then, as long as $q-q_c(t)>0$, the forward-in-time dynamics of the object are again governed by the equation of motion (2). Suppose, instead, that

$$\lim_{t\to t_0-} q(t)=q_c(t_0)\,,\ \lim_{t\to t_0-}\dot{q}(t)\leq\dot{q}_c(t_0) \tag{4}$$

for some time t_0, corresponding to the onset of collisional contact between the unilateral constraint and the object. Assuming an instantaneous contact phase, conservation of linear momentum coupled with a Newtonian impact law implies that

$$\lim_{t\to t_0+} q(t)=q_c(t_0)\,,\ \lim_{t\to t_0+}\dot{q}(t)=-e\lim_{t\to t_0-}\dot{q}(t)+(1+e)\dot{q}_c(t_0)\,, \tag{5}$$

where $0<e\leq 1$ again denotes the kinematic coefficient of restitution. Unless otherwise stated, we omit from consideration trajectories with degenerate contact between the object and the unilateral constraint, for example sustained contact over a finite interval of time.

4 Passive Response

As shown in [11], as long as $\mathscr{I}$ does not intersect the right boundary of $\mathscr{S}_0$, a subset of $\mathscr{S}_0$ is a persistent, invariant, local attractor. This subset consists of those relative equilibrium trajectories corresponding to at most zero-relative-velocity contact between the object and the oscillating constraint. Specifically, although small perturbations away from this subset result in initial phases of relative slip and possible low-velocity impacts, the subsequent trajectories return to the invariant subset after a finite time.

This state of affairs no longer holds for the singular parameter choice corresponding to grazing contact between the right boundary of $\mathscr{S}_0$ and $\mathscr{I}$. For example, as long as the angular frequency ω of the oscillating constraint is less than twice the natural frequency of the mass-spring system, a rigorous analysis establishes the asymptotic stability of the grazing relative equilibrium trajectory provided that

$$(1+e)^2\left(\frac{F_f}{k}+b\right)\frac{m\omega^2}{F_f}<4 \tag{6}$$

and the rapid growth in the deviation from this trajectory if the opposite inequality holds.

Under the conditions discussed above, a persistent family of stable low-contact-velocity periodic oscillations can be shown to emanate from the grazing trajectory in the case that it is asymptotically stable (cf. Figs 3 and 4). Specifically, in the cases that

$$(1+e)^2\left(\frac{F_f}{k}+b\right)\frac{m\omega^2}{F_f}<2\left(1-e^2\right) \tag{7}$$

and

$$2\left(1-e^2\right)<(1+e)^2\left(\frac{F_f}{k}+b\right)\frac{m\omega^2}{F_f}<2, \tag{8}$$

the post-grazing steady-state responses include bursts of rapid successions of impacts with the object in motion or at rest, respectively. In contrast, for

$$2<(1+e)^2\left(\frac{F_f}{k}+b\right)\frac{m\omega^2}{F_f}<4 \tag{9}$$

the post-grazing steady-state response is regular with a single impact per period. In all cases, it follows that the transition across the critical parameter choice corresponding to grazing contact is benign with sustained dynamics in the vicinity of the right boundary of $\mathscr{S}_0$ and a vanishing impact velocity in the limit of approaching the critical parameter choice. In analogy with the theory of smooth bifurcations, e.g., pitchfork and Hopf bifurcations, we refer to this bifurcation scenario as *supercritical*.

The loss of a persistent attractor at the critical parameter choice in the case of an unstable grazing trajectory is anticipated only by the shrinking size of the basin of

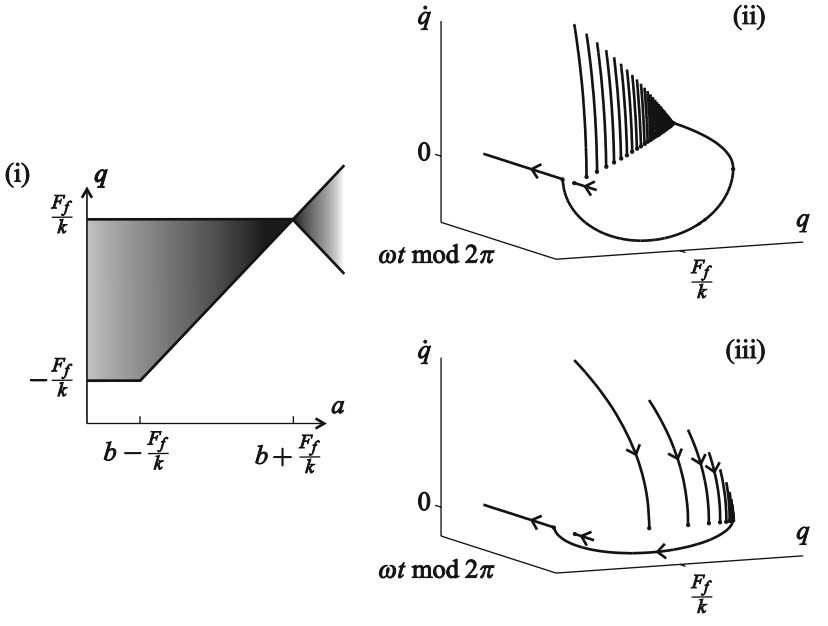

Fig. 3 (i) Schematic bifurcation diagram in the case of supercritical bifurcation scenarios for (ii) $(1+e)^2\left(\frac{F_f}{k}+b\right)\frac{m\omega^2}{F_f} < 2\left(1-e^2\right)$ and (iii) $2\left(1-e^2\right) < (1+e)^2\left(\frac{F_f}{k}+b\right)\frac{m\omega^2}{F_f} < 2$. In both cases, the post-grazing steady-state response shown in the rightmost panels is periodic and includes a sequence of infinitely many impacts in finite time

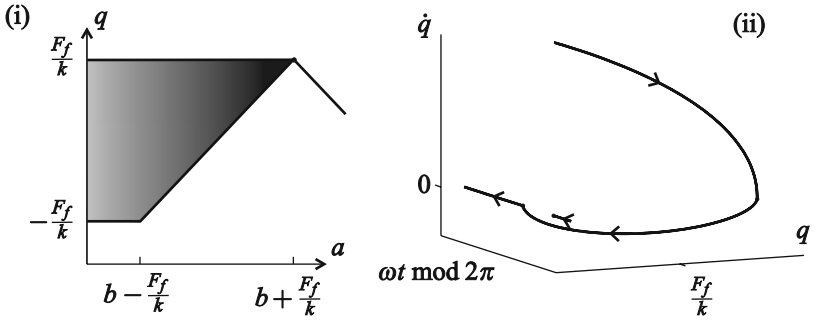

Fig. 4 (i) Schematic bifurcation diagram in the case of a supercritical bifurcation scenario for (ii) $2 < (1+e)^2\left(\frac{F_f}{k}+b\right)\frac{m\omega^2}{F_f} < 4$. In this case, the post-grazing steady-state response shown in the right panel is periodic with a single impact per period

attraction of the invariant subset of $\mathscr{S}_0$ prior to grazing. In fact, in this case, a family of unstable low-contact-velocity periodic oscillations can be shown to coexist with the pre-grazing invariant subset on some small region of parameter values (see

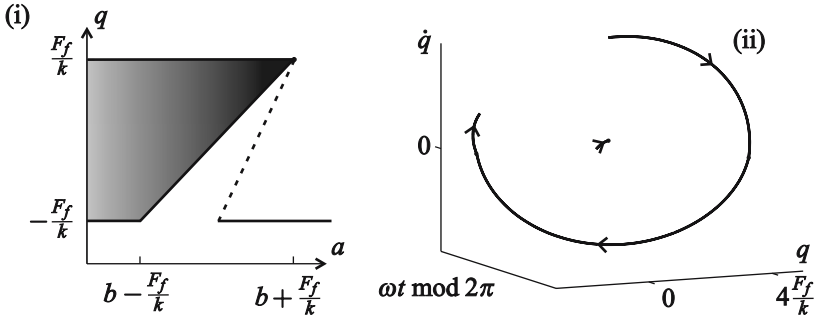

Fig. 5 (i) Schematic bifurcation diagram in the case of a subcritical bifurcation scenario for (ii) $4 < (1+e)^2\left(\frac{F_f}{k}+b\right)\frac{m\omega^2}{F_f}$. In this case, the post-grazing steady-state response shown in the right panel is periodic with a single impact per period and with an impact velocity that remains bounded away from zero as the critical, grazing parameter value is approached

Fig. 5). This family terminates at the critical parameter choice in a *nonsmooth fold* bifurcation point, such that the corresponding periodic oscillation coincides with the grazing trajectory. In particular, the disappearance of the invariant subset of $\mathscr{S}_0$ is in this case associated with a *discontinuous transition* of the system response to a distinct impacting oscillation, for which the impact velocity remains bounded away from zero on a neighborhood of the critical parameter choice. Again, in analogy with the theory of smooth bifurcations, we refer to this bifurcation scenario as *subcritical*.

5 Control Strategies

As demonstrated both analytically and numerically in detail in [12], the persistence of a low-contact-velocity response, even in the case of an unstable grazing trajectory, can be ensured using feedback-based, discrete changes in the value of b, i.e., the average displacement of the oscillating constraint (see also [2, 3] for a related approach in the absence of friction). Indeed, an open but bounded collection of local, nonlinear feedback strategies can be found that guarantees both the asymptotic stability of the grazing trajectory and the existence of a family of stable low-contact-velocity periodic oscillations that emanates from this grazing trajectory in the limit as the critical parameter choice is approached (see Fig. 6).

Specifically, under the assumption that the excitation frequency ω is less than twice the natural frequency $\sqrt{k/m}$ of the mass-spring system in the absence of friction, it can be shown that a near-grazing steady-state response must include a phase of sustained stick with the horizontal surface. Denote by $q^S \lesssim F_f/k$ the value of the position coordinate in such a state of stick. Then, as a is increased beyond some value a^*, the control strategy

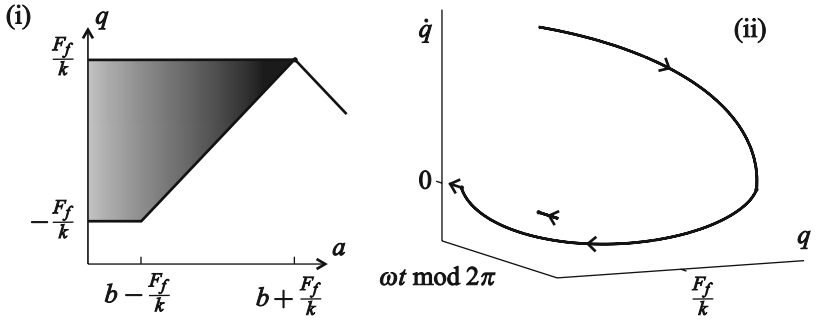

Fig. 6 (i) Schematic bifurcation diagram in the case of a controlled supercritical bifurcation scenario for (ii) 1. In this case, the post-grazing steady-state response shown in the right panel is periodic with a single impact per period

$$b \to a^* - \frac{F_f}{k} + \left(1 - \frac{4F_f c}{a^* m\omega^2 (1+e)^2}\right)\left(\frac{F_f}{k} - q^S\right) \tag{10}$$

with $0 < c < 1$ yields a branch of stable periodic trajectories emanating from the grazing relative equilibrium trajectory when $a = a^*$. In particular, along this branch

$$q^S(a) = \frac{F_f}{k} + \frac{a^* m\omega^2 (1+e)^2}{4F_f (1-c)}(a-a^*) + \mathcal{O}\left((a-a^*)^2\right), \tag{11}$$

such that

$$\lim_{a \to a^*+} q^S(a) = \frac{F_f}{k} \tag{12}$$

and

$$\lim_{a \to a^*+} b\left(q^S(a)\right) = a^* - \frac{F_f}{k}. \tag{13}$$

In fact, the collection of successful control strategies contains a superstable strategy, for which the grazing trajectory is reached within one excitation cycle at the critical parameter choice, namely

$$b \to -\frac{F_f}{k} + \left(\frac{F_f}{k} - q^S\right) + \frac{\omega_0}{(1+e)\omega}\sqrt{a^2(1+e)^2\frac{\omega^2}{\omega_0^2} - 4\frac{F_f}{k}\left(\frac{F_f}{k} - q^S\right) + \left(\frac{F_f}{k} - q^S\right)^2}. \tag{14}$$

When expanded in the deviation of q^S from F_f/k, this nonlinear strategy is found to correspond to the choice $c = 1/2$ in the linear control strategies shown above.

6 Discussion

The analysis and results of the previous sections give impetus to a number of observations on utility and comparison with related nonlinear phenomena and control strategies.

6.1 A Mechanism for Energy Transfer

The discontinuous transition to an impacting oscillation described above affords a means for directed energy transfer from the oscillating constraint to the object. Here, energy transfer would be triggered by sufficiently large oscillation amplitudes and would be of finite magnitude even at the critical parameter choice. This is a particularly interesting observation as it carries over to the case where the oscillating constraint is replaced by the excited oscillation of a second object of mass $M \gg m$ [11]. In this context, the directed energy transfer is a nonlinear damping mechanism that can be exploited to dissipate excess vibrational energy in one part of a mechanical system.

In the limiting case of $m/M \to 0$, the proposed control strategy is able to regulate the transition across the grazing condition and thus suppress the large energy transfer associated with the onset of low-velocity collisions. Suitably modified, this characterization should again carry over to the case of finite $M \gg m$ affording a robust method for controlling the onset of large energy dissipation.

6.2 A Mechanism for Sensor Design

An alternative use of the discontinuous transition observed in the example vibro-impacting system is in the design of limit switches, devices that change operating state in reaction to the crossing of a threshold value of their input [8]. Limit-switch designs relying on nonlinear circuitry or parametrically-excited microelectromechanical devices have been recently proposed by a number of authors [1, 6, 10, 13, 14, 15]. In these instances, the operating principle has been the occurrence of a smooth fold bifurcation characterized by the mutual annihilation of a stable and unstable periodic system response at the threshold value and the subsequent transient to a distinct steady-state response beyond the threshold value.

The nonsmooth fold bifurcation observed in the passive response of the vibro-impacting mechanism considered here affords an analogous transition in which the post-grazing response is directly characterized by a finite impact velocity. The persistence of this impacting steady-state response even below the critical grazing parameter value further prevents hunting dynamics of the limit switch near the threshold. This provides a mechanism for the design of a resettable limit switch.

As shown in previous sections, the inclusion of additional feedback allows one to regulate the post-grazing transition, e.g., replacing the nonsmooth fold bifurcation with the persistence, in the vicinity of the threshold parameter value, of a

low-impact-velocity steady-state attractor. Appropriately exploited, the feedback strategy could therefore be employed to adjust the sensitivity of the switch to noise and to introduce a staged trigger design, in which a secondary fail-safe mechanism would first need to be triggered in order to enable the limit switch.

6.3 *Vibro-Impacting Dynamics in the Absence of Friction*

Grazing-induced bifurcations occur also in the absence of friction, both in the case of rigid impacts considered here and in the case of compliant collisions. In the latter, a finite-time contact phase is modeled using the imposition of additional restoring and dissipative contact forces. Indeed, in both cases, control strategies may again be derived that ensure a persistent bifurcation scenario, where a discontinuous transition would result in the absence of control.

An example of a mechanical system with rigid impacts is the mechanism shown in Fig. 7 excited by harmonic motion of the suspension and in which impacts may occur between the rightmost mass and the stationary unilateral constraint. Here, for values of a below a critical value a^*, the oscillation amplitude of the rightmost mass remains below δ. For $a = a^*$, the steady-state response of the two-degree-of-freedom mechanism includes an instance of zero-relative-velocity contact with the unilateral constraint, corresponding again to a grazing periodic trajectory in the associated five-dimensional state space.

The post-grazing transient response of the mechanism for a particular choice of parameter values, initial conditions corresponding to the point of grazing contact, and $a \gtrsim a^*$ is represented by the solid curve in Fig. 8. Specifically, as seen in the figure, jumps in the velocity of the rightmost mass occur with some regularity and become increasingly large.

In contrast, the dashed curve in Fig. 8 represents the response in the presence of feedback-based adjustments to the value of δ. Here, impact velocities remain below the resolution of the figure yielding a sustained near-grazing steady-state response even for $a > a^*$. Indeed, as shown in [3], the existence of open sets of control

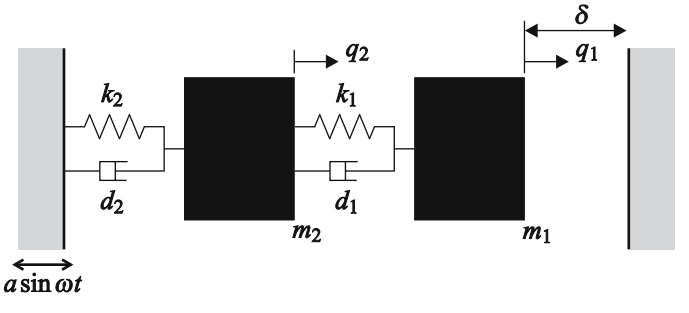

Fig. 7 An example two-degree-of-freedom vibro-impacting system without friction. Reprinted from [3] with permission from the publisher

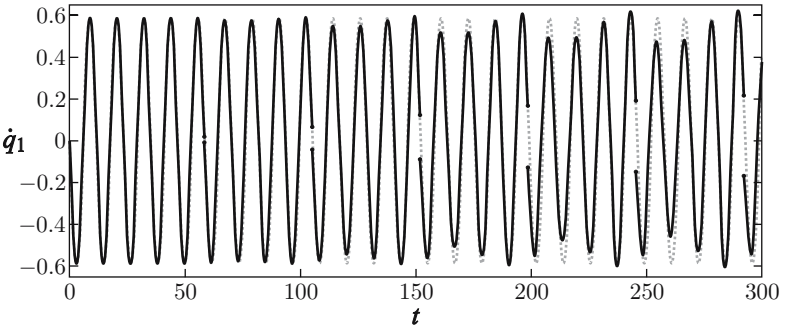

Fig. 8 A comparison of the time history of post-grazing, persistent low-impact-velocity steady-state motion (dashed) in the presence of feedback control and the transition to a high-impact-velocity steady-state motion (solid) in the absence of control. Reprinted from [3] with permission from the publisher

parameter values that yield a supercritical bifurcaton scenario may be established rigorously. In fact, the proof provides a constructive method for determining useful control parameter values.

Finally, as an example of a system with compliant contact in which subcritical transitions may be induced by the onset of grazing contact, consider the response of a microscale cantilever probe used in atomic force microscopy. Here, excitation of the cantilever support results in oscillations of the cantilever tip that, when of sufficient amplitude, result in intermittent interactions with the repulsive force field representative of nanoscale contact. As shown in [4] and [16], the onset of such interactions again results in discontinuous transitions from a low-amplitude response to a high-amplitude response with a relatively large duration of contact. In contrast to the rigid-impact case, here the bifurcation is delayed relative to the onset of grazing by an amount characterized by the stiffness of the contact. Recent work by the authors and their collaborators have again established the existence of an open collection of control strategies that may, at least locally, ensure a supercritical bifurcation.

Acknowledgements. This material is based upon work supported by the National Science Foundation under Grant Nos. 0237370 and 0635469 and by the Swedish Science Council under Grant Nos. 2003-3699 and 2004-6342.

References

1. Abdel-Rahman, E.M., Nayfeh, A.H.: Secondary resonances of electrically actuated resonant microsensors. J. Micromech. Microeng. 13(3), 491–501 (2003)
2. Dankowicz, H., Jerrelind, J.: Control of Near-grazing Dynamics in Impact Oscillators. P Roy. Soc. A-Math. Phys. 461(2063), 3365–3380 (2005)

3. Dankowicz, H., Svahn, F.: On the Stabilizability of Near-grazing Dynamics in Impact Oscillators. Int. J. Robust Nonlin. 17, 1405–1429 (2007)
4. Dankowicz, H., Zhao, X., Misra, S.: Near-grazing Dynamics in Tapping-mode Atomic-force Microscopy. Int. J. Nonlin. Mech. 42, 697–709 (2007)
5. Long, X.-H., Lin, G., Balachandran, B.: Grazing bifurcations in an elastic structure excited by harmonic impactor motions. Physica D 237(8), 1129–1138 (2008)
6. Mohr, T., Uhlmann, F.H.: Detecting Thresholds by Means of Jump-Phenomena. In: Proceeedings of 7th IEEE International Conference on Electronics, Circuits and Systems (2000)
7. Nordmark, A.B.: Effects Due to Low Velocity Impact in Mechanical Oscillators. Int. J. Bifurcat Chaos 2(3), 597–605 (1992)
8. Paques, J.-J.: Limit switches: Selection for safety. ISA Trans. 33(1), 99–103 (1994)
9. Pavlovskaia, E., Wiercigroch, M., Grebogi, C.: Modeling of an Impact System with Drift. Phys. Rev. E 64, 056224, 1–9 (2001)
10. Siddiqi, I., Vijay, R., Pierre, F., Wilson, C.M., Metcalfe, M., Rigetti, C., Frunzio, L., Devoret, M.H.: RF-driven Josephson bifurcation amplifier for quantum measurement. Phys. Rev. Lett. 93(20), 207002, 1–4 (2004)
11. Svahn, F., Dankowicz, H.: Energy Transfer in Vibratory Systems with Friction Exhibiting Low-velocity Collisions. J. Vib. Control 14(1-2), 255–284 (2008)
12. Svahn, F., Dankowicz, H.: Controlled Onset of Low-velocity Collisions in a Vibro-impacting System with Friction. Submitted to P. Roy. Soc. A-Math. Phys. (2009)
13. Turner, K.L., Baskaran, R., Zhang, W.: Using nonlinear dynamics for performance enhancement in resonant micro and nano-scale devices. In: Proceedings of the IEEE Conference on Decision and Control, vol. 3, pp. 2650–2651 (2003)
14. Zhang, W., Baskaran, R., Turner, K.L.: Effect of Cubic Nonlinearity on Auto-Parametrically Amplified Resonant MEMS Mass Sensor. Sensor Actuat A-Phys. 102(1-2), 139–150 (2002)
15. Zhang, W., Turner, K.L.: Application of parametric resonance amplification in a single-crystal silicon micro-oscillator based mass sensor. Sensor Actuat A-Phys. 122(1), 23–30 (2005)
16. Zhao, X., Dankowicz, H.: Characterization of Intermittent Contact in Tapping-mode Atomic Force Microscopy. J. Comput. Nonlin. Dyn. 1(2), 109–115 (2006)

Hydrodynamic Impact-Induced Vibration Characteristics of a Uniform Euler-Bernoulli Beam

Nabanita Datta, Dae-Hyun Kim, and Armin W. Troesch

Abstract. A hydroelastic analysis of slam-induced beam vibration is presented. The objective of the paper is to provide *response spectra* for transient water-structure dynamics subject to typical impact loads and time scales. Assuming small deflections of the Euler-Bernoulli beam, normal mode summation is used to calculate the dynamic deflections in space and time. The modal governing differential equation is non-dimensionalized in space and time, and the dynamic load factor (DLF) of the loading are numerically evaluated. The modal participation spectra relative to the dominant fundamental mode for various impact speeds is used to establish modal truncation guidelines. The effect of the fluid inertia on the DLF is examined in the two limits of dry vibrations and completely wet vibrations.

Nomenclature

L	Beam length.	$\Phi(x)$	j^{th} modeshape.
B	Width of the beam.	q(t)	j^{th} generalized coordinates.
h	Thickness of the beam.	z(x,t)	Total dynamic deflection.
g	Acceleration due to gravity.	$z_{st}(x,t)$	Static deflection.
m(x)	Mass per unit length.	t	Time-coordinate.
F(x,t)	Force.	x	Space-coordinate.
E	Modulus of elasticity.	l	Horizontal space step
I	Second moment of inertia of the cross-section about the NA.	X	Dummy length variable
		$Z1_{st}$	Maximum possible z_{st}
ρ_s	Density of steel.	$Z2_{st}$	Maximum z_{st} at each t
ρ_w	Density of water	$Z3_{st}$	Maximum z_{st} at each x
$\omega_{j,dry}$	j^{th} natural frequency of the beam.	V	downward impact velocity.
T_j	Period of the beam.	c	Speed of the moving load
d(t)	Impact jet head (horizontal)	φ	velocity potential
$\dot{d}(t)$	Impact jet head velocity	φ^*	j^{th} velocity potential
$\Phi_j^*(x)$	j^{th} added mass per unit length	$\omega_{wet,j}$	j^{th} wet natural frequency

Nabanita Datta, Dae-Hyun Kim, and Armin W. Troesch
Department of Naval Architecture and Marine Engineering,
University of Michigan, Ann Arbor Michigan, USA
ndatta@umich.edu, daehyun@umich.edu,
troesch@engin.umich.edu

R.A. Ibrahim et al. (Eds.): Vibro-Impact Dynamics of Ocean Systems, LNACM 44, pp. 53–66.
springerlink.com

1 Introduction

The subject of flexible fluid-structure interaction has been gaining prominence in research and applications in the last few decades. The prediction of the magnitude and distribution of hydrodynamic impact pressures is a useful criterion for the structural design of high-speed vessels. The study of global and local dynamic elastic behavior of marine vessels and structures forms the basis of marine hydroelasticity. Non-conventional high-speed crafts built of lighter materials like aluminum, GRP, FRP, non-metallic composites, etc. require hydroelastic analysis as an important component of the basic design spiral. The estimation of the global flexural strength notwithstanding, isolated hydroelastic analysis is necessary to incorporate local strength in regions like the bow, wetdeck, stern and bow flare. Slamming or impact is a common phenomenon, where in severe seas, the vessel hull emerges once every few wave encounters, followed by an inevitable slam.

Slam-induced impact pressures have been investigated widely, first pioneered by Von-Karman in 1929, then improved upon by Wagner in 1932. Accurate estimation of the peak impact pressure for various slam velocities and deadrise angles resulted from decades of intensive research, both analytical and experimental. Relatively less investigated is the area of dynamic elastic response of the structure subjected to such loads. For some applications, the dynamic system can be modeled as a distributed force sweeping across the length of the beam at a certain velocity, and the beam being set into vibratory motion, damped by the material friction or the radiation damping. The surrounding fluid is also set into motion, thereby increasing the effective system inertia. The restoring forces are the flexural rigidity of the structure, and the changes in buoyancy (especially in global-scale hull vibrations). The interaction of inertial, elastic and hydrodynamic forces generates the hydroelastic response.

As background, the dynamic response of moving loads across bridges has been investigated by various researchers in the field of mechanical and civil engineering. The analysis shows a consistent trend : modeling of the bridge as an Euler-Bernoulli beam/Timoshenko beam with various end conditions, modeling the moving load as a concentrated force, and using normal mode analysis to evaluate the dynamic response. The ratio of the maximum dynamic deflection to the equivalent maximum static deflection, called the dynamic load factor (DLF) or the dynamic amplification factor (DAF), is then evaluated as a parameter against the speed of the moving force. The DLF becomes a crucial design consideration in the construction of bridges.

Chatterjee et al [1] numerically evaluated the dynamic response to moving loads across continuous bridges, but it was a dimensional analysis with a concentrated load. Esmailzadeh and Ghorashi [2] numerically analyzed a Timoshenko beam, with a distributed load length as a fraction of the bridge length. Since the bridge undergoes small deflections, the shear deformation and rotary inertia can be ignored to reduce the analysis to an Euler-Bernoulli beam, enhancing computational efficiency. The speed of the moving load has been normalized into a non-dimensional parameter in different ways by different researchers. Yang et al [3] studied the passage of high speed trains, with the train length as another parameter influencing the DLF. Garinei and Risitano [4,5] applied harmonic loads and

several concentrated loads and their non-dimensional analysis led to the identification of critical speeds when the highest amplification is obtained. Henke [6] studied the transient dynamic response to plates under impulse loads. The governing differential equations of motion were non-dimensionalized, and the variation of the non-dimensional dynamic stress with space and time was also evaluated. In that work, however, the speed of the impulsive load moving across (pulse front velocity) was not considered. Wang and Chou [7] studied the dynamic load factor of Timoshenko beams subjected to concentrated moving loads, as a function of the velocity of the force. They also studied the change of the DLF with changing dimensions of the beam and the employment of three different beam theories of dynamic response.

The above research reiterated the validity of normal mode analysis in vibration studies, and defined the dynamic load factor and the non-dimensional speed parameter. However, the dynamic beam response was restricted to concentrated moving loads. The localized impact loading response of marine vessels under slamming is an extension of this problem. Slamming pressures are sweeping loads, which depend on the slam velocity and the local deadrise angle of the craft.

Lamb [9], Lewis [10], and McLachlan [11] were the pioneers in the investigation of hydroelasticity. Bishop and Price [13,14], more recently, considered the elastic behavior of marine vehicles and structures subjected to time-dependent excitations. The hull girder was considered as a uniform beam, undergoing global vibrations analyzed by modal superposition. The hydrodynamic radiation force was modeled as a sum of the acceleration-dependent added mass and the velocity-dependent radiation damping. They also went on to show the equivalency between dry modes and the more traditional wet mode analysis. A recent survey article of ship hydroelasticity is given by Senjanovic et al [17]. Troesch [15] investigated the global vibrations of the hull subjected to waves. Superposition of heave, pitch and experimental 'model' springing produced the net response, whose numerical and experimental results were compared. Faltinsen [16] emphasized the choice of the time scale in the slamming phenomenon, comparing the duration of water entry to the fundamental natural period of the structure. The magnitude of this time scale ratio influenced the nature (intensity and distribution) of the response. He also distinguished the structural inertia phase and the free vibration phase of the response, extending the non-dimensional analysis from a beam to a plate. Yadykin [12] expanded the study to flexible oscillating plates, and investigated the dependence of the added mass to the aspect ratio of the plate, and the mode-wise contribution to this hydrodynamic force. Both 2-D and 3-D theories are used to numerically evaluate the fluid forcing for both cantilevered and simply-supported plates.

The study of local elastic responses of flexible structures subjected to transient loads in the perspective of two distinct time scales, i.e. the impact time and the dry/wet fundamental natural period of the structure is presented. The two-dimensional impact response problem is formulated with normal mode summation, including modal truncation analysis. First, the dynamic load factor (DLF) for a uniform moving load is studied. Then the methodology is extended to dry impact forcing to generate the DLF for various deadrise angles. Finally, the radiation pressure for fully submerged vibrations is included to calculate the wet natural frequencies, and evaluate the wet response DLF at particular deadrise angle.

2 Problem Formulation

The transient impact loads can be modeled as a distributed load moving across a beam of unit breadth with clamped ends, at a constant speed c, as shown in Fig.1. Considering undamped forced vibrations, the dynamic response z(x,t) of the beam as a function of space and time is evaluated numerically by the fourth-order Runge-Kutta method. Since the fundamental mode is dominant, it is sufficient to consider only 'pure bending' of the beam (Euler-Bernoulli beam), ignoring shear deformation and rotary inertia (Timoshenko beam). This is a dual time-scale problem, with the time taken by the force to sweep across the beam (splash time Tsp) and the fundamental natural period of the beam T_1 both influencing the dynamic load factor. The corresponding static deflections z_{st} (x,t) are calculated by numerical integration given the impact load f(x,t). The ratios of the dynamic and static deflections give the DLF.

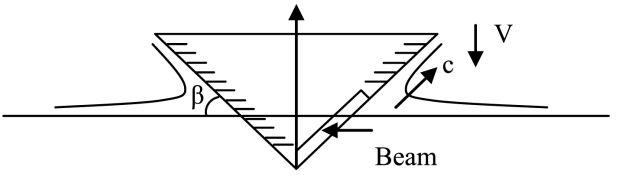

Fig. 1 2-D model of Impact Hydrodynamics

2.1 Modal Analysis

The forced vibration of a multi-degree-of-freedom system can be solved efficiently by the normal mode summation method. A short summary is given below.

The free vibration equation of motion for the beam, ignoring gravity, is

$$m(x)\frac{\partial^2 z(x,t)}{\partial t^2} + EI\frac{\partial^4 z(x,t)}{\partial x^4} = 0 \tag{2.1}$$

The deflection is a linear superposition of the Eigen vectors $z(x,t) = \sum_{j=1}^{\infty} \Phi_j(x)\, q_j(t)$ where Φ_j (x) = j th modeshape function and q_j (t) = j th principle coordinate. The modeshape are the Eigen vectors of (2.1)

$$\Phi_j(x) = A1_j \cos(\gamma_j x) + A2_j \sin(\gamma_j x) + A3_j \cosh(\gamma_j x) + A4_j \sinh(\gamma_j x)$$

where

$$\gamma_j^4 = \frac{m(x)\omega_{j,dry}^2}{EI(x)} \tag{2.2}$$

are the corresponding Eigen values of (2.1)

The four constants A1, A2, A3 and A4 are calculated from the four boundary conditions of a clamped-clamped beam, i.e. $z(0,t) = 0;\ z(L,t) = 0;\ \frac{dz(0,t)}{dx} = 0;\ \frac{dz(L,t)}{dx} = 0.$

There are an infinite number of distinct values of γ_j, each of which corresponds to distinct natural frequencies ω_j and modeshapes $\Phi_j(x)$. For modes > 6, the values of γ and the closed form expressions for the modeshape $\Phi_j(x)$ are given by Goncalves et al [8]. Calculation of γ (2.2), determines ω_j, the dry natural frequencies of the beam.

The governing system of differential equations is non-dimensionalized with respect length and time as follows $: d\tau = \omega_{1,dry}\, dt$ and $dx' = \frac{dx}{L}$. The total non-dimensional deflection is $z(x',\tau) = \sum_{j=1}^{\infty} \Phi_j(x')\, q_j(\tau)$; and the governing differential equation including the hydrodynamic external sectional force is

$$\sum_{j=1}^{\infty} m(x')\, \Phi_j(x') \frac{d^2 q_j(\tau)}{d\tau^2} + \sum_{j=1}^{\infty} EI\ \frac{d^4 \Phi_j(x')}{dx'^4} q_j(\tau) = F(x',\tau).$$

Taking advantage of the orthogonality of the Eigenvectors (2.2), the resulting uncoupled non-dimensional modal equation of motion is

$M'_{jj}\, \omega^2_{1,dry} \frac{d^2 q_j(\tau)}{d\tau^2} + K'_{jj}\, q_j(\tau) = gf(x',\tau)$; with gen. mass $= M'_{jj} = \int_0^L \Phi_j(x')\, m(x')\, \Phi_j'(x)\, dx'$;

gen. force $= gf_j(x,\tau)' = \int_0^L \Phi_j(x)\, F(x',\tau)\, dx'$, gen. stiffness $= K'_{jj} = \int_0^L \Phi_j(x)\, EI\, \frac{d^4 \Phi_j(x')}{L^4 dx'^4}\, dx'$

and $\frac{K'_{jj}}{M'_{jj}} = \omega^2_{j,dry}$. Dividing by $M'_{jj}\omega^2_{1,dry}$ yields $\frac{d^2 q_j(\tau)}{d\tau^2} + \frac{\omega^2_{j,dry}}{\omega^2_{1,dry}} q_j(\tau) = \frac{gf_j(x',\tau)}{M'_{jj} \cdot \omega^2_{1,dry}}$. (2.3)

Thus we obtain the uncoupled ODE (2.3) for the principal coordinates. This system non-dimensional governing differential equations is solved by numerical time integrators, Euler's implicit-explicit scheme and the Fourth order Runge-Kutta method. Once the principle coordinates have been evaluated, they are multiplied by the pre-calculated modeshape functions to generate the total dynamic deflection as a function of space and time.

2.2 Radiation Pressure

When the maximum dynamic response occurs early in the impact sequence, with most of the beam nearly dry, the inertia of the water on the vibratory response can be ignored. The equation of motion for dry vibrations is

$$m(x) \frac{\partial^2 z(x,t)}{\partial t^2} + EI(x) \frac{\partial^4 z(x,t)}{\partial x^4} = F_{impact}(x,t) \tag{2.4}$$

When the impact force acts for a duration enough to immerse the whole beam, the fluid inertia cannot be ignored. The radiation forces have to be included in the

governing differential equation for this fluid-structure interaction. Here, the beam is considered to be fully submerged, which makes the wave radiation forces negligible. The total excitation force is considered to be a linear superposition of the impact force and the radiation force, i.e.

$$F_{total}(x,t) = F_{impact}(x,t) + F_{radiation}(x,t) \tag{2.5}$$

The boundary value problem of 2-D water impact is set up as follows (Fig.2)

Fig. 2 Radiation BVP

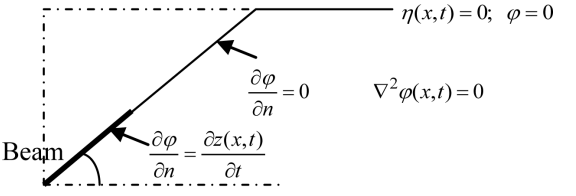

The governing equation in the fluid domain is $\Delta\varphi(x,t) = 0$, subject to the following boundary conditions: Linearized combined free surface boundary condition (FSBC) $\frac{\partial^2 \varphi}{\partial t^2} + g\,\varphi_z = 0$ at $\eta = 0$, where the high frequency limit becomes $\varphi = 0$ at $\eta = 0$. Body boundary condition on the flexible beam $\frac{\partial \varphi}{\partial n} = \frac{\partial z(x,t)}{\partial t} = \sum_{j=1}^{\infty} \Phi_j(x) \frac{dq_j(t)}{dt}$. Body boundary condition on the rigid surface elsewhere $\frac{\partial \varphi}{\partial n} = 0$. Linear hydrodynamic pressure $P(x,t) = -\rho_w \frac{\partial \varphi(x,t)}{\partial t}$. Consider the velocity potential to be a linear superposition of an infinite number of modal velocity potentials, each of which satisfies the corresponding modal structural equation of motion, that is the velocity potential is $\varphi(x,t) = \sum_{j=1}^{\infty} \varphi_j^*(x)\, \dot{q}_j(t)$, where $\varphi_j^*(x)$ is the velocity potential per unit modal velocity of the structure. It is numerically evaluated in a separate numerical analysis involving linear potential theory for fluid dynamics (e.g. Katz and Plotkin [23]).

For the j[th] modal velocity potential, the governing equation in the fluid domain is $\nabla^2 \varphi_j(x,t) = 0$, satisfying the following boundary condition: FSBC $\varphi_j^* = 0$ BBC on the beam $\frac{\partial \varphi_j^*}{\partial n} = \Phi_j(x)$, Hydrodynamic pressure $P_j(x,t) = -\rho_w \varphi_j^*(x) \frac{d^2 q_j(t)}{dt^2}$.

The structural governing differential equation with the impact and radiation forces is $\sum_{j=1}^{\infty} m(x)\, \Phi_j(x) \frac{d^2 q_j(t)}{dt^2} + \sum_{j=1}^{\infty} EI\ \frac{d^4 \Phi_j(x)}{dx^4} q_j(t) = F_{total}(x,t) = F_{impact}(x,t) + F_{radiation}(x,t)$,

$F_{radiation}(x,t) = -\rho_w \sum_{j=1}^{\infty} \varphi_j^*(x) \frac{d^2 q_j(t)}{dt^2} B$

2.3 Wet Natural Frequencies : Added Mass

Consider a fully wet beam undergoing free vibration. The equations of motion employing normal mode summation can be expressed as :

$$\sum_{j=1}^{\infty} m(x)\Phi_j(x)\frac{d^2q_j(t)}{dt^2}+\sum_{j=1}^{\infty} EI\frac{d^4\Phi_j(x)}{dx^4}q_j(t)=-\rho_w\sum_{j=1}^{\infty}\varphi_j^*(x)\frac{d^2q_j(t)}{dt^2}B$$

Premultiplying the system of equations by $\Phi_k(x)$ and taking advantage of the orthogonality properties of the dry modeshapes gives the following :

$$M_{kk}^{'}\frac{d^2q_k(\tau)}{d\tau^2}+K_{kk}^{'}q_k(\tau)=-\sum_{j=1}^{\infty}A_{jk}^{'}\frac{d^2q_j(\tau)}{d\tau^2}$$

where

$$A_{jk}^{'}=\int_0^L\Phi_k(x')\rho_w\varphi_j^*(x')B\,dx'$$

Numerically, however, it is found for this case that $A_{jk}^{'}(x')=10^{-8}*A_{jj}^{'}(x')$, $j \neq k$, i.e. the non-diagonal terms of the added mass matrix are nearly zero relative to the diagonal terms. Thus the approximately decoupled system of equations for free submerged vibrations becomes $M_{jj}^{'}\omega_{i,dry}^2\frac{d^2q_j(\tau)}{d\tau^2}+K_{jj}^{'}q_j(\tau)\cong -A_{jj}^{'}\frac{d^2q_j(\tau)}{d\tau^2}$;

with natural frequency

$$\omega_{wet,j}=\sqrt{\frac{K_{jj}^{'}}{M_{jj}^{'}+A_{jj}^{'}}} \tag{2.7}$$

2.4 Dynamic Load Factor

The dynamic load factor DLF can be defined in one of the following four ways, where z(x,t) is the dynamic deflection and $z_{st}(x,t)$ is the equivalent static defection.

1) The maximum dynamic deflection is divided by the maximum static deflection in space and time. $DLF_1=Max\left[\frac{z(x,t)}{Z1_{st}}\right]$ is the overall static maximum. (2.8)

2) The dynamic deflection at every time step is divided by the maximum static deflection at the corresponding time-step. The matrix z(x,t) is divided by a vector along time. $DLF_2=Max\left[\frac{z(x,t)}{Z2_{st}(t)}\right]$ is the maximum at each time step.

3) The dynamic deflection at every location is divided by the maximum static deflection at the corresponding location. The matrix z(x,t) is divided by a vector along space. $DLF_3=Max\left[\frac{z(x,t)}{Z3_{st}(x)}\right]$ is the maximum at each location.

4) The dynamic deflection at every location and time-step is divided by the static deflection at the corresponding location and the time-step. DLF_4 is then the maximum of this matrix. $DLF_4 = Max\left[\frac{z(x,t)}{z_{st}(x,t)}\right]$ at each time step and each location.

For the analysis and discussion, $DLF_1(2.8)$ is chosen. It is the most robust DLF, since the structural designer will not require the spatial and temporal distribution of the static deflection to calculate the corresponding maximum dynamic deflection. In a separate comparative study, the above four definitions of the dynamic load factor was evaluated for a uniform load moving across a clamped-clamped beam, resulting in near-equivalency for a range of splash times.

2.5 Relative Modal Contribution

For the loading conditions studied in this work, the fundamental mode of vibration is the principal contributor to the total displacement, the contributions of the higher modes decreasing exponentially. Modal truncation studies demonstrated that modes contributing less than 10^{-6} times the fundamental mode could be safely ignored. The j^{th} principle coordinate q_j is normalized by the fundamental principle coordinate q_1 to generate the relative modal contribution (rmc) for different impact velocities, i.e. $rmc_j = MAX\left[\log_{10}\left(\frac{q_j(\tau)}{q_1(\tau)}\right)\right]$. The rmc is plotted in Fig.4a as a function of mode index and the splash velocity, generating a consistent trend uptil an upper limit of the velocity.

3 Results

The above methodology is applied to three cases of increasing complexity: an external uniform load sweeping across the beam at a constant velocity, an external impact load distribution sweeping across the beam at different deadrise angles, and the impact loading excitation including the radiation pressure, for different density ratios between the fluid and the structure.

3.1 Uniform Loading

The dynamic response of the clamped-clamped beam to a uniformly distributed load of unit magnitude, moving at a speed c across the beam, is analyzed with normal mode summation, generating the dynamic load factor (DLF) and the modal contribution (RMC) surface.

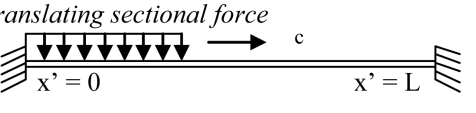

Fig. 3 Uniform load moving across the beam at a speed c

Define Splash time $Tsp = \frac{L}{c}$, Non-D splash time $= Tsp \frac{\omega_{1,dry}}{2\pi} = \frac{L}{c} \frac{\omega_{1,dry}}{2\pi} = \frac{L}{cT_{1,dry}}$ (3.1)

The DLF of the above moving load has been shown in Fig.4b. At low speeds, it is nearly 1, i.e. the structural response is quasi-static. At increasing speeds, the DLF steeply rises to asymptote to 2, which is the DLF for a uniformly distributed load instantaneously acting on the beam. For Tsp = 0, a separate numerical analysis for a uniformly distributed load would yielded a DLF = 2.005. To operate in the quasi-static range, the forcing speed should be low, or the natural frequency of the beam must be high.

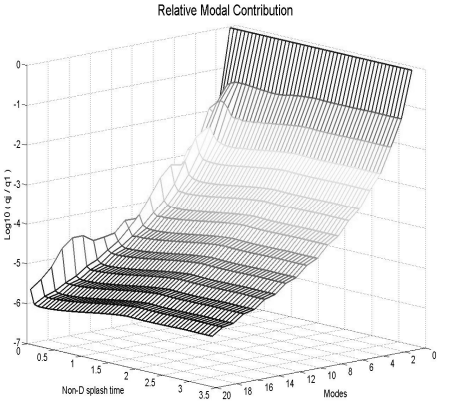

Fig. 4a (RMC): Uniform load

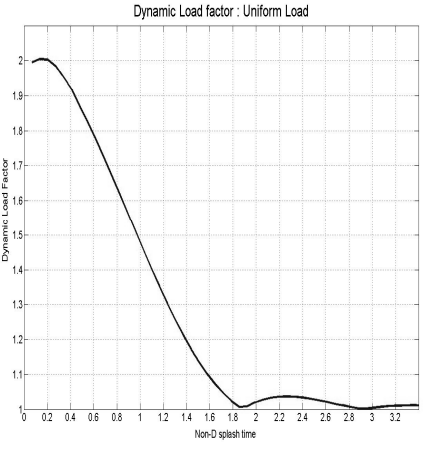

Fig. 4b Dynamic Load factor (DLF)

The modal contribution of the uniform moving load at various transient speeds has been shown in Fig.4a. It is seen that the 20th mode contributes to the order of 10^{-6} times the first mode. This modal truncation study serves as a representative guideline for other forcing configurations, where the normal mode superposition limit is set to the first 20 modes.

Interestingly, at realtively high speeds (small Tsp), the rmc surface shows a particular higher mode (hence a corresponding higher frequency of vibration) is excited for a given speed. The modal contribution for non-D Tsp<0.25 is inconsistent, with each speed associated with a particular vibratory overtone.

3.2 Impact Loading

The impact of the 2-D wedge section on a calm water surface at a downward velocity V (Fig.5) produces a rise up and a spray jet above the mean free surface. The impact pressure depends on V and β. The maximum impact pressure occurs at the spray root d(t), which is defined as the jet head translation at that instant.

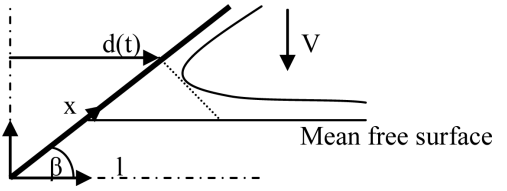

Fig. 5 Impact forcing model with chines dry

However, subsequent research by Cointe [18], Korobkin et al [21] and Faltinsen [22] indicates a superposition of asymptotic expansions of extremely high pressures at the spray root and lower pressures away from it.

Peseux et al [19] define a closed form solution of the impact force as a function of space and time, using the following independent variables :

Jet head $d(t) = \frac{Vt\pi}{2\tan(\beta)}$, Jet head velocity $\dot{d(t)} = \frac{V\pi}{2\tan(\beta)}$, Jet Thickness $\delta(t) = \frac{\pi V^2 d(t)}{8\dot{d(t)}^2}$.

Total non-dimensional impact pressure is: $P_{impact} = \frac{P_{outer} + P_{inner} - P_{common}}{\frac{1}{2}\rho_w V^2}$ (3.2)

where $P_{outer}(x,t) = \rho_w \frac{Vd(t)\dot{d(t)}}{\sqrt{d^2(t) - (x\cos(\beta))^2}}$, $P_{common}(x,t) = \rho_w \frac{Vd(t)\dot{d(t)}}{\sqrt{2d(t)[d(t) - x\cos(\beta)]}}$.

The internal pressure is expressed by Howiden et al [20] as a stretching transformation with respect to the moving jet head d(t). ξ is a parameter for this transformation, and X is a dummy variable along the horizontal, scaled by the jet thickness and the deadrise angle (3.5). Stretching the length :

$x\cos(\beta) - d(t) = \tan^2(\beta)\cdot X$ with $X = \frac{\delta(t)}{2\tan^2(\beta)}\left[\frac{6+4\xi}{1+\xi} - 4\sqrt{\frac{\xi-1}{\xi+1}} + \log\left|\frac{\xi+1}{\xi-1}\right|\right]$ $\xi > 1;\ \xi < -1$

,

$P_{inner}(x,t) = \frac{\delta(t)}{\pi}[1 - \{\xi - (\xi^2 - 1)^{1/2}\}^2]$. Thus we get $F_{impact}(x,t) = P_{impact}(x,t).B$ for (2.4).

The impact pressure (3.2) has been further non-dimensionalized by the deadrise angle (β), and is shown in Fig.6. With decreasing β, the pressure distribution gets more and more localized, and the peak pressure increases in magnitude. The actual non-D impact pressure is calculated from Fig.6 by multiplying by $\tan^2(\beta)$. Applying the impact forcing on the dry beam at various impact speeds, the dynamic load factor (DLF) is estimated as shown in Fig. 7. At large splash times, the response is nearly quasi-static (DLF ≈ 1) irrespective of the deadrise angle. With increasing impact speeds and deadrise angles, the DLF asymptotes to higher and higher values, approaching DLF = 2 for β > 30, when the impact loading distribution approximates a translating uniform load (e.g. Fig. 4b). Further non-dimensionalization of the non-D splash time Tsp (3.1) with respect to cot(β) collapses the results.

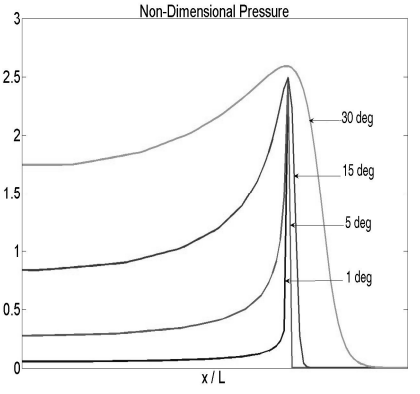

Fig. 6 Non-D impact forcing

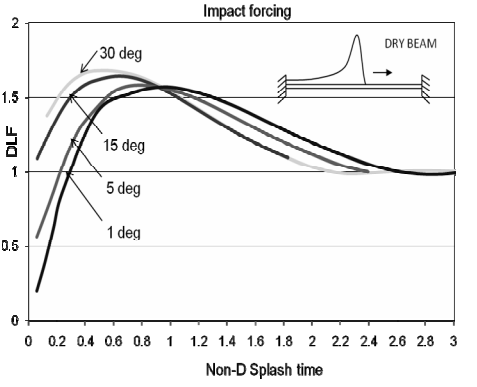

Fig. 7 DLF: Dry vibrations

3.3 Wet Vibrations with Impact Loading

Manipulation of (3.6) using the relations $m(x) = \rho_s hB$, $I = \frac{1}{12}Bh^3$ gives

$$\sum_{j=1}^{\infty} \frac{Eh^3}{12}\frac{d^4\Phi_j(x)}{dx^4} q_j(t) + \frac{d^2 q_j(t)}{dt^2}\rho_s h\left(\sum_{j=1}^{\infty}\Phi_j(x) + \left\{\frac{\rho_w L}{\rho_s h}\right\}\sum_{j=1}^{\infty}\varphi_j^*(x)\frac{1}{L}\right) = F_{impact}(x,t) \; .$$ Putting

$\alpha \equiv \frac{\rho_w L}{\rho_s h}$ = 0.1, 1.0, 10; the DLF is calculated for a range of impact speeds, as shown in Fig. 8. The parameter α is the ratio of the fluid to the solid density, scaled by the aspect ratio (Length-to-thickness) of the beam. This operation is used to study the influence of the added mass on the DLF with respect to the non-dimensional splash time Tsp. The dimensional governing differential equations are non-dimensionalized by the dry fundamental (lowest) period for a given α. α = 0 return the dry vibratory response, which is one of the limiting cases of (3.8). Again, α = ∞ models the vibration of a massless beam, or conversely, an extremely dense fluid.

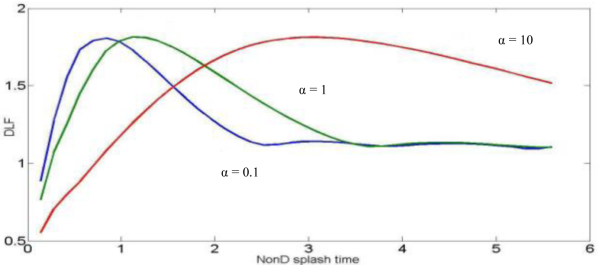

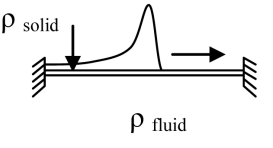

Fig. 8 DLF for various density ratios α; β = 5 degrees, normalized by $T_{1,\,dry}$

When plotted against the splash time non-dimensionalized by the dry fundamental period, increasing the ratio α stretches the DLF over the time scale, keeping the DLF magnitude and trend intact (Fig.8). However, non-dimensionalization of the splash time by the corresponding wet fundamental period (3.7) collapses the DLF's into one self-similar plot. Though this section studied the wet vibratory response only for a single deadrise angle, similar results can be obtained for other β's.

4 Discussion

A hydroelastic study of a clamped-clamped beam subjected to various loading conditions is presented. The primary motivation behind this work was to provide a basic interface between dynamic response to concentrated moving loads and marine slamming-induced vessel vibrations. A straightforward numerical analysis of an elastic beam yields to several dynamic response results and non-dimensional formulations. The dynamic response of the Euler-Bernoulli beam subjected to a uniform load sweeping across at a constant speed is considered as a benchmark result of this investigation. Applying impact forcing as an external force on the dry beam, at various deadrise angles, results in varying trends of the DLF, especially at very high speeds of the impact. Inclusion of fluid inertia at various ratios to the beam mass yields the wet frequencies of vibration. The non-dimensionalization of the loading time (splash time) by three distinct parameters, i.e. natural frequency, deadrise angle, and inertia ratio can serve as generic vibration analyses parameters.

The non-D splash time serves as input to evaluate the local elastic responses of structures subjected to impact loads. For example, a 1 m bow frame of a vessel with a fundamental natural frequency of 10 Hz, slamming against the water at a vertical velocity of 15 m/s, generates a non-dimensional splash time of 0.67. The corresponding DLF can be read from Fig. 7. The DLF for high speed crafts subjected to impact loading would be better estimated from Fig.8, since they are made of different materials (different solid densities) and operate widely (different fluid densities). The inertia ratio α becomes another design input parameter.

The choice of the definition of the DLF is based on returning a complete maximum dynamic response corresponding to the equivalent maximum static response. The evaluation of the configuration of the static deflection in space and time should not be a part of the already cumbersome design procedure.

This comparative study of dry vs. completely wet vibrations, however, considers only the two limiting cases of flexible fluid-structure interaction. The dry vibration assumes that the maximum structural response (hence the maximum stresses and strains) occurs early in the impact sequence, with most of the beam dry. Thus, the impact forcing can be considered as an external loading on a dry beam. In the other limit, the completely wet vibration assumes that the maximum structural response occurs later in the impact sequence, when the beam is completely submerged. Now, the impact forcing gets augmented by a radiation pressure, which is the inertia of the fluid set into motion by the beam. The dry modeshapes of the beam have been employed in the numerical modal analysis of the dynamic structural response. The impact-induced local hull vibrations involve

complicated hydrodynamics, with the maximum response occurring with the beam nearly halfway into the water. Local changes in the structure geometry, stiffness, deadrise angle further complicate the response and its analysis. The impact forcing model would be affected by wet chines. A probabilistic analysis in various sea states with forward vessel speed can, in fact, generate the slamming spectrum and the slam-induced flexural response spectrum for both long-crested and short-crested seas. This is an idealized study of uncoupled hydroelastic behavior of flexible beams to slamming loads, as a basic step to solve the fully coupled boundary value problem, where the fluid pressure and the structural response are evaluated simultaneously. This preliminary investigation forms the basis to understand more complicated geometries and forcing configurations.

Acknowledgements. This work was partially supported by the Office of Naval Research (ONR) grant titled "Design Tools for the Sea-Base connector Transformable Craft (T-Craft) Prototype Demonstrator", Award Number N00014-07-1-0856, under the direction of Kelly Cooper, ONR grant Award Number N00014-06-1-0474 under the administration of Dr. Patrick Purtell, and the Department of Naval Architecture and Marine Engineering, University of Michigan.

References

[1] Chatterjee, P.K., Datta, T.K., Surana, C.S.: Vibration of continuous bridges under moving vehicles. Journal of Sound and Vibration 169(5), 619–632 (1994)
[2] Esmailzadeh, E., Ghorashi, M.: Vibration Analysis of a Timoshenko beam subjected to a travelling mass. Journal of Sound and Vibration 1994(4), 615–628 (1997)
[3] Yang, Y., Yau, J., Hsu, L.: Vibration of simple beams due to trains moving at high speeds. Engineering Structures 19(11), 936–944 (1997)
[4] Garinei, A.: Vibrations of simple beam-like modeled bridge under harmonic moving loads. International Journal of Engineering Science 44, 778–787 (2006)
[5] Garinei, A., Risitano, G.: Vibrations of railway bridges for high-speed trains under moving loads varying in time. Engineering Structures 30, 724–732 (2008)
[6] Henke, D.J.: Transient response of plates to travelling loads with application to slamming damage. International journal of Impact Engineering 15(6), 769–784 (1994)
[7] Wang, R.T., Chou, T.H.: Non-linear vibration of Timoshenko beam due to a moving force and the weight of the beam. Journal of Sound and Vibration 218(1), 117–131 (1998)
[8] Goncalves, P.J.P., Brennan, M.J., Elliott, S.J.: Numerical evaluation of high-order modes of vibration in uniform Euler-Bernoulli beams. Journal of Sound and Vibration 301, 1035–1039 (2007)
[9] Lamb, H.: On the vibrations of an elastic plate in contact with water. Proceedings of the Royal Society of London, Series A 98(690), 205–216 (1920)
[10] Lewis, F.M.: The inertia of water surrounding a vibrating ship. SNAME transactions 37, 1–20 (1929)
[11] Mclachlan, N.W.: The accession to inertia of flexible discs vibrating in a fluid. Proceedings of the Physical Society of London (1932)

[12] Yadykin, Y., Tenetov, V., Levin, D.: The added mass of a flexible plate oscillating in a fluid. Journal of Fluids and Structures 17, 115–123 (2003)
[13] Bishop, R.E.D., Price, W.G.: On the relationship between “dry modes” and “wet modes” in the theory of ship response. Journal of Sound and Vibration 45(2), 157–164 (1976)
[14] Bishop, R.E.D., Price, W.G.: An introduction to ship hydroelasticity 87(3), 391–407 (1983)
[15] Troesch, A.W.: Wave-induced hull vibrations: an experimental and theoretical study. Journal of Ship Research 28(2), 141–150 (1984)
[16] Faltinsen, O.M.: Hydroelastic Slamming. Journal of Marine Science and Technology 5, 49–65 (2000)
[17] Senjanavic, I., Malenica, S., Tomasevic, S.: Investigation of ship hydroelasticity. Ocean Engineering (2008), doi:10.1016/j.oceaneng.2007.11.008
[18] Cointe, R.: Two-dimensional water-solid impact. Journal of Offshore Mechanics and Arctic Engineering 111, 109–114 (1989)
[19] Peseux, B., Gornet, L., Donguy, B.: Hydrodynamic impact: numerical and experimental investigations. Journal of Fluids and Structures 21, 277–303 (2005)
[20] Howison, S.D., Ockendon, J.R., Wildon, S.K.: Incompressible water-entry problems at small deadrise angles. Journal of Fluid Mechanics 222, 215–230 (1991)
[21] Khabakhpasheva, T.I., Korobkin, A.A.: Approximate models of elastic wedge impact. In: 18th IWWFB (April 2003)
[22] Faltinsen, O.M.: Water entry of a wedge by hydroelastic orthotropic plate theory. Journal of Ship Research 43(3), 180–193 (1999)
[23] Katz, Plotkin: Low-Speed Aerodynamics. McGraw-Hill, Inc., New York

Random Vibrations with Inelastic Impacts

Mikhail Dimentberg, Oleg Gaidai, and Arvid Naess

Abstract. The paper presents a study of single-degree-of-freedom stochastic vibroimpact problems using numerical path integration (PI). This is a challenging problem due to discontinuities in the state space paths of displacement and velocity response. It is shown that by introducing a suitable transformation of the state space variables, PI can be much simplified, and very accurate numerical results can be obtained. This is verified by comparison with extensive Monte Carlo simulation results.

1 Introduction

Problems of random vibration with inelastic impacts are particularly difficult for analysis whenever response probability densities (PDFs) are required rather than just some moments of the response. Indeed, the first solutions for response PDFs for cases of elastic impacts were obtained as far back as in the sixties [1, 8] using appropriate transition to the limit for the corresponding piecewise-continuous systems as described in [2]. However, the case of inelastic impacts was analyzed much later [5] (see also [4]) and only under condition of small impact losses; more specifically, the quantity $1 - r$ was assumed to be proportional to a small parameter, where $0 \le r \le 1$ is a restitution factor, which expresses the decrease of return velocity after impact. The analysis was facilitated by the work [13] (see also [14]) where a certain "mirror-image" transformation had been introduced for response displacement and velocity which resulted in transformed ODEs with only asymptotically small velocity jumps. Application of the quasi-conservative stochastic averaging (QCSA) method [4, 9] resulted in an approximate first-order stochastic differential equation (SDE) for the response energy $H(t)$ and finally a quadrature analytical solution was derived for the stationary PDF $p(H)$ of the energy H. Similar analysis by the QCSA is also presented in [3] as based on using another transformation to exclude the main part of velocity jump (certain deterministic

Mikhail Dimentberg
Mechanical Engineering Department, Worcester Polytechnic Institute, Worcester, Massachusetts 01609

Oleg Gaidai
Det Norske Veritas (DNV), NO-7496, Trondheim, Norway

Arvid Naess
Centre for Ships and Ocean Structures and Department of Mathematical Sciences, Norwegian University of Science and Technology, NO-7491, Trondheim, Norway

R.A. Ibrahim et al. (Eds.): Vibro-Impact Dynamics of Ocean Systems, LNACM 44, pp. 67–78.
springerlink.com

problems are considered there as well). Still the above results are valid only for systems with small impact losses.

In this paper a simple single-degree-of-freedom (SDOF) system is considered with impacts at a rigid barrier at the system's equilibrium position. The system is excited by an external stationary zero-mean random force *f (t),* so that its differential equation of motion *between impacts* is

$$\ddot{u} = f\left(t,u,\dot{u}\right), \quad f\left(t,u,\dot{u}\right) = -\Omega^2 u + g(t) \quad \text{for } u > 0, \tag{1}$$

where $g(t)$ denotes a random excitation, whereas the impact/rebound condition for the "classical" instantaneous impact is

$$\dot{u}_+ = -r\dot{u}_- \text{ for } u = 0, \text{ where } 0 \le r \le 1 \cdot \tag{2}$$

Here subscripts "minus" and "plus" refer to values of response velocity just before and after the (instantaneous) impact whereas *r* is the restitution factor so that impact losses are increasing with *1 – r*. For simplicity it is assumed here that these losses dominate those involved in motion between impacts. Whilst the above problem should be regarded mainly as a model for analysis of basic effects involved in the case of high impact losses, it may have potential direct applications to the dynamics of moored bodies subjected to ocean waves.

The main part of this paper is devoted to a numerical study of the response PDF for the system given by Eqs. (1) and (2) using the path integration (PI) method [11, 12] together with the following transformation of variables $(u,\dot{u}) \to (x, y)$, which is explained in detail in [6, 7],

$$\begin{aligned} &u = |x| = x \operatorname{sgn} x, \ \dot{u} = Sy \operatorname{sgn} x, \\ &\text{where } S = 1 - k \operatorname{sgn}(xy), \ k = \frac{1-r}{1+r} \end{aligned} \tag{3}$$

which *completely* excludes a velocity jump at the instants of impact. The transformation (3) leads to the following set of two first-order equations for the new state variables *x(t), y(t):*

$$\begin{aligned} &\dot{x} = Sy, \\ &\dot{y} = S^{-1} f(t, |x|, Sy \operatorname{sgn} x) \operatorname{sgn} x, \end{aligned} \tag{4}$$

since $\dot{u} = \dot{x} \operatorname{sgn} x$, that is, $Sy = \dot{x}$ and $\ddot{u} = S\dot{y} \operatorname{sgn} x$, that is, $\dot{y} = S^{-1}\ddot{u} \operatorname{sgn} x$.

In the special case $r = 1$ (thus $S = 1$) the transformation (6) reduces to one proposed in [13] and therefore it may be called Zhuravlev-Ivanov transformation. This transformation greatly facilitates path integration (PI) by removing the open boundary at *x = 0*.

The case of small impact losses, with *1 – r* being proportional to a small parameter, may be based on the transformation (3) with *k = 0* as long as it leads to

transformed impact condition as $y_+ = ry_-$. The remaining asymptotically small velocity jump may be incorporated into the SDE of motion using the Dirac delta-function represented as, $(y_+ - y_-)\cdot\delta(t-t_*) \cong (1-r)\,y\cdot\delta(t-t_*) = (1-r)\,y|y|\delta(y)$. Here y is arbitrary value satisfying double inequality $|y_+| < |y| < |y_-|$ (for example, arithmetic mean of y_+, y_-) with the above approximation being valid up to higher-order terms in $1 - r$. Rigorous proof of this "delta-function treatment" of asymptotically small impact losses can be found in Sect. 28 of the book [14]. However, this treatment as used in [4, 5] may not be necessary with the full transformation (3) available which completely removes velocity jump at $x = 0$. Thus, another goal of this paper is to rederive the asymptotic analytical solution for response PDF in the system (1), (2) for the case of small $1 - r$ and broadband $g(t)$. Introducing the response energy for the transformed system as $H = (1/2)\left(y^2 + \Omega^2 x^2\right)$ and applying the Eqs. (4) yields

$$\begin{aligned} \dot{H} &= y\dot{y} + \Omega^2 x\dot{x} = \Omega^2\left(S\cdot xy - S^{-1}\cdot xy\right) + S^{-1} y g(t)\, sgn\, x \\ &\cong -2k\Omega^2 |xy| + y g(t)\, sgn\, x \end{aligned} \tag{5}$$

Here terms with higher-than-first powers of k were neglected; in particular, we may put $S^{-1} \cong 1 + k\,\mathrm{sgn}(xy)$ in the damping term; also the small k-term may be neglected in the expression for random excitation.

2 Stochastic Averaging Analysis for the Case of Small Impact Losses

The basic version of the stochastic averaging method [4, 9] may be applied to the quasilinear system (5) where the state variables x, y may be expressed in terms of the slowly varying energy $H(t)$ and phase $\phi(t)$ as

$$x = \left(\sqrt{2H}/\Omega\right) sin\psi,\; y = \sqrt{2H}\; cos\psi,\; \psi = \Omega t + \phi \tag{6}$$

These relations are substituted into the Eq. (5) and averaging over the "rapid" time t within period $2\pi/\Omega$ is then applied with slowly varying H and ϕ being held fixed. This results in the limiting Ito SDE (with second term in the RHS representing the corresponding Wong-Zakai correction)

$$\dot{H} = -2\alpha_{eq} H + D_\varsigma/2 + \sqrt{H}\,\varsigma(t)\;, \tag{7}$$

where $\alpha_{eq} = 2k\Omega/\pi \cong (1-r)(\Omega/\pi)$ and $\varsigma(t)$ is a limiting "equivalent" white noise with intensity $D_\varsigma = 2\pi\Phi_{gg}(\Omega)$ where $\Phi_{gg}(\omega)$ is a power spectral density (PSD) of *g(t)*.

The stationary PDF *p(H)* of *H(t)* satisfies the corresponding Fokker-Planck-Kolmogorov (FPK) equation

$$(d/dH)\left[\left(-2\alpha_{eq}H + D_\varsigma/2\right)p\right] = \left(D_\varsigma/2\right)\cdot\left(d^2/dH^2\right)\left(dp/dH\right) \quad (8)$$

which has the following solution

$$p(H) = \left(1/\sigma^2\right)exp\left(-H/\sigma^2\right),$$
$$\text{where } \sigma^2 = \frac{D_\varsigma}{4\alpha_{eq}} = \frac{D_\varsigma\pi}{4(1-r)\Omega} \quad (9)$$

This result clearly coincides with the relevant special case of the solution for *p(H)* obtained in [4, 5] for more general case of nonzero offset between the barrier and the system's equilibrium position. This general case may also be analyzed using proper adjustment of the transformation (3) [6, 7] and applying QCSA. The solution (9) is seen to be (asymptotically!) the same as for the linear system without barrier with the "equivalent" viscous damping ratio $(1-r)/\pi$. Furthermore, joint PDF of the transformed displacement and velocity *x* and *y* is found to be asymptotically Gaussian in the present case which may be called "pseudolinear". This can be demonstrated by returning in the Eq. (9) to original variables *x, y* according to relations (6) with the phase being independent of *H* and uniformly distributed within $[0, 2\pi)$ so that $p(H,\phi) = p(H)/2\pi$.

3 The PI Method

The main goal of this paper, however, is to demonstrate the efficiency of the PI method in predicting response PDFs for stochastic vibroimpact systems with high energy losses at impacts. The Zhuravlev-Ivanov transformation (3) greatly facilitates implementation of the PI by removing the open boundary at *x=0*. For a detailed description of the PI-method and its implementation, we refer to [11,12]. In the present paper a recently developed path integration (PI) technique based on FFT is used which incorporates cubic B-splines interpolation [10]. As a simple convergence criterion we chose to match the first few moments estimated from Monte Carlo (MC) simulations and from the PDF as calculated by the PI.

In section 5 of this paper we shall need a three dimensional (3D) version of the PI method since the stochastic excitation is expressed as a white noise passed through a nonlinear first-order filter. This kind of dynamic system, discretized with constant time steps Δt using the fourth order Runge-Kutta scheme (RK4)

and with the random excitation entering only in the third dimension, can be written as,

$$\begin{aligned} X &= X' + r_1(X', Y', Z', \Delta t) \\ Y &= Y' + r_2(X', Y', Z', \Delta t) \\ Z &= Z' + r_3(X', Y', Z', \Delta t) + \sqrt{D_W}\,\Delta B(t)\,, \end{aligned} \tag{10}$$

where $\mathbf{Z} = (X, Y, Z)^T$ and $\mathbf{Z}' = (X', Y', Z')^T$ represent the state space vectors at the present time instant t and at the previous time instant $t' = t - \Delta t$, respectively. $B(t)$ denotes a standard Brownian motion process, and $\Delta B(t) = B(t) - B(t')$. To study the discretized SDE (10), the PI technique is used. It is based on the total probability law

$$p(\mathbf{z}, t) = \int_{\mathbb{R}^n} p(\mathbf{z}, t \mid \mathbf{z}', t') p(\mathbf{z}', t') d\mathbf{z}' \tag{11}$$

where $p(\mathbf{z}, t)$ denotes the PDF of $\mathbf{Z}$ at time instant t, and $p(\mathbf{z}, t \mid \mathbf{z}', t')$ denotes the transition PDF of $\mathbf{Z}$ at time instant t given $\mathbf{Z}' = z'$ at time instant t'. This means that for any $\mathbf{z}$, the PDF at a time t can be calculated as an integral (11), based on the PDF at the previous time $t' = t - \Delta t$, if the path from $\mathbf{z}'$ to $\mathbf{z}$ can be calculated. The required (incremental) transition probability density (TPD) for sufficiently small Δt is a degenerated multivariate Gaussian distribution according to Eq. (10). Namely,

$$\begin{aligned} p(\mathbf{z}, t \mid \mathbf{z}', t') = {} & \delta(x - x' - r_1(\mathbf{z}', \Delta t)) \delta(y - y' - r_2(\mathbf{z}', \Delta t)) \\ & \cdot \frac{1}{\sqrt{2\pi D_W \Delta t}} \cdot \exp\left(\frac{-(z - z' - r_3(\mathbf{z}', \Delta t))^2}{2 D_W \Delta t} \right) \end{aligned} \tag{12}$$

Note that one needs to evaluate the PDF at time t' at values of the state space variable arguments that do not coincide with the initially chosen grid points. This is where the interpolation technique is required, which makes it possible to represent the PDF at all points in the requisite domain. It is shown in [10] that by combining equations (11) and (12) with transformation of variables z', the integral can be reduced to a convolution; this makes it possible to use FFT techniques to obtain fast iterations of the integration process needed to produce the PI solution.

An advantage of the PI method, if it is properly implemented, is its ability to produce very accurate solutions. However, the main drawback is the limited number of dimensions it can handle. Currently, 4D problems can be solved at acceptable computational cost. Of course, an alternative numerical solution approach is always offered by the Monte Carlo (MC) simulation method. While the latter is very attractive due to its versatility and simplicity, it cannot in practice provide information on the same level of detail as PI. Since our models in this paper are 2D and 3D, PI is a very attractive method to use.

4 Response PDFs for the Case of White-Noise Excitation

In this section the excitation *g(t)* in Eq. (1) is a stationary zero-mean Gaussian white noise $\varsigma(t)$ with intensity D_ς, i.e.

$$E[\varsigma(t)\varsigma(t+\tau)] = D_\varsigma \delta(\tau). \tag{13}$$

The numerical studies in this section are made for the case of white-noise intensity D_ς = 1.0. The restitution coefficient *r* is at first chosen as *r* = 0.5. This corresponds to substantial impact losses, so that only numerical tools are available. Figs. 1 and 2 present marginal PDFs obtained by numerical PI, which are seen to be well matched with the MC results. The left figures show the PDF of *x,* while

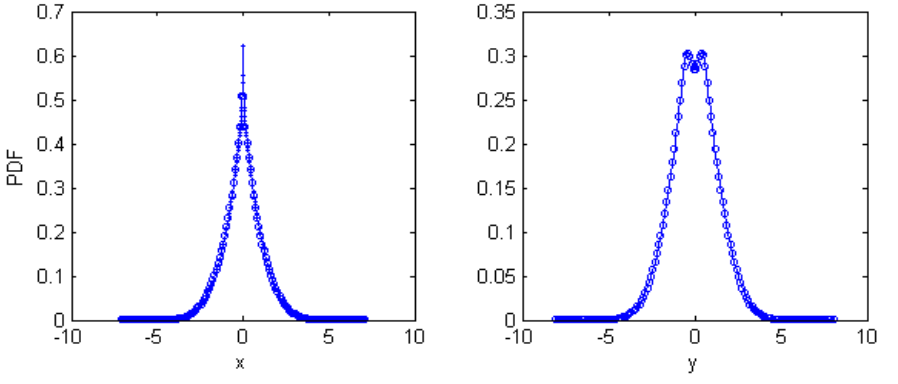

Fig. 1 1D PDF: PI (–), MC(o), $r = 0.5$

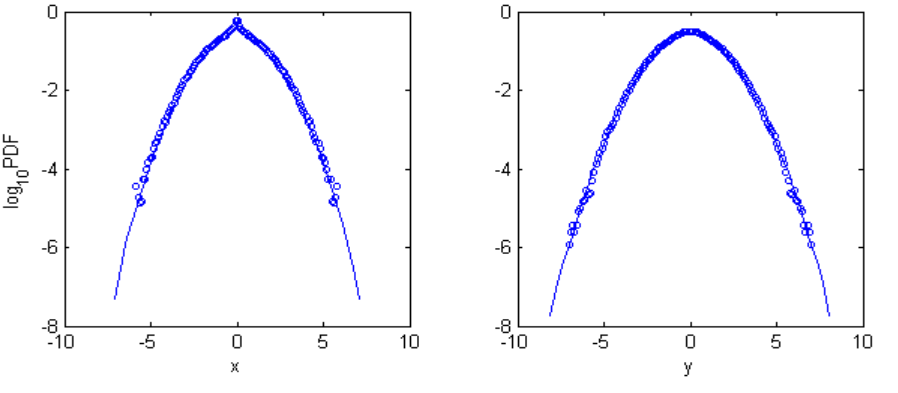

Fig. 2 Log plot of 1D PDF: PI (–), MC (o), $r = 0.5$

the figures on the right show the PDF of *y*. Fig. 2 highlights the merits of PI compared to MC. It is clearly visible that PI is very accurate in the tail estimation, which is essential for statistics of extremes. In Fig. 3 is shown a 3D plot of the joint PDF of *x* and *y*. This figure indicates that PI can be used to provide very detailed information about the dynamics, which is not easily available by other methods.

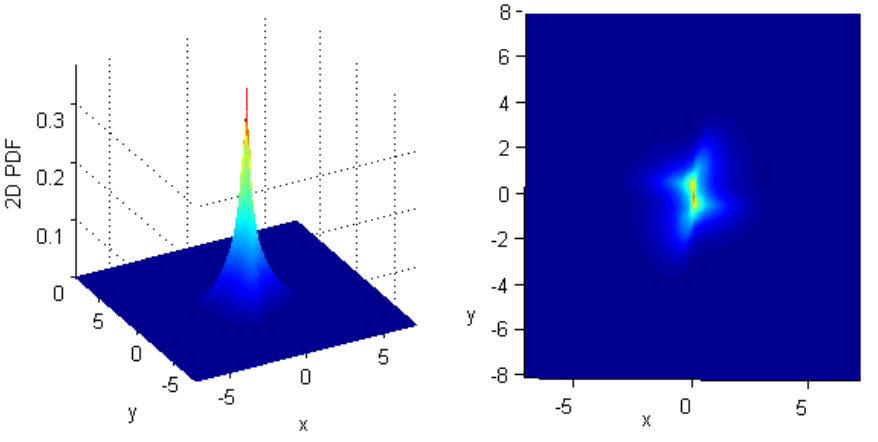

Fig. 3 Surface plot of 2D PDF obtained by PI, $r = 0.5$

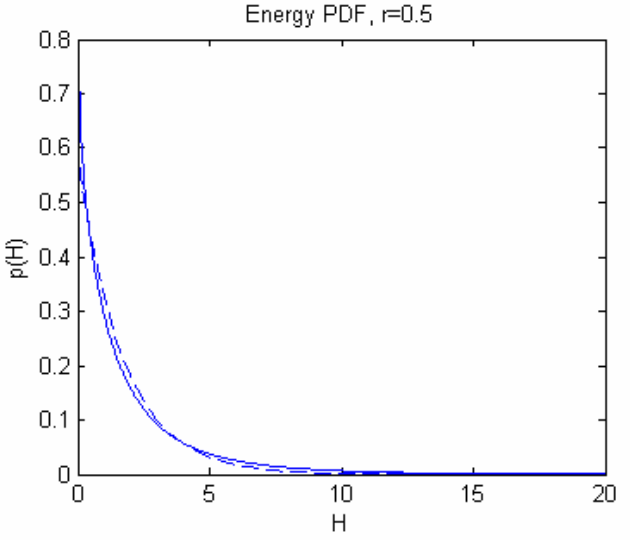

Fig. 4 Energy PDF obtained by PI (–) and QCSA approximation (--), $r = 0.5$

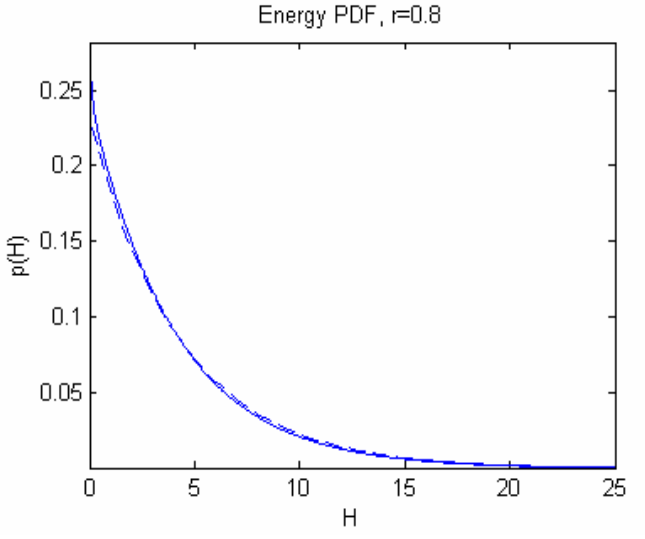

Fig. 5 Energy PDF obtained by PI (–) and QCSA approximation (--), $r = 0.8$

For a second set of runs, the value $r = 0.8$ is chosen. One may hope that QCSA would be reasonably accurate in this case, so it is of interest to compare numerical PI results with the analytical approximation. To establish a relation between the joint PDF $p_{XY}(x, y)$ obtained by PI and the target PDF $p_{U\dot{U}}(u, \dot{u})$ we may write

$$p_{U\dot{U}}(u,\dot{u}) = \frac{p_{XY}\left(u, \dfrac{\dot{u}}{1-k\,\mathrm{sgn}\,\dot{u}}\right) + p_{XY}\left(-u, -\dfrac{\dot{u}}{1-k\,\mathrm{sgn}\,\dot{u}}\right)}{1-k\,\mathrm{sgn}\,\dot{u}} = \frac{2p_{XY}\left(u, \dfrac{\dot{u}}{1-k\,\mathrm{sgn}\,\dot{u}}\right)}{1-k\,\mathrm{sgn}\,\dot{u}} \tag{14}$$

Next, from (3) one obtains,

$$p_H(H) = \int_{-\sqrt{2H}}^{\sqrt{2H}} \frac{p_{U\dot{U}}\left(\dfrac{\sqrt{2H-\dot{u}^2}}{\Omega}, \dot{u}\right) d\dot{u}}{\Omega\sqrt{2H-\dot{u}^2}} = 2\Omega^{-2} \int_{-\sqrt{2H}/(1+k)}^{\sqrt{2H}/(1-k)} \frac{p_{XY}\left(f(s,H), s\right) ds}{f(s,H)} \tag{15}$$

where $s = \dot{u}[1 - k \operatorname{sgn} \dot{u}]^{-1}$ and $f(s,H) = \Omega^{-1}\sqrt{2H - s^2[1 - k \operatorname{sgn} s]^2}$. Figs. 4 and 5 compare the energy PDF by PI with the QCSA approximation (9).The agreement is seen to be quite good, especially in the case $r = 0.8$, for which it should be expected.

5 Response PDFs for the Case of Narrow-Band Random Excitation

In this section the excitation *g(t)* in the Eq. (1) is of the form

$$g(t) = \lambda \sin z(t), \quad \dot{z} = \nu + W(t), \tag{16}$$

where $W(t)$ is a zero-mean Gaussian white noise with intensity D_W , i.e.

$$E[W(t)W(t+\tau)] = D_W \delta(\tau). \tag{17}$$

The process (15) is non-Gaussian and has a following PSD with finite bandwidth [9]

$$S_{gg}(\omega) = \frac{\left(\lambda^2 D_W/2\right)\left(\omega^2 + \nu^2 + D_W^2/4\right)}{\left(\nu^2 + D_W^2/4 - \omega^2\right)^2 + \omega^2 D_W^2} \tag{18}$$

As can be seen from the Eq. (18), the process *g(t)* is narrow-band if $D_W << \nu$

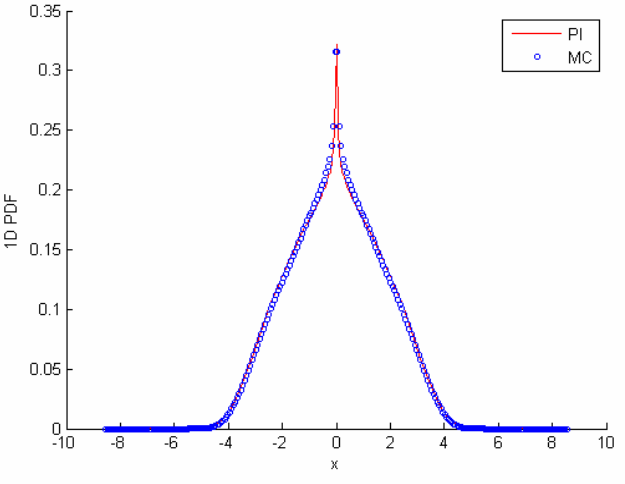

Fig. 6 PDF of *x*-variable, PI (–), MC (o)

Two numerical examples are considered here. The first one highlights a potential "singularity" in the joint response PDF, physically reflecting the energy absorption by the wall. (Actually, this is just a very sharp peak at zero although with a finite peak value for a finite *r*; the quotation marks with the name "singularity" has been used to indicate that the peak value may become infinite in the extreme case of plastic impact, i.e. for *r = 0*). This happens for a certain choice of parameter values, for example if

$$\Omega = 1, \quad \nu = 2, \quad \lambda = 2, \quad D_W = 1, \quad r = 0.5 \tag{19}$$

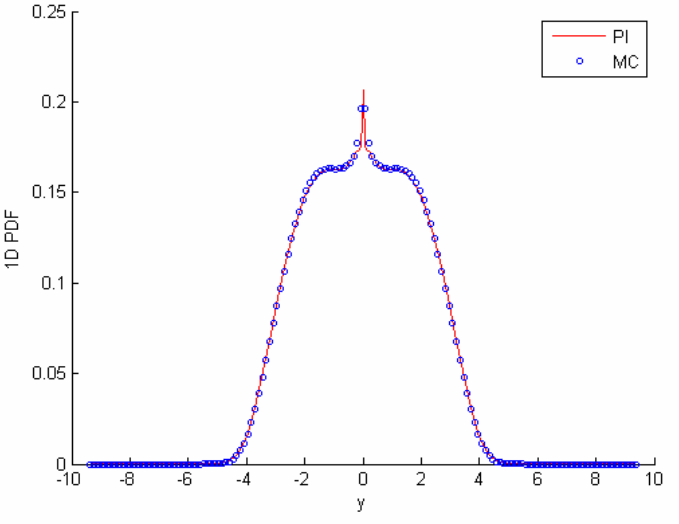

Fig. 7 PDF of *y*-variable, PI (–), MC (o)

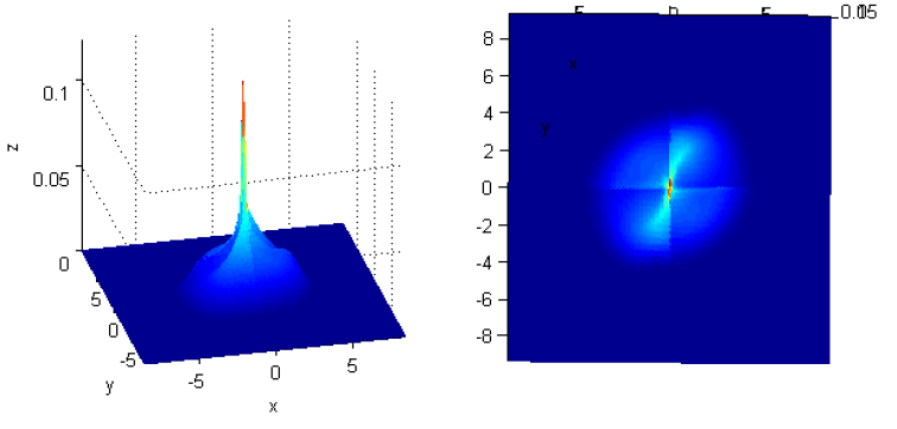

Fig. 8 Joint PDF *p(x,y)*, as obtained by PI for the case of strong noise

According to Eq. (18) this is the case of relatively high noise level and thus rather broadband excitation with the expected excitation frequency at the main or second-order resonance $\nu = 2\Omega$. Figures 6 – 8 present PDFs for Zhuravlev-Ivanov transformed variables. The marginal PDFs are seen in Figures 6 and 7 to be in good agreement with MC simulation results. The joint PDF possesses a "singularity" at (0,0) (Fig.8).

Next we consider the case of narrow-band excitation $D_W = 0.01$ with all other parameters being the same as in (18). This results in a crown-like PDF typical for sinusoidal-like signals, see Fig. 9.

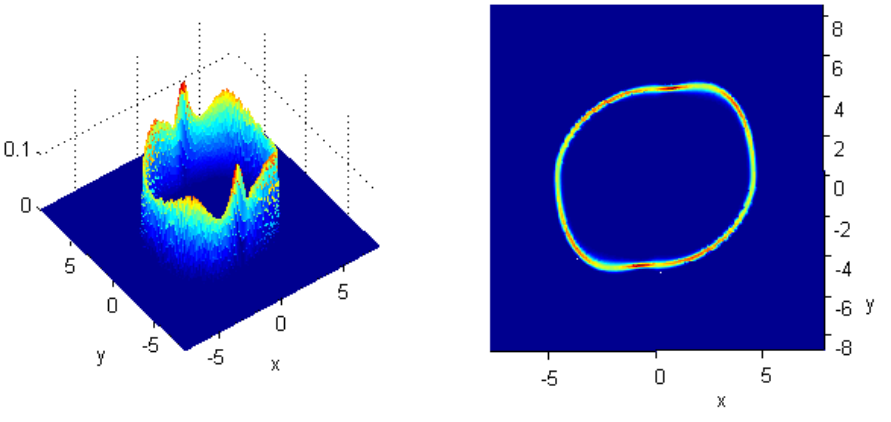

Fig. 9 Joint PDF(x,y) by PI, weak noise, $D_W = 0.01$

The above results clearly demonstrate the potential for use of the present version of the PI-method together with the Zhuravlev-Ivanov transformation for predicting response PDFs in stochastic vibroimpact problems with high impact losses. In particular, extension to the case of nonzero offset between the barrier and the system's equilibrium position seems straightforward. The PI-method has an advantage compared with the MC approach since it is free from the inherent scatter of results; this is especially important for estimating tails of the PDFs.

Acknowledgements. This work was supported by the Research Council of Norway (NFR) through the Centre for Ships and Ocean Structures (CeSOS) at the Norwegian University of Science and Technology (NTNU). Authors are thankful to Dr. E. Mo from NTNU for his collaboration in path integration FORTRAN coding.

References

[1] Babitsky, V.I., Kolovsky, M.Z.: Response of a linear system with barriers to random excitation. Engineering Journal, MTT (Mechanics of Solids) 3, 147–151 (1967)

[2] Babitsky, V.I., Krupenin, V.L.: Vibration of Strongly Nonlinear Dis-continuous Systems. Springer, Berlin (2001)

[3] Babitsky, V.I., Kovaleva, A.S., Krupenin, V.L.: Analysis of quasicon-servative vibroimpact systems by the method of averaging. In: Proceedings of the USSR Academy of Sciences, MTT (Me-chanics of Solids), vol. 1, pp. 41–50 (1982) (in Russian)
[4] Dimentberg, M.F.: Statistical Dynamics of Nonlinear and Time-Varying Systems. Research Studies Press, Taunton (1988)
[5] Dimentberg, M.F., Menyailov, A.: Response of a Single-Mass Vibro-impact System to White-Noise Random Excitation. ZAMM (Germany) 59, 709–716 (1979)
[6] Ivanov, A.P.: Impact Oscillations: Linear Theory of Stability and Bi-furcations. Journal of Sound and Vibrations 178(3), 361–378 (1994)
[7] Ivanov, A.P.: Dynamics of Systems with Mechanical Impacts. Moscow. International Education Program, 336 p. (1997) (in Russian)
[8] Larin, V.B.: On the selection of free gap for an resilience system in case of random vibrations. In: Proceeding of the Ukrain-ian Academy of Sciences, vol. 11, pp. 1449–1453 (1965) (in Ukrainian)
[9] Lin, Y.K., Cai, G.Q.: Probabilistic Structural Dynamics. Advanced Theory and Applications. McGraw Hill, New York (1995)
[10] Mo, E., Naess, A.: Efficient path integration by FFT. In: Proceedings 10th International Conference on Applications of Statistics and Probability in Civil Engineering (ICASP10), Tokyo, Japan (August 2007)
[11] Naess, A., Johnsen, J.M.: Response statistics of nonlinear, compliant offshore structures by the path integral solution method. Probabilistic Engineering Mechanics 8(2), 91–106 (1993)
[12] Naess, A., Moe, V.: Efficient Path Integration Methods for Non-linear Dynamic Systems. Probabilistic Engineering Mechanics 15(2), 221–231 (2000)
[13] Zhuravlev, V.F.: A method for analyzing vibration-impact systems by means of special functions. Mechanics of Solids 11, 23–27 (1976)
[14] Zhuravlev, V.F., Klimov, D.M.: Applied Methods for Theory of Oscillations, Nauka, Moscow (1988) (in Russian)

Performance of a Bi-unit Damper Using Digital Image Processing

S. Ekwaro-Osire, E. Nieto, F. Gungor, E. Gumus, and A. Ertas

Abstract. This paper deals with passive vibration control using a bi-unit impact damper, also referred to as bi-unit impact vibration absorber. The main contribution of this work is to experimentally analyze the performance of a bi-unit impact vibration absorber using digital image processing. With the use of this technique, two or three bodies will be tracked simultaneously, namely, the primary system, and either the response of one or two impacting steel balls. The absorption pattern of the bi-unit is studied under free vibrations, constant frequency excitation, and sweep excitations. These results reveal that the use of digital image processing can eliminate the use of existing limitations which can sometimes change the dynamics of the system. The optical technique used captures reliably the detailed vibro-impact dynamics of the bodies. The detailed dynamic patterns of the particles during varying levels of energy absorption from the primary system are discussed in context of published theoretical results.

1 Introduction

Vibration dampers are used extensively to control excessive vibrations of resonant systems. The impact damper or impact vibration absorber (IVA) is an auxiliary oscillator added to a primary system in order to mitigate vibrations. Proper control can be achieved by tuning the parameters of the IVA so that the oscillations of the primary system are reduced through energy transfer [1]. Impact vibration absorbers can be classified as, single unit IVA, multi-unit IVA, compound IVA, and hybrid IVA [2].

Sevin [3] used the free motion of a compound IVA and studied the basis of approximate nonlinear equations of motion. The IVA was a pendulum type vibration absorber where the mechanical system exhibits the phenomena of auto parametric excitation. Through numerical solution, approximately 150 cycles of the beam oscillation take place during a single cycle of energy interchange.

Kato [4] investigated an IVA with a spring-supported additional mass. Theoretical analyses were conducted, where the main mass system is subjected to forced displacement. The system showed that an IVA of one-sided impact design

S. Ekwaro-Osire, E. Nieto, F. Gungor, E. Gumus, and A. Ertas
Mechanical Engineering Department, Texas Tech University, Lubbock, USA.

R.A. Ibrahim et al. (Eds.): Vibro-Impact Dynamics of Ocean Systems, LNACM 44, pp. 79–90.
springerlink.com

is superior in damping effect to one of two sided impact design. In order to achieve a damping effect over a wide range of frequencies, the static distance between the IVA and the stopper must be chosen properly, so the ratio between the natural frequency of the primary system versus the IVA must be set in the range of 0.6 – 0.8. Duncan et al. [5] used computer simulations to study a single particle vertical impact damper. They showed that the extent of damping increased with increasing coefficient of restitution and mass ratio.

Saeki [6] performed an experimental and analytical study of a multi-unit IVA in a horizontally vibrating system. He showed that the energy absorption depended on the relationship between the mass ratio and the number of cavities. Xu et al. [7] considered particle damping for application as passive vibration suppression. It was shown that shear friction plays a major role in the particle damper, particularly for the case of high volumetric packing ratios of the particles.

Collette and Semercigil [8] combined a spring-mass absorber with a secondary IVA. This three degree of freedom system consisted of three mechanical oscillators. The IVA controlled the response of the primary system quite effectively. Li and Darby [9] performed experiments on the effect of a multiple degree of freedom IVA. Due to the degrees of freedom, the results contradicted results from other studies for certain parameters, including the size of impact mass. For this configuration of IVA, the impact mass did not lead to an increased energy absorption for all modes. Also, the effect of clearance is unpredictable, particularly for higher modes.

In all the previous works on IVA discussed above, the movements of the primary system and impact masses were tracked using mechanically attached devices. But it is known that attaching transducers on a system has a potential to alter the dynamics of the system. The use of non-contact techniques eliminates the need for any attachment on the system which can sometimes change the dynamics of the system's response. The most widely used non-contact techniques include: laser vibrometry, vision-based techniques, holographic techniques, and electronic speckle pattern interferometry [10-12].

Marhadi [13] successfully measured particle impact damping for a cantilevered beam with a particle-filled enclosure attached to its free end. The material velocity was successfully measured using a laser vibrometer. Different materials were measured including lead spheres, glass spheres, tungsten carbide pellets, lead dust, steel dust, and sand. The materials were tested to see which one was a better IVA. Servahent et al. [14] designed a low-cost, simple, non-contact displacement sensor using the self-mixing effect inside a clock wise single-mode laser diode. The laser sensors successfully captured the resonance frequencies of thin clamped metallic plates. The measurements gave a true power spectrum often not been able to be captured with an accelerometer.

Tang and Lu [15] showed the feasibility of using vision-based techniques to successively control a robot arm. Chung et al. [16] published a "proof of concept" study in non linear system identification by three experiments, namely the coulomb friction coefficient associated with a pendulum sliding on a rigid board, the characteristics of base-isolation devices and the non-linear constitutive law of a rubber-like membrane. Wang et al. [10] proposed a vision-based technique for

sinusoidal vibration measurement based on motion blurred images. The authors showed that their proposed technique required less images compared to the un-blurred-image-based techniques.

The objective of this research is to study the effectiveness of a bi-unit IVA with the use of digital image processing. With the use of digital image processing, two or three objects will be tracked simultaneously, namely, the system's response, and either the response of one or two impact balls for the case of transient and forced vibrations. The effect of the distance between the limiting walls and the number of impact balls in the configuration will be studied. The time series data that will be acquired will include: (1) free vibrations, (2) constant frequency excitation, and (3) frequency sweep excitations. The time series data will be used to obtain motion plots and frequency responses. The data will be used to show the effectiveness of the IVA for various parameter configurations. For the first time, the data will also be used to precisely study the detailed dynamics of the impact ball relative to the limit walls.

2 Experimental Setup

The experimental setup is shown in Fig. 1. For the experiment, one or two impact balls will be placed in the structure (f). Using a signal generating software (a), the shaker (c) is excited horizontally through the amplifier (b) with deterministic signals. A piezoelectric low inductance accelerometer (d) will be placed on the shaker to measure the output from the software. The signal conditioners (e) will send the acceleration readings from the accelerometers. The steel impact ball(s) (g) will be placed in acrylic tubes and will impact the steel limit walls during excitations. A high speed camera (h) will be used to capture the position of the impact balls through the duration of the experiment at 500 or 1,000 frames per second. The frames captured will be stored in the second computer (i). The high speed camera captured the position of the one or two impact balls and the position of the primary system. The frames captured were then stored in a personal computer and later analyzed with the built in digital image processing toolbox in Matlab.

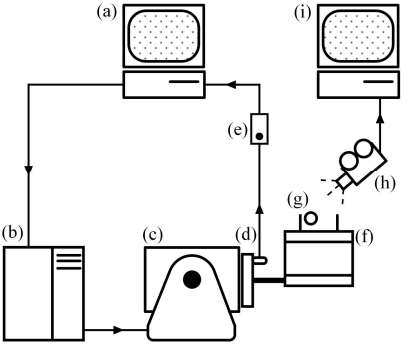

Fig. 1 Experimental setup (a) signal generating unit, (b) amplifier, (c) shaker, (d) accelerometer, (e) signal conditioner, (f) primary system, (g) impact vibration absorber, (h) high speed camera, (i) data acquisition and analysis unit

A high speed camera, running at 500 frames per second at 1280 × 1024 resolution camera, was used. Due to the frame grabber limitations of 1 gigabyte of memory, the maximum recording time for a single impact ball obtained was 26 seconds at a frame rate of 500 frames per second. For all free vibrations and constant frequency tests, a frame rate of 1,000 frames per second was used. For all downsweep tests, a frame rate of 500 frames per second was used. Matlab was used to analyze the frames captured from the high speed camera.

3 Methodology

The natural frequency of the system was tuned to 8.2 Hz without the IVA. Transient vibration experiments were conducted with an initial displacement applied to the system. The system parameters used in this study are shown in Table 1.

Table 1 System parameters

Parameter	Unit	Value			
Distance between limit walls, L_i	mm	50	75	100	-
Mass of impact ball, m_i	g	18	28	-	-
Initial Deflection, ξ_i	mm	10	20	30	-
Mass Ratio, μ_i	-	0.01	0.016	0.02	0.032

Forced vibration tests consisted of constant frequency excitation tests and a frequency sweep tests. For all frequency sweep experiments, the system was allowed to dwell at 8 Hz for ninety seconds in order to reach stability. The system would sweep up from 8 to 9 Hz and would sweep down from 9 to 8 Hz. Due to the limitations of recording time for data acquisition, a sweep rate of 0.04 Hz per second was used. The software limitations only allowed one impact ball to be used for sweep tests. Downsweep tests were performed as opposed to upsweep since several researchers have shown that a downsweep test corresponds well to the dwell test [2].

During constant frequency excitation experiments or dwell experiments [9], the test was programmed to run for ninety seconds. The data was collected one minute into the test. The initial time is necessary in order for the system to reach stability [2]. All parameters altered for the transient vibrations case were used in the constant excitation experiments with exception of the initial deflection.

4 Results and Discussions

4.1 Transient Vibrations

Fig. 2 portrays the decay characteristics of the primary system without an IVA (ζ_i = 20 mm) and with two 28 g impact balls for the case of (L_i = 50 mm, ζ_i = 20

mm). According to Fig. 2(a) the decay without the IVA is exponential whereas the decay with the IVA is linear for about one second followed by an exponential decay until the system ceases oscillating. It can be observed from Fig. 2(b) that the system's max oscillation becomes exponential at the moment the impact balls stop impacting the walls. Initially, the oscillations of the two impact balls are synchronized in the region where the decay is linear. It is observed that the two impact balls absorb the energy effectively when their oscillation is synchronized.

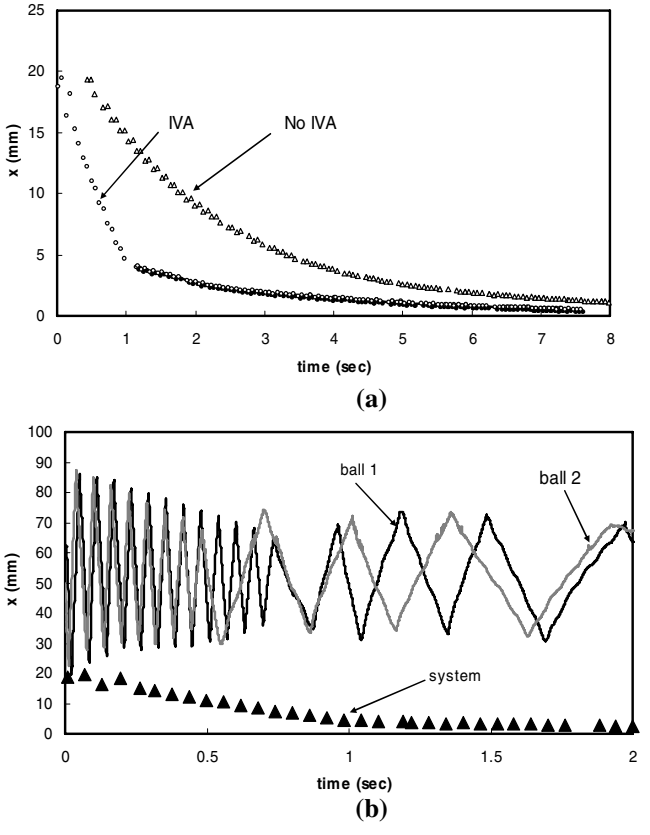

Fig. 2 Transient response (a) primary system with IVA and without IVA (b) primary system and impact balls (L_i = 50 mm, m_i = 28 g, ζ_i = 20 mm)

The effect of the mass ratios on the decaying characteristics of the system was investigated. The configurations considered were: one 18 g ball with a mass ratio of $\mu_i = 0.01$, one 28 g ball with a mass ratio of $\mu_i = 0.016$, two 18 g impact balls with a mass ratio of $\mu_i = 0.02$, and two 28 g impact balls with a mass ratio of $\mu_i = 0.032$. The mass ratio of the one 28 g impact ball and the mass ratio of the two 18 g impact balls almost remain unchanged. The decaying characteristics of the two similar mass ratios were almost identical. This is a good indication the decaying characteristics are not dependent on the number of impact balls used. It was also

demonstrated that increasing the mass ratio results in an increase of the slope of the linear portion of decay. This result is consistent with that by other researchers [9, 17]. As previously mentioned, once the impact balls stop impacting in a regular manner, the oscillations of the primary system begins to decay exponentially. It is noted that the result of the exponential decay after the linear decay is different from results of other researchers that used a simple and compound IVA [2].

It is also noted that as the distance between the limit walls increases, the decay becomes shallower. The effect of the initial displacement on the decaying characteristics of the system was also investigated. The largest initial deflection had the highest inclination and the smallest initial deflection had the lowest inclination. This result showed that as initial deflection reduced, the shallowness of the exponential decay decreased. These previous results are in agreement with the result in reference [18].

4.2 Forced Vibration

Fig. 3 and Fig. 4 show the characteristics of one 18 g ball with the distance between the limit walls of L_i = 50 mm and L_i = 100 mm, respectively. From Fig. 3, the impact ball oscillates during the entire test time but is ineffective most of the time. At around 8.2 Hz, the impact ball absorbs the most energy. The corresponding region, for the case without the IVA, depicts a peak displacement. Fig. 4 depicts the response of the primary system and single ball for the case when the distance between the limit walls is L_i = 100 mm. The region of 8.5 Hz is where the system with IVA has the least absorption and the impact ball is not impacting a wall. This is also observed before 8.4 Hz. Once the response of the system picks up, the wall makes contact with the impact ball and the impact ball absorbs the energy at 8.4 Hz, which is in the range of the natural frequency of the system. For the 100 mm length case depicted, the most oscillations during vibration absorption. This resulted into points of most and least energy absorption compared to the case of L_i = 50.

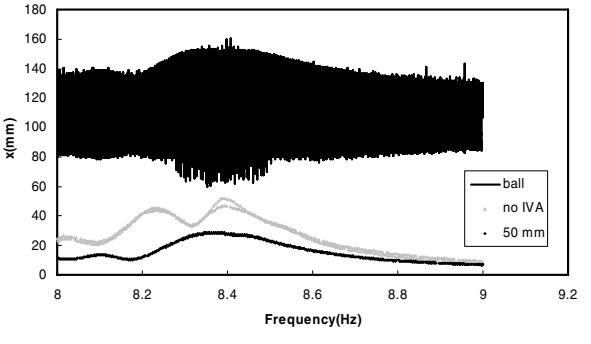

Fig. 3 Frequency sweep response of primary system and impact ball (L_i = 50 mm, m_i = 18 g)

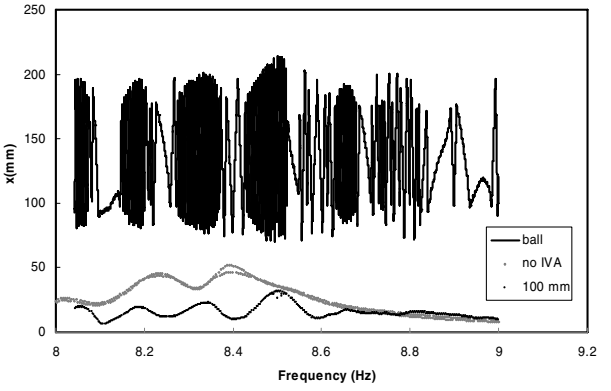

Fig. 4 Frequency sweep response of system and an impact ball (L_i = 100 mm, m_i = 18 g)

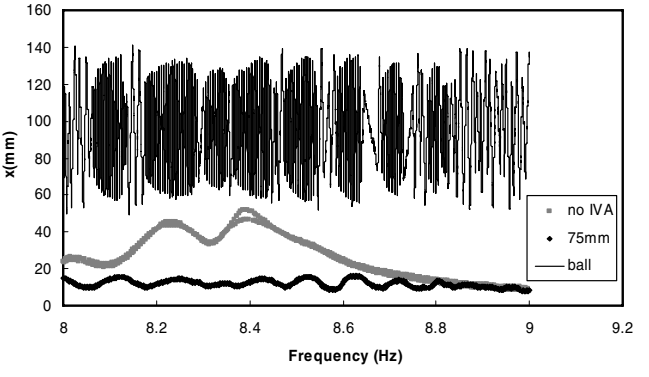

Fig. 5 Frequency sweep response of system and impact ball (L_i =75 mm, m_i = 28 g)

Fig. 6 System and ball response due to excitation frequency at 8.5 Hz (L_i = 50 mm, m_i = 18 g)

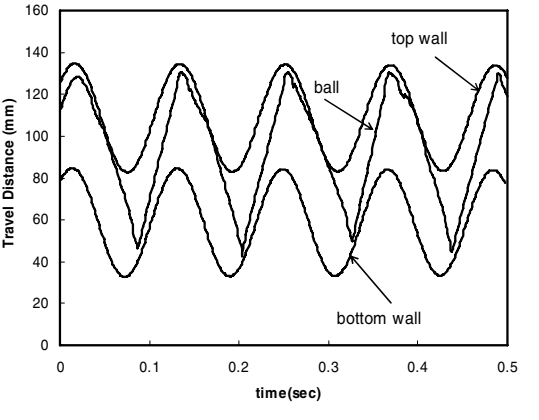

Fig. 5 depicts the characteristics of one 28 g ball with the distance between the limit walls of L_i = 75 mm. It was also shown that the impact ball oscillates continuously until in the neighborhood of the resonance region. In this region, the absolute oscillation of the impact ball is greatest. This results in high energy absorption. The energy absorption at this point causes the system to have very low response amplitudes, that are not sufficient for the impact ball to continue oscillating and therefore the impacting mass comes close to a stand still. Shortly after this, the response of the system drastically increases amplitude and causes the point of least energy absorption. This eventually leads to the impact balls to start oscillating again.

The configuration of m_i = 28 g, L_i = 75 mm, shown in Fig. 5, has the most energy absorption. From 9 to 8.8 Hz, the impact ball begins to slowly oscillate and ineffectively absorb energy. At around 8.7 Hz, the system experiences the least energy absorption and due to the unchanged amplitude of the system. The limit walls excite the impact ball almost through the rest of the duration of the test causing this test to be the most effective.

It was also shown that the impacting mass is least effective in the first resonance peak absorbing a small amount of energy. Due to the amplitudes at this stage, the impact ball absorbs energy effectively until 8.3 Hz. The large distance between the limit walls results in the ineffective energy absorption. The same characteristic can also be seen from the 18 g ball in Fig. 4.

The distance between the walls of L_i = 50 mm had the lowest amplitude. L_i = 75 mm was the most consistent absorber while L_i = 100 mm absorbed the least energy. It was also demonstrated how the increase in mass of IVA results in better energy absorption. The same results were obtained by Popplewell and Liao [19].

Fig. 6 demonstrates one 18 g ball at the indicated distance L_i between the limit walls. Fig. 6 demonstrates the consistency of the impacting mass. At the point of impact between the impacting mass and the wall, it can be noted the impacting ball follows the wall upon impact before changing direction. This is one

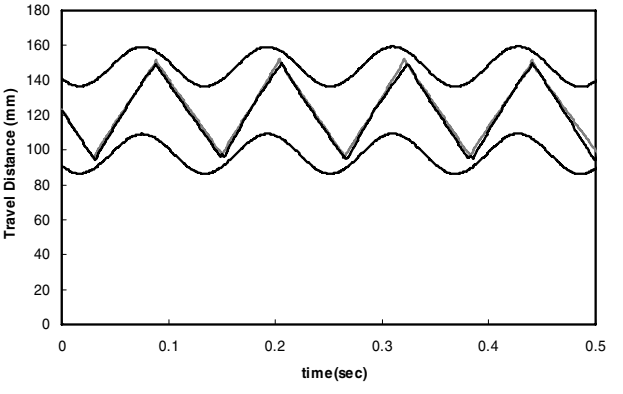

Fig. 7 System and ball response due to excitation frequency at 8.5 Hz (L_i = 50 mm, m_i = 18 g, 2 impact balls)

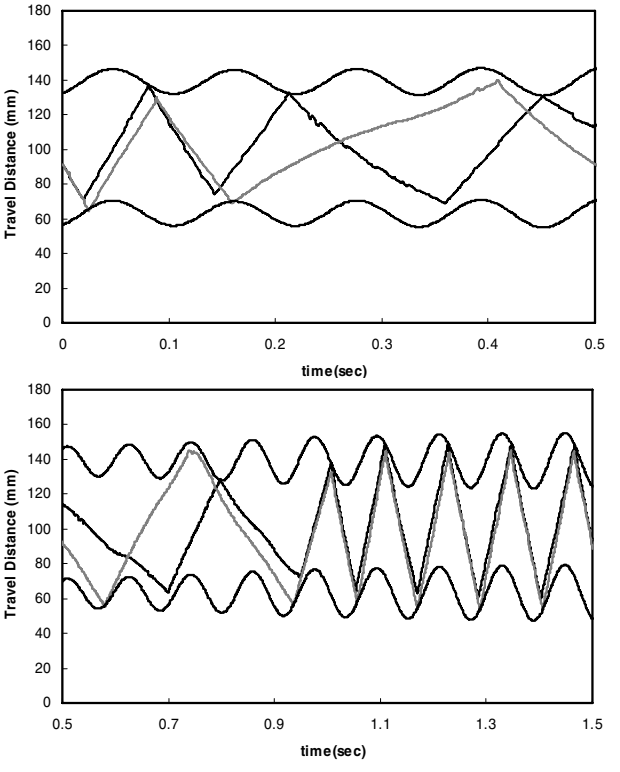

Fig. 8 System and ball response due to excitation frequency at 8.5 Hz (L_i = 75 mm, m_i = 18 g, 2 impact balls)

interesting observation made after looking at the actual footage during some of the tests. The power spectra of the three cases mentioned versus the case with no IVA were also extracted. Due to the consistency of the L_i = 50 mm and L_i = 75 mm, the system absorbs more energy. Researchers made an assumption of two impacts per cycle for theoretical studies [20]. The power spectra investigated indicated two impacts per cycle is a good assumption, however, inconsistency can occur for larger lengths between the limit walls in which result in less than two impacts per cycle. The dynamics of the 28 g impact ball is consistent to the case of the 18 g impact ball. For the four seconds data was collected, this pattern was observed twice. The 18 g impact balls and the 28 g impact balls behave similarly when excited at a constant frequency for the case of only one impact ball.

Fig. 7 and Fig. 8 demonstrate two 18 g impact balls at the indicated distance L_i between the limit walls. The responses of the two impact balls in Fig. 7 are consistent throughout the entire test. The motion of the impact balls becomes synchronized with the motion of the wall, hence they all move with the same frequency. Fig. 8 demonstrates how the impact balls can sometimes initially take an independent path and become synchronized with each other shortly there after.

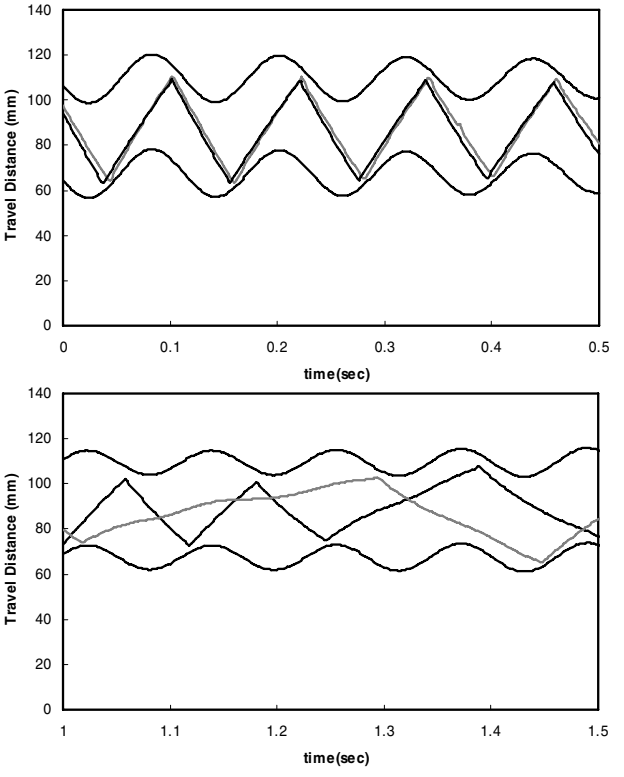

Fig. 9 System and ball response due to excitation frequency at 8.5 Hz (L_i = 50 mm, m_i = 28 g, 2 impact balls)

Fig. 9 depicts the response of the two 28 g impact balls at L_i = 50 mm. Here the motion of the two balls is initially synchronized and after some time the motions become unsynchronized. It is noted that for all cases where the impact balls were unsynchronized, the amplitude of the system was lower than when the impact balls were synchronized.

5 Conclusions

A vision-based technique was successfully used to study the detailed dynamics of a bi-unit impact damper or IVA. One or two impact balls were successfully tracked and the response of the system and the impact ball(s) were obtained. For the free vibrations of the primary system without the IVA, the decay is exponential, whereas the decay with the IVA is linear for about one second followed by an exponential decay until the system comes to a stand still. The response of the system becomes exponential at the moment the impact balls stop impacting the walls in a synchronized manner.

The largest initial deflection of $\zeta_i = 30$ mm resulted in the most energy absorption. The shortest distance between the limit walls of $L_i = 50$ mm absorbed the most energy. The mass ratio of $\mu_i = 0.020$ of the two 18 g impact balls and the mass ratio of $\mu_i = 0.016$ of the one 28 g ball had almost the same decaying slope. This is a good indication that the decaying characteristics of the system are not dependent on the number of impact balls used. The most energy absorption occurs at the highest mass ratio of $\mu_i = 0.032$ of the two 28 g impact balls.

For the frequency downsweep experiment, the 18 g ball, with the distance between the limit walls of $L_i = 50$ mm, oscillates throughout the entire test and absorbs the most energy near resonance of the system. Although the ball did not stop oscillating, the energy absorption was ineffective from 9 to 8.2 Hz. The 28 g ball with the distance between the limit walls of $L_i = 75$ mm was the most effective. For both impact balls, the distance between the limit walls of $L_i = 100$ mm was the least effective. The 28 g ball was more effective in energy absorption than the 18 g ball.

For the system and single ball response for both balls of 18 g and 28 g due to excitation frequency at 8.5 Hz, the shortest distance between the limit walls of $L_i = 50$ mm was the most consistent and absorbed the most energy. The frequency of the system is the same as the ball in the case where the ball is continuously impacting the wall. This is also the region where the most energy absorption occurs.

For the two ball case, the shortest distance between the limit walls of $L_i = 50$ mm resulted in the impact balls impacting the walls the most and resulted in the most energy absorption. The motion of the impact balls becomes synchronized with the motion of the walls. For the four seconds the data was collected, this pattern was repeated twice. As the distance between the limit walls increased, the ball loses consistency for both single and double ball cases. For the first time, the behavior of the impact balls are accurately tracked which is a step towards developing strategies to maximize its performance and control its behavior.

References

[1] Nayeri, R.D., Masri, S.F., Caffrey, J.P.: Studies of the performance of multi-unit impact dampers under stochastic excitation. J. Vib. Acoust. Trans. ASME 129, 239–251 (2007)

[2] Ekwaro-Osire, S., Desen, I.C.: Experimental study on an impact vibration absorber. J. Vib. Control 7, 475–493 (2001)

[3] Sevin, E.: On the parametric excitation of pendulum-type vibration absorber. J. Appl. Mech. Trans. ASME 28, 330–334 (1961)

[4] Kato, M., Dazai, M., Takase, H.: Study on impact damper having a spring-supported additional mass. Bull JSME 19, 103–109 (1976)

[5] Duncan, M.R., Wassgren, C.R., Krousgrill, C.M.: The damping performance of a single particle impact damper. J. Sound Vib. 286, 123–144 (2005)

[6] Saeki, M.: Analytical study of multi-particle damping. J. Sound Vib. 281, 1133–1144 (2005)

[7] Xu, Z., Wang, M.Y., Chen, T.: Particle damping for passive vibration suppression: Numerical modelling and experimental investigation. J. Sound Vib. 279, 1097–1120 (2005)
[8] Collette, F., Semercigil, S.E.: Response of a light secondary system with a modified tuned absorber to transient excitation. In: Imac - Proceedings of the 16th International Modal Analysis Conference, Vols 1 and 2, vol. 3243, pp. 595–601 (1998)
[9] Li, K., Darby, A.P.: Experiments on the effect of an impact damper on a multiple-degree-of-freedom system. J. Vib. Control 12, 445–464 (2006)
[10] Wang, S., Guan, B., Wang, G., Li, Q.: Measurement of sinusoidal vibration from motion blurred images. Pattern Recogn. Lett. 28, 1029–1040 (2007)
[11] Monsoriu, J.A., Gimenez, M.H., Riera, J., Vidaurre, A.: Measuring coupled oscillations using an automated video analysis technique based on image recognition. Eur. J. Phys. 26, 1149–1155 (2005)
[12] Patsias, S., Staszewski, W.J., Tomlinson, G.R.: Image sequences and wavelets for vibration analysis - part 1: Edge detection and extraction of natural frequencies. P I Mech. Eng. C-J Mec. 216, 885–900 (2002)
[13] Marhadi, K.S., Kinra, V.K.: Particle impact damping: Effect of mass ratio, material, and shape. J. Sound Vib. 283, 433–448 (2005)
[14] Servagent, N., Bosch, T., Lescure, M.: A laser displacement sensor using the self-mixing effect for modal analysis and defect detection. IEEE T Instrum. Meas 46, 847–850 (1997)
[15] Tang, P.C., Lu, S.S.: A video signal-processing technique for vibration measurement of a flexible beam. Int. J. Robot Res. 11, 579–583 (1992)
[16] Chung, H.C., Liang, J., Kushiyama, S., Shinozuka, M.: Digital image processing for non-linear system identification. Int. J. Non-Linear Mech. 39, 691–707 (2004)
[17] Bapat, C.N., Sankar, S.: Single unit impact damper in free and forced vibration. J. Sound Vib. 99, 85–94 (1985)
[18] Ekwaro-Osire, S., Ozerdim, C., Khandaker, M.P.H.: Effect of attachment configuration on impact vibration absorbers. Exp. Mech. 46, 669–681 (2006)
[19] Popplewell, N., Liao, M.: A simple design procedure for optimum impact dampers. J. Sound Vib. 146, 519–526 (1991)
[20] Egle, D.M.: An investigation of an impact vibration absorber. J. Eng. Ind. 9 (1967)

Dynamics of an Impacting Spherical Pendulum

A. Ertas and S. Garza

Since Newton first considered the motion of a spherical pendulum over two hundred years ago, many researchers have studied its dynamic response under a variety of conditions. The characteristic of the problem that has invited so much investigation was that spherical pendulum paradigms much more complex phenomena. Understanding the response of a paradigm gives an almost multiplicative effect in the understanding of other phenomena that can be modeled as a variant of the paradigm.

The spherical pendulum has been used to damp irregular motion in helicopters and on space stations as well as for many other applications. In this study an inverted impacting spherical pendulum with large deflection was investigated. The model was designed to approximate an ideal pendulum, with the pendulum bob contributing the vast majority of the mass moment of inertia of the system. Two types of bearing mechanisms and tracking devices were designed for the system, one of which had low damping coefficient and the other with a relatively high damping coefficient.

An experimental investigation was performed to determine the dynamics of an inverted, impacting spherical pendulum with large deflection and vertical parametric forcing. The pendulum system was studied with nine different bob and two different base configurations, for twenty times the natural frequency at shaker powers of 0 to 125 mm-Hz. It was found that sustained conical motions did not naturally occur. The spherical pendulum system was analyzed to determine under what conditions the onset of the following two types of motion:

Type I is a repetitive motion in which the pendulum bob does not traverse through the apex, $\theta = \pi$. The bob strikes the same general area of the restraint without striking the opposite side of the restraint.

Sustainable Type II response, which is the repetitive motion in which the pendulum bob traverses through the apex, $\theta = \pi$. The bob strikes opposite sides of the restraint.

A. Ertas and S. Garza
Department of Mechanical Engineering
Texas Tech University
Lubbock, Texas 79409

R.A. Ibrahim et al. (Eds.): Vibro-Impact Dynamics of Ocean Systems, LNACM 44, p. 91.
springerlink.com

Elastic and Inelastic Impact Interaction of Ship Roll Dynamics with Floating Ice

I.M. Grace and R.A. Ibrahim

Impact interaction of ships with floating ice or stationary rigid structures is a serious problem that affects the safe operation and navigation in arctic regions. Impact of ship roll dynamics with one-sided ice barrier is studied for elastic and inelastic impact cases. An analytical model of ship roll motion interacting with ice is developed based on Zhuravlev non-smooth coordinate transformation. This transformation has the advantage of converting the vibro-impact oscillator into an oscillator without barriers such that the corresponding equation of motion does not contain any impact term. Extensive numerical simulations are carried out for all initial conditions covered by the ship grazing orbit for different values of excitation amplitude and frequency of external wave roll moment. The basins of attraction of safe operation are obtained and reveal the coexistence of different response regimes such non-impact periodic oscillations, modulation impact motion, period added impact oscillations, chaotic impact motion and unbounded rotational motion. A comparison of the response for inelastic impact and elastic impact revealed that the additional damping associated with inelastic impact is significant than the linear and nonlinear damping terms.

Keywords: Ship roll dynamics, ice impact, grazing bifurcation, zhuravlev coordinate transformation, periodic motion, inelastic impact.

1 Introduction

In arctic regions, ice impact loading can cause significant damage to offshore structures and ships. The impact arises when drifting ice sheets, ice floes, and icebergs are moving with considerable speed under the action of environmental conditions. When a fast-moving ice feature crushes against a narrow structure, the force of

I M. Grace and R.A. Ibrahim
Wayne State University, Department of Mechanical Engineering,
Detroit, MI, 48202

R.A. Ibrahim et al. (Eds.): Vibro-Impact Dynamics of Ocean Systems, LNACM 44, pp. 93–104.
springerlink.com

impact is irregular, random and contains repetitive fluctuations. The random fluctuation can be explained by random variations of ice properties as well as ice failure at random locations along the contact area [1]. Zou [2] showed that ice loads are highly localized within high pressure regions. A design curve was proposed for the estimation of the extreme ice loads. Ice related problems encountered by offshore structures and navigating vessels experiencing roll instability due to their interaction with ice were reviewed by Ibrahim et al. [3].

The problem of continuous indentation of a ship or offshore structure into an ice sheet was examined by Karr et al. ([4], [5]) and Troesch et al. [6]. The impacting ship or offshore structure was represented by a mass-spring-dashpot system having a constant velocity relative to the ice sheet. The nonlinear dynamic response was due to intermittent ice breakage and intermittent contact of the structure with ice blocks. Periodic motions were predicted and the periodicity of a particular system was found to be dependent on initial conditions.

In studying vibro-impact systems one may encounter critical orbits that are neither free trajectories nor impact motion. For example, the trajectory of an oscillating mass reaching a barrier at zero velocity separates two regimes of motion, namely, non-impact and impact oscillations. The bifurcation associated with zero velocity just at the barrier is referred to as grazing bifurcation. Grazing bifurcation sensitively depend on initial conditions: small variations in initial conditions can cause the oscillator to cross the border between non-impact and impact oscillations. Shaw and Holmes ([7], [8]) and Shaw [9] studied the dynamic behavior of a periodically forced oscillator with one-sided barrier. They modeled the impact dynamics using a discontinuous map, which exhibited period-doubling bifurcations followed by a complex sequence of transitions of long super-stable periodic oscillations. Nordmark [10] expanded solutions in the neighborhood of a grazing orbit for an impact oscillator and obtained a two-dimensional map representing the dynamics of an orbit in the neighborhood of the grazing state. Nordmark [11] also studied the creation of a set of periodic orbits branching off from the grazing bifurcation point. Chin et al. [12] presented an analysis of grazing bifurcations for a simple impact oscillator system using Nordmark map, and predicted the occurrence of a series of transitions from a non-impacting period-1 orbit to period-M orbits, Weger et al [13] called this series by period-adding transitions. They also called the M-periodic orbits with one impact per period as “maximal” periodic orbits. Maximal orbits imply the occurrence of a single impact per period in M-periodic orbits. In an experiment, they explored the dynamics in the vicinity of period adding transitions.

The present work examines the impact of a ship roll dynamics with one-sided ice barrier for elastic and inelastic impact cases. An analytical model of impact interaction adopting Zhuravlev non-smooth coordinate transformation is presented. The unperturbed ship roll dynamics will be studied to identify the grazing orbit in terms of initial conditions. For all initial conditions covered by the grazing orbit, the perturbed ship dynamics will be estimated numerically in terms of excitation amplitude and frequency. The influence of the coefficient of restitution other than unity on the ship capsizing will be explored.

2 Elastic Impact

In the absence of ice impact, the nonlinear equation of motion of ship in beam sea waves takes the non-dimensional form

$$q'' + \bar{\zeta} q' + \gamma q' |q'| + q + C_3 q^3 + C_5 q^5 = Z(\tau) \tag{1}$$

where $q = \phi/\phi_c$, ϕ is the roll angle, ϕ_c is the ship capsizing angle, a prime denotes differentiation with respect to the non-dimensional time parameter $\tau = \omega_n t$, ω_n is the ship undamped natural frequency, $Z(\tau)$ is the external non-dimensional hydrodynamic moment applied on the ship, $\bar{\zeta} = 2\zeta$, ζ is the linear damping ratio, $C_3 < 0$, and $C_5 > 0$ are the nonlinear coefficients of the restoring moment. The third term on the left hand side represents the nonlinear damping moment where γ is a constant parameter and can be determined experimentally. In this section equation (1) will be examined for the case of purely elastic impact interaction.

Equation (1) is a nonlinear differential equation describing the ship roll dynamics under nonlinear hydrodynamic sea waves. One can adopt a non-smooth coordinate transformation introduced by Zhuravlev [14]. Zhuravlev assumed rigid barriers and converts the vibro-impact system into an oscillator without barriers such that the equations of motion do not contain any impact terms. The transformed system is then solved using any asymptotic technique. With reference to Fig. 1, the ship roll motion may experience impact when its roll angle reaches the impact angle, $\phi = -\phi_i$, i.e., $q = -q_i$, where $q_i = \phi_i/\phi_c$, the following transformation may be used for perfectly elastic impact

$$q = z\,sgn(z) - q_i \tag{2}$$

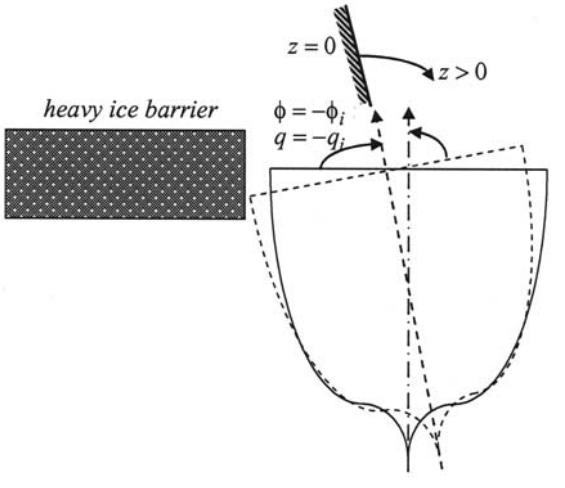

Fig. 1 Schematic diagram of a ship in roll against one-sided ice barrier

This transformation shifts the barrier to the axis $z = 0$ and maps the domain $q > -q_i$ of the phase plane trajectories on the original plane $\left(q, q^{'}\right)$ to the new phase plane $\left(z, z^{'}\right)$. The ship equation of motion takes the following form

$$z^{''} + \bar{\zeta} z^{'} + \gamma z^{'2} sgn(z^{'}) + z + sgn(z) \left\{ -q_i + C_3 \left[z sgn(z) - q_i \right]^3 + \right.$$
$$\left. + C_5 \left[z sgn(z) - q_i \right]^5 \right\} = Z(\tau) sgn(z) \tag{3}$$

In the absence of damping and external moment the unperturbed motion is governed by the equation

$$z^{''} + \Gamma(z) = 0 \tag{4}$$

where $\Gamma(z) = z + sgn(z) \left\{ -q_i + C_3 \left[z sgn(z) - q_i \right]^3 + C_5 \left[z sgn(z) - q_i \right]^5 \right\}$ is the nonlinear restoring moment and is shown in Fig. 2(a) for an impact angle $q_i = -0.4$, and nonlinear coefficients $C_3 = -1.1$, and $C_5 = 0.1$. It is seen that the restoring moment vanishes at $z = 0.4$. The potential energy, $\Pi(z)$, is obtained by integrating the restoring moment $\Gamma(z)$ over the limits q_i and z, i.e.,

$$\Pi(z) = \int_{q_i}^{z} \Gamma(y) dy = a_6 z^6 + a_5 z^5 + a_4 z^4 + a_3 z^3 + a_2 z^2 + a_1 z + a_0 \tag{5}$$

where the coefficients a_i are functions of q_i and the nonlinear restoring moment coefficients.

Note that the choice of the lower limit, q_i, is chosen such that at q_i the potential energy is minimum as shown in Fig. 2(b). It is seen at $z = 0$ (corresponding to ship angle $q = -q_i$) the potential has the maximum value $\Pi(z = 0) = 0.0730283$. The Hamiltonian of system (4), $H = z^{'2}/2 + \Pi(z)$, possesses the first integral of motion

$$z^{'} = \pm \sqrt{2 \left[H - \Pi(z) \right]} \tag{6}$$

As long as $H > \Pi(z)$ the phase diagram is periodic closed orbit in the phase space $\left(z, z^{'}\right)$ as shown in Fig. 3. With reference to Fig. 2(b), H reaches its maximum value $H_{\max} = \Pi(z = 0) = 0.0730283$. The periodic orbits are only restricted

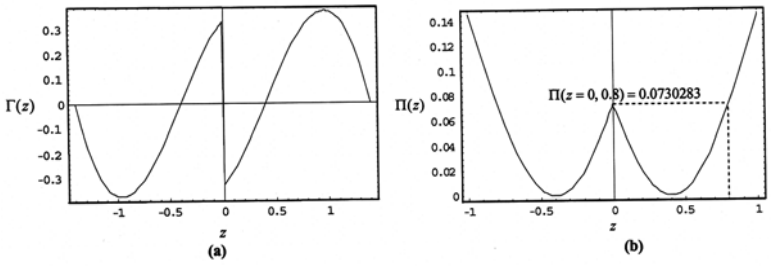

Fig. 2 (a) Restoring moment and (b) Potential energy in terms of Zhuravlev coordinate z

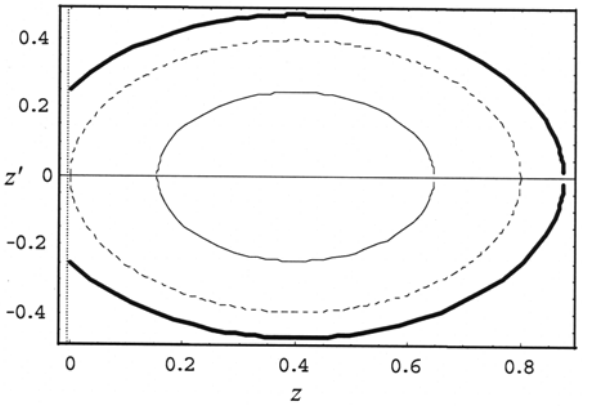

Fig. 3 Phase portrait for —— $H = 0.11$, - - - $H = 0.0730283$(Grazing), and thin curve $H = 0.03$

inside the domain $D = \{(z, z^{\cdot}) \,|H \leq H_c\}$, where $H_c = H_{\max} - \Delta H$, and ΔH is sufficiently small. H_c is the critical energy level above which impact of the ship will take place, and the trajectories of the motion will be structurally unstable. The motion corresponding to $H_{\max} = 0.0730283$ follows a critical orbit shown by the dashed curve in Fig. 3. This orbit describes the grazing impact of the ship with one-side barrier.

Under sinusoidal excitation $Z(\tau) = a\sin\nu\tau$, where a is the excitation amplitude, and $\nu = \Omega/\omega_n$, Ω is the excitation frequency, equation (3) is solved numerically under different values of excitation amplitude and frequency. The numerical solution is generated for all initial conditions occupying the grazing orbit shown in Fig. 3 by the dashed closed curve. For relatively low excitation amplitude the response is found to be periodic and the ship roll oscillation experiences free flight and does not reach the barrier. As the excitation amplitude increases the response experiences grazing bifurcation and assumes amplitude modulation. Further increase of the excitation amplitude results in a bounded chaotic motion with multi-impacts. Different motion scenarios are observed as the excitation amplitude increases. Finally, for an excitation amplitude exceeding a critical value, the ship is found to experience rotational motion indicating the occurrence of capsizing. However, for other initial conditions there is a possibility of other attractors that may coexist under the same excitation parameters. Fig. 4 shows samples of basins of attraction for different values of excitation amplitude and for excitation frequency parameter $\nu = 0.88$. It is seen that for relatively small values of excitation amplitude the entire domain bounded by the grazing orbit experiences non-impact bounded oscillations of period-one as shown in Fig. 4(a) by the black region. As the excitation amplitude gradually increases the response assumes modulated motion shaded by dark gray region as shown in Fig. 4(b). This motion is characterized by one impact every ten excitation periods. For excitation amplitudes a$= 0.062$ and 0.088, the modulated motion coexists with multi-periodic oscillation (shown by empty squares, □) as shown in Figs. 4(c) and

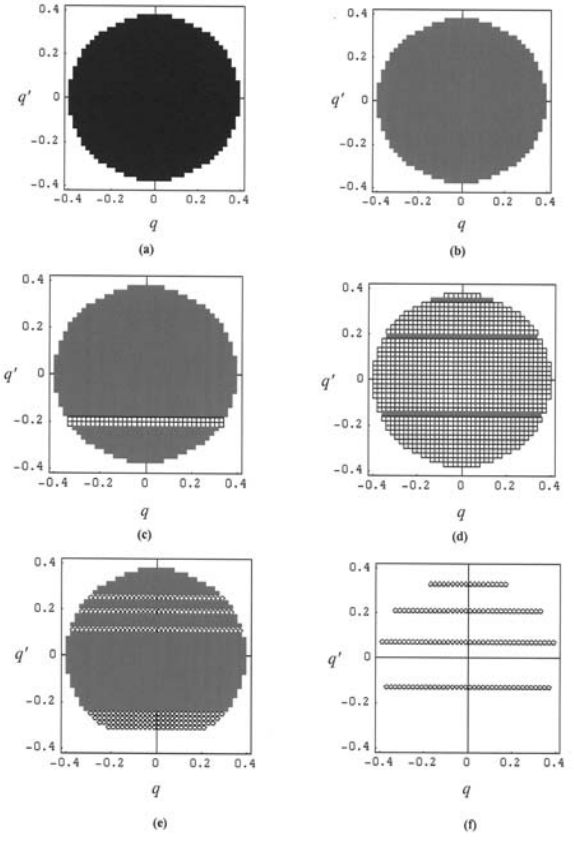

Fig. 4 Domains of attraction for different values of excitation amplitude a : (a) 0.02, (b) 0.046, (c) 0.062, (d) 0.088, (e) 0.096, and (f) 0.114. ■ Period-one response, □ Multi-periodic response, ■ Modulated response, ⬠ Chaotic motion, empty space: rotational motion

(d) respectively. For a$=0.062$, the multi-periodic motion is characterized by one impact every six excitation periods. For a$=0.088$, the multi-periodic motion is characterized by three impacts every ten excitation periods. For excitation amplitude a$=0.096$ the modulated motion coexists with chaotic motion (indicated by the cathedral symbol) as shown in Fig. 4(e). Also, the region is eroded by regions of rotational motion. As the excitation amplitude increases, the eroded area indicating regions of rotational motion increases as shown in Fig. 4(f).

Fig. 5 shows the bifurcation diagram on the plane of response-excitation amplitudes for frequency ratio $\nu = 0.88$. This figure summarizes all possible regimes of ship dynamics. The rotational motion exists over an excitation amplitude range $0.94 \leq a \leq 0.12$. For excitation amplitude a≥ 0.12 the entire region belongs to ship rotational motion or capsizing. Note that for other values of excitation frequency, the bifurcation diagram may be different particularly as the excitation frequency approaches the resonance frequency.

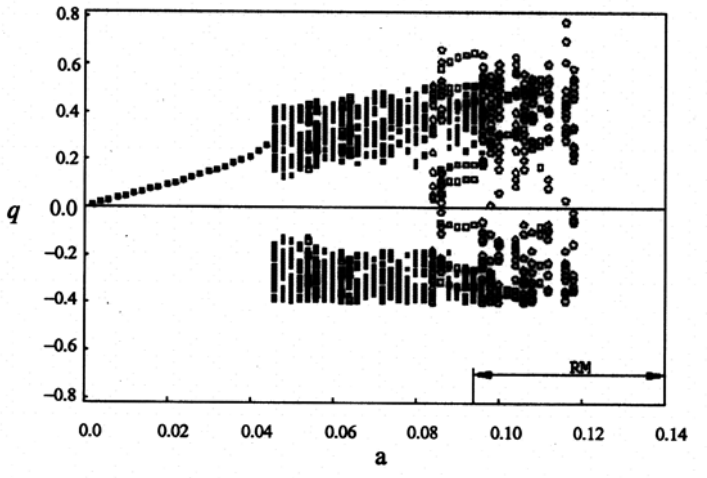

Fig. 5 Bifurcation diagram for excitation frequency ratio ν=0.88. ■ Period-one response, □ Multi-periodic response, ■ Modulated response, ⬠ Chaotic motion, RM=Rotational Motion

3 Inelastic Impact

For the case of inelastic impact, the condition $\dot{q_+} = -e\dot{q_-}$ must be introduced, where e is the coefficient of restitution, $\dot{q_+}$ and $\dot{q_-}$ are the system velocities just after and before impact, respectively. Note that the additional damping associated with inelastic impact may be significant than the inherent system linear and nonlinear damping terms. The impact condition $\dot{q_+} = -e\dot{q_-}$ specified at $q = -q_i$, is transformed to

$$\dot{z_+} = e\dot{z_-} \qquad at\ z = 0 \tag{7}$$

The transformed velocity jump is reduced by an amount proportional to $(1-e)$. It is possible to introduce this jump into the equation of motion using the Dirac delta-function, and thus one avoids using condition (7). To this end, one may expand $z(\tau)$ around the time instant of impact, τ_i, where $z(\tau_i) = 0$,

$$z(\tau) = z(\tau_i) + \dot{z}(\tau_i)(\tau - \tau_i) = \dot{z}(\tau_i)(\tau - \tau_i), \qquad for\ z(\tau_i) = 0 \tag{8}$$

Equation (8) implies that $\delta(\tau - \tau_i) = \delta\left(z(\tau)/\dot{z}(\tau_i)\right)$. From the definition of Dirac function one can write

$$\int_{-\infty}^{\infty} f(z)\delta(\lambda z)dz = \frac{1}{\lambda}\left[\int_{-\infty}^{\infty} f(u/\lambda)\delta(u)du\right] = \frac{f(0)}{\lambda} \tag{9}$$

Thus one can write

$$\delta(\tau - \tau_i) = \dot{z}\delta(z) \tag{10}$$

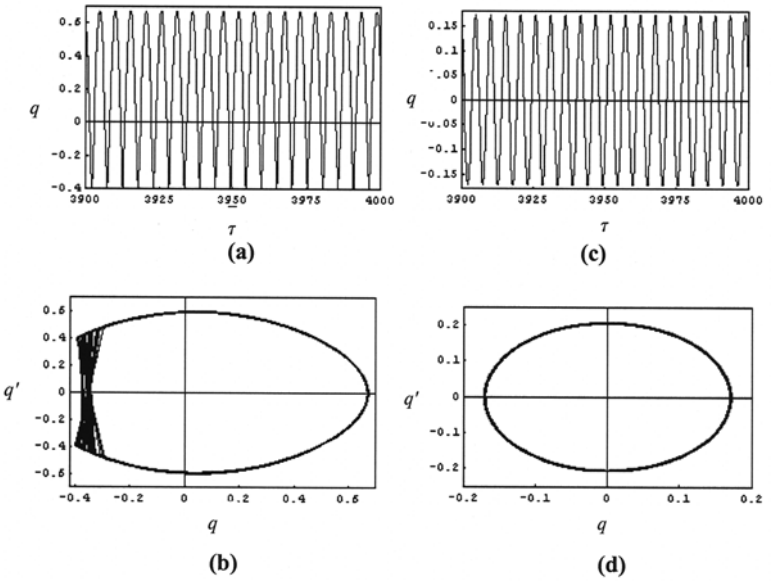

Fig. 6 Time history records and phase portraits for excitation frequency ratio $\nu = 1.2$ and excitation amplitude a$= 0.08$, initial condition $(0.15, 0.05)$: Left plots are for purely elastic impact, right plots are for inelastic impact $e = 0.8$

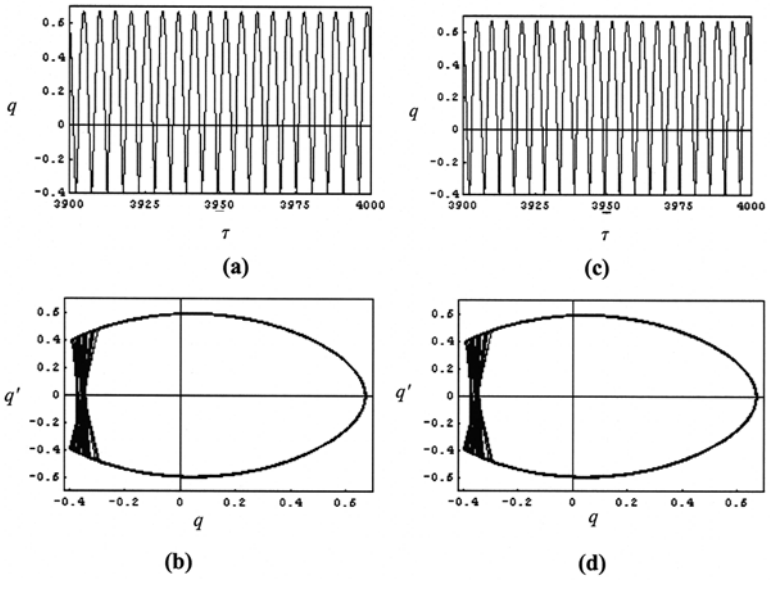

Fig. 7 Time history records and phase portraits for excitation frequency ratio $\nu = 1.2$ and excitation amplitude a$= 0.08$, initial condition $(0.15, -0.09)$: Left plots are for purely elastic impact, right plots are for inelastic impact $e = 0.8$

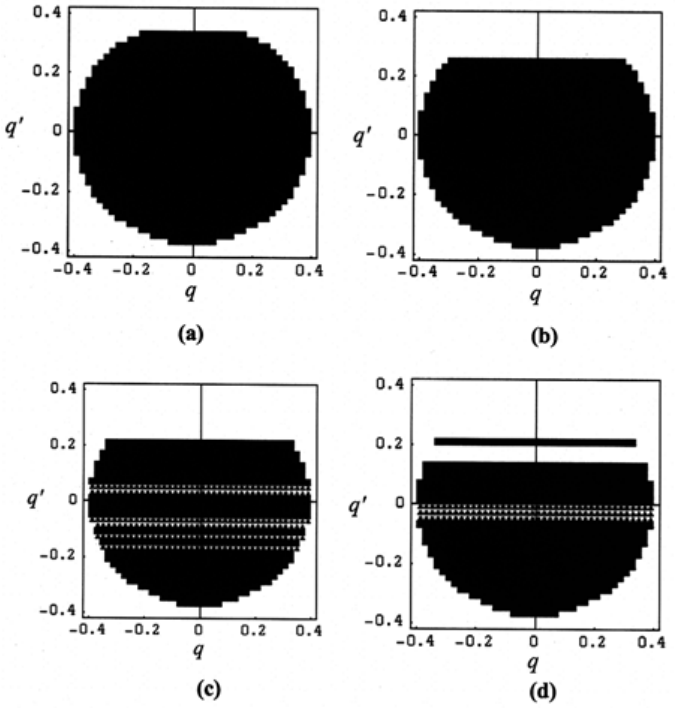

Fig. 8 Domains of attraction for the case of purely elastic impact under excitation frequency ratio $\nu = 1.2$, and for different values of excitation amplitude a: (a) 0.044, (b) 0.066, (c) 0.08, (d) 0.088. ■ Period - one response, ▲ Period - one response experiencing impact, empty space: rotational motion

The additional damping term due to impact may be written in the form

$$\left(\dot{z_+} - e\dot{z_-}\right)\delta(\tau - \tau_i) = (1-e)\dot{z}\delta(\tau - \tau_i) \tag{11}$$

provided $|\dot{z_+}| < |\dot{z}| < |\dot{z_-}|$.In this case, equation (11) can be written after using equation (10)

$$(1-e)\dot{z}\delta(\tau - \tau_i) = (1-e)\dot{z}|\dot{z}|\delta(z) \tag{12}$$

Zhuravlev [14] introduced transformation of variables from the time domain to the space domain. Dimentberg [15] provided a systematic description of Zhuravlev coordinate transformation and demonstrated its application to vibro-impact systems under random excitation. A modified form of Zhuravlev transformation was proposed by Privalov ([16], [17]). The transformation was used to investigate a typical example of a vibro-impact system with unilateral motion constraint. Ivanov [18] developed a modified non-smooth coordinate transformation for the case of inelastic impact for which the duration of impact is physically related to the stiffness and damping ratio of the barrier.

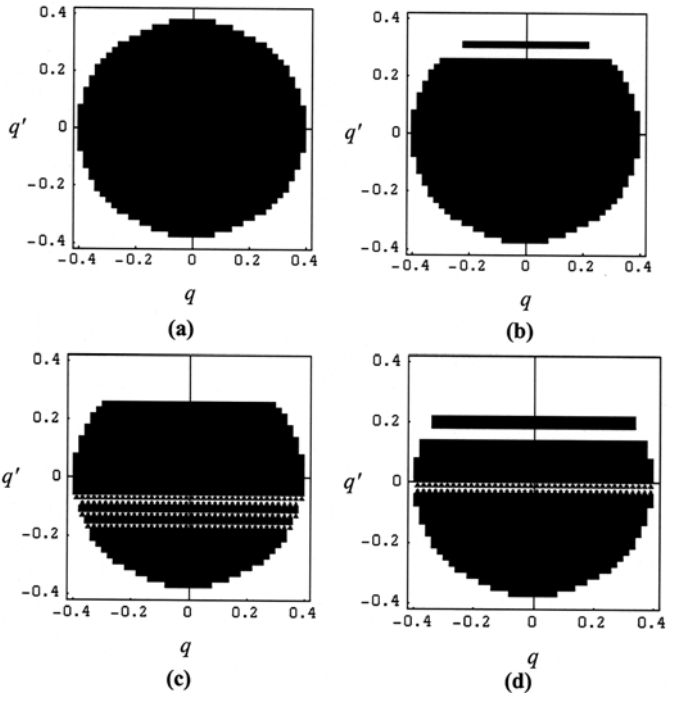

Fig. 9 Domains of attraction for the case of inelastic impact, $e = 0.8$, under excitation frequency ratio $\nu = 1.2$, and for different values of excitation amplitude a: (a) 0.044, (b) 0.066, (c) 0.08, (d) 0.088. ■ Period - one response, ▲ Period - one response experiencing impact, empty space: rotational motion.

Introducing the new impact damping term (12), equation (3) takes the following form

$$z'' + \zeta \dot{z} + \gamma \dot{z}^2 sgn(\dot{z}) + z + sgn(z)\left\{-q_i + C_3\left[z sgn(z) - q_i\right]^3 + C_5\left[z sgn(z) - q_i\right]^5\right\} + (1-e)\dot{z}|\dot{z}|\delta(z) = Z(\tau) sgn(z) \tag{13}$$

Under sinusoidal excitation $Z(\tau) = a \sin \nu\tau$, and for coefficient of restitution $e = 0.8$, equation (13) is solved numerically under different values of excitation amplitude for excitation frequency ratio $\nu = 1.2$. A comparison of the response for inelastic impact ($e = 0.8$) and elastic impact ($e = 1$) for excitation frequency $\nu = 1.2$ and excitation amplitude a$= 0.08$ is shown in Figs. 6 and 7 for two different sets of initial conditions. For initial displacement $z_0 = 0.15$, and initial velocity $\dot{z}_0 = 0.05$, Fig. 6 reveals that the response experiences impact for the elastic case, while for the inelastic case the response is non-impact periodic mainly due to the inherent inelastic damping. Note that for the inelastic case, the ship experiences impact during the first few cycles during the transient response period. The damping imparted by this inelastic impact resulted in the non-impact steady state motion. For

a relatively larger initial velocity, the damping associated with inelastic impact does not have any appreciable effect on the response as shown Fig. 7. However, for initial conditions $z_0 = 0.29$, and $z_0^{'} = 0.23$, the response experiences rotational motion for purely elastic impact, while it is periodic for the inelastic case.

Figs. 8 and 9 show samples of safe basins of attraction for different values of excitation amplitude for excitation frequency ratio $\nu = 1.2$ for elastic impact ($e = 1$) and inelastic impact ($e = 0.8$), respectively. Comparing the two figures reveals that the area eroded by regions of rotational motion in case of inelastic impact is less than the case of elastic impact. Meanwhile the region of impact periodic response, indicated by the symbol ▲, for the elastic case is larger than that for the inelastic case.

4 Conclusions

Impact interaction of ship roll dynamics with floating ice has been studied using Zhuravlev non-smooth coordinate transformation for purely elastic impact and inelastic impact. The advantage of this transformation is that it eliminates the discontinuity associated with impact events such that one can use numerical simulation or analytical asymptotic techniques. Under sinusoidal ocean waves, the ship dynamics was examined for all possible initial conditions covered by the grazing orbit for different values of excitation amplitude and frequency. The response exhibited different regimes of motion depending on excitation parameters and initial conditions. These regimes include non-impact periodic oscillations, impact bounded oscillations such as modulated, and multi-periodic, and chaotic oscillations. A comparison of the response for inelastic impact and elastic impact showed that for certain initial conditions the response experiences impact for the elastic case, while for the inelastic case the response is non-impact periodic. For other initial conditions the response experiences rotational motion for purely elastic impact, while it is periodic for the inelastic case. It can be seen that the additional damping associated with inelastic impact is significant than the linear and nonlinear damping terms.

Acknowledgements. This work is supported by a grant from ONR under Award No: N00014-05-1-0040. Dr. Kelly B. Cooper is the Program Director.

References

1. Cammaert, A.B., Muggeridge, D.B.: Ice interaction with offshore structures. Van Nostrand Reinhold, New York (1988)
2. Zou, B.: Ships in Ice; the Interaction Process and Principles of Design. PhD Thesis, Memorial University of Newfoundland (1996)
3. Ibrahim, R.A., Chalhoub, N.G., Falzarano, J.: Ice interaction with ships and ocean structures and their control. ASME Appl. Mech. Rev. 60(5), 246–289 (2007)

4. Karr, D.G., Troesch, A.W., Wingate, W.C.: Nonlinear dynamic response of a simple ice-structure interaction model. In: Proceedings of the 11^{th} International Offshore Mechanics and Arctic Engineering Symposium, Arctic/Polar Technology, Calgary, Alberta, vol. 4, pp. 231–237 (1992)
5. Karr, D.G., Troesch, A.W., Wingate, W.C.: Nonlinear dynamic response of a simple ice-structure interaction model. ASME Journal of Offshore Mechanics and Arctic Engineering 115(4), 246–252 (1993)
6. Troesch, A.W., Karr, D.G., Beier, K.P.: Global contact dynamics of an ice-structure interaction model. International Journal of Bifurcation and Chaos in Applied Sciences and Engineering 2(3), 607–620 (1992)
7. Shaw, S.W., Holmes, P.J.: A periodically forced piecewise linear oscillator. Journal of Sound and Vibration 90, 129–155 (1983)
8. Shaw, S.W., Holmes, P.J.: A periodically forced impact oscillator with large dissipation. ASME Journal of Applied Mechanics 50, 849–857 (1983)
9. Shaw, S.W.: Forced vibration of a beam with one-sided amplitude constraint: Theory and experiment. Journal of Sound and Vibration 99(2), 199–212 (1985)
10. Nordmark, A.B.: Non-periodic motion caused by grazing incidence in an impact oscillator. Journal of Sound and Vibration 145, 279–297 (1991)
11. Nordmark, A.B.: Existence of periodic orbits in grazing bifurcations of impacting mechanical oscillators. Nonlinearity 14, 1517–1542 (2001)
12. Chin, W., Ott, E., Nusse, H.E., Grebogi, C.: Grazing bifurcations in impact oscillators. Physical Review E 50, 4427–4444 (1994)
13. de Weger, J., van de Water, W., Molenaar, J.: Grazing impact oscillations. Physical Review E 62(2), 2030–2041 (2000)
14. Zhuravlev, V.P.: Investigation of certain Vibro-impact systems by the method of non-smooth transformations. Izvestiva AN SSSR Mehanika Tverdogo Tela (Mechanics of Solids) 12, 24–28 (1976)
15. Dimentberg, M.F.: Statistical Dynamics of Nonlinear and Time-Varying Systems. Research Studies Press/ John Wiley, Somerset, England (1988)
16. Privalov, E.A.: One form of the non-smooth-transformation method for use in analysis of vibro-impact systems. Mechanics of Solids 27(4), 34–37 (1992)
17. Privalov, E.A.: Modification of the method of non-smooth transformations for vibration-impact systems with bilateral motion constraint. Mechanics of Solids 28(3), 99–101 (1993)
18. Ivanov, A.P.: Impact oscillations: Linear theory of stability and bifurcations. Journal of Sound and Vibration 178(3), 361–378 (1994)

Periodic Motion Stability of a Dual-Disk Rotor System with Rub-Impact at Fixed Limiter

Qingkai Han, Zhiwei Zhang, Changli Liu, and Bangchun Wen

Abstract. The stability of periodic motions of a dual-disk rotor system, in which rub-impacts occur between a disk and a fixed limiter, is investigated. The dynamical model of the system is proposed with ordinary differential equations with two dimensional freedoms of transverse vibrations of the two rigid disks along the shaft. With the first order approximation of the piece-wisely rub-impact force, the solutions of periodic motions are deduced with harmonic expansion technique. Then, the stability and bifurcations of the system are discussed via the Floquet theory analytically. In the same range of rotating frequency, the stability analysis of the analytical solution shows good agreement with the stability and bifurcation diagrams from direct numerical integration.

Keywords: Dual-disk rotor system, rub-impact, periodic motion, stability.

1 Introduction

Unlike the traditional Jeffcott rotor model, a dual-disk rotor model is more suitable for multi-stage compressors and aero-engines when analyzing their transverse vibrations, especially when some faults exist along the shaft. Among well-known faults of a rotor system, the rub-impact between stator and rotor is a common and significant fault in many rotating machines.

As a case of vibro-impact, a mechanical system with rub-impact will behave in strong nonlinearity, e.g. the responses of the system could jump at some frequencies, and it often shows very complicated vibration phenomena, including periodic components, quasi-periodic and chaotic motions [1]. In recent decades, intensive

Qingkai Han and Bangchun Wen
School of Mechanical Engineering and Automation, Northeastern University, Shenyang 110004, China

Zhiwei Zhang
Wolfson School of Mechanical and Manufacturing Engineering, Loughborough University, Leicestershire LE11 3TU, UK

Changli Liu
School of Mechanical and Power Engineering, East China University of Science and Technology, Shanghai, 200237, China

R.A. Ibrahim et al. (Eds.): Vibro-Impact Dynamics of Ocean Systems, LNACM 44, pp. 105–119.
springerlink.com

work has been conducted on rub-impacts related dynamical phenomena in the rotor systems, partly as summarized in [2]. Based on the Jeffcott rotor system with rub-impact, Goldman and Muszynska found the supercritical subharmonic phenomenon and chaotic behavior of rotor systems [3]. The complicated behaviors of periodic, quasi-periodic and chaotic motions of them are also discussed based on the chaos and bifurcation theories in [4].

A rotor system with rub-impact can be regarded as a piecewise linear oscillator system in mathematics, where the trajectories are not smooth in its phase space due to the discontinuity of rub-impact. The typical mathematical model for rub-impact forces was introduced in a form of piecewise-linear stiffness by Beatty [5]. Many important results focusing on the periodic motion and complex dynamical behaviors of the rotor systems with rub-impacts are also documented. For example, Groll and Ewins used a numerical algorithm based on the harmonic balance method to calculate the periodic responses of a non-linear rotor/stator contact system under periodic excitation [6]. Lu gave a criterion for periodicity condition in an eccentric rotor system with analytical and numerical techniques [7]. Chu completed some experiments of rotor-to-stator full rub with various forms of periodic and chaotic vibrations [8].

In the author's previous research, periodic motions of a dual-disk rotor system with rub-impacts at fixed limiters are investigated using finite element simulations. The obtained rotor transverse vibrations with different rotating speeds, rub-impact clearances, rub-impact stiffness and rub frictions are compared with the experimental measurements [9]. It demonstrates that there are different motion patterns of the rotor system with rub-impacts, possessing periodic, dual-periodic and quasi-periodic characteristics.

In the present work, the stability of periodic motions of a dual-disk rotor system with rub-impact at a fixed limiter is investigated both analytically and numerically. The paper consists of five sections. After introduction of the research background in Section 1, a dynamical model of the rotor system with rub-impact at a fixed limiter is established in Section 2. The periodic solutions of the system are deduced in this section. In Section 3, the stability analysis of periodic motions of the system is conducted via Floquet theory. In Section 4, an example is used to demonstrate the analytical results of the periodic motions of the system compared with results from numerical simulations. Finally, some conclusions are drawn in Section 5.

2 Model Developments and Periodic Motions Analysis of the Rotor System with Rub-Impact at Fixed Limiter

2.1 Dynamical Model of the Rotor System with Rub-Impact at a Fixed Limiter

The schematic plot of the rotor system with rub-impacts is shown in Figure 1(a). The shaft rotates at an angular speed ω, and is supported by two journal bearings. There are two rigid disks mounted along the shaft. Two fixed elastic limiters are

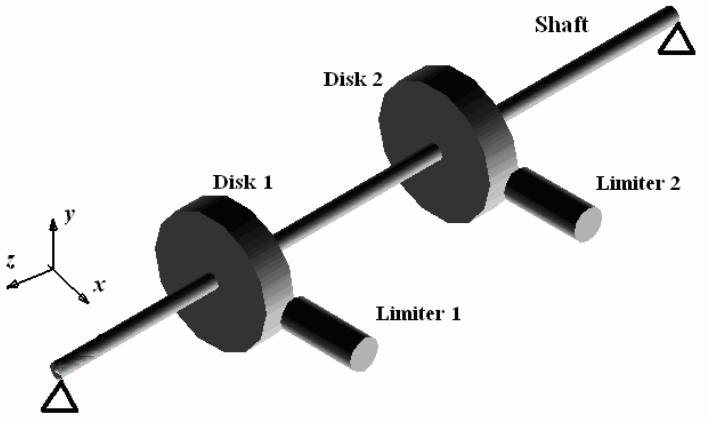

(a) Schematic plot of the dual-disk rotor system with rub-impacts at fix limiters

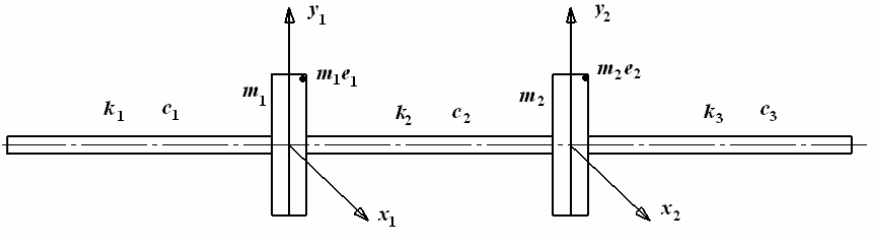

(b) Dynamical model of the rotor system

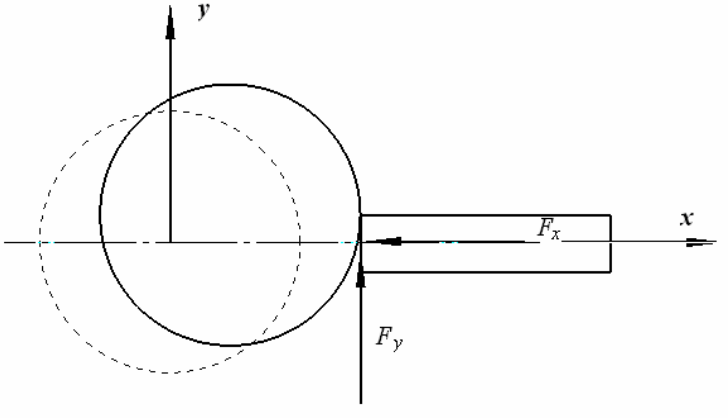

(c) The section view at the rub-impact location

Fig. 1 The dual-disk rotor system with rub-impacts at fixed limiters

mounted on the base of the test-rig. Rub-impacts can happen at one or two disks by setting the clearances between limiters and the disks.

Only transverse vibrations of the rotor system are considered. The equivalent lumped masses of the two disks are m_1, m_2. The shaft is considered as massless elastic beam. There are two unbalances at the Disk 1 and Disk 2, m_1e_1 and m_2e_2, which have the same phase. Through Figure 1(b), the differential equations of motion are written into the two groups with the total degrees of freedom (DOF) of n=4 as follows,

$$\begin{bmatrix} m_1 & 0 \\ 0 & m_2 \end{bmatrix}\begin{Bmatrix} \ddot{y}_1 \\ \ddot{y}_2 \end{Bmatrix}+\begin{bmatrix} c_{11} & c_{12} \\ c_{21} & c_{22} \end{bmatrix}\begin{Bmatrix} \dot{y}_1 \\ \dot{y}_2 \end{Bmatrix}+\begin{bmatrix} k_{11} & k_{12} \\ k_{21} & k_{22} \end{bmatrix}\begin{Bmatrix} y_1 \\ y_2 \end{Bmatrix}=\begin{Bmatrix} m_1e_1 \\ m_2e_2 \end{Bmatrix}\omega^2\sin\omega t+\begin{Bmatrix} F_{y1} \\ F_{y2} \end{Bmatrix}$$

$$\begin{bmatrix} m_1 & 0 \\ 0 & m_2 \end{bmatrix}\begin{Bmatrix} \ddot{x}_1 \\ \ddot{x}_2 \end{Bmatrix}+\begin{bmatrix} c_{11} & c_{12} \\ c_{21} & c_{22} \end{bmatrix}\begin{Bmatrix} \dot{x}_1 \\ \dot{x}_2 \end{Bmatrix}+\begin{bmatrix} k_{11} & k_{12} \\ k_{21} & k_{22} \end{bmatrix}\begin{Bmatrix} x_1 \\ x_2 \end{Bmatrix}=\begin{Bmatrix} m_1e_1 \\ m_2e_2 \end{Bmatrix}\omega^2\cos\omega t+\begin{Bmatrix} F_{x1} \\ F_{x2} \end{Bmatrix} \quad (1)$$

where $y_1, y_2, \dot{y}_1, \dot{y}_2, \ddot{y}_1, \ddot{y}_2$, $x_1, x_2, \dot{x}_1, \dot{x}_2, \ddot{x}_1, \ddot{x}_2$ are displacements, velocities and accelerations of the transverse vibrations of the two disks in y and x directions, respectively. k_{11}, k_{12}, k_{21}, k_{22} are shaft segment stiffness, which can be obtained by flexible deformations at the two disks. $c_{11}, c_{12}, c_{21}, c_{22}$ are effective damping coefficients calculated following the proportional damping assumption.

The rub-impact forces at the two disks in y and x directions of $F_{y1}, F_{y2}, F_{x1}, F_{x2}$, as shown in Figure 1(c), are

$$F_{x1}=-k_{r1}(x_1-\delta_1)H_1,\ F_{x2}=-k_{r2}(x_2-\delta_2)H_2$$
$$F_{y1}=F_{x1}f_{r1}=-k_{r1}(x_1-\delta_1)H_1f_{r1},\ F_{y2}=F_{x2}f_{r2}=-k_{r2}(x_2-\delta_2)H_2f_{r2} \quad (2)$$

where, k_{r1}, k_{r2} are the axial stiffness coefficients of the two limiters; f_{r1}, f_{r2} are the Coulomb friction coefficients at rub-impact points. δ_1, δ_2 are the initial clearances between the two limiters and disks. H_1 would be equal to 0 or 1 if $(x_1-\delta_1)$ is smaller or larger than 0, and H_2 would be equal to 0 or 1 if $(x_2-\delta_2)$ is smaller or larger than 0.

2.2 Analytical Periodic Motion Solutions of the Rotor System

Fourier expansion technique is used to derive the stable periodic solutions of the rotor system with rub-impacts. With the assumption $\theta=\omega t$, Eq (1) can be rewritten to the following differential equations as function of θ, where the differentials with respect to θ are denoted by "$''$" and "$'$":

$$
\begin{aligned}
&y_1'' + \beta_{11} y_1' + \beta_{12} y_2' + \alpha_1 k_{11} y_1 + \alpha_1 k_{12} y_2 = e_1 \sin\theta + \alpha_1 F_{y1} \\
&y_2'' + \beta_{21} y_1' + \beta_{22} y_2' + \alpha_2 k_{21} y_1 + \alpha_2 k_{22} y_2 = e_2 \sin\theta + \alpha_2 F_{y2} \\
&x_1'' + \beta_{11} x_1' + \beta_{12} x_2' + \alpha_1 k_{11} x_1 + \alpha_1 k_{12} x_2 = e_2 \omega^2 \cos\theta + \alpha_1 F_{x1} \\
&x_2'' + \beta_{21} x_1' + \beta_{22} x_2' + \alpha_2 k_{21} x_1 + \alpha_2 k_{22} x_2 = e_2 \omega^2 \cos\theta + \alpha_2 F_{x2}
\end{aligned} \tag{3}
$$

where, $\alpha_1 = 1/(m_1\omega^2), \alpha_2 = 1/(m_2\omega^2), \beta_{11} = c_{11}/(m_1\omega)$, $\beta_{21} = c_{21}/(m_2\omega)$, $\beta_{22} = c_{22}/(m_2\omega)$.

Taking N harmonics into account, the stable periodic solutions of Eq (3) are assumed to be

$$
y_1 = a_{10} + \sum_{j=1}^{N} (a_{1j}\cos j\theta + b_{1j}\sin j\theta),\ y_2 = a_{20} + \sum_{j=1}^{N} (a_{2j}\cos j\theta + b_{2j}\sin j\theta)
$$

$$
x_1 = a_{30} + \sum_{j=1}^{N} (a_{3j}\cos j\theta + b_{3j}\sin j\theta),\ x_2 = a_{40} + \sum_{j=1}^{N} (a_{4j}\cos j\theta + b_{4j}\sin j\theta). \tag{4}
$$

In order to solve the coefficients in Eq (4), i.e. a_{10}, a_{20} , a_{30}, a_{40} , a_{1j}, b_{1j} , a_{2j}, b_{2j} , a_{3j}, b_{3j} , a_{4j}, b_{4j} , the following steps are important. Firstly, Eq (4) is substituted into Eq (3). And then all the coefficients of $\cos j\theta, \sin j\theta$ should be checked separately in different *j*-th orders. The obtained coefficients of equations are derived as follows. For the 0-th order, they are

$$
\begin{aligned}
&P_{0,1} = \frac{\alpha_1}{2\pi}\int_0^{2\pi} F_{y1} d\theta - \alpha_1 k_{11} a_{10} - \alpha_1 k_{12} a_{20} = 0, \\
&P_{0,2} = \frac{\alpha_2}{2\pi}\int_0^{2\pi} F_{y2} d\theta - \alpha_2 k_{21} a_{10} - \alpha_2 k_{22} a_{20} = 0 \\
&P_{0,3} = \frac{\alpha_1}{2\pi}\int_0^{2\pi} F_{x1} d\theta - \alpha_1 k_{11} a_{30} - \alpha_1 k_{12} a_{40} = 0, \\
&P_{0,4} = \frac{\alpha_2}{2\pi}\int_0^{2\pi} F_{x2} d\theta - \alpha_2 k_{21} a_{30} - \alpha_2 k_{22} a_{40} = 0
\end{aligned} \tag{5}
$$

For the *j*-th order, they are

$$
P_{cj,1} = j^2 a_{1j} + \frac{\alpha_1}{\pi}\int_0^{2\pi} F_{y1}\cos j\theta d\theta + \beta_{11} j b_{1j} + \beta_{12} j b_{2j} - \alpha_1 k_{11} a_{1j} - \alpha_1 k_{12} a_{2j} = 0
$$

$$
P_{cj,2} = j^2 a_{2j} + \frac{\alpha_2}{\pi}\int_0^{2\pi} F_{y2}\cos j\theta d\theta + \beta_{21} j b_{1j} + \beta_{22} j b_{2j} - \alpha_2 k_{21} a_{1j} - \alpha_2 k_{22} a_{2j} = 0
$$

$$
\begin{aligned}
P_{cj,3} = {} & j^2 a_{3j} + \frac{\alpha_1}{\pi}\int_0^{2\pi} F_{x1}\cos j\theta d\theta + \beta_{11} j b_{3j} + \beta_{12} j b_{4j} - \alpha_1 k_{11} a_{3j} - \alpha_1 k_{12} a_{4j} \\
& + e_1 N^2 \delta(j, N) = 0
\end{aligned}
$$

$$P_{cj,4} = j^2 a_{4j} + \frac{\alpha_2}{\pi}\int_0^{2\pi} F_{x2}\cos j\theta d\theta + \beta_{21} j b_{3j} + \beta_{22} j b_{4j} - \alpha_2 k_{21} a_{3j} - \alpha_2 k_{22} a_{4j}$$
$$+ e_2 N^2 \delta(j,N) = 0$$
$$P_{sj,1} = -j^2 b_{1j} + \frac{\alpha_1}{\pi}\int_0^{2\pi} F_{y1}\sin j\theta d\theta + \beta_{11} j a_{1j} + \beta_{12} j a_{2j} + \alpha_1 k_{11} b_{1j} + \alpha_1 k_{12} b_{2j}$$
$$+ e_1 N^2 \delta(j,N) = 0$$
$$P_{sj,2} = -j^2 b_{2j} + \frac{\alpha_2}{\pi}\int_0^{2\pi} F_{y2}\sin j\theta d\theta + \beta_{21} j a_{1j} + \beta_{22} j a_{2j} + \alpha_2 k_{21} b_{1j} + \alpha_2 k_{22} b_{2j}$$
$$+ e_2 N^2 \delta(j,N) = 0$$
$$P_{sj,3} = -j^2 b_{3j} + \frac{\alpha_1}{\pi}\int_0^{2\pi} F_{x1}\sin j\theta d\theta + \beta_{11} j a_{3j} + \beta_{12} j a_{4j} + \alpha_1 k_{11} b_{3j} + \alpha_1 k_{12} b_{4j} = 0$$
$$P_{sj,4} = -j^2 b_{4j} + \frac{\alpha_2}{\pi}\int_0^{2\pi} F_{x2}\sin j\theta d\theta + \beta_{12} j a_{3j} + \beta_{22} j a_{4j} + \alpha_2 k_{21} b_{3j} + \alpha_2 k_{22} b_{4j} = 0 \quad (6)$$

All these $4(N+1)$ equations are assembled into a nonlinear equation set. At last, the parameter vector of $\{a_{10}, a_{20}, a_{30}, a_{40}, a_{11}, ..., b_{4N}\}^T$ can be solved by numerical method such as the Inverse-Broyden Rank One Method.

3 Stability Analyses of Periodic Solutions of the Rotor System

3.1 Basic Theory of Floquet Stability

The stability of the fixed points of solutions of the rotor system represents the stability of its periodic motions. The original differential equations of the system, assuming that it has *n*-DOF, can be transferred into the following boundary value problem with 2*n*-DOF for the periodical solution:

$$\begin{cases} \dot{\boldsymbol{y}} = \boldsymbol{f}(t, \boldsymbol{y}) \\ \boldsymbol{f}(t+T, \boldsymbol{y}) = \boldsymbol{f}(t, \boldsymbol{y}) \\ \boldsymbol{y}(0) - \boldsymbol{y}(T) = 0 \end{cases} \quad (7)$$

Assume the periodical solution of the above Eq (7) is $\boldsymbol{y}^*(t)$. With a perturbation of $x(t) = \boldsymbol{y}(t) - \boldsymbol{y}^*(t)$ and considering the Taylor's theorem, the lowest-order term of the system retains

$$\dot{\boldsymbol{x}} = \frac{\partial \boldsymbol{f}}{\partial \boldsymbol{y}^*}\boldsymbol{x} \quad (8)$$

Equation (8) can be written as the following form with periodic coefficient matrix $\boldsymbol{A}(t)$

$$\begin{cases} \dot{\boldsymbol{x}} = \boldsymbol{A}(t)\boldsymbol{x} \\ \boldsymbol{A}(t+T) = \boldsymbol{A}(t) \end{cases} \quad (9)$$

The stability of periodical solution of $\boldsymbol{y}^*(t)$ is determined by the stability of the zero solution of Eq (9). Let $\boldsymbol{x}(0)$ be equal to $\boldsymbol{I}$, where $\boldsymbol{I}$ is the unit matrix with $2n \times 2n$ dimensions, the same as $\mathbf{A}(t)$. From Eq (9), the monodromy matrix of $\boldsymbol{S} = \boldsymbol{x}(T)$ can be obtained with numerical integration from 0 to *T*. The eigenvalues of $\boldsymbol{S}$ are the Floquet multipliers, i.e. λ_i, which are solved from $(\boldsymbol{S} - \lambda_i \boldsymbol{I})\boldsymbol{\alpha}_i = 0$. Therefore, it is possible to use the Floquet theory to discuss the stability of the periodic solutions of the rotor system.

The typical modes of Floquet multipliers leaving unit circle is plotted in Figure 2. They can be described as follows. (1) When the dominating Floquet multiplier (the eigenvalue with the largest module) lies inside the unit circle, the stable periodic solutions are asymptotically stable. (2) When the dominating Floquet multiplier lies outside of unit circle passing through (+1, 0) while the other multipliers are still inside unit circle, the stable periodic solution will lose its periodic stability and have the saddle-node bifurcation. (3) When the dominating Floquet multiplier lies outside of unit circle passing through (-1, 0) while the other multipliers are still inside unit circle, the stable periodic solution will have the period-doubling bifurcation. (4) When a pair of conjugate Floquet multipliers lies out of unit circle while other multipliers are still inside unit circle, the stable periodic solution will have the Hopf bifurcation or second Hopf bifurcation and the bifurcation will lead to an invariant torus.

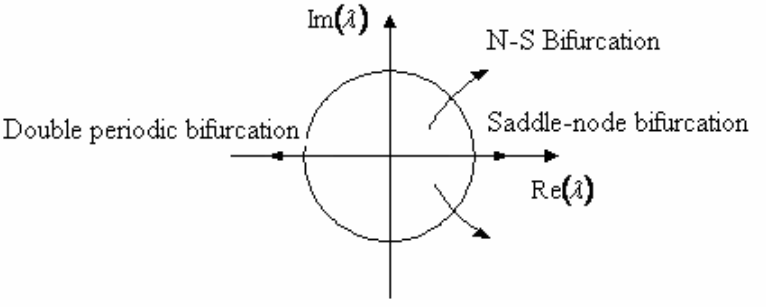

Fig. 2 Three modes of Floquet multipliers leaving unit circle

3.2 The Analytical Floquet Stability Analysis for Periodic Solutions of the Rotor System with Rub-Impact

The Floquet theory is used to discuss the stability of the obtained analytical periodic motions of the above rotor system. The dynamical equations of Eq (3) are perturbed firstly. That is, let $y_1(t) = y_{10}(t) + \Delta y_1(t)$, $y_2(t) = y_{20}(t) + \Delta y_2(t)$,

$x_1(t) = x_{10}(t) + \Delta x_1(t)$, $x_2(t) = x_{20}(t) + \Delta x_2(t)$, where $y_{10}(t)$, $y_{20}(t)$, $x_{10}(t)$, $x_{20}(t)$ are the periodic solutions obtained above. The non-linear terms of the system are also expanded into the Taylor series at the neighborhoods of stable solutions $y_{10}(t), y_{20}(t), x_{10}(t), x_{20}(t)$ and only remaining their first order terms. For Eq. (1), the obtained analytical matrix $\boldsymbol{A}(t)$ with periodic coefficients, as stated in Eq (9), is

$$\boldsymbol{A}(t)=\begin{bmatrix} 0 & 1 & 0 & 0 & 0 & 0 & 0 & 0 \\ -\alpha_1 k_{11} & -\beta_{11} & -\alpha_1 k_{12} & -\beta_{12} & \alpha_1 \dfrac{\partial F_{y1}}{\partial x_1} & 0 & 0 & 0 \\ 0 & 0 & 0 & 1 & 0 & 0 & 0 & 0 \\ -\alpha_2 k_{21} & -\beta_{21} & -\alpha_2 k_{22} & -\beta_{22} & 0 & 0 & \alpha_2 \dfrac{\partial F_{y2}}{\partial x_2} & 0 \\ 0 & 0 & 0 & 0 & 0 & 1 & 0 & 0 \\ 0 & 0 & 0 & 0 & \alpha_1(\dfrac{\partial F_{x1}}{\partial x_1} - k_{11}) & -\beta_{11} & -\alpha_1 k_{12} & -\beta_{12} \\ 0 & 0 & 0 & 0 & 0 & 0 & 0 & 1 \\ 0 & 0 & 0 & 0 & -\alpha_2 k_{21} & -\beta_{21} & \alpha_2(\dfrac{\partial F_{x2}}{\partial x_2} - k_{22}) & -\beta_{22} \end{bmatrix} \tag{10}$$

3.3 *Numerical Method for Floquet Stability Analysis for the Rotor System*

The traditional strategy of analyzing Floquet stability of a rotor system is to conduct numerical integrations based on the governing equations of the system. The commonly used method is the Runge-Kutta integration method. After the periodical responses of the rotor system are obtained with numerical integrations, i.e. the general displacement vector $\boldsymbol{y}^*$ at time T, the perturbed value of it can be approximately written as $\boldsymbol{y}^{*\prime} = (1+\Delta)\boldsymbol{y}^*$, where Δ is a small value. According to Eq. (7), the matrix of $\boldsymbol{A}(t)$ in Eq. (9) is then approximated to be

$$\boldsymbol{A}(t) = \boldsymbol{A}(t+T) \doteq \frac{\boldsymbol{f}\left(t+T, \boldsymbol{y}^*\right) - \boldsymbol{f}\left(t+T, \boldsymbol{y}^{*\prime}\right)}{\boldsymbol{y}^* - \boldsymbol{y}^{*\prime}} \tag{11}$$

With $\boldsymbol{A}(t)$ of Eq (11) and the initial value of $\boldsymbol{x}(0) = \boldsymbol{I}$, Eq (9) can be solved easily with Runge-Kutta method. Then the Floquet multipliers of the rotor system of Eq (1) are calculated as stated in Section 3.1.

4 Examples

4.1 The Model Parameters of the Rotor System

The dual-disk rotor system, as shown in Figure 1, is used to illustrate the discussions above on the stability of periodic motions. There is an unbalance on the out edge of Disk2. The rub-impact only happens at Disk 2 too. The fixed limiter is an elastic rod made of copper. The operating speeds of the shaft are between the first and the second critical speeds of the system. The parameters of the rotor system are listed in Table 1.

Table 1 Parameters of the rotor system

Parameters	Values
Shaft diameter	10mm
Shaft length	480mm
Disks' diameter	80mm
Disks' width	20mm
Density of shaft and disks	7860kg/m^3
Youg's modulus of shaft and disks	2.06e11Pa
Disks' mass	0.7902kg
Rub-impact stiffness k_rub	1e5 N/m
Rub-impact friction coefficient	0.1
Initial clearance of rub-impact	$\delta_0 = 2\text{e-}5$ m
First critical rotor speed	30.82Hz
Second critical rotor speed	119.36Hz
Shaft segement stiffness	k_{11} =2.3704e5N/m
	$k_{12} = k_{21}$ =-2.0741e5N/m
	k_{22} =2.3704e5 N/m
Damping coefficients	c_{11} =53.12N/(m/s)
	$c_{12} = c_{21}$ =-37.33 N/(m/s)
	c_{22} =53.12 N/(m/s)
Unbalance mass	1.5g at Disk 2
Unbalance radius	30mm at Disk 2
Effective unbalance distance of e2	5.695e-2mm
α_1, α_2	1.2655
β_{11}, β_{22}	67.2235
β_{12}, β_{21}	-47.2412

4.2 Analytical Solutions of the Rotor System

For the periodical motions of the rotor system with rub-impact at a fixed limiter, their first order solutions in *x* directions are

$$x_1 = a_{30} + a_{31}\cos\theta + b_{31}\sin\theta\,,\ x_2 = a_{40} + a_{41}\cos\theta + b_{41}\sin\theta \tag{12}$$

In order to make the integrations of Eq. (5) and (6) easier, the cubic polynomials are used to approximate the rub-impact forces at Disk 2 of F_{y2} and F_{x2}. For F_{x2}, it becomes

$$F_{x2} = p_1 x_2^3 + p_2 x_2^2 + p_3 x_2 + p_4 \tag{13}$$

For F_{y2}, it is easy to be obtained as $F_{y2} = f_{r2} F_{x2}$.

After substituting the rub-impact parameter values in Table 1, the four coefficients of Eq (13) are: p_1 = -8.026e+012, p_2 = -6.183e+008, p_3 = -8605, p_4 = 0.07482 with 95% confidence bounds.

For the system of Eq (3), with the 1st harmonic approximation of stable periodic solutions, the Equations (5) and (6) give the explicit expressions of $P_{0,1},.....,P_{sN,4}$. Nonlinear components of rub-impact forces are integrated in the interval of $[0, 2\pi]$ with respect to θ, and the coefficient equations can be written as follows,

$$\begin{aligned}
&P_{0,3} = -\alpha_1 k_{11} a_{30} - \alpha_1 k_{12} a_{40} = 0 \\
&P_{0,4} = \frac{\alpha_2}{2}(2p_1 a_{40}^3 + 3p_1 a_{41}^2 a_{40} + 3p_1 b_{41}^2 a_{40} + 2p_2 a_{40}^2 + p_2 a_{41}^2 + p_2 b_{41}^2 + 2p_3 a_{40} + 2p_4) - \\
&\alpha_2 k_{21} a_{30} - \alpha_2 k_{22} a_{40} = 0 \\
&P_{c1,3} = a_{3j} + \beta_{11} b_{3j} + \beta_{12} b_{4j} - \alpha_1 k_{11} a_{3j} - \alpha_1 k_{12} a_{4j} = 0 \\
&P_{c1,4} = a_{41} + \alpha_2(\frac{3}{4} p_1 a_{41} b_{41}^2 + 3p_1 a_{40}^2 a_{41} + 2p_2 a_{40} a_{41} + \frac{3}{4} p_1 a_{41}^3 + p_3 a_{41}) + \beta_{21} b_{31} \\
&+ \beta_{22} b_{41} - \alpha_2 k_{21} a_{31} - \alpha_2 k_{22} a_{41} + e_2 = 0 \\
&P_{s1,3} = -b_{3j} + \beta_{11} a_{31} + \beta_{12} a_{41} + \alpha_1 k_{11} b_{31} + \alpha_1 k_{12} b_{41} = 0 \\
&P_{s1,4} = -b_{41} + \alpha_2(3p_1 b_{41} a_{40}^2 + \frac{3}{4} p_1 a_{41}^2 b_{41} + 2p_2 a_{40} b_{41} + \frac{3}{4} p_1 b_{41}^3 + p_3 b_{41}) \\
&+ \beta_{21} a_{31} + \beta_{22} a_{41} + \alpha_2 k_{21} b_{31} + \alpha_2 k_{22} b_{41} = 0
\end{aligned} \tag{14}$$

Table 2 Coefficients and amplitudes of first order periodic solutions of x1 and x2

Rotating frequency	57.5 Hz	69 Hz	82 Hz
a_{30}	-3.0451e-6	-9.6994e-7	1.4114e-6
a_{31}	-5.1258e-5	-5.0808e-5	-5.7900e-5
b_{31}	-2.0418e-6	4.8913e-8	3.6793e-6
a_{40}	-3.4801e-6	-1.1085e-6	1.6130e-6
a_{41}	-3.3155e-5	-2.1993e-5	-8.6888e-6
b_{41}	-3.9047e-6	-3.9041e-6	-6.3502e-6
Amplitude of x_1 (m)	4.8239e-5	4.9838e-5	5.9428e-5
Amplitude of x_2 (m)	2.9903e-5	2.1226e-5	1.2375e-5

With Eq (14) and the parameters in Table 1, the coefficients of $a_{30}, a_{31}, b_{31}, a_{40}, a_{41}, b_{41}$ can be solved. Then the harmonic solutions of Eq (12), i.e. the periodic motions of the rotor system are obtained. The coefficients and vibration amplitudes of periodic motions under three different rotating frequencies are listed in Table 2.

4.3 *Stability Analysis of the Analytical Solutions with Floquet Theory*

Assuming that rub-impacts only occur at Disk 2, the partial differentials of rub-impact forces $\frac{\partial F_{y2}}{\partial x_2}, \frac{\partial F_{x2}}{\partial x_2}$, can be calculated based on Eq (12) and Eq (13). With the parameters in Table 1 and Table 2, Eq (9) gives

$$\boldsymbol{A}(t)=\begin{bmatrix} 0 & 1 & 0 & 0 & 0 & 0 & 0 & 0 \\ -3.00e5 & -67.22 & 2.62e5 & 47.25 & 0 & 0 & 0 & 0 \\ 0 & 0 & 0 & 1 & 0 & 0 & 0 & 0 \\ 2.62e5 & 47.25 & -3.00e5 & -67.22 & 0 & 0 & \alpha_2\frac{\partial F_{y2}}{\partial x_2} & 0 \\ 0 & 0 & 0 & 0 & 0 & 1 & 0 & 0 \\ 0 & 0 & 0 & 0 & -3.00e5 & -67.22 & 2.62e5 & 47.25 \\ 0 & 0 & 0 & 0 & 0 & 0 & 0 & 1 \\ 0 & 0 & 0 & 0 & 2.62e5 & 47.25 & \alpha_2(\frac{\partial F_{x2}}{\partial x_2}-k_{22}) & -67.22 \end{bmatrix} \tag{15}$$

where, $\frac{\partial F_{x2}}{\partial x_2} = 3p_1x_2^2 + 2p_2x_2 + p_3$, $\frac{\partial F_{y2}}{\partial x_2} = f_r(3p_1x_2^2 + 2p_2x_2 + p_3)$.

The Floquet multipliers with analytical method are calculated based on Section 3.1. On the other hand, the Floquet multipliers of the same rotor system based on the numerical integration method in Section 3.3 are also calculated. The two sets of Floquet multipliers are plotted against rotating frequency for comparison in Figure 3. It is obvious that periodic motion of the rotor system is unstable around 64Hz and 70Hz.

In addition, as shown in Figure 3, the analytical results of Floquet multipliers can not be achieved when the rotating frequency is over 72Hz. But the results with numerical integration method of $\boldsymbol{A}(t)$ can be carried on for the higher speeds. It is mainly due to the assumptions of the first order periodic solution in deducing $\boldsymbol{A}(t)$ of Eq (15).

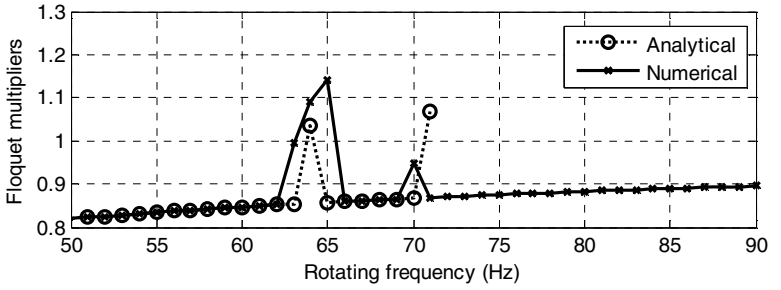

Fig. 3 Floquet multipliers vs rotating frequencies

The bifurcation charts are directly obtained with Runge-Kutta method for the rotor system of Eq (1) with parameters in Table 1. The bifurcation control parameter is the rotating speed with a range of (50, 90) Hz. As shown in Figure 4(a) and (b), when the rotating speed is less than 63Hz, the motions of the rotor system with rub-impact are stable with period 1. When rotating speed is greater than 63Hz, the system shows double periodic bifurcation. In the range from 63Hz to 70Hz of rotating speeds, the motions are in period 2 and multi-periodic. When the rotating frequency is over 70Hz, the multi-periodic motions lose their stability and the period-1 motions appear again.

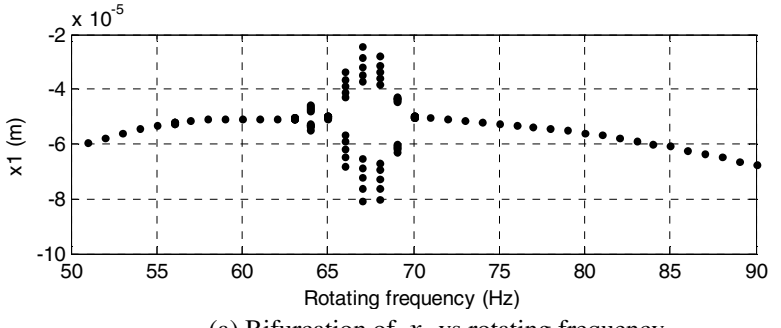

(a) Bifurcation of x_1 vs rotating frequency

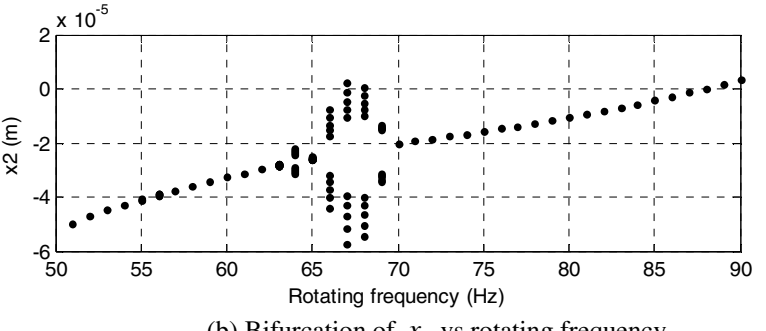

(b) Bifurcation of x_2 vs rotating frequency

Fig. 4 Bifurcations of the rotor system with rub-impact at fixed limiter

Compared with the curves in Figure 3 and 4, it can be seen that, there are many Floquet multipliers greater than 1 in the rotating frequency range of (63, 70) Hz. It means that the periodic motions tend to lose their stability in the frequency range, and meanwhile the rotor vibrations will bifurcate into double periodic motions at 63Hz. The system returns to periodic 1 after 70 Hz.

4.4 Comparisons with Numerical Integrations for Periodic Responses

The direct numerical simulations based on Runge-Kutta method are used to validate the analytical results. The numerical integrated responses of the two disks are described with transverse vibration responses and the rotor center trajectory orbits. The numerical integrated responses of the two disks with three different rotating frequencies are shown in Figure 5~7.

Figure 5 shows that rotor vibrations are periodic when rotating frequency is at 57.5Hz. The rotating frequency locates in the left region in Figure 3 and corresponds to period-1 motion.

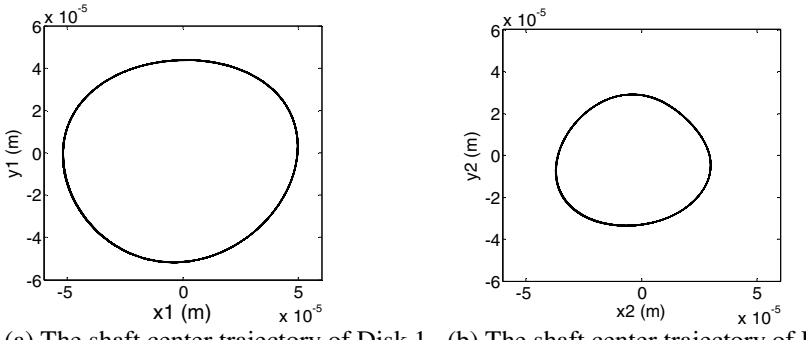

(a) The shaft center trajectory of Disk 1 (b) The shaft center trajectory of Disk 2

Fig. 5 The simulated responses of rotor system at 57.5Hz

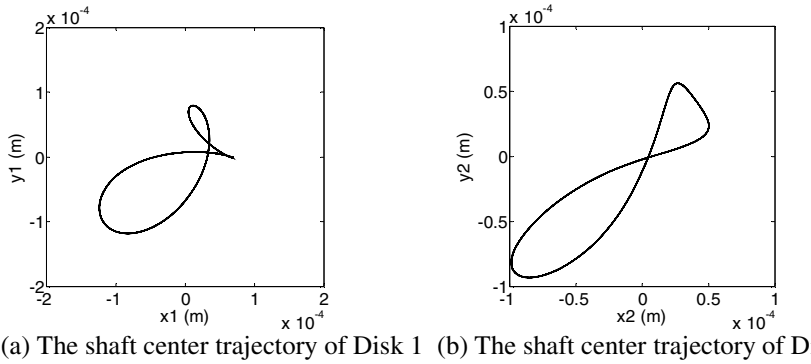

(a) The shaft center trajectory of Disk 1 (b) The shaft center trajectory of Disk 2

Fig. 6 The simulated responses of the rotor system at 69Hz

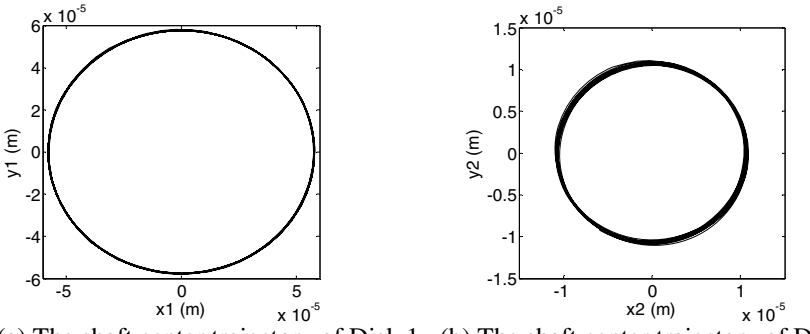

(a) The shaft center trajectory of Disk 1 (b) The shaft center trajectory of Disk 2

Fig. 7 The simulated responses of the rotor system at 82Hz

When the rotor frequency is at 69Hz, fundamental rotating frequency is disturbed by some other frequency components, as shown in Figure 6. The behavior of the shaft at 69Hz may be due to double-periodic bifurcation. This case corresponds to the middle region in Figure 3.

In Figure 7 the period-1 motion is seen again when the rotating speed is 82Hz. This case locates at the right region in Figure 3.

The simulated vibration amplitudes of the system in the above three typical cases of different rotating frequencies are listed in Table 3.

Table 3 Vibration peak-to-peak amplitudes of two disks with numerical integrations of the rotor system

Rotating freq.(Hz)	y_1 (m)	y_2 (m)	x_1 (m)	x_2 (m)
57.5	4.3929e-005	2.9221e-005	4.9751e-005	2.9959e-005
	-5.1920e-005	-3.3639e-005	-5.1944e-005	-3.7157e-05
69	7.9006e-005	5.6342e-005	6.8806e-005	5.0170e-005
	-1.1836e-004	-9.3414e-005	-1.2397e-004	-9.9102e-005
82	5.7957e-005	1.1036e-005	5.7840e-005	1.0883e-005
	-5.7941e-005	-1.1037e-005	-5.7874e-005	-1.0912e-005

5 Conclusions

The dynamical responses and their periodic motion stability analysis are carried out for a dual-disk rotor system with rub-impacts at fixed limiters.

The analytical periodic motion solutions of transverse vibrations of the rotor system due to rub-impacts at fixed limiters are deduced firstly. The motion stability is then discussed by both analytical and numerical methods based on Floquet theory. Numerical integration simulations of the rotor system are also conducted under different rotating frequencies to validate the periodical stability results.

For the presented rotor system, the stability analysis for the dual-disk rotor with rub-impact at fixed limiter indicates that there exist stable periodic motions in a large range of rotating frequency; however, in a small range of rotating frequency from 63Hz to 70Hz, the rotor system shows period-doubling bifurcations.

The analytical stability discussions for periodic motions are interesting and of great importance for understanding dual-disk rotor system with rub-impacts.

Acknowledgments. The authors gratefully acknowledge that the work was supported by Natural Science Foundation of China (Grant no. 50775028) and the 863 High-Tech Scheme (2007AA04Z418) by the Ministry of Science and Technology.

References

[1] Babitsky, V.I.: Theory of vibro-impact systems and applications. Springer, Berlin (1998)

[2] Beatty, R.: F, Differentiating rotor response due to radial rubbing, Transactions of the ASME. Journal of Vibration, Acoustics, Stress, and Reliability in Design 107, 151–160 (1995)

[3] Chu, F.: Zhang Z, Bifurcation and chaos in rub-impact Jeffcott rotor system. Journal of Sound and Vibration 210(1), 1–18 (1998)

[4] Chu, F.: Lu W, Experimental observation of nonlinear vibrations in a rub-impact rotor system. Journal of Sound and Vibration 283, 621–643 (2005)

[5] Goldman, P.: Muszynska A, Chaotic behavior of rotor/stator systems with rubs. ASME Journal of Engineering for Gas Turbine and Power 116, 692–701 (1994)

[6] von Groll, G., Ewins, D.J.: The harmonic balance method with arc-length continuation in rotor/stator contact problems. Journal of Sound and Vibration 241(2), 223–233 (2001)

[7] Muszynska, A.: Rotor-to-stationary element rub-related vibration phenomena in rotating machinery-literature survey. The Shock and Vibration Digest 21(3), 3–11 (1989)

[8] Lu, Q., Li, Q., Twizell, E.: The existence of periodic motions in rub-impact rotor systems. Journal of Sound and Vibration 264, 1127–1137 (2003)

[9] Han, Q., Zhang, Z., Wen, B.: Periodic Motions of a Dual-Disk Rotor System with Rub-Impact at Fixed Limiter, Proceedings of the Institution of Mechanical Engineers, Part C. Journal of Mechanical Engineering Science 222(C10), 1935–1946 (2008)

A Theory of Cavitation Erosion in Metals Based on the Concept of Impact Fatigue

Alan A. Johnson and Randall J. Storey

In developing a theory of cavitation erosion in metals some of the main features to be explained are:

(i) The surface damage, which is caused by the collapse of bubbles at or near the metal surface, is of two kinds: (a) surface craters, and (b) surface pits involving cracking.
(ii) After an incubation period, the erosion rate increases, goes through a maximum and them settles down to a constant value.
(iii) As the erosion rate increases, the surface roughness increases because of the cratering and pitting.
(iv) The evolution of the surface roughness enhances the cavitation but causes the mean bubble size to decrease and hence the mean impact magnitude to decrease.
(v) The sub-surface micro-hardness increases as the cavitation erosion develops.

All of these features can be explained if we assume that the cavitation erosion is caused by impact fatigue (A. A. Johnson and R. J. Storey, J. Sound and Vibration, 2007, 308, 458). When a smooth metal surface is freshly exposed to cavitation, impacts caused by the implosion of large bubbles cause cratering, pitting, and loss of material by low cycle impact fatigue. The surface roughness created in this process causes the mean bubble size and resulting mean impact magnitude to decrease so that loss of material then occurs mainly by high cycle impact fatigue. It is this buildup of low cycle impact fatigue, followed by the transition to high cycle impact fatigue, which causes the peak in the erosion rate vs. time curve. There is an incubation period because the number of impacts from individual bubble events has to reach a critical value determined by the impact fatigue characteristics before fatigue leads to loss of material from the surface by cracking. The cratering produces the sub-surface increases in micro-hardness.

Alan A. Johnson and Randall J. Storey
Metals Research Inc., 101 West Chestnut Street
Louisville, Kentucky 40202
barbalan@bellsouth.net

R.A. Ibrahim et al. (Eds.): Vibro-Impact Dynamics of Ocean Systems, LNACM 44, p. 121.
springerlink.com

Sloshing-Slamming Dynamics – S^2 – Analogy for Tuned Liquid Dampers

Ahsan Kareem, Swaroop Yalla, and Megan McCullough

Abstract. Tuned liquid dampers (TLDs) have been successfully utilized in structures to suppress their motions under wind, waves and earthquakes. Examples of such installations in structures range from skyscrapers, chimneys, masts, airport control towers, bridges and offshore structures. Unlike other passive inertial systems such as tuned mass dampers (TMDs), which are linear by design, TLDs are inherently non-linear. The non-linear behavior of TLDs is characterized by an amplitude dependent frequency response function, which translates into changes in frequency and damping of sloshing with amplitude. Therefore, despite the advantage of their simple installation, operation and maintenance, very few theoretical models exist to completely characterize their dynamic features. In this study, TLDs are modeled using a sloshing-slamming (S^2) analogy, which combines the dynamic features of liquid sloshing and slamming/impact. The parameters needed to capture the dynamics of sloshing-slamming in this model may be derived from experimental data or theoretical considerations.

Introduction

Containers partially filled with liquid experience sloshing and slamming of waves on their walls which leads to extreme loading conditions during earthquakes as the container base is set in motion. A similar situation arises for containers aboard ships, barges and offshore structures carrying liquids. Ocean waves impart base excitation to liquid containers on board, leading to wave-induced loads as well as wave slamming loads on container walls. On the other hand the sloshing dynamics of liquids can be harnessed by way of utilizing these as motion control devices, generally known as tuned liquid dampers (TLDs) [Kareem & Sun, 1987; Modi & Welt, 1987]. TLDs have been successfully implemented in structures to suppress their motions under wind, waves and earthquakes. Examples of such installations in structures range from skyscrapers, chimneys, masts, airport control towers, bridges and offshore structures.

Ahsan Kareem and Megan McCullough
NatHaz Modeling Laboratory, University of Notre Dame, Notre Dame, IN 46556
kareem@nd.edu; www.nd.edu/~nathaz

Swaroop Yalla
Morgan Stanley, New York, NY

R.A. Ibrahim et al. (Eds.): Vibro-Impact Dynamics of Ocean Systems, LNACM 44, pp. 123–133.
springerlink.com

A Tuned Liquid Damper (TLD)/Tuned Sloshing Damper (TSD) consists of a container that is partially filled with liquid, usually water, placed on top of a structure. Similar to a tuned mass damper (TMD), the liquid sloshing imparts indirect damping to the primary system, thereby reducing response. The TLDs can be broadly classified into two categories, i.e., shallow-water and deep-water dampers, based on the ratio of the water depth to the water surface length in the direction of the motion. In the shallow water case, the TLD damping originates primarily from energy dissipation through the action of viscous forces, such as wave breaking and wave slamming, on the container walls. For the deep-water damper, baffles or screens are needed to enhance the inherent damping.

For convenient implementation in design, liquid sloshing can be represented by a mechanical model. This is helpful in analyzing the dynamics of an overall system consisting of a TLD system with a given structural system. This model is based on linear wave theory and does not include wave breaking observed typically at larger amplitudes of motion. Since it is a linear model it does not account for changes in the frequency and damping that take place as the amplitude of sloshing increases.

Attempts to address this issue have been reported in the literature by introducing TMD based analogies to capture nonlinear sloshing in TLDs [Sun & Fujino, 1994; Yu *et al*., 1999; Yalla, 2001]. The TMD parameters are expressed in terms of experimentally derived amplitude dependent equivalent mass, frequency and damping. Typically a model based on the similarities between a nonlinear TLD system and a linear TMD tends to neglect higher harmonics and higher order nonlinearities unless they are accounted for in the global behavior. While these models may adequately serve their purpose for analysis and design by capturing the global behavior of sloshing they do not focus on the anatomy of fundamental sources of nonlinearities. In shallow-water TLDs, various mechanisms associated with free surface topology come into play to cause energy dissipation, including hydraulic jumps, bores, breaking waves and turbulence. Observations of sloshing in scale models reveal that one of the key mechanisms of energy dissipation is associated with the liquid impact on the walls. At large amplitudes of sloshing, this is portrayed by a rolling convective liquid mass, which slams/impacts on the damper walls periodically and dramatically increases dissipative effects.

In this study, TLDs are modeled using a sloshing-slamming – S^2 – analogy, which combines the dynamic features of liquid sloshing and slamming. The – S^2 - analogy reveals the metamorphosis of linear sloshing to nonlinear hardening-type sloshing-slamming and the enhanced level of damping observed. The model is a combination of a linear secondary damped inertial system and an impact damper in which the mass rolls periodically and impacts the container walls. Central to this analogy is the exchange of mass between the sloshing and the convective mass that slams the damper walls. This implies that at higher amplitudes of sloshing, some portion of the linear sloshing mass is transferred to the mass that rolls and impacts the sides, resulting in combined sloshing-slamming action. The periodic impact of convective mass on the walls characterizes both the hardening feature and observed increase in dissipative effects. The parameters needed to capture the dynamics of sloshing-slamming in this model can be derived experimentally or

from theoretical considerations. The model can be further refined within the proposed framework should it become possible to delineate more accurately the mass exchange between sloshing and slamming modes. The paper discusses the development of the model and some results. Other phenomenological theories based on a pendulum model of sloshing that includes wall impact are discussed in Ibrahim (2005). Although not included in the presentation is an experimental study in which simultaneous measurements of pressure on a base excited rectangular tank were made to better understand the sloshing slamming dynamics. Additionally, the data was analyzed in a time-frequency domain to better capture underlying transient features during the impact of liquid on the side walls.

1 Modeling of Sloshing-Slamming

The motion of liquids in rigid containers has been the subject of many studies in the past few decades because of its frequent application in several engineering disciplines. This can be modeled through numerical and mechanical models or experimental methods.

1.1 Numerical Modeling

One of the approaches in the modeling of sloshing liquids involves numerical schemes based on linear and/or non-linear potential flow theory. These types of models are applicable under small amplitude sloshing with no wave breaking and represent extensions of the classical theories by Airy and Boussinesq for shallow water tanks. Faltinsen (1978) introduced a fictitious term to artificially include the effect of viscous dissipation. For large motion amplitudes, additional studies have been conducted by Lepelletier and Raichlen (1988); Okamoto and Kawahara (1990); Chen *et al.* (1996) among others. Numerical simulation of sloshing waves in a 3-D tank has been conducted by Wu *et al.* (1998). However, in the absence of viscous effects, the sloshing period tends to become longer with an increase in amplitude, i.e., the system exhibits a softening effect [Wu *et al.* 1998]. The model presented by Lepelletier and Raichlen (1988) recognized the fact that a rational approximation of viscous liquid damping has to be introduced in order to model sloshing at higher amplitudes. Following this approach, a semi-analytical model was presented by Sun and Fujino (1994) to account for wave breaking in which the linear model was modified to account for breaking waves.

The attenuation of the waves in the mathematical model due to the presence of dissipation devices is also possible through a combination of experimentally derived drag coefficients of screens to be used in a numerical model [Hsieh *et al.,* 1988]. Additional models of liquid sloshing in the presence of flow dampening devices are available, e.g., Warnitchai and Pinkaew (1998).

1.2 Mechanical Modeling

For convenient implementation in design, liquid sloshing can be represented by a mechanical model. Typically a model based on the linear wave theory without

considering wave breaking is utilized, which cannot account for changes in the frequency and damping at higher amplitudes of motion [Yalla & Kareem, 2002].

New studies have emerged in the modeling of TLDs in terms of mechanical models. Sun *et al.* (1995) presented a TMD analogy for non-linear sloshing TLDs. A virtual mass and damping for a TLD attached to an undamped linear SDOF system were calculated from experimental results which were then translated into amplitude dependent equivalent mass, frequency and damping using the TMD analogy. Reed *et al.* (1998), Yu *et al.* (1999), and Yalla (2001) formulated non-linear models by way of an equivalent mass damper system with amplitude dependent non-linear stiffness and damping derived from experimental studies.

These models adequately serve their purpose by capturing the global effects of sloshing, but do not shed light on the nature and origin of nonlinearities associated with sloshing. In shallow-water TLDs, various mechanisms associated with the free liquid surface come into play to cause energy dissipation, including hydraulic jumps, bores, breaking waves and turbulence [Yalla, 2001]. One of the key mechanisms of energy dissipation is associated with the liquid impact on the walls. This sloshing feature at high amplitudes is indeed portrayed by a rolling convective liquid mass, which slams/impacts on the container walls periodically. Similar observations have been made in a later study by Faltinsen *et al.* (2005).

In this paper, the sloshing phenomenon for shallow-intermediate liquid depths has been represented by a sloshing-slamming (S^2) analogy. The S^2 analogy reveals the metamorphosis of linear sloshing to nonlinear hardening-type sloshing-slamming and the observed increase in the damping currently not fully encapsulated by the empirical correction due to wave breaking. Such an analogy in comparison with other models provides additional insights into the nature of liquid sloshing and associated effects such as increase in damping and changes in the sloshing frequency.

2 S^2 Analogy

The S^2 analogy is a combination of two analytical models: the linear sloshing and the liquid slamming/impact models. These models are discussed in the following sections.

2.1 Liquid Sloshing

A simplified model of sloshing in rectangular tanks is based on an equivalent mechanical analogy using lumped masses, springs and dashpots to describe liquid sloshing. The lumped parameters are determined from the linear wave theory [Abramson, 1966]. The equivalent mechanical model is shown schematically in Figure 1(a). The two key parameters are given by

$$m_n = M_l \left(\frac{8 \tanh\{(2n-1)\pi r\}}{\pi^3 r (2n-1)^3} \right); \quad n = 1,2... \tag{1}$$

$$\omega_n^2 = \frac{g(2n-1)\pi \tanh\{(2n-1)\pi r\}}{a}; \quad n = 1,2... \tag{2}$$

where n is the sloshing mode; m_n is the mass of liquid acting in that mode; ω_n is the frequency of sloshing; $r=h/a$ where h is the height of water in the tank and a is the length of the tank in the direction of excitation; M_l is the mass of the total water in the tank; m_0 is the 'inactive mass' which does not participate in sloshing and is given by:

$$m_0 = M_l - \sum_{n=1}^{\infty} m_n \tag{3}$$

Usually, only the fundamental mode of liquid sloshing, $n = 1$, is used for analysis. This model works well for small amplitude excitations, where the wave breaking and the influence of non-linearities is rather miniscule concerning the overall system response.

2.2 Liquid Slamming

The slamming of liquid on the container walls is analogous to an impact damper, which is characterized by the motion of a small rigid mass placed in a container firmly attached to the primary system, as shown in Figure 1(b) [Masri and Caughey, 1966; Semercigil *et al.* 1992; Babitsky, 1998]. A gap between the container and the impact damper, denoted by d, is kept by design so that collisions take place intermittently as soon as the displacement of the primary system exceeds this clearance. The collision produces energy dissipation and an exchange of momentum. The primary source of attenuation of motion in the primary system is due to this exchange of momentum. This momentum exchange reverses the direction of motion of the impacting mass. The equations of motion in between impacts of the combined primary and the secondary damper system (Equation 4) and the rolling mass (Equation 5) are given by:

$$M\ddot{x} + C\dot{x} + Kx = F(t) \tag{4}$$

$$m\ddot{z} = 0 \tag{5}$$

The velocity of the primary system after collision is given as [Masri and Caughey, 1966]

$$\dot{x}_{ac} = \frac{(1-\mu e)}{(1+\mu)}\dot{x}_{bc} + \frac{\mu(1+e)}{(1+\mu)}\dot{z}_{bc} \tag{6}$$

where e is the coefficient of restitution of the fluid involved in the slamming or collision, $\mu = m/M$ is the mass ratio, and the subscripts *ac* and *bc* refer to the *after-collision* and *before-collision* state of the variables. The velocity of the rolling mass involved in impact is reversed after each collision.

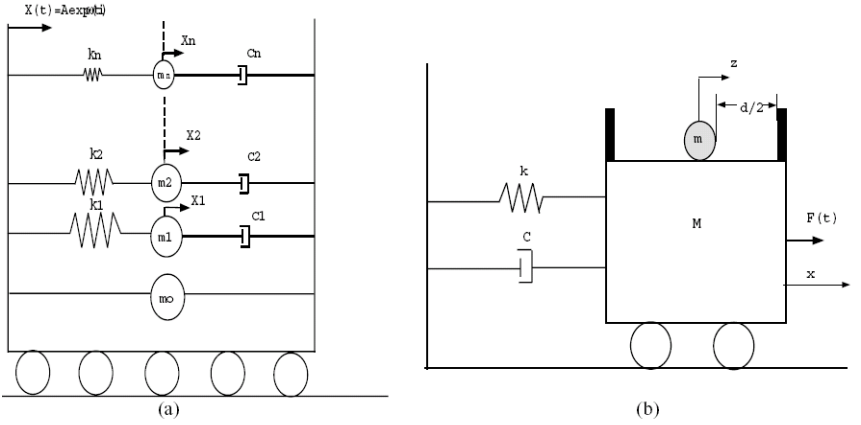

Fig. 1(a) Equivalent mechanical model of sloshing liquid in a tank (b) Impact damper model

2.3 Proposed S^2 Analogy

The key experimental results are summarized in Figures 2(a) and (b), where the jump frequency and the damping ratio are shown to increase with the amplitude of the base excitation of the TLD. The non-dimensional amplitude is given by $\Lambda = A_e / a$ where A_e is the amplitude of excitation and a is the length of the tank in the direction of excitation. The jump phenomenon is typical of nonlinear systems in which the system response drops sharply at a certain frequency known as the jump frequency.

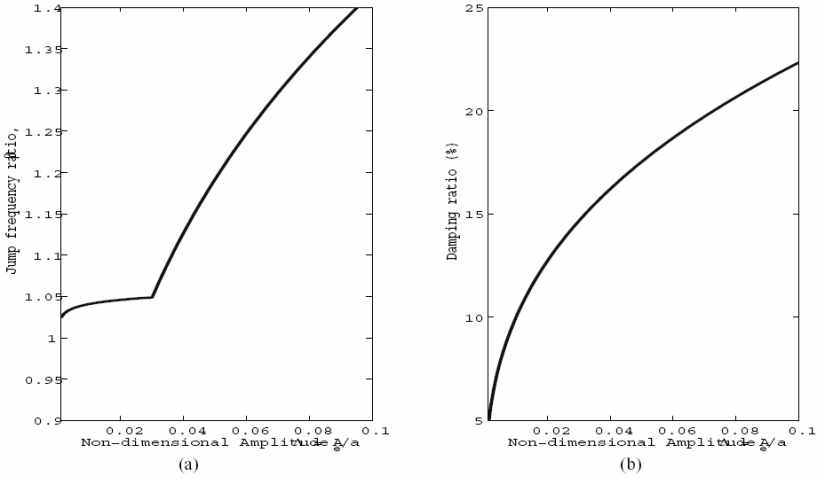

Fig. 2 Variation of (a) jump frequency and (b) Damping ratio of the Sloshing damper with the base amplitude [Yu et al. 1999]

Figure 2(a) shows that there is an increase in the jump frequency at higher amplitudes of excitation for the frequency ratios (ω_e / ω_1) greater than 1.0 suggesting a hardening effect, where ω_e is the frequency of excitation and ω_1 is the linear sloshing frequency. It has been noted that as the amplitude of excitation increases, the energy dissipation occurs over a broader range of frequencies. This feature establishes enhanced robustness exhibited by TLDs. The increased damping (introduced by wave breaking and slamming) causes the frequency response function of a combined TLD-structure system to change from a double-peak to a single peak function which has been observed experimentally, e.g., Sun and Fujino, 1994. Similar changes are noted as the damping of a TMD is increased [Yalla & Kareem, 2001; Chen & Kareem, 2003].

It is noted from the experimental observations at higher amplitudes ($\Delta \geq 0.03$), the liquid motion is characterized by slamming/impacting of water mass (Figure 3). This includes wave breaking and the periodic impact of a bore-like convecting lumped mass on the TLD walls. Some of the energy is also dissipated in upward deflection of liquid along the container walls. The S^2 analogy is schematically illustrated in Figure 4. The secondary system consists of a combination of the equivalent mechanical model of sloshing and the impact damper. Central to this analogy is the exchange of mass between the sloshing and convective mass that impacts the TLD walls. This implies that at these amplitudes, some portion of the mass m_1 (the linear sloshing liquid), is exchanged to mass m_2 (the impact mass), which results in a combined sloshing-slamming action.

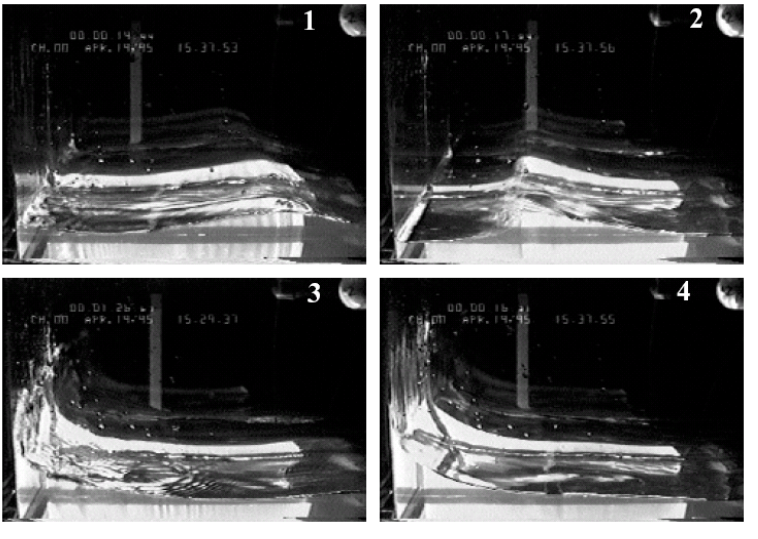

Fig. 3 Frames from the sloshing experiments video at high amplitudes: a part of the water moves as a lumped mass and impacts the container wall (Video Courtesy: Dr. D.A. Reed)

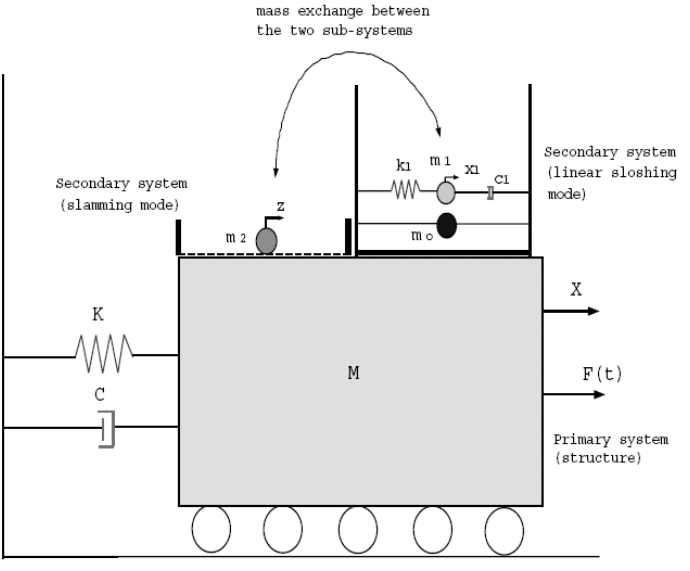

Fig. 4 Schematic diagram of the proposed S^2 analogy

The level of mass exchange is related to the change in the frequency ratio as shown in Figure 2(a). To model this, a mass exchange parameter γ is introduced here, which is an indicator of the portion of the linear mass m_1 acting in the linear mode as the exchange materializes. Since the total mass is conserved, this implies that the rest of the mass is acting in the impact mode. For example, γ=1.0 means that all of the mass m_1 is acting in the linear sloshing mode. After the mass exchange has taken place, the new masses $\tilde{m}_1$ and $\tilde{m}_2$ in the linear sloshing mode and the impact mode, respectively, are given by:

$$\tilde{m}_2 = m_2 + (1-\gamma)m_1 \tag{7}$$

$$\tilde{m}_1 = \gamma m_1 \tag{8}$$

At low amplitudes, there is almost no or very small mass exchange, therefore, the linear theory for all practical purposes holds in this regime. However, as the TLD excitation amplitude increases, γ decreases and the slamming mass increases concomitantly. Moreover, as m_1 is decreasing due to mass exchange, the sloshing frequency accordingly increases, which may explain the noted hardening behavior of the liquid sloshing. The mass exchange parameter can be related to the frequency ratio, $\beta = \frac{\tilde{\omega}_1}{\omega_1}$. Since $\tilde{\omega}_1^2 = \frac{k_1}{\tilde{m}_1} = \frac{\omega_1^2 m_1}{\tilde{m}_1}$, therefore using Equation 8, one can obtain $\beta = \sqrt{1/\gamma}$. The observation shown in Figure 2(a), therefore, can

be utilized to relate the mass exchange parameter to the amplitude of excitation. This scheme can be further refined should it become possible to quantify more accurately the mass exchange between the sloshing and slamming modes from theoretical considerations. The equations of motion for the system shown in Figure 4 can be expanded as

$$\begin{aligned} &M\ddot{X} + (C + c_1)\dot{X} + (K + k_1)X - c_1\dot{x}_1 - k_1 x_1 = F(t) \\ &m_1\ddot{x}_1 + c_1\dot{x}_1 + k_1 x_1 - c_1\dot{X} - k_1 X = 0 \\ &m_2\ddot{z} = 0 \end{aligned} \tag{9}$$

where $F(t) = F_0 \sin(\omega_e t)$; $F_0 = M\omega_e^2 A_e$; ω_e is the frequency of excitation and A_e is the amplitude of excitation. After each impact, the velocity of the convecting liquid is changed in accordance with Equation 6. An impact is numerically simulated at the time when the relative displacement between m_1 and m_2 is within a prescribed error tolerance of $d/2$, i.e., $|x_1 - z| \pm \varepsilon = d/2$. In this study the error tolerance has been assumed as $\varepsilon/d = 10^{-6}$. Since the relative displacements have to be checked at each time step, a time domain integration scheme is employed to solve the system of equations. In order to construct the frequency response curves, the maximum steady-state response was observed at each excitation frequency and the entire procedure was repeated for a range of excitation frequencies.

2.4 Numerical Simulation

A numerical study was conducted using the parameters employed in the experimental study [Fujino *et al*. 1992]. It should be noted that the initial mass ratio, prior to the mass exchange, has been assumed to take on a very serious small value, i.e., m_2/m_1=0.01, which is essential to realize the system in Figure 4 described by Equation 8. A parameter study suggests that this initial mass ratio between 0.001-0.01 does not have any notable influence on the dynamics of the overall system. This range of values is not unjustified since experimental results show signs of nonlinearity in the transfer function, albeit small, even at very low amplitudes of excitation (e.g., at A_e/a=0.004, β=1.02).

Figure 5 shows the changes that take place in the frequency response functions as the mass exchange parameter is varied. This can also be viewed as the amplitude dependent variation in the frequency response function. It is noted that the frequency response function undergoes a change from a double-peak to a single-peak function at higher amplitudes of excitation. Also shown in Figure 5 is the experimental data for the damper parameters used in the simulation. These results demonstrate that the frequency response function of the combined system derived from the sloshing-slamming model is in close agreement with the experimental data and capture salient features of the system both at low and high amplitudes of excitation.

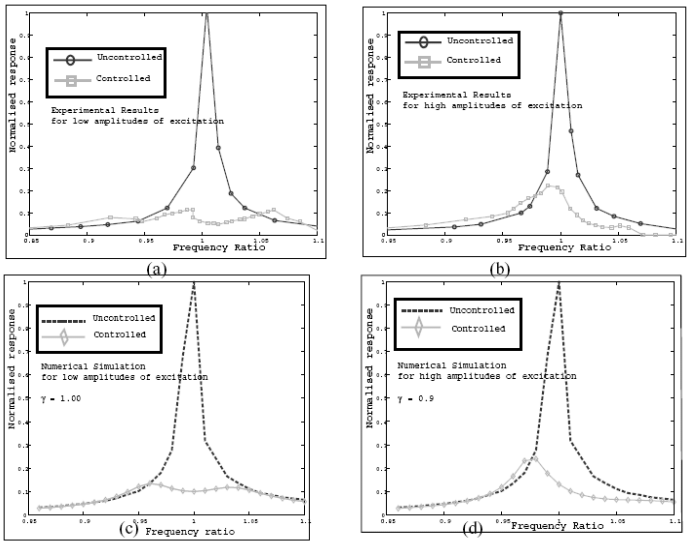

Fig. 5 Comparison of experimental results with S^2 simulation results: (a), (b): experimental results; (c), (d): simulation results for $\gamma = 1.0$ and $\gamma = 0.9$

Experimental studies were conducted to improve insight into wave-wall interaction. Space limitations do not permit reporting major findings.

3 Concluding Remarks

In this paper, a mechanical analogy of sloshing-slamming features of a TLD is presented. This analogy reproduces the TLD dynamic features at both low and high amplitudes of excitation. At low amplitudes, the S^2 analogy serves as a conventional linear sloshing damper. Whereas, as higher amplitudes, the system accounts for the convection of periodically slamming lumped liquid mass on the container walls, thus characterizing both the hardening feature and the observed increase in dissipative effects. The model can be further refined within the proposed framework, should it become possible to delineate more accurately the mass exchange between the sloshing and slamming modes from theoretical considerations.

References

Abramson, H.N. (ed.): The Dynamic Behavior of Liquids in Moving Containers. NASA, SP-106 (1966)

Babitsky, V.I.: Theory of Vibro-Impact Systems and Applications. Springer, New York (1998)

Chen, W., Haroun, M.A., Liu, F.: Large Amplitude Liquid Sloshing in Seismically Excited Tanks. Earthquake Engineering and Structural Dynamics 25, 653–669 (1996)

Chen, X., Kareem, A.: Curve Veering of Eigenvalue Loci of Bridges with Aeroelastic Effects. Journal of Engineering Mechanics, ASCE 129(2), 146–159 (2003)

Faltinsen, O.M.: A Numerical Nonlinear Method of Sloshing in Tanks with Two-Dimensional Flow. Journal of Ship Research 22 (1978)

Faltinsen, O.M., Rognebakke, O.F., Timokha, A.N.: Classification of three-dimensional nonlinear sloshing in a square-base tank with finite depth. Journal of Fluids and Structures 20, 81–103 (2005)

Fujino, Y., Sun, L.M., Paceno, B., Chaiseri, P.: Tuned Liquid Damper (TLD) for Suppressing Horizontal Motion of Structures. ASCE Journal of Engineering Mechanics 118(10), 2017–2030 (1992)

Hsieh, C.C., Kareem, A., Williams, A.N.: Wave Phase Effects on Dynamic Response of Offshore Platforms. In: Proceedings of the Offshore Mechanics and Arctic Engineering, ASME, Houston, TX (1998)

Ibrahim, R.: Liquid sloshing dynamics: theory and applications. Cambridge University Press, Cambridge (2005)

Kareem, A., Sun, W.J.: Stochastic Response of Structures with Fluid-containing Appendages. Journal of Sound and Vibration 119(3), 389–408 (1987)

Lepelletier, T.G., Raichlen, F.: Nonlinear Oscillations in Rectangular Tanks. Journal of Engineering Mechanics, ASCE 114(1), 1–23 (1988)

Masri, S.F., Caughey, T.K.: On the Stability of the Impact Damper. Journal of Applied Mechanics, ASME, 586–592 (1966)

Modi, V.J., Welt, F.: Vibration control using Nutation Dampers. In: King, R. (ed.) International conference on Flow induced Vibrations, BHRA, London, pp. 369–376 (1987)

Okomoto, T., Kawahara, M.: Two-dimensional Sloshing Analysis by Lagrangian Finite Element Method. International Journal for Numerical Methods in Fluids 11, 453–477 (1990)

Reed, D., Yu, J., Yeh, H., Gardarsson, S.: An Investigation of Tuned Liquid Dampers under large amplitude excitation. Journal of Engineering Mechanics, ASCE 124, 405–413 (1998)

Semercigil, S.E., Lammers, D., Ying, Z.: A new Tuned Vibration Absorber for Wide-band Excitations. Journal of Sound and Vibration 156(3), 445–459 (1992)

Sun, L.M., Fujino, Y.: A Semi-analytical model for Tuned Liquid Damper (TLD) with wave breaking. Journal of Fluids and Structures 8, 471–488 (1994)

Sun, L.M., Fujino, Y., Paceno, B., Chaiseri, P.: The Properties of Tuned Liquid Dampers using a TMD analogy. Earthquake Engineering and Structural Dynamics 24, 967–976 (1995)

Warnitchai, P., Pinkaew, T.: Modeling of Liquid Sloshing in Rectangular Tanks with Flow Dampening Devices. Engineering Structures 20(7), 593–600 (1998)

Wu, G.X., Ma, Q.W., Taylor, E.R.: Numerical Simulation of Sloshing Waves in a 3D tank based on a Finite Element Method. Applied Ocean Research 20, 337–355 (1998)

Yalla, S.K.: Liquid dampers for mitigations of structural response: theoretical development and experimental validation. Dissertation, the Graduate School of the University of Notre Dame in partial fulfillment of the requirements of Ph.D degree (2001) (submitted)

Yalla, S.K., Kareem, A.: Beat phenomenon in combined structure-liquid damper systems. Engineering Structures 23, 622–630 (2001)

Yalla, S.K., Kareem, A.: Discussion of Paper: Tuned liquid dampers for controlling earthquake response of structures by P. Banerji et al., Earthquake Engng. Struct. Dyn. 29(5), 587–602 (2000); Earthquake Engng Struct. Dyn. 31, 1037–1039 (2002)

Yu, J., Wakahara, T., Reed, D.A.: A Non-linear Numerical Model of the Tuned Liquid Damper. Earthquake Engineering and Structural Dynamics 28, 671–686 (1999)

A Dynamic Model and a Robust Controller for a Fully Actuated Marine Surface Vessel

Nassim Khaled and Nabil G. Chalhoub

Abstract. A nonlinear six degree-of-freedom dynamic model has been developed for a marine surface vessel. The formulation closely follows the existing literature on ship modeling. It accounts for the effects of inertial forces, wave excitations, retardation forces, nonlinear restoring forces, wind and current loads. The model is used herein to predict the response of a ship in a turning-circle maneuver. Furthermore, a nonlinear robust controller has been designed based on a reduced-order version of the ship model, which only takes into consideration the surge, sway and yaw motions. The controller is formulated by implementing the sliding mode methodology. It considers the ship to be fully actuated. The simulation results, generated based on the reduced-order model of the ship, illustrate the robust performance and the good tracking characteristic of the controller in the presence of significant modeling uncertainties and environmental disturbances.

Nomenclature

A_T, A_L	transverse and longitudinal areas of the ship's superstructure.
A_{rud}, D_{pr}	area of the rudder and diameter of the propeller, respectively.
A_{disk}	area of the propeller disk.
k, χ	wave number for infinite sea depth and wave encounter angle, respectively.
L, L_{pp}	overall length and length between the perpendiculars of the ship, respectively.
m, I	mass and mass moment of inertia of the ship.
p, q, r	angular velocity of the ship along the $\underset{\sim}{i}_o, \underset{\sim}{j}_o$ and $\underset{\sim}{k}_o$ directions, respectively.
T	draft of the ship.

Nassim Khaled and Nabil G. Chalhoub
Mechanical Engineering Department
Wayne State University
Detroit, MI 48202, USA

R.A. Ibrahim et al. (Eds.): Vibro-Impact Dynamics of Ocean Systems, LNACM 44, pp. 135–148.
springerlink.com

u, v, w translational velocity of the ship along the $\underset{\sim}{i}_o, \underset{\sim}{j}_o$ and $\underset{\sim}{k}_o$ directions, respectively.

x_G, y_G, z_G coordinates of the ship mass center with respect to the body-fixed frame.

ρ_{water}, ρ_{air} density of water and air, respectively.

1 Introduction

The dynamic behavior of marine surface vessels is highly nonlinear. Moreover, it is significantly influenced by environmental disturbances induced by winds, random sea waves and currents. Therefore, good track-keeping and course-changing characteristics of the ship can only be achieved by implementing controllers that are robust to both modeling uncertainties and external disturbances.

Nonlinear control theory has been extensively used in both track-keeping and course-changing maneuvers of marine vessels (Fossen, 2000; Pivano et al., 2007). However, many of these compensators, such as state feedback linearization techniques (Moreira et al., 2007; Berge et al., 1998; Fossen, 1993), output feedback controllers and backstepping schemes (Fossen and Grovlen, 1998; Godhavn, 1996; Strand et al., 1998; Fossen and Strand, 1999; Pettersen and Nijmeijer, 2001) are model-based schemes. As a consequence, these techniques are susceptible to modeling inaccuracies. On the other hand, the sliding mode methodology (Slotine and Li, 1991) enables one to design robust controllers without requiring a full knowledge of the system's nonlinearity (Le et al., 2004). The design of sliding mode controllers is mainly based on knowing the upper bounds of the modeling inaccuracies. The performance of these controllers tends to be robust to both structured and unstructured uncertainties.

The focus of the current work is to develop a nonlinear controller, based on the sliding mode methodology, to yield a robust performance of the ship during track-keeping maneuvers. The controller is designed based on the assumption that the marine vessel is fully actuated and all state variables are available through direct measurements.

A six degree-of-freedom nonlinear model for a marine surface vessel has been developed in this work to serve as a test bed for assessing the performance of the proposed controller as well as controllers to be designed in subsequent studies. The current model, covered in the next section, follows closely the existing literature on ship modeling (Fossen, 2005). Its formulation accounts for the wave excitation forces, retardation forces, inertial forces, nonlinear restoring forces, wind and current loads. The proposed nonlinear robust controller is discussed in section 3. It is based on a reduced-order version of the ship model, which only considers the surge, sway and yaw motions. The digital simulation results are presented in section 4. They demonstrate the capability of the nonlinear six degree-of-freedom model in predicting the ship response in a turning-circle maneuver. Moreover, they illustrate the controlled response of the ship, which is generated by implementing the proposed controller on the reduced-order model. The results exhibit a robust performance of the controller in the presence of

significant modeling uncertainties and environmental disturbances. Finally, the work is summarized and the main conclusions are drawn.

2 Dynamic Model of the Ship

The ship is treated as a rigid body having six degrees of freedom, namely, surge, sway, heave, roll, pitch and yaw (see Fig. 1). Two coordinate systems have been used. The first one is an inertial frame $\{X,Y,Z\}$ whose origin is located at an arbitrary point on the calm sea surface. The second coordinate system, $\{x_o, y_o, z_o\}$, is a non-inertial, body-fixed coordinate system attached to the ship at point o, which coincides with the center of floatation of the ship. The $(x_o, z_o)-$ plane is chosen to coincide with the vertical plane of symmetry of the ship hull. The x_o- and y_o- axes are directed towards the bow and the starboard of the ship.

Fig. 1 Schematic of the ship hull

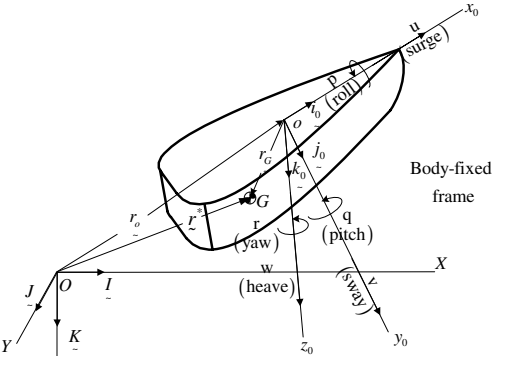

Following the SNAME convention (1950), both the position and orientation of the ship are defined with respect to the inertial frame. However, the ship translational and angular velocity vectors are expressed with respect to the body-fixed frame. The scalar equations, describing the translational motion of the ship, are derived from the linear momentum balance. They are given as

$$\begin{aligned} m\left[\dot{u} - vr + wq - x_G(q^2 + r^2) + y_G(pq - \dot{r}) + z_G(pr + \dot{q})\right] &= F_X \\ m\left[\dot{v} - wp + ur - y_G(r^2 + p^2) + z_G(qr - \dot{p}) + x_G(pq + \dot{r})\right] &= F_Y \\ m\left[\dot{w} - uq + pv - z_G(p^2 + q^2) + x_G(rp - \dot{q}) + y_G(rq + \dot{p})\right] &= F_Z \end{aligned} \tag{1}$$

where F_X, F_Y and F_Z are the components of the resultant force, $\underset{\sim}{F}$, of all externally applied forces on the ship along the $\underset{\sim}{i}_o, \underset{\sim}{j}_o$ and $\underset{\sim}{k}_o$ directions, respectively. Moreover, the angular momentum balance around point o will yield the following three scalar equations governing the rotational motion of the marine vessel:

$$
\begin{aligned}
&I_x\dot{p}-I_{xy}\dot{q}-I_{xz}\dot{r}-I_{xz}pq-I_{yz}q^2+I_zrq+I_{xy}pr-I_yqr+I_{yz}r^2+my_G(\dot{w}+pv-uq)-mz_G(\dot{v}+ur-pw)=M_X^o\\
&-I_{xy}\dot{p}+I_y\dot{q}-I_{yz}\dot{r}+I_{xz}p^2+I_{yz}pq-I_zrp+I_xpr-I_{xy}qr-I_{xz}r^2+mz_G(\dot{u}+qw-vr)-mx_G(\dot{w}+pv-uq)=M_Y^o\\
&-I_{xz}\dot{p}-I_{yz}\dot{q}+I_z\dot{r}-I_{xy}p^2+I_ypq-I_{yz}pr-I_xpq+I_{xy}q^2+I_{xz}rq+mx_G(\dot{v}+ur-pw)-my_G(\dot{u}+qw-vr)=M_Z^o
\end{aligned}
\tag{2}
$$

where $\underset{\sim}{M}_o$ is the resultant of all externally applied moments on the ship. Both $\underset{\sim}{F}$ and $\underset{\sim}{M}_o$ reflect the effects of wave excitations, retardation forces, wind and current loads, nonlinear restoring forces along with the control actions generated by the propeller, the rudder and the side thrusters.

Long-crested sea waves are considered in the current study. The wave height, h, at an arbitrary point (X,Y), defined with respect to the inertial frame, is commonly described by (Newman, 1977; Perez, 2005)

$$h(X,Y,t)=\sum_{i=1}^{650}A_i\cos\left(\omega_i t+\varepsilon_i-k\left(X\cos\beta+Y\sin\beta\right)\right) \tag{3}$$

where β is the incident wave angle. A_i and ε_i are the amplitude and the phase angle of the i^{th} frequency component of the wave height, respectively. ε_i is considered to be a random variable with a uniform distribution between 0 and 2π. A_i is determined from $\sqrt{2S(\omega_i)\Delta\omega}$ where $S(\omega)$ is the wave spectrum. The latter is assumed to be the Modified Pierson-Moskowitz wave spectrum. It is defined as (Perez, 2005)

$$S(\omega)=\frac{A_S}{\omega^5}e^{\left(-B_S/\omega^4\right)} \tag{4}$$

where $A_S=0.312H_{1/3}^2\omega_o^4$, $B_S=1.25\omega_o^4$ and ω_o is the modal frequency at which the wave spectrum reaches its maximum value. The wave spectrum corresponding to $H_{1/3}=2\ m$ and $\omega_0=0.69$ rad/s is shown in Fig. 2. Moreover, to avoid risking $h(X,Y,t)$ from repeating itself, ω_i is selected randomly in the interval $\left[(i-1)\Delta\omega, i\Delta\omega\right]$ (Perez, 2005). It should be noted that $\Delta\omega$ is considered herein to be constant and equal to 0.01 rad/s.

The formulation of the seakeeping problem, which customarily considers the ship motion to be harmonic with small amplitudes, has been used herein to determine the wave excitation forcing functions along with the frequency dependent added mass and damping terms (Faltinsen, 1990; Newman, 1977; Perez, 2005). In addition, the fluid is assumed to be inviscid, incompressible and irrotational. The wave excitation forces and moments are then computed as follows

$$F_j^{w-e}(t)=\sum_{i=1}^{650}\left|X_j(\chi,\omega_i)\right|\sqrt{2S(\omega_i)\Delta\omega}\cos\left(\omega_i t+\varepsilon_i+\varphi_j(\chi,\omega_i)\right) \qquad j=1,\cdots,6 \quad (5)$$

where $\left|X_j(\chi,\omega_i)\right|$ and $\varphi_j(\chi,\omega_i)$ are the magnitude and phase angle of the force transfer function defined by the ratio of the wave excitation force influencing the j^{th} degree-of-freedom of the ship over a unit wave amplitude. The six force transfer functions are determined numerically by using a 3-D potential theory software WAMIT (Lee and Newman, 2004). It should be mentioned that the latter does not account for the effect of the ship forward speed.

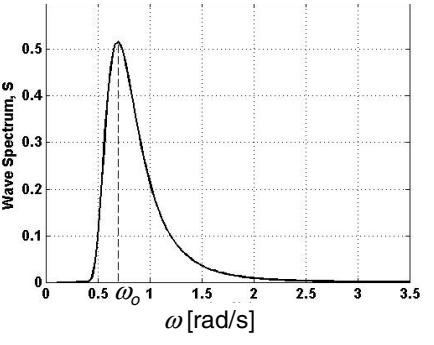

Fig. 2 Modified Pierson-Moskowitz wave spectrum

The ship response is determined from (Perez, 2005)

$$\zeta_j(t)=\sum_{i=1}^{650}\left|R_j(\chi,\omega_i)\right|\sqrt{2S(\omega_i)\Delta\omega}\cos\left(\omega_i t+\varepsilon_i+\Phi_j(\chi,\omega_i)\right) \quad j=1,\cdots,6 \quad (6)$$

where the $\left|R_j(\chi,\omega_i)\right|$ and $\Phi_j(\chi,\omega_i)$ are the magnitudes and phase angles of the motion transfer functions or the response amplitude operator (RAO), which is defined by the ratio of the ship motion in the j^{th} direction over a unit wave amplitude (Fossen, 2005). All RAO's are determined numerically by WAMIT (Lee and Newman, 2004).

The frequency dependent added mass, $a_{kl}(\omega)$, and added damping, $b_{kl}(\omega)$ terms are also computed by using WAMIT (Lee and Newman, 2004) for a frequency range between 0 and 6.5 rad/sec. The impulse response $k_{kl}(t)$ in the k^{th} direction due to a unit velocity impulse in the l^{th} direction can be related to the added damping term, $b_{kl}(\omega)$, as follows (Ogilivie, 1964; Kristiansen et al, 2005)

$$k_{kl}(t)=\frac{2}{\pi}\int_0^\infty\left[b_{kl}(\omega)-b_{kl}(\infty)\right]\cos(\omega t)\,d\omega \quad (7)$$

The convolution integral associated with $k_{kl}(t)$, based on an arbitrary velocity term $\dot{\zeta}_l$ in the l^{th} direction, can be written as

$$\int_0^{\infty} k_{kl}(t-\tau)\dot{\zeta}_l(\tau)d\tau \quad for \quad k,l=1,\cdots,6 \tag{8}$$

This will result in a 6×6 retardation matrix $K(t)$. Following the procedure outlined by Kristiansen et al (2005), the singular value decomposition method was used to generate a non-minimal state space realization for a single-input single-output (SISO) system whose input and output variables are $\dot{\zeta}_l(t)$ and $y_{kl}(t)$, respectively. A model reduction procedure was then implemented to reduce the order of the state space realization to eight without significantly compromising its accuracy. This is illustrated in Fig. 3 for the case of $k_{15}(t)$. The state space representation corresponding to the (k,l) entry of the retardation matrix $K(t)$ can be described as

$$\dot{\underset{\sim}{\xi}}^{(kl)} = A^{(kl)}\underset{\sim}{\xi}^{(kl)} + B^{(kl)}\dot{\zeta}_l \qquad and \qquad y_{kl} = C^{(kl)}\underset{\sim}{\xi}^{(kl)} + D^{(kl)}\dot{\zeta}_l \tag{9}$$

where the retardation force, $F_k^{retardation}$, in the k^{th} equation of motion is given by $\sum_{l=1}^{6} y_{kl}$.

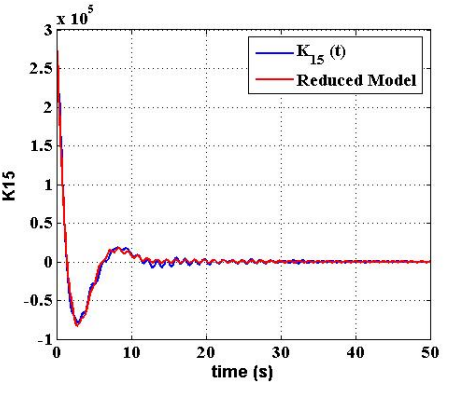

Fig. 3 Curves illustrating the accuracy of the state space formulation

Next, the buoyancy force and moment are computed based on the instantaneous submerged volume of the ship with respect to the sea free-surface. These forcing functions, which are balanced by the ship's own weight, are determined by multiplying the specific weight of the fluid with the instantaneous submerged volume of the ship. This is done herein by defining a 3-D mesh that partitions the

ship hull into 32000 cubes. The dimensions of each cube are selected to be 5, 2 and 0.04 m in the $\underset{\sim}{i}_o, \underset{\sim}{j}_o$ and $\underset{\sim}{k}_o$ directions, respectively. The computation of the instantaneous submerged volume of the ship involves the evaluation of a "degree of submergence", α, for each block. α_i corresponding to the i^{th} block is defined by

$$\alpha_i = sat\left(\frac{Z_c^i - h\left(X_c^i, Y_c^i\right)}{block\ thickness} + \frac{1}{2}\right) \tag{10}$$

where $\left(X_c^i, Y_c^i, Z_c^i\right)$ are the coordinates of the centroid of the i^{th} block and h is the elevation of the sea free-surface at (X_c^i, Y_c^i). Both the centroid and h are defined with respect to the inertial frame. The lower and upper saturation limits are set to 0 and 1, respectively. Note that $\alpha_i = 0$ reflects the case in which the i^{th} block is located above the sea free-surface. However, $\alpha_i = 1$ or $0 < \alpha_i < 1$ correspond to either total or partial submergence of the i^{th} block. The instantaneous submerged volume of the ship can now be computed from $V_{sub} = \sum_{i=1}^{32000} \alpha_i V_{i_{block}}$. It should also be pointed out that the hydrostatic moment is determined herein with respect to the origin of $\{x_o, y_o, z_o\}$.

Moreover, linear damping forces and moments have been introduced in the formulation whereby $\underset{\sim}{F}_{damp}$ is defined as $\left[\left(mb_u\right)u, \left(mb_v\right)v, \left(mb_w\right)w, \left(I_x b_p\right)p, \left(I_y b_q\right)q, \left(I_z b_r\right)r\right]^T$ (Ueng et al., 2008). In this study, b_u, b_v, b_w, b_p, b_q and b_r are chosen to be 1, 1, 3, 8, 8 and 8, respectively.

The wind resistive forces and yawing moment are computed as follows (Isherwood, 1973; Journée and Massie, 2001; Fossen, 1994; Perez, 2005; OCIMF, 1994)

$$f_{x_w} = 0.5 C_{x_w} \rho_{air} A_T V_{r_w}^2(10) \qquad f_{y_w} = 0.5 C_{y_w} \rho_{air} A_L V_{r_w}^2(10)$$

$$m_{z_w} = 0.5 C_{z_w} \rho_{air} A_L V_{r_w}^2(10) L \tag{11}$$

where $V_{r_w}(10)$ is the wind velocity relative to the ship evaluated at 10 m above the calm sea surface. Note that m_{z_w} is applied about an axis perpendicular to the calm sea surface and passing through the midpoint between the aft and forward perpendiculars of the ship. The formulation for determining the C_{x_w}, C_{y_w} and C_{z_w} coefficients are provided by Isherwood (1973).

The formulation used for computing the current induced forces and yawing moment are similar to those employed in the calculation of the wind loads with the exception that they are only being applied on the submerged portion of the ship. They are given by

$$f_{x_c} = 0.5 C_{x_c} \rho_{water} V_{r_c}^2 L_{pp} T \qquad f_{y_c} = 0.5 C_{y_c} \rho_{water} V_{r_c}^2 L_{pp} T$$
$$m_{z_c} = 0.5 C_{z_c} \rho_{water} V_{r_c}^2 L_{pp} T \tag{12}$$

where V_{r_c} is the velocity of the current relative to the ship. The numerical values for C_{x_c}, C_{y_c} and C_{z_c} are obtained from the OCIMF report (1994).

The propeller is responsible for delivering the thrust required to keep the ship on track. The present work considers a fixed pitch, sub-cavitating, Wageningen B4-70 screw propeller (Roddy at al, 2006; Journée and Massie, 2001). The propeller thrust, F_{th}, and the corresponding torque, T_{pr}, that should be applied on the propeller shaft are determined from (Journée and Massie, 2001)

$$T_{pr} = (\pi/8) C_Q \rho_{water} V_r^2 D_{pr}^3 \qquad F_{th} = (\pi/8) C_T \rho_{water} V_r^2 D_{pr}^2 \tag{13}$$

where V_r is the speed of the flow in the blade section evaluated at $r = 0.7(D_{pr}/2)$. It is given by

$$V_r = \sqrt{V_{pr}^2 + \left(0.7\pi n_{pr} D_{pr}\right)^2} \tag{14}$$

where n_{pr} is the angular velocity of the propeller shaft. V_{pr} is the mean value of the fluid speed at the entrance of the propeller disk. It is determined from (Journée and Massie, 2001; Blanke, 1982)

$$V_{pr} = (1 - w) u \tag{15}$$

Typical values for the wake fraction number, w, are between 0.1 and 0.4 (Fossen, 1994). w is assumed herein to be 0.1. Moreover, for a ship maneuvering task, four-quadrant data on dimensionless thrust, C_T, and torque, C_Q, coefficients should be used (Kuiper, 1992; Journée and Massie, 2001; Roddy at al, 2006). Kuiper (1992) provided such data for a B4-70 open-propeller as a function of the hydrodynamic pitch angle, δ, which is calculated as follows

$$\delta_{0.7(D_{pr}/2)} = \arctan\left(\frac{V_{pr}}{0.7\pi n_{pr} D_{pr}}\right) \tag{16}$$

Note that the present formulation has some provision to ensure that the propeller thrust, specified by the controller, does not exceed the physical limitation of the ship propulsion system. This is done by using Eq. (14) into Eq. (13) to substitute V_r by its expression with respect to n_{pr} in both F_{th} and T_{pr}. The resulting expression of F_{th} will then be implemented to solve for n_{pr} that is required to yield the thrust assigned by the controller. If n_{pr} is less than the maximum speed deliverable by the ship's engine then its value will be used;

otherwise, n_{pr} is set to its maximum value. Based on the current value of n_{pr}, Eq. (13) will be used to compute T_{pr}. Once again, if the calculated value of T_{pr} is smaller than the maximum torque that can be generated by the ship's propulsion system then both n_{pr} and F_{th} will be used in the digital simulation. Otherwise, n_{pr} will be recalculated based on the maximum value of T_{pr}. The new n_{pr} value will now be used to compute the deliverable thrust, F_{th}^{deliv}. This value will replace the unrealistic F_{th} assigned by the controller.

Next, the rudder dynamics are considered. Its lift, f_L, and drag, f_D, forces are determined from (Perez, 2005; Journée and Pinkster, 2002)

$$f_L = 0.5 C_L \rho_{water} V_{rud}^2 A_{rud} \qquad f_D = 0.5 C_D \rho_{water} V_{rud}^2 A_{rud} \tag{17}$$

Numerical values for C_L and C_D, based on an aspect ratio (AR) of 6 and a rudder section between 0.06 and 0.18, are provided by Abbott and Von Doenhoff (1958) and Journée and Pinkster (2002). In evaluating V_{rud}, the effect of the propeller on the flow heading towards the rudder has been accounted for by considering an idealized, steady, one-dimensional flow through the propeller. The latter is modeled by a thin actuator disk across which, the flow velocity is considered to be continuous while the pressure is assumed to undergo a sudden change. Based on this simplified model, one can express V_{rud} as (Fox and McDonald, 1992; Perez, 2005; Lewis, 1988)

$$V_{rud} = \sqrt{\left(\frac{2 F_{th}^{deliv}}{\rho_{water} A_{disk}} + V_{pr}^2 \right)} \tag{18}$$

The rudder angle of attack, α_r, is a new degree-of-freedom that has been introduced in this work to account for the rudder dynamics. The angular momentum balance, applied around the axis of rotation of the rudder, is used to derive the following equation of motion of the rudder:

$$I_{rud} \ddot{\alpha}_r = M_{rud}^{cont} + \left[\underset{\sim}{r}_{o_r C_P} \times \left(-f_D \underset{\sim}{i}_o + f_L \underset{\sim}{j}_o \right) \right] \cdot \underset{\sim}{k}_o \tag{19}$$

where M_{rud}^{cont} is the rudder control moment determined by the ship's controller. The lift and drag forces are applied at the center of pressure, C_P (Perez, 2005; Journée and Pinkster, 2002).

3 Controller Design

The controller is designed based on a reduced order model whose formulation is obtained from Eqs. (1) and (2) by only retaining the second order differential

equations governing the surge, sway and yaw motions of the ship. In addition, all terms pertaining to the heave, pitch and roll motions have been deleted from the selected equations. Defining the state vector to be $\underset{\sim}{x}^T = \left[\int u\,d\tau, \int v\,d\tau, \int r\,d\tau, u, v, r\right]$, the three second order differential equations of motion can be converted to six first order state equations that can be expressed in the following compact form:

$$\dot{\underset{\sim}{x}} = \underset{\sim}{f}\left(\underset{\sim}{x}\right) + G\left(\underset{\sim}{x}\right)\underset{\sim}{u} \tag{20}$$

where $\underset{\sim}{f}\left(\underset{\sim}{x}\right)$ represents the effects of inertial forces, gravitational acceleration, buoyancy forces, wave excitation forces, retardation forces, wind and current resistive forces. It should be pointed out that the dynamic equation of the rudder was also used to express the lift force by the control rudder moment in the yaw equation of motion, which corresponds to the sixth state equation. The $G_{6\times 3}\left(\underset{\sim}{x}\right)$ matrix is given by $\left[0_{3\times 3}\ diag(g_1, g_2, g_3)\right]^T$.

In the current work, the marine vessel is assumed to be fully actuated. Its three control variables represent the propeller thrust, $F_{th\_surge}^{cont}$, the side thrust, $F_{th\_sway}^{cont}$, and the rudder moment, M_{rud}^{cont}. As a consequence, the control vector, $\underset{\sim}{u}$, in Eq. (20) can now be defined as $\left[F_{th\_surge}^{cont}, F_{th\_sway}^{cont}, M_{rud}^{cont}\right]^T$. Moreover, all state variables of the system are assumed to be available through measurements.

The reduced-order model, described in Eq. (20), has been used in the current work to design a nonlinear robust controller in order to control the ship motion during maneuvering tasks. The proposed controller is designed based on the sliding mode methodology. The latter does not require exact knowledge of $\underset{\sim}{f}\left(\underset{\sim}{x}\right)$. As a result, a nominal model, based on an approximate expression $\hat{\underset{\sim}{f}}\left(\underset{\sim}{x}\right)$ for $\underset{\sim}{f}\left(\underset{\sim}{x}\right)$, has been used in the design of the compensator. It should be stressed that the good performance of the controller hinges upon the full knowledge of the upper bounds of the modeling uncertainties, which are defined by $\left|\Delta f_i\right| = \left|f_i\left(\underset{\sim}{x}\right) - \hat{f}_i\left(\underset{\sim}{x}\right)\right| \le \bar{F}_i$ with $i = 1, \cdots, 6$. For the ship maneuvering problem, the following three sliding surfaces are selected:

$$s_i = \dot{e}_i + \lambda_i e_i \qquad i = 1, \cdots, 3 \tag{21}$$

where the i^{th} tracking error is defined to be $e_i = x_i - x_{i_d}$. The control signals are calculated from

$$u_i = u_{i_{eq}} - g_i^{-1} k_i \operatorname{sgn}\left(s_i\right) \cong u_{i_{eq}} - g_i^{-1} k_i\, sat\left(s_i / \Phi_i\right) \qquad i = 1, \cdots, 3 \tag{22}$$

where the equivalent control laws, $u_{i_{eq}}$'s, are determined by setting $\dot{s}_i = 0$ with $i = 1, \cdots, 3$. The switching terms are responsible for keeping the system on the

sliding surfaces. Their gains, k_i's, are determined by satisfying the following sliding conditions:

$$\frac{1}{2}\frac{d}{dt}s_i^2\left(e_i,t\right)\leq-\eta_i\left|s_i\right| \quad i=1,\cdots,3 \tag{23}$$

To alleviate the chattering problem associated with the switching terms, the $\mathrm{sgn}\left(s_i\right)$ functions are replaced by the saturation functions $sat\left(s_i/\Phi_i\right)$ where Φ_i is the thickness of the boundary layer surrounding the i^{th} sliding surface.

4 Digital Simulation Results

The purpose of the digital simulations is twofold. First, it focuses on examining the capability of the nonlinear six degree-of-freedom model in predicting the ship response in maneuvering tasks. Second, it serves to assess the performance of the proposed nonlinear robust controller in the presence of significant modeling uncertainties and environmental disturbances. Throughout this study, the simulations results were generated based on a barge of 100 m in length, 20 m in beam and 4.8 m in draft. The duration of the simulation was selected to be 300 sec. All initial conditions of the marine vessel were set to zero. The wind speed was considered to be 30 m/sec and the current speed was defined to be 1 m/sec. Moreover, the Modified Pierson-Moskowitz wave spectrum, discussed in Section 2 and shown in Fig. 2, was used in the simulation.

In assessing the performance of the six degree-of-freedom model, a two-segment maneuver was used. The first segment consisted of a straight line with the ship sailing in a following sea. The second segment is a turning-circle maneuver with the wave encounter angle varying based on the instantaneous heading of the ship. The propeller thrust, F_{th}, was kept constant at its maximum value of 5×10^7 N, while the rudder angle of attack, α_r, was assigned 0^o and 25^o values in the first and second segments of the maneuver, respectively. The simulation results are illustrated in Fig. 4. The tactical diameter, D_T (see Fig. 4), is found to be 340.6 m. Its corresponding non-dimensional tactical diameter is computed from $D_T^{'}=\left(D_T\left|\alpha_r\right|/35L_{pp}\right)$ and determined to be 2.43, which agrees with experimental data provided by Lewis (1988) and Barr et al. (1981) for ships of comparable geometric dimensions and weight. Furthermore, ships undergoing turning-circle maneuvers are expected to exhibit lateral drifts (Lewis, 1988). This fact is confirmed in Fig. 4, which reveals a lateral drift, L_D, of 4.5 m.

Next, the performance of the robust controller is assessed by considering the reduced-order model described in Eq. (20). The desired trajectory is a straight line parallel to the X-axis. The desired Y-coordinate is kept constant at 10 m while the desired yaw angle is set to zero. The desired ship velocity profile in the surge direction involves an acceleration period, a constant velocity period, and a

deceleration period (see Fig. 5). The initial location of the ship is selected to be away from the desired trajectory. Therefore, the task of the controller is to ensure that the ship converges and tracks the desired trajectory in the presence of modeling uncertainties and external disturbances. It should be stressed that the nonlinear reduced-order model of the ship, accounts for the effects of inertial forces, nonlinear restoring forces, wave-induced excitations, retardation forces,

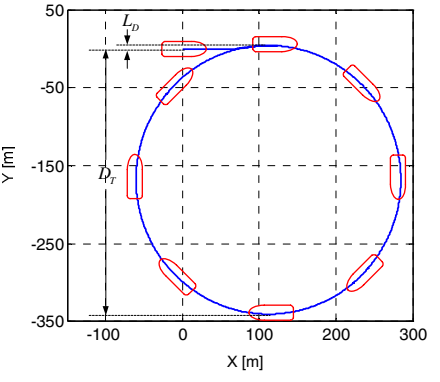

Fig. 4 Turning-circle maneuver of the ship

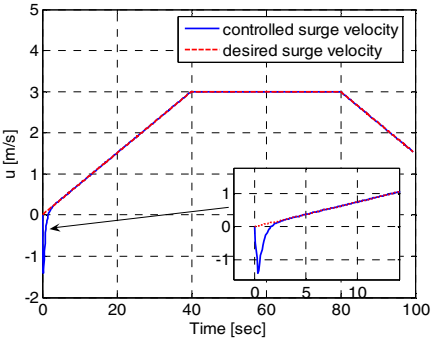

Fig. 5 Desired and actual ship responses in surge

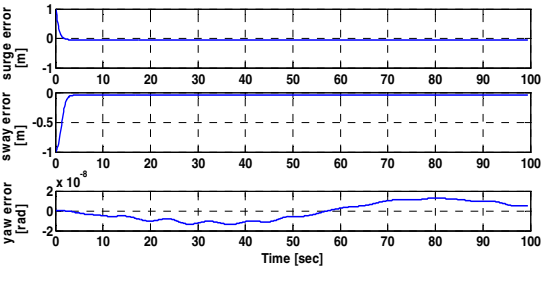

Fig. 6 Tracking errors in surge, sway and yaw

wind and current loads. The results, shown in Figs. 5 and 6, demonstrate the robustness and the good tracking characteristic of the proposed controller. The steady-state errors shown in Figs. 5 and 6 stem from the boundary layers surrounding the sliding surfaces used in the design of the controller. The magnitude of the errors is directly impacted by the selected thickness of the boundary layers.

5 Summary

A nonlinear six degree-of-freedom dynamic model has been developed for the purpose of control of marine surface vessels. The formulation closely follows the existing literature on ship modeling. It accounts for the effects of inertial forces, wave excitation forces, retardation forces, nonlinear restoring forces, wind and current loads. This model has been used herein to predict the response of the ship in a turning-circle maneuver. Furthermore, a nonlinear robust controller has been developed based on a reduced-order model that takes into consideration the surge, sway and yaw motions of the ship. The system is considered to be fully actuated. The simulation results demonstrate the robustness and good tracking characteristic of the proposed controller.

Acknowledgment. The authors would like to acknowledge the financial support provided by the ONR grant under Award No.: N00014-05-1-0040. Dr. Kelly B. Cooper is the Program Director.

References

Abbott, I.A., Von Doenhoff, A.E.: Theory of Wing Sections, Including a Summary of Airfoil Data. Dover Publications Inc., New York (1958)

Barr, R.A., Miller, E.R., Ankudinov, V., Lee, F.C.: Technical Basis for Maneuvering Performance Standards. U.S. Coast Guard Report CG-8-81, NTIS ADA 11474 (1981)

Berge, S.P., Ohtsu, K., Fossen, T.I.: Nonlinear Control of Ships Minimizing the Position Tracking Errors. In: Proceedings of the IFAC Conference on Control Applications in Marine Systems (CAMS 1998), Fukuoka, Japan, pp. 141–147 (1998)

Blanke, M.: Ship Propulsion Losses Related to Automatic Steering and Prime Mover Control, Technical University of Denmark, Denmark (1982)

Faltinsen, O.M.: Sea Loads on Ships and Offshore Structures. Cambridge University Press, Cambridge (1990)

Fossen, T.I.: A Survey on Nonlinear Ship Control: From Theory to Practice," Plenary Talk. In: Proceedings of the 5th IFAC Conference on Manoeuvring and Control of Marine Craft, Aalborg, Denmark (2000)

Fossen, T.I.: A Nonlinear Unified State-Space Model for Ship Maneuvering and Control in a Seaway. In: Int. Journal of Bifurcation and Chaos, ENOC 2005, Plenary (2005)

Fossen, T.I., Grøvlen, Å.: Nonlinear Output Feedback Control of Dynamically Positioned Ships Using Vectorial Observer Backstepping. IEEE Transactions on Control Systems Technology 6(1), 121–128 (1998)

Fossen, T.I.: Guidance and Control of Ocean Marine Vehicles. John Wiley and Sons Ltd., New York (1994)

Fossen, T.I.: High Performance Ship Autopilot With Wave Filter. In: Proceedings of the 10th Ship Control System Symposium (SCSS 1993), Ottawa, Canada (1993)

Fossen, T.I., Strand, J.P.: A Tutorial on Nonlinear Backstepping: Applications to Ship Control. Modelling, Identification and Control 20(2), 83–135 (1999)

Fox, R.W., McDonald, A.T.: Introduction to Fluid Mechanics. John Wiley & Sons, New York (1992)

Godhavn, J.M.: Nonlinear Tracking of Underactuated Surface Vessels. In: Proc. 35th Conf. Decision Control Kobe, Japan (1996)

Isherwood, R.M.: Wind Resistance of Merchant Ships. The Royal Institution of Naval Architects 15, 327–338 (1973)

Journée, J.M.J., Massie, W.W.: Offshore Hydrodynamics, Delft University of Technology (2001), http://www.shipmotions.nl/LectureNotes.html

Journée, J.M.J., Pinkster, J.: Introduction in Ship Hydromechanics (2002), http://www.shipmotions.nl/LectureNotes/ShipHydromechanics_Intro.pdf

Kristiansen, E., Hjulstad, Å., Egeland, O.: State Space Representation of Raditation Forces in Time Domain Vessel Models. Oceanic Engineering 32, 2195–2216 (2005)

Kuiper, G.: The Wageningen Propeller Series. MARIN Publication No. 92-001 (1992)

Le, M.D., Tran, Q.T., Nguyen, T.N., Gap, V.D.: Control of Large Ship Motions in Harbor Maneuvers by Applying Sliding Mode Control. In: 8th IEEE International Worshop, Avanced Motion Control, pp. 695–700 (2004)

Lee, C.H., Newman, J.N.: Computation of Wave Effects Using the Panel Method. In: Chakrabarti, S. (ed.). WIT Press, Southhampton (2004)

Lewis, E.V.: Principles of Naval Architecture, 2nd edn. Society of Naval Architects and Marine Engineers, SNAME (1988)

Moreira, L., Fossen, T.I., Guedes Soares, C.: Path Following Control System for a Tanker Ship Model. Ocean Engineering OE-34, 2074–2085 (2007)

Newman, J.N.: Marine Hydrodynamics. MIT Press, Cambridge (1977)

Oil Companies International Marine Forum, OCIMF, Prediction of Wind and Current Loads on VLCCs, Witherby & Co., London (1994)

Ogilvie, T.F.: Recent Progress toward the Understanding and Prediction of Ship Motion. In: The ONR 5th Symp. on Naval Hydrodynamics, Bergen, Norway (1964)

Perez, T.: Ship Motion Control. Springer, Heidelberg (2005)

Pettersen, K.Y., Nijmeijer, H.: Underactuated Ship Tracking Control: Theory and Experiments. International Journal of Control 74(14), 1435–1446 (2001)

Pivano, L., Johansen, T.A., Smogeli, Ø.N., Fossen, T.I.: Nonlinear Thrust Controller for Marine Propellers in Four-Quadrant Operations. In: American Control Conference, New York (2007)

Roddy, R.F., Hess, D.E., Faller, W.E.: Neural Network Predictions of the 4-Quadrant Wageningen B-Screw Series. In: Fifth International Conference on Computer and IT Applications in the Maritime Industries, Leiden, Netherlands (2006)

Slotine, J.J.E., Li, W.: Applied Nonlinear Control. Prentice-Hall, Englewood Cliffs (1991)

Strand, J.P., Ezal, K., Fossen, T.I., Kokotovic, P.V.: Nonlinear Control of Ships: A Locally Optimal Design. In: Preprints of the IFAC NOLCOS 1998, Enschede, The Netherlands, pp. 732–738 (1998)

The Society of Naval Architectures and Marine Engineers, SNAME, 1950, Nomenclature for Treating the Motion of Submerged Body Through a Fluid, 74 Trinity Place, New York, N. Y. 10006.

Ueng, S.K., Lin, D., Liu, C.H.: A Ship Motion Simulation System. Virtual reality 12, 65–76 (2008)

Random Rocking Dynamics of a Multidimensional Structure

Agnessa Kovaleva

Abstract. In this paper we investigate the effect of structural flexibility on rocking motion of a system consisting of a free standing rigid block with an attached chain of uniaxially moving point masses. Motion is excited by random acceleration of the ground; instability is directly associated with overturning of the overall structure. The condition of instability is constructed by the stochastic Melnikov method. As an example, the dynamics of a system with a single-mass secondary structure is discussed. The paper is restricted to the consideration of seismic vulnerability of the structure. A similar approach can be applied to systems with wind or wave loading.

1 Introduction

The classic model for the effect of an earthquake on a rigid block, standing free on its foundation, is due to Housner [1]. For last decades, seismic behavior of a rigid block has been under intensive study see, e.g. [2] - [4] for the detailed review and discussion of various approaches and examples. Among the examples that fit well into such a framework are petroleum storage tanks, concrete radiation shields, water towers, concrete radiation shields, computer-type equipment, etc. The approaches on the subject involve both deterministic and stochastic studies. Different methods of the probabilistic analysis of rocking oscillations are discussed, e.g., in [5] - [7]; a large number of relevant references can be found in [2].

In this paper we examine the effect of flexibility on the dynamics of a rocking structure. As an example, we consider a system designed as a rectangular symmetric rigid block (or a frame) with an embedded chain of point masses coupled by linear visco-elastic suspensions and moving along the vertical axis of symmetry of the block (Fig. 1). We will show that, under some non-restrictive assumptions, the rigid model is acceptable but the basin of stability and the probability of overturning depend on the parameters of the secondary structure.

Note that a precise calculation of the overturning probability is unavailable. Numerical procedures require a large number of combinations of the parameters,

Agnessa Kovaleva
Space Research Institute, Russian Academy of Sciences,
84/32 Profsoyuznaya ul. Moscow 117997 Russia
a.kovaleva@ru.net

R.A. Ibrahim et al. (Eds.): Vibro-Impact Dynamics of Ocean Systems, LNACM 44, pp. 149–160.
springerlink.com

the initial states of the block and the masses, and the intervals of motion; in practice, they are restricted to a rigid block model. The purpose of the present paper is to show that an approximate analysis of the rocking dynamics can be performed by the asymptotic Melnikov method [8], [9], [10]. We will introduce the techniques that can be applied to even broader classes of problems; then we define the domain of stability and calculate the probability of exit from this domain. The solution will be obtained as an explicit function of the parameters of the structure and noise but it is independent of the initial state and the interval of motion.

The landmark Housner model is invoked to describe the rocking dynamics. Assuming rigid foundation, large friction to prevent sliding, and the Newton restitution law at impact, the only possible response of the structure is rocking about the corners of the block accompanied by relative oscillations of the secondary structure. The initiation of the motion is due to an initial impulse. After a system is set to motion, oscillations are sustained by a relatively weak horizontal acceleration $a(t)$ of the ground. We suppose that the excitation is effective in the vertical plane of symmetry, and the planar response is investigated.

The structural model is shown in Fig. 1. We consider a symmetric slender block/frame of width $2r$ and height $2h$, $r << h$. The block has mass M and mass moment of inertia $I = M\rho^2$, where ρ is the radius of inertia with respect to the bottom corner points O_R or O_L. The location of the centre of mass C on the vertical axis of symmetry is determined by the angle α between the right vertical of the block and the segment O_RC; the distance from the bottom corners of the block to the point C is $O_RC = O_LC = L = r/\sin\alpha$; the distance from the base to the point C calculated along the vertical axis of symmetry is $h = L\cos\alpha$.

Fig. 1 Model of the structure

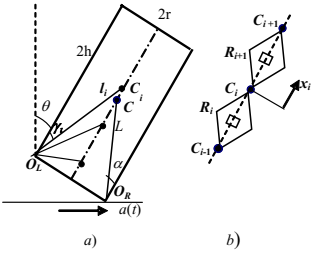

The secondary structure is modelled as a chain of N point mass m_i embedded within the rigid block and connected with each other by visco-elastic suspensions R_i. The stiffness and damping parameters of the *i-th* suspension are denoted by c_i and b_i, respectively. The location of the *i-th* mass C_i at the rest position is determined by the angle γ_i between the left vertical and the segment O_LC_i; the distance from the bottom corners of the block to the point C_i is $l_i = r/\sin\gamma_i$; the distance from the base along the axis of symmetry is $h_i = l_i\cos\gamma_i$. The angular displacement from vertical is denoted by θ. The coordinate $x_i = r\xi_i$ describes the dimensionless displacement of the *i-th* mass along the vertical axis of symmetry; $\xi_0 = \xi_{N+1} = 0$. Ground acceleration $a(t)$ is presumed to be a zero-mean stationary Gaussian process.

In an industrial environment, it is unlikely that any free-rocking structure would be undamped. Pipework or electrical cables inside the structure as well as the air resistance contribute to the damping in the "smooth" motion between impacts [4]. In this paper, damping of the rigid block is assumed to be negligible against small dissipation at impact and in the secondary structure; an angular moment produced by the response of the visco-elastic suspension is assumed to be small against the moment of the gravitation force. Under these assumptions, the dynamic response of the visco-elastic suspension can be interpreted as weak forcing.

Using this model, we demonstrate that the leading order equation of tracking motion describes the dynamics of a conservative sdf rocking oscillator with additional fixed masses. The boundary of the basin of stability of the overall structure is associated with the separatrix of the rocking oscillator. We assume that an initial impulse alone is unable to produce overturning but the magnitude of rocking oscillations is close to a limiting value. Under these assumptions, weak noise helps to bring about transitions across the boundary of the stability region, i.e., to induce overturning. The necessary condition of the separatrix-crossing is given by the Melnikov criterion, established for a planar systems with periodic perturbations [8] and then extended to systems with polyharmonic [9] and random [10] perturbations. Earlier the Melnikov approach has been applied to the study of the rocking response of a rigid object to earthquakes [6] but the effect of structural flexibility has not been investigated. Here we construct the stochastic Melnikov criterion for a flexible rocking structure subjected to random excitation.

The paper is organized as follows. Section 2 contains the governing equations together with the necessary notations. In Section 3 we investigate the periodic motion of the structure in the absence of noise, construct the separatrix of rocking oscillations, and find the corresponding response of the secondary structure. Section 4 introduces the Melnikov condition of instability and investigates the effect of the secondary structure on the system stability.

2 Mathematical Model

The Euler-Lagrange equations of motion between the consecutive impacts are

$$I\ddot{\theta} + \sum_{i=1}^{N} m_i r^2(\ddot{\theta} + \ddot{\xi}) - \{MgL\sin(\theta - \alpha\operatorname{sgn}\theta) + \sum_{i=1}^{N} m_i g[l_i\sin(\theta - \gamma_i\operatorname{sgn}\theta)$$

$$r\xi_i\sin|\theta]\} = -a(t)\{ML\cos(\theta - \alpha\operatorname{sgn}\theta) + \sum_{i=1}^{N} m_i[l_i\cos(\theta - \gamma_i\operatorname{sgn}\theta) + r\xi_i\cos\theta]\} \quad (1a)$$

$$r[m_i(\ddot{\theta} + \ddot{\xi}) + (c_i + c_{i+1})\xi_i - (c_{i-1}\xi_{i-1} + c_{i+1}\xi_{i+1}) + (b_i + b_{i+1})\dot{\xi}_i - (b_{i-1}\dot{\xi}_{i-1} +$$

$$b_{i+1}\dot{\xi}_{i+1} = m_i g(\cos\theta - 1) + m_i a(t)\sin\theta, \ i = 1,\ldots, N, \quad (1b)$$

At the moment of impact, the Newton restitution law is applied

$$t = t^*, \ \theta = 0, \ \dot{\theta}_+ = \kappa\dot{\theta}_-, \quad (2)$$

where $\kappa \in (0, 1]$ is the restitution coefficients, $\dot{\theta}_{\pm}(t^*) = \dot{\theta}(t^* \pm 0)$. The impact response of the ground can be formalized as [11], [12]

$$R_{\text{imp}}(\theta, \dot{\theta}) = -(1 - \kappa)\dot{\theta}\,|\dot{\theta}|\,\delta_{-}(\theta). \tag{3}$$

where $\delta_{-}(\theta) = \delta(\theta - 0)$ is the "left" Dirac δ-function. In this paper we consider a slender block. As indicated in [4], the effect of "slenderness" of the block is not significant in the Melnikov analysis but this assumption allows linearizing the equation of motion between the consecutive impacts For a slender block, the characteristic quantities of the system are $|\theta| << 1$, $\alpha << 1$, $\gamma_i << 1$, $(r/\rho)^2 = \varepsilon << 1$. In particular, this implies $\sin\theta \approx \theta$, $\cos\theta \approx 1$, etc. Assuming weak excitation and weak dissipation at impact and introducing the small parameter ε, we write $1 - \kappa = \varepsilon k$, $a(t) = \varepsilon g\zeta(t)$, where g is gravity acceleration. Using the new notations, we rewrite (3) in the form

$$R_{\text{imp}}(\theta, \dot{\theta}) = -\varepsilon k\dot{\theta}\,|\dot{\theta}|\,\delta_{-}(\theta) = \varepsilon R_1(\theta, \dot{\theta}). \tag{4}$$

Linearization of Eqs (1) with respect to small angles θ, α, γ_i and substitution of the contact force (4) in the right hand side of (1) reduce Eqs (1), (2) to the form

$$\ddot{\theta} - n_1^2\theta = -\alpha_1 n^2 \operatorname{sgn}\theta - \varepsilon n_1^2\zeta(t) + \varepsilon R_1(\theta, \dot{\theta}) + \varepsilon R_2(\ddot{\theta}, \ddot{\xi}) + o(\varepsilon) \tag{5a}$$

$$\ddot{\xi}_i + (\Omega_i^2 + \Omega_{i,i+1}^2)\xi_i - (\Omega_{i,i-1}^2\xi_{i-1} + \Omega_{i,i+1}^2\xi_{i+1}) + (\beta_i + \beta_{i,i+1})\dot{\xi}_i - (\beta_{i,i-1}\dot{\xi}_{i-1} + \beta_{i,i+1}\dot{\xi}_{i+1}) = -\ddot{\theta} + o(\varepsilon),\ i = 1, \ldots, N, \tag{5b}$$

where we denote

$$n^2 = MgL/I = gL/\rho^2,\ n_1^2 = n^2(1 + \lambda),\ \alpha_1 = \alpha(1 + \mu),$$

$$\lambda = \sum_{i=1}^{N}\mu_i\eta_i,\ \mu = \sum_{i=1}^{N}\mu_i,\ \mu_i = m_i/M,\ \eta_i = h_i/h,$$

$$\Omega_{i,k}^2 = c_k/m_i,\ \Omega_{i,i}^2 = \Omega_i^2 = c_i/m_i,\ \beta_{i,k} = b_k/m_i,\ \beta_{i,i} = \beta_i = b_i/m_i.$$

The impact response R_1 and the response of the secondary structure R_2 are written as

$$R_1(\theta, \dot{\theta}) = -k\dot{\theta}\,|\dot{\theta}|\,\delta_{-}(\theta), \quad R_2(\ddot{\theta}, \ddot{\xi}) = -\sum_{i=1}^{N}\mu_i(\ddot{\theta} + \ddot{\xi}_i). \tag{6}$$

Sufficient dissipation in the secondary structure allows avoiding undesirable resonance oscillations of high magnitude. In the absence of resonance, the effect of the secondary structure on the rocking response is small; it is characterized by the small parameter ε (Eq. (5*a*)).

3 Periodic Motion of the Structure

In this section we construct a boundary of stability and find a response of the secondary structure corresponding to rocking oscillations near this boundary. If $\varepsilon = 0$, Eq (5a) is independent of relative oscillations of the secondary structure. This implies that the boundary of the basin of stability corresponds to the separatrix of the conservative rocking oscillator

$$\ddot{\theta} - n_1^2\theta = -\alpha_1 n^2 \operatorname{sgn}\theta, \quad \theta = 0, \quad \dot{\theta}_+ = \dot{\theta}_- . \tag{7}$$

The Melnikov criterion requires calculating the responses R_1 and R_2 of the system moving along the separatrix. The complexity of the problem is associated with the existence of a planar separatrix S: $\{\Theta(t), \dot{\Theta}(t)\}$ in an $(N + 2)$-dimensional system. In order to calculate the response R_2, we construct the separatrix $\Theta(t)$, $\dot{\Theta}(t)$ as a limiting periodic solution $\theta^{\mathrm{T}}(t)$, $\dot{\theta}^{\mathrm{T}}(t)$ of Eq. (7) as $T \to \infty$. In this case, the corresponding response $\Xi(t)$, $\dot{\Xi}(t)$ of the secondary structure can be found as a limit as $T \to \infty$ of the periodic solution $\xi^{\mathrm{T}}(t)$, $\dot{\xi}^{\mathrm{T}}(t)$ to the system

$$\ddot{\xi}_i + (\Omega_i^2 + \Omega_{i,i+1}^2)\xi_i - (\Omega_{i,i-1}^2 \xi_{i-1} + \Omega_{i,i+1}^2 \xi_{i+1}) + (\beta_i + \beta_{i,i+1})\dot{\xi}_i -$$

$$(\beta_{i,i-1}\dot{\xi}_{i-1} + \beta_{i,i+1}\dot{\xi}_{i+1}) = -\ddot{\theta}^{\mathrm{T}}(t), \quad i = 1,\ldots, N. \tag{8}$$

1. The periodic motion of the rocking oscillator. The conservative system (7) exhibits multiple periodic solutions. In this paper, we analyze the most intensive antisymmetric T - periodic motion with the $T/2$-interval between impacts. We construct this solution by the integral equations method [13], [14]. In order to apply this approach, we reduce the equations of motion to the operator form [15]. We denote the differential operator d/dt by s and rewrite a linear differential equation as an algebraic equation depending on the parameter s. As a result, we obtain the equation in the symbolic form

$$X = L(s)\Phi, \tag{9}$$

where $L(s)$ is the transfer function (the dynamic admittance operator) from an input Φ to an output X [14], [15]. Formally, Eq. (9) connects the Laplace transforms of $X(t)$ and $\Phi(t)$ [15]. Informally, one can consider (9) as a symbolic representation of a relevant differential equation.

Let $\Phi(t)$ be an antisymmetric T - periodic function such that $\Phi(t + T/2) = -\Phi(t)$; then the corresponding T-periodic antisymmetric response $X^{\mathrm{T}}(t)$ is calculated as [13], [14]

$$X^{\mathrm{T}}(t) = \int_0^{T/2} \chi^T(t-s)\Phi(s)ds\,, \; 0 < t < T/2, \tag{10}$$

where the kernel $\chi^T(t)$ is defined by the Fourier series

$$\chi^T(t) = \frac{2}{T}\sum_{k=-\infty}^{\infty} L[(2k+1)i\omega]\exp[(2k+1)i\omega t], \quad \omega = \frac{2\pi}{T}\,, \; i = \sqrt{-1}\,. \tag{11}$$

The function $\chi^T(t)$ is referred to as the *periodic Green function* (*pGf*) of the second kind satisfying the condition $\chi^T(t + T/2) = -\chi^T(t)$ [13], [14].

If $L(s) = m(s)/d(s)$, where $m(s)$ and $d(s)$ are polynomials of order m and $d > m$, respectively, and s_r is a simple root of the equation $d(s) = 0$, then the series (11) can be presented in the closed form [13], [14]

$$\chi^{\mathrm{T}}(t) = \sum_{r=1}^{d} \frac{m(s_r)}{d'(s_r)} \frac{\exp(s_r t)}{1+\exp(s_r T/2)}, \quad 0 < t < T/2, \tag{12}$$

where $d'(s_r)$ is the derivative of the polynomial $d(s)$ at $s = s_r$. Extensions to the intervals $(l-1)T/2 < t < lT/2$ ($l = 2, 3,\ldots$) are defined by the condition $\chi^{\mathrm{T}}(t + T/2) = -\chi^{\mathrm{T}}(t)$.

We now apply formulas (10), (12) to Eq. (7). Considering the moment of an initial impact as $t = 0$ and assuming $\theta(t) > 0$, $0 < t < T/2$, $\theta(t) < 0$, $T/2 < t < T$, $\theta(T/2) = 0$, we rewrite the equation of the unperturbed motion in the form

$$\ddot{\theta} - n_1^2\theta = \alpha_1 n^2 \operatorname{sgn}(t - T/2),\ 0 < t < T. \tag{13}$$

It follows from (10), (13) that the T-periodic solution of Eq (13) can be written as

$$\theta^{\mathrm{T}}(t) = -\alpha_1 n^2 \int_0^{T/2} \chi^T(t-s)ds,\ 0 < t < T/2.$$

$$\theta^{\mathrm{T}}(t) = \alpha_1 n^2 \int_0^{T/2} \chi^T(t-s)ds,\ T/2 < t < T. \tag{14}$$

Using (12), we obtain the periodic Green function $\chi^{\mathrm{T}}(t)$ for the operator $L(s) = (s^2 - n_1^2)^{-1}$ as

$$\chi^{\mathrm{T}}(t) = \frac{1}{2n_1} \frac{\sinh n_1(t - T/4)}{\cosh n_1 T/4},\ 0 < t < T/2. \tag{15}$$

Now, from (14), (15) we easily obtain the closed-form solution

$$\theta^{\mathrm{T}}(t) = \varphi\left[1 - \frac{\cosh n_1(t - T/4)}{\cosh n_1 T/4}\right], \quad 0 < t < T/2, \tag{16a}$$

where $\varphi = \alpha_1(n/n)^2$. In a similar way, we find

$$\theta^{\mathrm{T}}(t) = \varphi\left[\frac{\cosh n_1(t + T/4)}{\cosh n_1 T/4} - 1\right],\ T/2 < t < T. \tag{16b}$$

The periodic antisymmetric extension to the intervals $(l-1)T/2 < t < lT/2$ is defined by the condition $\theta^{\mathrm{T}}(t + T/2) = -\theta^{\mathrm{T}}(t)$.

2. The basin of stability. Denote by $\theta_+^{\mathrm{T}}(t)$ and $\theta_-^{T}(t)$ the segments of the orbit (16*a*) and (16*b*) corresponding to $\dot{\theta}^{\mathrm{T}}(t) > 0$ and $\dot{\theta}^{\mathrm{T}}(t) < 0$, respectively. Taking the limit as $T \to \infty$, we obtain the corresponding segments of the separatrix

$$\Theta_{\pm}(t) = \lim_{T\to\infty} \theta_{\pm}^{\mathrm{T}}(t) = \pm\varphi[1 - \exp(-n_1|t|)]\mathrm{sgn}t,$$

$$\dot{\Theta}_{\pm}(t) = \lim_{T\to\infty} \dot{\theta}_{\pm}^{\mathrm{T}}(t) = \pm\varphi n_1 \exp(-n_1|t|), -\infty < t < \infty. \qquad (17)$$

The functions (17) coincide with the branches of the homoclinic separatrix obtained by a standard way [2], [3]. The phase portrait of system (7) is shown in Fig. 2. The domain of bounded oscillations is circumscribed by the diamond-shape separatrix (17). Escape from the inner domain of bounded oscillations to the outer area of unbounded motion corresponds to overturning.

Fig. 2 Phase portrait of the rocking oscillator

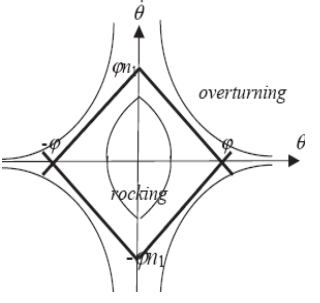

It follows from (17) that the critical angular displacement $\varphi = \alpha_1 n^2/n_1^2$ and velocity $\omega = \varphi n_1$ have the form

$$\varphi = \alpha\frac{1+\mu}{1+\lambda}, \ \omega = \alpha n \frac{1+\mu}{(1+\lambda)^{1/2}}.$$

We now investigate the effect of the secondary structure on the size of the basin of stability. Consider the following special cases:

1). $\mu > \lambda$. This inequality holds if the point masses are concentrated near the bottom of the block, far below the centre *C*, so that $\eta_i << 1$, $\lambda << \mu$. In this case $\varphi > \alpha$, $\omega > \alpha n$ (Fig. 3*a*). This implies that the admissible values of the angular displacement and velocity of the structure exceed the similar parameters for a single rigid block of the same configuration and mass.

2). $(1 + \mu)^2 < 1 + \lambda$. This inequality when the point masses are located near the top of the block, far above *C*, so that $\eta_i >> 1$. In this case $\varphi < \alpha$, $\omega < \alpha n$ (Fig. 3*b*) , that is admissible values of the angular displacement and velocity for the structure are less than for the rigid block.

3). $1+\mu < 1 + \lambda < (1 + \mu)^2$. In this intermediate case, $\varphi < \alpha$ but $\omega > \alpha n$ (Fig. 3*c*). Hence, the admissible angular displacement for the structure is less than for the rigid block but the angular velocity of the structure may exceed the admissible velocity of the block.

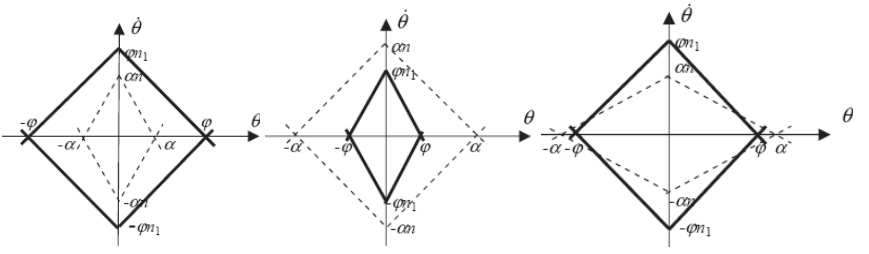

a) *b)* *c)*

Fig. 3 Separatrix of the rigid block (dashed line) and block-like structure (solid line)

3. The response of the secondary structure. The Melnikov analysis requires calculating the dynamic responses R_1 and R_2 in the system moving along the separatrix. The impact response R_1 is obtained by the direct substitution of (17) into formula (6). In order to calculate the dynamic response R_2, it is necessary to construct the solution $\Xi_{\pm}(t)$ of (8) corresponding to the segments $\Theta_{\pm}(t)$ of the separatrix (17). As an example, we find this solution for a single-mass secondary structure ($N = 1$). An extension to a multidimensional case is obvious.

We take $c_1 = c_2 = c$, $b_1 = b_2 = b$ and denote $\xi_1 = \xi$, $m_1 = m$, $c/m = \Omega^2/2$, $b/m = \beta/2$. In addition, we accept a commonly used assumption $\beta/\Omega < 1$. In these notations, system (8) is reduced to the form

$$\ddot\xi^{\mathrm{T}} + \beta\dot\xi^{\mathrm{T}} + \Omega^2\xi^{\mathrm{T}} = -\ddot\theta^{\mathrm{T}}(t), \tag{18}$$

or, in the operator form,

$$\xi^{\mathrm{T}} = L(s)F^{\mathrm{T}},\ L(s) = \frac{s^2}{(s^2 + \beta s + \Omega^2)(s^2 - n^2)}. \tag{19}$$

where $F^{\mathrm{T}}(t) = \alpha_1 n^2 \mathrm{sgn}(t - T/2)$, $0 < t < T$. The limiting response $\Xi(t)$ is calculated as $\lim\xi^{\mathrm{T}}(t)$ as $T \to \infty$. In order to calculate $\Xi(t)$ we use formulas (10) – (14), in which $X^{\mathrm{T}}(t) = \xi^{\mathrm{T}}(t)$, $\Phi^{\mathrm{T}}(t) = F^{\mathrm{T}}(t)$, $L(s)$ is defined by (19), and then take the limit as $T \to \infty$. Skipping intermediate transformations and ignoring the terms $o(\beta/\Omega)$, we obtain the limiting solution in the close form

$$\Xi_{\pm}(t) = \pm\psi_1[\exp(-n_1|t|) - \exp(-\beta|t|)\cos\Omega t]\mathrm{sgn}t \mp \beta\psi_2\exp(-\beta|t|)\sin\Omega t,\ -\infty < t < \infty,$$

$$\psi_1 = \frac{\varphi n_1^2}{\Omega^2 + n_1^2} = \frac{\alpha_1 n^2}{\Omega^2 + n_1^2},\ \ \psi_2 = \frac{2\Omega\psi_1}{\Omega^2 + n_1^2}. \tag{20}$$

4 The Melnikov Condition of Stability

In this section, we present some basic ideas of the stochastic Melnikov theory [10] and then employ these results to obtain a criterion of stability for rocking oscillations of a rigid block with an attached mass.

Suppose that $t = 0$ is the moment of impact at which $\theta(0) = 0$, and τ is the phase shift of the excitation $\zeta(t)$ with respect to the initial condition. Then Eq. (5a) can be rewritten as

$$\ddot{\theta} - n_1^2\theta = -\alpha_1 n^2 \operatorname{sgn}\theta + \varepsilon R(t+\tau, \theta, \dot{\theta}, \ddot{\theta}, \ddot{\xi}), \tag{21}$$

where $R(t+\tau, \theta, \dot{\theta}, \xi, \dot{\xi}) = -n_1^2\zeta(t+\tau) + R_1(\theta, \dot{\theta}) + R_2(\ddot{\theta}, \ddot{\xi})$. The loss of stability is associated with the transition from the domain of oscillations to the domain of overturning (Fig. 2). The necessary condition of escape through the separatrix is given by the Melnikov inequality [8] – [10]

$$F_{\pm}(\tau) = \int_{-\infty}^{\infty} R_{\pm}(t, \tau)\dot{\Theta}_{\pm}(t)\mathrm{d}t > 0, \tag{22}$$

where $R_{\pm}(t, \tau) = R(t+\tau, \Theta_{\pm}(t), \dot{\Theta}_{\pm}(t), \Xi_{\pm}(t), \dot{\Xi}_{\pm}(t))$. The process $F_{\pm}(\tau)$ is referred to as *the stochastic Melnikov process* generated by system (21); the indices + and – define the Melnikov processes calculated along the respective branches of the heteroclinic orbit.

The probability of overturning is defined as $P_{\text{over}} = \Pr\{F_{\pm}(\tau) > 0\}$. Since the system is symmetric, $F_{-}(\tau) = F_{+}(\tau) = F(\tau)$, and

$$\mathrm{P}_{\text{over}} = \Pr\{F(\tau) > 0\}. \tag{23}$$

In order to avoid ambiguity, we take $F(\tau) = F_{+}(\tau)$ and, hence,

$$\Theta(t) = \Theta_{+}(t), \dot{\Theta}(t) = \dot{\Theta}_{+}(t) > 0\ , \Xi(t) = \Xi_{+}(t),\ \dot{\Xi}(t) = \dot{\Xi}_{+}(t).$$

Let $\zeta(t)$ be a stationary zero mean Gaussian process with covariance $K_{\zeta}(t)$. Then $F(\tau)$ is a stationary Gaussian process with expectation $\phi = \mathbf{E}F(\tau)$ and variance $\sigma^2 = \mathbf{E}[f^2(\tau)]$, where $f(\tau) = F(\tau) - \phi$. The probability of overturning for the Gaussian process is calculated as

$$P_{\text{over}} = \Pr\{F(\tau) > 0\} = 1 - \Phi(-\phi/\sigma), \tag{24}$$

where

$$\Phi(x) = \frac{1}{\sqrt{2\pi}} \int_{-\infty}^{x} \exp\left(-\frac{u}{2}\right)^2 du\ ,\ \Phi(\infty) = 1$$

is standard normal distribution function. It follows from (21), (22) that

$$f(\tau) = -n_1^2 \int_{-\infty}^{\infty} \zeta(t+\tau)\dot{\Theta}(t)\mathrm{d}t\ , \tag{25}$$

and $\phi = \phi_1 + \phi_2$, where

$$\phi_1 = \int_{-\infty}^{\infty} R_1(\Theta(t), \dot{\Theta}(t))\,\dot{\Theta}(t)\mathrm{d}t, \quad \phi_2 = \int_{-\infty}^{\infty} R_2(\ddot{\Theta}(t), \ddot{\Xi}(t))\,\dot{\Theta}(t)\mathrm{d}t. \tag{26}$$

Inserting (6) into (26), we obtain

$$\phi_1 = -k\int_{-\infty}^{\infty} \dot{\Theta}^2(t)\delta(t)dt = -k(\varphi n_1)^2 < 0,$$

$$\phi_2 = -\mu\int_{-\infty}^{\infty} [\ddot{\Theta}(t) + \ddot{\Xi}(t)]\dot{\Theta}(t)dt = -\mu\beta\Omega^2\varphi\psi_2 < 0. \tag{27}$$

If $\zeta(t)$ is white noise with covariance $K_\zeta(t) = \Delta^2\delta(t)$, then

$$\sigma^2 = n_1{}^4 \int_{-\infty}^{\infty} \dot{\Theta}(t)\mathrm{d}t \int_{-\infty}^{\infty} K_\zeta(t-s)\,\dot{\Theta}(s)\mathrm{d}s = n_1{}^4\Delta^2 \int_{-\infty}^{\infty} \dot{\Theta}^2(t)\mathrm{d}t = \varphi^2 n_1{}^5\Delta^2. \tag{28}$$

For a single rigid block we have $\varphi = \alpha$, $n_1 = n$, $\mu = 0$, and, therefore

$$\sigma^2 = \sigma_0{}^2 = \alpha^2 n^5\Delta^2, \ \phi_1 = \phi_0 = -k(\alpha n_1)^2, \ \phi_2 = 0. \tag{29}$$

Formulas (24), (27) imply that dissipation at impact and in the secondary structure diminish both the probability of overturning and the mean value of the Melnikov integral. We now estimate the effect of the mass location on the probability of overturning. For brevity, we let $\phi_2 << \phi_1$. In this case

$$\frac{\phi}{\sigma} = -\frac{k\varphi}{\Delta n_1^{1/2}} = -\frac{k\alpha}{\Delta n^{1/2}}\frac{1+\mu}{(1+\mu\eta)^{5/2}} = \frac{\phi_0}{\sigma_0}\,d, \tag{30}$$

where $d = (1 + \mu)/(1 + \mu\eta)^{5/2}$. We denote by $P_0 = \Phi(-\phi_0/\sigma_0) = \Phi(|\phi_0/\sigma_0|)$ the overturning probability of the rigid block in the absence of an additional mass. It follows from (24), (29) that $P_{\text{over}} > P_0$ if $d < 1$, and $P_{\text{over}} < P_0$ if $d > 1$.

As expected, if the steady-state position C_1 of the mass m is above the mass center of the block C, then $\eta = h_1/h > 1$, $d < 1$, and $P_{\text{over}} > P_0$. If the mass is located under the point C, then $\eta < 1$. Let $\mu = m/M < 1$; then $(1 + \mu\eta)^{5/2} \approx 1 + (5/2)\mu\eta$. This implies that $d < 1$ if $2/5 < \eta < 1$ but $d > 1$ if $\eta < 2/5$. Therefore, if the mass m is situated far below the mass center of the block and $\eta < 2/5$, then the probability of overturning of the structure is less than for the single block, $P_{\text{over}} < P_0$. In the converse case $\eta > 2/5$ we have $P_{\text{over}} > P_0$. We note that the dissipation in the secondary structure diminishes the probability of overturning for the structure. This implies that we may obtain $P_{\text{over}} < P_0$ even if $\eta > 2/5$.

5 Conclusions

We have investigated the effect of structural flexibility on rocking motion of a system consisting of a free standing rigid block with an attached chain of uniaxially moving point masses. Motion is excited by random acceleration of the ground; instability is directly associated with overturning of the overall structure. Whilst an analytic expression for the overturning probability of a strongly nonlinear multidimensional structure is unavailable and numerical approximations are limited to low dimensional problems (i.e., in our setting, to a single rigid block model), an asymptotic analysis may be of help. In this paper we have applied the asymptotic Melnikov method to the analysis of overturning. A twofold effect of the secondary structure on the rocking response has been demonstrated. The attached structure may increase the critical angular displacement and velocity against the similar parameters of the single rigid block. This allows increasing an admissible initial impulse. At the same time, the enlargement of the domain of stability and the modification of the separatrix may enhance the contribution of perturbations in the Melnikov process. As a result, a lower level of random forcing can result in overturning. The model in Fig. 1 is taken as an example. A similar effect of flexibility on the overturning of the overall system can be demonstrated in the case of transversal or shear oscillations of the structure (the latter case is typical for multi-storeys buildings).

Acknowledgments. The work was partially supported by the Russian Foundation for Basic Research (project 08-01-00068).

References

1. Housner, G.W.: The behaviour of inverted pendulum structures during earthquakes. Bull. Seism. Soc. Am. 53, 403–417 (1963)
2. Spanos, P.D., Roussis, P.C., Politis, N.P.A.: Dynamic analysis of stacked rigid blocks. Soil Dynamics and Earthquake Eng. 21, 559–579 (2001)
3. Lenci, S., Rega, G.: Heteroclinic bifurcations and optimal control in the nonlinear rocking dynamics of generic and slender rigid blocks. Int. J. Bifur. Chaos 15, 1901–1918 (2005)
4. Hogan, S.J.: Damping in rigid block dynamics contained between sidewalls. Chaos, Solitons & Fractals 11, 495–506 (2000)
5. Dimentberg, M., Lin, Y.K., Zhang, R.: Toppling of computer-type equipment under base excitation. J. Eng. Mechs 119, 145–160 (1993)
6. Lin, H., Yim, S.C.S.: Nonlinear rocking motions. J. Eng. Mechs. 122, 719–735 (1996)
7. Kovaleva, A.: A reliability-based criterion of structural performance for structures with linear damping. Smart Struct. Syst. 2, 313–320 (2006)
8. Melnikov, V.K.: On the stability of the center for time-periodic perturbations. Trans. Moscow Math. Soc. 12, 1–57
9. Wiggins, S.: Introduction to Applied Nonlinear Dynamical Systems and Chaos. Springer, New York (1997)

10. Simiu, E.: Chaotic Transitions in Deterministic and Stochastic Dynamical Systems. In: Applications of Melnikov Processes in Engineering, Physics and Neuroscience. Princeton University Press, Princeton (2002)
11. Babitsky, V.: Theory of Vibro-Impact Systems and Applications. Springer, New York (1998)
12. Kovaleva, A.: Optimal Control of Mechanical Oscillations. Springer, New York (1999)
13. Rosenwasser, E.: Oscillations of Non-Linear Systems. Nauka, Moscow (1969) (in Russian)
14. Rosenwasser, E., Lampe, B.: Multivariable Computer-controlled Systems: A Transfer Function Approach. Springer, New York (2006)
15. Meirovitch, L.: Dynamics and Control of Structures. Springer, New York (1990)

Dynamic Response of a Marine Vessel Due to Wave-Induced Slamming

Donghee Lee, Kevin Maki, Robert Wilson, Armin Troesch,
and Nickolas Vlahopoulos

Abstract. This paper presents simulation results of the structural response of a surface vessel advancing in head seas. In this particular fluid-structure interaction problem, the discretized geometry in the fluid domain is significantly different than that of the structural model. It is therefore necessary to use interpolation to transfer information between the two domains. In this paper we discuss a numerical procedure to obtain the dynamic response of a marine vessel based on fluid-structure interaction as applied to the test case of the S175 container ship. The vessel is advancing in head seas, and the sea conditions result in bow-flare and bottom impact slamming. The fluid and structure interact in a one-way coupled scheme where the fluid stresses are applied to the structural modal model. The simulation results are compared to previously published experimental data.

1 Introduction

For several decades, fluid-structure interaction (FSI) problems have been studied in many diverse research areas. Examples of problems where fluid-structure coupling is important are reactor-coolant systems, blood flow in an artery, wind flow over a bridge, and flow over aircraft wing. There are many FSI problems that are relevant in the naval research area such as sloshing in a tanker ship, propulsion system, and wave-induced loads on a ship structure.

Traditionally, hydroelasticity has been studied for surface vessels using velocity-potential based methods for predicting the fluid forces, and modal expansion of the ship modeled as a beam to represent the structural response. An authoritative example of such method is presented in (2). One of the valuable attributes of their theory is that it is general or flexible in that different potential flow theories and modal models can be used to describe the hydroelastic response of the structure.

Donghee Lee, Kevin Maki, Armin Troesch, and Nickolas Vlahopoulos
University of Michigan, USA

Robert Wilson
The University of Tennessee Chattanooga, USA

R.A. Ibrahim et al. (Eds.): Vibro-Impact Dynamics of Ocean Systems, LNACM 44, pp. 161–172.
springerlink.com

Throughout the past several decades, there has been a great deal of attention to ship hydroelasticity, where hydrodynamic models of varying complexity have been applied to modal models of a ship. An example of such work, that uses experimental data to corroborate their numerical results, can be found in (10). That paper will be the basis of comparison for our simulation results.

More recently, viscous flow solvers and finite-element (FE) methods have been used on marine fluid-structure interaction problems. For example (9), uses a computational fluid dynamics (CFD) solver that is coupled in a one-way sense to a finite-element solver. They study the two-node vibration mode, and use Lewis forms to estimate the added mass of the water due to the flexure of the ship.

Additionally, water-impact and slamming has been studied from the structural or hydroelastic perspective by many researchers. The article by (4) provides an excellent review of slamming and hydroelasticity for ship problems. Also of note is the paper of (1) that uses a compressible FE solver for the fluid phase to study the free-surface impact of a small-deadrise elastic wedge.

To perform a FSI simulation, governing equations for the structure and fluid domains need to be coupled and solved. These methods have been widely studied in aeroelasticity and categorised into three schemes in the paper of (6). The first is a fully coupled scheme, where the governing equations for both structure and fluid are combined into a single system of equations of motion and solved simultaneously. Consequently, use of this method requires that a new dedicated solver be developed. The second is loosely coupled scheme. In this method, the governing equations are computed using two independent solvers for each domain and information is passed only in one direction, namely the fluid solver provides forcing for the structural model. This method has the advantage that existing solvers can be used to solve the equations at each domain and stability issues that arise when coupling multiphysics solvers are completely avoided. The data is exchanged via an external method after partial or complete convergence, and consequently this scheme may not be effective for highly non-linear problems. The third method is referred to as a closely coupled sheme. This is similar to the loosely coupled scheme in that the governing equations are solved in each domain independently, however, unlike in loose coupling, the solvers are connected into single module and the data is exchanged at the interface or the boundary in both directions. In this way, it is usually necessary to use iteration and often under-relaxation to converge the unified solution in both physics domains.

When using either the loosely or closely coupled scheme, most often there will be two different mesh discretizations corresponding to the different physics domains. Therefore, a method to exchange data across their interface must be implemented. This problem has been studied in great detail by many researchers and the body of literature is vast. (11) offer an overview of different ways to accomplish data transfer.

The present paper describes a simulation process for performing a loosely-coupled fluid-structure interaction simulation on a surface vessel advancing in waves. We use a fully non-linear unstructured viscous CFD solver and couple it with a commercial FE solver. There are two key tasks that must be addressed to

successfully perform a loosely coupled simulation. Firstly, the exchange of data must be accurate and efficient. Fortunately, there are many papers on this subject, and the references of (11; 8; 3; 5) were instructive during the development of our subroutines. And secondly the added mass associated with the flexural deformations must be accounted for in some way. Since the fluid solver does not see any flexural deformation, the pressure or added mass associated with the flexural degrees-of-freedom must be accounted for in the modal model. This is accomplished by discretizing both the water and the ship structure in one finite-element model. By using solid elements for the water, the zero-gravity added mass is captured in the structural analysis and the modal transformation yields the *'wet'* mode shapes and frequencies. We note that our method is very similar to that of (9), but differs in that we use solid elements in the structural model instead of Lewis forms to account for the added mass of the flexural degrees-of-freedom, and we integrate the modal equations of motion instead of the fully coupled FE equations in the physical coordinate.

2 Simulation Process

Our loosely coupled simulation process is shown schematically in Fig. 1. The first step in performing the analysis by the independent solvers is to discretize the relevant geometry. The crucial step in coupling the solvers is the matching of the two grids or defining the association of the elements on each side of the interface (which in this case is the hull shell). These fluid-to-structural-element relationships are used to transfer the fluid stresses to the structural nodal-forces. Since neither the structural or fluid are deforming in time, the association does not change with time and therefore must be performed only once. The CFD simulation is performed to compute the fluid pressures, surface tractions, and motion of the ship as a rigid body. Independently, the structural simulation proceeds to determine the wet modal frequencies and shapes of the complete finite element model. Then, using the predetermined elemental associations between the two domains, the fluid stresses are transferred to the finite element model. Finally, the modal equations of motion are integrated in time to yield the time-domain dynamic response of the vessel.

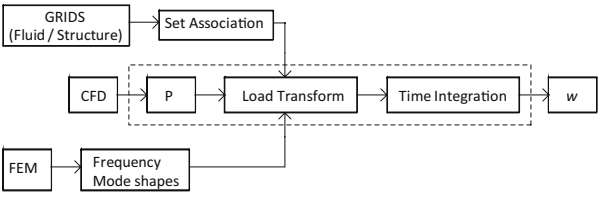

Fig. 1 Overall simulation process

Grid Matching

Two principle methods are used in this work to transform fluid stresses to structural forces. The first is the widely used projection method, and the second relies upon proximity between fluid and structural element pairs. Additionally, a third hybrid method is implemented that simply uses a combination of the first two ideas.

The first method uses the concept of projection of the fluid quantity along the normal of the structrual element that pierces the relevant fluid element. This method was developed in the field of aeroelasticity and several pioneering references that describe its formulation are those of (8), (5) and (3). (8) and (5) suggested an algorithm to match unstructured fluid and structure grids based on the concept of conservation of the load on the interface between fluid and structure. This method requires that each Gauss point in a structure element to be associated with a fluid element. The pressure and viscous stresses are transferred to Gauss points using the pre-defined association relationship that is established by the normal of the structural element. The force at a structure node can be expressed by Eqn. (1) (5).

$$f_i^{(e)} = \int_{\Omega_S^{(e)}} N_i(-p\mathrm{n} + \sigma_F \cdot \mathrm{n})\mathrm{d}s \tag{1}$$

where, n is the normal to the structural element $\Omega_S^{(e)}$, and N_i is the shape function. Using Gaussian quadrature the integration can be expressed as the sum of stress components at the Gauss points (Eqn. 2)

$$f_i^{(e)} = \sum_{g=1}^{g=n_g} w_g N_i(X_g)\,(-p(X_g)\mathrm{n} + \sigma_F(X_g) \cdot \mathrm{n}) \tag{2}$$

where, w_g is the weight of the Gauss point X_g, and n_g is the number of Gauss points used for approximating $f_i^{(e)}$.

When using the original method of (8), the two grids should have piecewise planar elements, and the fluid mesh should entirely envelop the structural mesh. The second condition is necessary since structural elements only search along their positive normal direction for a fluid associate. If any part of the structure grid lies outside of the fluid grid, then those Gauss points will not have have associates. This is the principle drawback in using the original projection method for the current study.

Our analysis is of a typical ship geometry and the different grids were generated by experienced users in their respective fields. Fig. 2 shows the bow region of two grids imposed upon each other, and it can be seen that indeed the fluid grid does not fully envelope the structural grid. A modification to the original method is to use both positive and negative surface normals of a structure element. However, this alternative may result in more that one associate candidate, some of which can be unrealistic, and a decision has to be made as to which of the candidates is most appropriate.

The second method uses the concept of proximity to establish the elemental relationship. Simply, a structural Gauss point is paired the nearest fluid element by

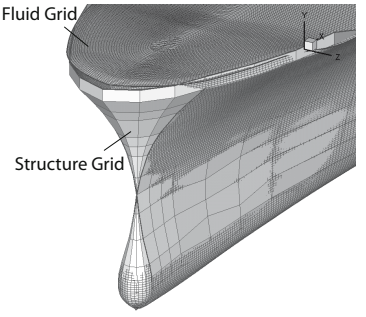

Fig. 2 Comparison of fluid and structure meshes

measuring the distance to the fluid element centroid. This method is known to be robust, though also susceptible to unphysical associations. A favorable attribute of the closest-distance based association is that the false associations will be localized, and presumably less harmful to the accuracy of the data transfer. For example, in the projection method, a structural element normal may barely miss an appropriate fluid element and instead find an element that is on the other side of the ship in a region that is very far from where it should be, whereas the false associations using the proximity condition will always be physically near to where the proper element should be.

A third approach performs the association between the two domains using a combination of the previous two. The projection method is used primarily, but in the case when zero or multiple fluid associates are found, the candidate closest to the Gauss point is chosen.

The performance of the two different association methods is demonstrated in Figures 3 and 4. In Figure 3, a portion of the fluid grid in the region of the bow is shown, along with a single structural grid element. There are four fluid elements that are highlighted in the subfigure on the left where the normal projection method is

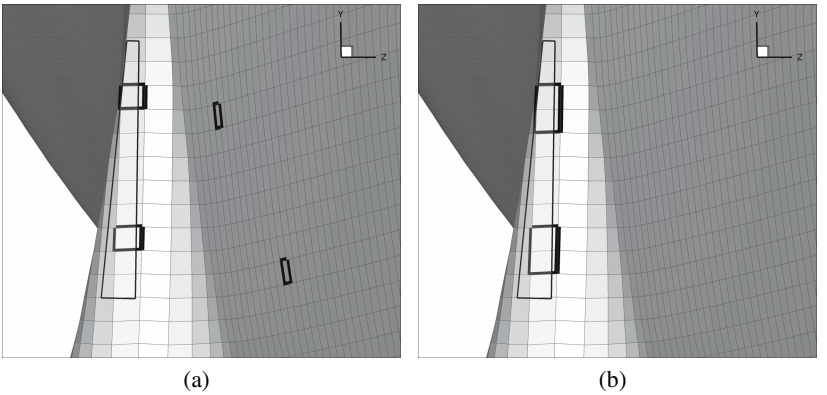

(a) (b)

Fig. 3 Results of associatioin methods: (a) orthogonal projection using positive and negative normals, (b) proximity method

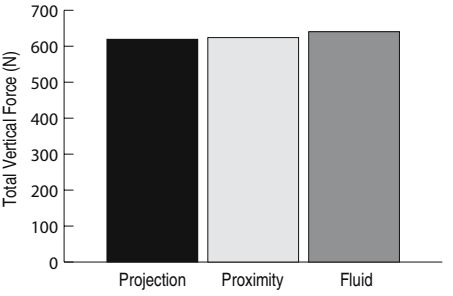

Fig. 4 Comparison of the total vertical force in structure grid and fluid grid. Projection and proximity mean the association method

used. The two fluid associates on the starboard side of the vessel are plausible, while the other two physically are not justifiable. These two outliers were selected by the algorithm while searching along the structural element normal, and in this case fluid elements that are far away from the Gauss point fit the search criteria. Anomalies of this type can be avoided by using the hybrid method previously described. The subfigure on the right shows that the four Gauss points on the structural element chose a total of two fluid elements for its associates, both of which are plausible.

Figure 3 depicts an example of how the the modified projection method can fail. This shortcoming can be easily remedied, as was previously explained, by using a combination of the projection and proximity strategies, though the extra logic and programming does contribute to extra expense in performing completing grid matching process. In Figure 4, the total force on the vessel is plotted for both the projection and proximity methods along with the force on the original fluid grid. It can be seen that the proximity method does outperform the projection method, though the difference is quite small. In this case, the false associations are practically negligible from the viewpoint of total force. The proximity method is used for all further results in this paper.

Dynamic Response of a Structure

The dynamic response of the ship is solved using modal transient analysis. The general equations of motion can be written in standard form as,

$$[M]\ddot{\mathbf{x}} + [K]\mathbf{x} = \mathbf{F} \tag{3}$$

where, $\ddot{\mathbf{x}}, \mathbf{x}$ are the nodal acceleration and displacement respectively, and $\mathbf{F}$ is the nodal force. The displacement and acceleration can be transformed from nodal to modal coordinates by using the modal matrix of eigenvectors. Successive pre-multiplication of the transpose of the eigenvector matrix transforms the equation of motion to modal coordinate.

$$[I]\ddot{\mathbf{Z}} + [\Omega^2]\mathbf{Z} = \mathbf{R} \tag{4}$$

where, **R** is modal force, **Z** is modal displacement, Ω contains the natural frequencies. Eqn. 4 becomes a n-independent system of linear equations for modal displacement z_i.

$$\ddot{z}_i(t) + \omega_i^2 z_i(t) = r_i(t) \quad i = 1, 2, ..., n \tag{5}$$

where, i is mode number. The modal equations of motion are integrated in time using the Newmark-β method (7). Once the nodal displacement **z** is obtained, the physical displacement of the structure nodes can be computed using the same transformation.

Fluid Solver

In this study we employ the CFD program *Tenasi*, which was developed at the University of Tennessee at Chattanooga SimCenter. *Tenasi* is a unstructured flow solver that can simulate multiple regimes consisting of fully compressible, arbitrary Mach number, or fully incompressible flow. In this application, the incompressible Navier-Stokes equations are solved while allowing variable viscosity and density. The volume-of-fluid method is used to solve for multiple phases, and the artificial-compressibility approach is used to couple the velocity and pressure solutions. The non-dimensional continuity, Reynolds-Averaged Navier-Stokes, and volume fraction equations are given as:

$$\frac{1}{\rho\beta}\frac{\partial}{\partial\tau}\left(P + \frac{\rho y}{Fr^2}\right) + \frac{\partial u_i}{\partial x_i} = 0 \tag{6}$$

$$\rho\frac{\partial u_i}{\partial\tau} + \frac{\partial(\rho u_i u_j)}{\partial x_j} + u_i\Delta\rho\frac{\partial\alpha}{\partial\tau} = -\frac{\partial P}{\partial x_i} + \frac{1}{Re}\frac{\partial\tau_{ij}}{\partial x_j} - \frac{\rho}{Fr^2}\frac{\partial x_i g_i}{\partial x_i} \tag{7}$$

$$\frac{\partial\alpha}{\partial\tau} + \frac{\partial(\alpha u_j)}{\partial x_j} + \frac{\alpha}{\rho\beta}\frac{\partial}{\partial\tau}\left(P + \frac{\rho x_i g_i}{Fr^2}\right) = 0 \tag{8}$$

where x_i, u_i, and g_i are the Cartesian coordinate, velocity vector, and gravity vector. The Reynolds and Froude numbers are $Re = UL/\nu$ and $Fr = U/\sqrt{gL}$ respectively, α is the volume fraction variable, and P is the total pressure. The Reynolds stress-tensor is modeled using the Boussinesq approximation and the Spalart-Allmaras one-equation turbulence model. Further details on the flow solver can be found in (12) and (13).

The rigid body equations of motion are solved using a four-variable quaternion approach where the quaternion-rate equation is integrated using a four-stage Runge-Kutta scheme.

3 Simulation and Results

A case with large amplitude waves is chosen to simulate the dynamic response of ITTC tanker ship (S175). The pressure, viscous stress and rigid body motion is computed by the fluid solver for regular incident head-waves at $Fr = 0.2$ and

$Re = 2.6M$. Simulation results are shown here corresponding to wave amplitudes of $A/L = 0.0142$ with wavelength $\lambda/L = 1.0$. This condition corresponds to case 9 from (10).

Ship Geometry

Fig. 5 shows a schematic of the model ship used in the experiment of (10). The geometric scale ratio was 1-to-70 and the experiments were conducted in the ballast condition. The model was divided into four segments and the segments were interconnected with flexible bars. The vertical shear forces and bending moments were measured via strain gauges attached on the connectors. Fig. 5 shows the longitudinal positions of the strain gauges and Table 1 summarizes the principal particulars of the model ship.

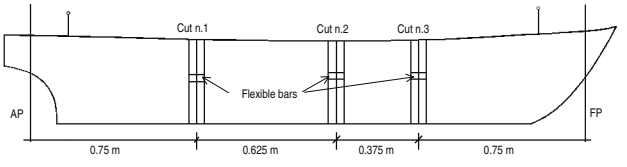

Fig. 5 Schematics of the container ship used in the experiment (10)

Table 1 Principal particulars of the model ship

L_{pp} (m)	2.5
B (m)	0.363
T (m)	0.10
m (kg)	48.8
LCG(% L_{pp} aft of midship)	0.8
Pitch radius of gyration (m)	0.61

Natural Frequencies and Mode Shapes

The wet natual frequencies and mode shapes were obtained using the commercial finite-element solver ABAQUS. Fig. 6 depicts the finite-element model where the shell elements modeling the hull, and the solid elements modeling the water can be seen. In order to match the weight and mass-moment-of-inertia of the experiment, there are 21 concentrated masses distributed longitudinally along the line formed by the intersection of the calm-water plane and vessel center-plane. A no-reflection condition is applied on the outer-surface of the half cylinder to simulate semi-infinite extent of the water, and a total reflection condition is applied to the boundary of the water elements in the calm-water plane. The material properties used in the FE model are summarized in Table 2.

Fig. 7 contains the comparison between the experimentally-measured and finite-element-predicted modal results. The experiment utilized decrement tests to identify

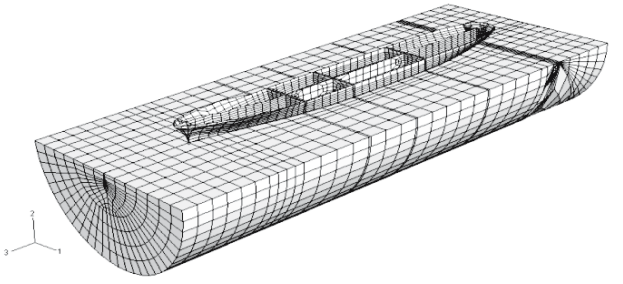

Fig. 6 ABAQUS finite-element model

Table 2 Material properties used in the FE model

	Structure	Elastic Connector	Fluid
Density (kg/m^3)	0.01	1200	997
Young's modulus (GPa)	17000	14	2.2
Poisson ratio	0.29	0.29	N/A

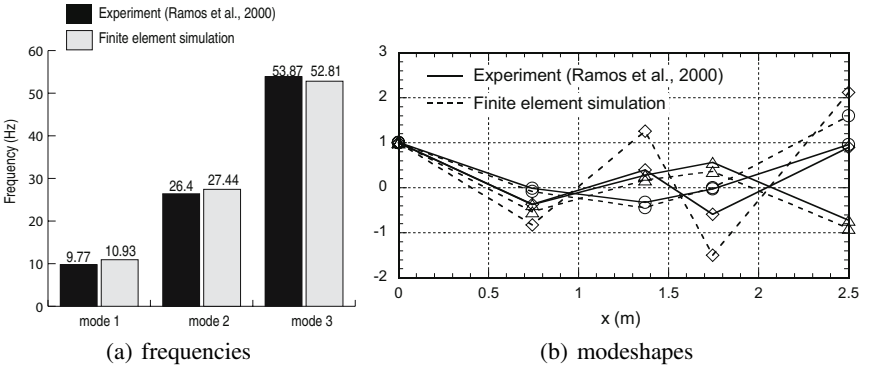

(a) frequencies (b) modeshapes

Fig. 7 Comparison of modal frequencies and shapes. (a) solid bar: (10), lightly shaded bar: present work (b) solid lines: (10), dashed-lines: present work, ◯: mode 1, △: mode 2, ♢: mode 3

the modal frequencies and shapes. The decrement tests were performed in water, so the results correspond to the zero-speed calm-water *'wet'* modes. The subfigure on the left shows the values of the first three natural frequencies. In general the agreement is sufficient to confirm that our solid elements properly account for the added mass of the flexural modes. The subfigure on the right shows the corresponding three mode shapes. The first two modes are closely matched between experiment and prediction. The third mode has the same shape in both cases, but the amplitude of the prediction is larger than that of experiment.

Vertical Bending Moment

Fig. 8 shows the time series of vertical bending moment at first two inter-segment connectors. The environmental condition (wave steepness) results in bottom-impact slamming that occurs around the time of 0.1 s, and the large negative moment around time of 0.45 s coincides with bow-flare slamming. The results show that the maximum dynamic stress is due to the excitation of the first mode in the short time duration bottom-impact slam, and the large negative bending moment of the bow immersing at the frequency of wave-encounter. The simulation estimates the maximum negative bending moment to within approximately 15% of the experimental value. The whipping response is dominated by the fundamental mode, and its amplitude and frequency closely matches the experimental measurement.

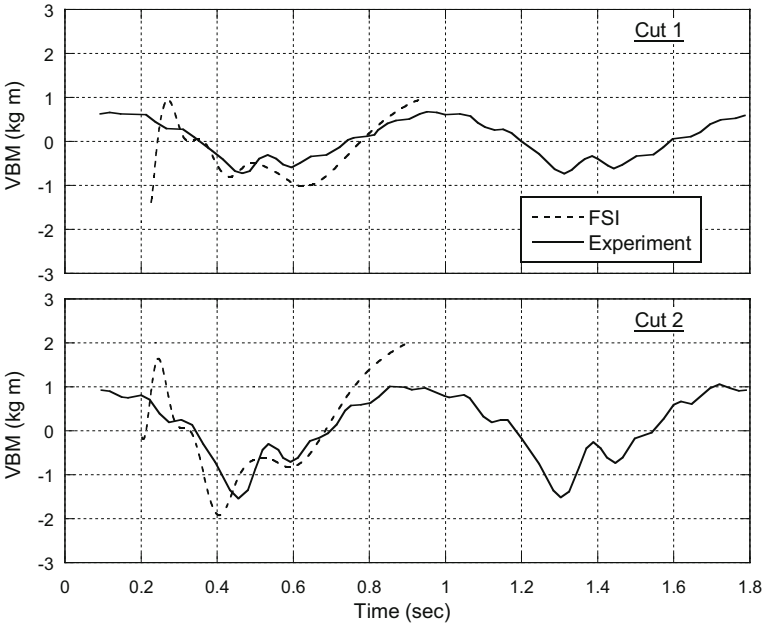

Fig. 8 Time series of vertical bending moment

4 Conclusion

In this paper we present a methodology to simulate the dynamic response of a surface ship advancing in waves. The methodology relies on a one-way or loosely coupled fluid-structure interaction concept, where the fluid stress field is transfered to the structure, but structural displacements are not passed to the fluid domain. One of the principal benefits of one-way coupling is that the solvers of the different physics

domains are operated independently, as their standard output is synthesized within the separate FSI program.

The methodology is flexible in that any hydrodynamic or structural modal analysis tool may be used to predict the dynamic structural response of a ship. In this paper we use the CFD solver *Tenasi* to predict the rigid-body motion and surface stress field on the hull, and the commercial code ABAQUS to perform modal analysis of the hull and the water.

The simulation results are compared with experimental measurements on a segmented model of a container-ship. The modal analysis closely agrees with the experimental analysis of the wet modes. Finally, the vertical bending moment at the locations where the hull segments were interconnected are compared and the agreement is satisfactory.

Acknowledgements. This work is sponsored by the US Office of Naval Research (ONR) grant titled "Design Tools for the Sea-Base Connector Transformable Craft (T-Craft) Prototype Demonstrator", N00014-07-1-0856, under the direction of Kelly Cooper, and the ONR grant N00014-06-1-0474 under the administration of Dr. Patrick Purtell.

References

[1] Berenznitski, A.: Slamming: The role of hydroelasticity. Int. Shipbuild. Progr. 48, 333–351 (2001)

[2] Bishop, R.E.D., Price, W.G., Wu, Y.: A general linear hydroelasticity theory of floating structures moving in a seaway. Phil. Trans. R. Soc. Lond. A 316, 375–426 (1986)

[3] Cebral, J.R., Löhner, R.: Conservative load projection and tracking for fluid-structure problems. AIAA Journal 34(4), 687–692 (1997)

[4] Faltinsen, O.D.: Hydroelastic slamming. J. Sci. Technol. 5, 49–65 (2000)

[5] Farhat, C., Lesoinne, M., LeTallc, P.: Load and motion transfer algorithms for fluid/structure interaction problems with non-matching discrete interface: Momentum and energy conservation, optimal discretization and application to aeroelasticity. Comput. Methods Appl. Mech. Engrg. 157, 95–114 (1998)

[6] Kamakoti, R., Shyy, W.: Fluid-structure interaction for aeroelastic applications. Progress in Aerospace Science 40, 535–558 (2004)

[7] Komzsik, L.: What every engineer should know about computational techniques of finite element analysis. CRC Press, Florida (2005)

[8] Maman, C., Farhat, C.: Matching fluid and structure meshes for aeroelastic computations: A parallel approach. Computers & Structures 54(4), 779 (1995)

[9] Moctar, O.E., Schellin, T.E., Priebe, T.: CFD and FE methods to predict wave loads and ship structural response. In: 26th Symposium on Naval Hydrodynamics, Rome, Italy, pp. 333–351 (September 2006)

[10] Ramos, J., Incecik, A., Guedes Soares, C.: Experimental study of slam-induced stresses in a containership. Marine Structures 13, 25–51 (2000)

[11] Smith, M.J., Hodges, D.H., Cesnik, C.E.S.: Evaluation of computational algorithms suitable for fluid-structure interactions. J. Aircr. 37(2), 282–294 (2000)
[12] Wilson, R.V., Nichols, D.S., Mitchell, B., Karman, S.L., Hyams, D.G., Sreenivas, K., Taylor, L.K., Briley, W.R., Whitfield, D.L.: Application of an unstructured free surface flow solver for high speed transom stern ships. In: 26th Symposium on Naval Hydrodynamics, Rome, Italy (September 2006)
[13] Wilson, R.V., Nichols, D.S., Mitchell, B., Karman, V., Betro, S.L., Hyams, D.G., Sreenivas, K., Taylor, L.K., Briley, W.R., Whitfield, D.L.: Simulation of a surface combatant with dynamic ship maneuvers. In: 9th International Conference on Numerical Ship Hydrodynamics, Ann Arbor, Michigan (August 2007)

Complex Structure of Periodic Orbits in an Oscillator with a Vibro-Impact Attachment

Young Sup Lee, Francesco Nucera, Alexander F. Vakakis,
D. Michael McFarland, and Lawrence A. Bergman

Abstract. We show that a linear oscillator with a vibro-impact attachment possesses a very complicated structure of periodic orbits. These periodic orbits can be studied numerically by depicting them in a frequency-energy plot (FEP), where the (conserved) energy of a periodic orbit is plotted against its fundamental frequency. The results reported herein are a brief summary of a more detailed study (Lee et al., 2008).

1 Introduction

The regular and chaotic dynamics and bifurcations of vibro-impact (VI) oscillators have been extensively studied (Shaw and Rand, 1989; Babitsky, 1998; Brogliato, 1999). In recent works vibro-impact attachments have been used for shock (Georgiades et al., 2005; Georgiades, 2006; Karayannis et al., 2008) and seismic mitigation (Nucera et al., 2007, 2008), by theoretically and experimentally proving that these attachments can act as broadband energy absorbers of energy at a fast time scale. A basic study of transient resonance captures and of the dynamical mechanisms governing targeted energy transfers in oscillators with vibro-impact attachments was performed in (Lee et al., 2008), and a brief summary of these results will be reported herein. In the process we will discuss some new numerical tools that can be successfully applied to problems in vibro-impact dynamics.

Young Sup Lee
Mechanical and Aerospace Engineering, New Mexico State University,
younglee@nmsu.edu

Francesco Nucera
Mechanics and Materials, Mediterranean University of Reggio Calabria,
francesco.nucera@unirc.it

Alexander F. Vakakis
Mechanical Science and Engineering, University of Illinois at Urbana – Champaign,
avakakis@illinois.edu

D.Michael McFarland, Lawrence A. Bergman
Aerospace Engineering, University of Illinois at Urbana – Champaign,
lbergman@illinois.edu, dmmcf@illinois.edu

R.A. Ibrahim et al. (Eds.): Vibro-Impact Dynamics of Ocean Systems, LNACM 44, pp. 173–178.
springerlink.com

2 Frequency – Energy Plot (FEP)

We consider a single-degree-of-freedom (SDOF) linear oscillator (LO) coupled to a VI attachment (Fig. 1). We consider the system with no dissipative forces and perfectly elastic impacts; for results regarding the weakly dissipative system we refer to (Lee et al., 2008). By studying the structure of periodic orbits of the Hamiltonian system, we can also understand the dynamics of the weakly dissipative system and interpret them as complex multi-frequency transitions and resonance captures leading to strong energy exchanges. In fact, damped transitions can be comprehensively studied by depicting their wavelet spectra in the FEP (Vakakis et al., 2008; Lee et al., 2008).

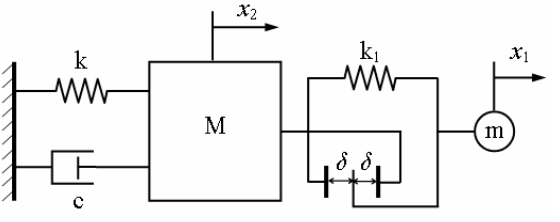

Fig. 1 The linear oscillator with VI attachment

Considering the system depicted in Figure 1 we note that between impacts the normalized equations of motion are linear,

$$\begin{aligned} &\mu\ddot{u}_1 + \sigma(u_1 - u_2) = 0 \\ &\ddot{u}_2 + \lambda\dot{u}_2 + u_2 + \sigma(u_2 - u_1) = 0 \end{aligned} \tag{1}$$

where dots denote differentiation with respect to the transformed time $\xi = t\sqrt{k/M}$, and $\mu = m/M$, $\sigma = k_1/k$, $\lambda = c/\sqrt{Mk}$, $u_i = x_i/\delta$, $i = 1,2$ (see Figure 1 for the corresponding notations); in terms of normalized displacements vibro-impacts occur when $|u_2 - u_1| = 1$. Assuming zero viscous damping (i.e., $\lambda = 0$) and considering purely elastic impacts (i.e., with restitution coefficient $\rho = 1$), the VI system of Fig. 1 becomes Hamiltonian. The velocities of the LO and the VI attachment after an impact (denoted by superscripts '+') are computed in terms of the corresponding velocities before the impact (denoted by superscripts '-') by the following relations:

$$\dot{u}_1^+ = \frac{(\mu-1)\dot{u}_1^- + 2\dot{u}_2^-}{1+\mu},\ \dot{u}_2^+ = \frac{(1-\mu)\dot{u}_2^- + 2\mu\dot{u}_1^-}{1+\mu} \tag{2}$$

In the numerical algorithm employed to compute the VI responses, the linear equations (1) are integrated for as long as the no-impact condition $|u_2 - u_1| < 1$ is satisfied. When $|u_2 - u_1| = 1$, a (purely elastic) impact occurs, and discontinuities in the velocities take place, whereas the displacements remain continuous throughout the impact. The velocities immediately after the impact are computed

by relations (2), and the numerical integration of the linear system (1) resumes with the new initial conditions until the next impact occurs, where this procedure is iterated.

The anticipated high complexity of the Hamiltonian VI periodic orbits dictates the use of careful notation for their representation in the FEP (Lee et al., 2008). To this end, we employ the following notation for depicting the various types of VI periodic orbits in the FEP. *Symmetric VI periodic orbits* are denoted as $SmnE(O)pp\pm$, and satisfy the conditions, $u_i(t) = \pm u_i(\xi + T/2),\ \forall t \in R,\ i = 1,2$, where T is the period of the motion; these orbits correspond to synchronous oscillations of the LO and the VI attachment, and typically are represented by curves in the configuration plane (u_1, u_2). *Unsymmetric VI periodic orbits* labeled as $Umnpq\pm$, do not satisfy the conditions of the symmetric ones (for notational simplicity, whenever $p = q$ we will adopt the convention, $Umnpp\pm \equiv Umn\pm$). These orbits correspond to asynchronous motions of the two oscillators and are represented by open or closed (Lissajous) curves in the configuration plane (u_1, u_2). The integer index m denotes the number of half-waves in the VI NES response within a half-period, whereas, the integer index n denotes the corresponding number of half-waves in the LO response; clearly, the ratio $(m:n)$ indicates the order of nonlinear resonance that occurs between the VI attachment and the LO on the given VI periodic orbit. The index *E* or *O* denotes the symmetry pattern of the vibro-impacts, and has meaning only for symmetric VI orbits: $E(O)$ denotes an even (odd) symmetry of occurring vibro-impacts within a half-period; it follows that the notation $E(O)$ implies that a vibro-impact occurs (does not occur) at quarter-period $\xi = \alpha \equiv T/4$. The integer indices p and q denote the number of vibro-impacts that occur in the first and second quarter-period, rescpectively, of a given VI periodic orbit; it follows that for symmetric orbits it holds that $p = q$. Finally, the (+) sign corresponds to *in-phase* VI periodic motions, where, for zero initial displacements the initial velocities of the LO and the NES possess identical signs at the beginning of both the first and second half-periods of the periodic motion; otherwise, the VI periodic motion is deemed to be *out-of-phase* and the (-) sign is used. Finally, the two in-phase and out-of-phase linear modes of the system with zero clearance ($\delta = 0$) are denoted by $Lmm\pm$, and are, in fact, equivalent to $L11\pm$.

The FEP of the hamiltonian VI system for $\mu = \sigma = \delta = 0.1$ is depicted in Figure 2, with some representative VI periodic orbits presented in Figure 3. We note that for larger (or smaller) clearances, the entire FEP is just shifted towards higher (or lower) energy regimes. So, the introduced normalization allows us to study all possible VI responses of the original system by considering a single 'normalized' FEP for fixed mass and coupling stiffness ratios. The two dots in Figure 2 indicate the critical energy thresholds below which oscillations without vibro-impacts occur, and the dynamics of the two-DOF system becomes purely linear. Clearly, only the in-phase and out-of-phase linear modes $L11\pm$ exist

below these energy thresholds. As we increase the energy the motion above these energy thresholds vibro-impacts start occurring, giving rise to two main branches of symmetric periodic VI NNMs: the branch of out-of-phase symmetric VI nonlinear normal modes (NNMs) $SmmO11-$, which bifurcates from the out-of-phase linear mode $L11-$, after which this mode becomes unstable; and the branch of symmetric in-phase VI NNMs $S13O11+$ which bifurcates out of the in-phase linear mode $L11+$, after which this linear mode also becomes unstable. For convenience, from hereon the shortened notations, $SmmO11- \equiv S11-$ and $S13O11+ \equiv S13+$, will be adopted for these two main backbone branches, which will be referred to as *backbone (global) branches* of the FEP. Both backbone branches exist over broad frequency and energy ranges, and, except for the neighborhoods of the bifurcation points with $L11\pm$, they correspond to oscillations that are mainly localized to the VI NES. A basic bifurcation in the VI FEP is the saddle node (SN) bifurcation of the two backbone branches $S11-$ (at Hamiltonian $h \approx 0.06$), which signifies the elimination of the unstable branch $S11-$ that bifurcates out of $L11-$; the stable branch $S11-$ that is generated after this SN bifurcation maintains its stability for increasing energies. As shown below, this SN bifurcation of the backbone branch $S11-$ affects the capacity of the VI NES for TET. The additional in-phase backbone branch $S13+$ that bifurcates out of the in-phase linear mode $L11+$ is stable until high energies where zones of instability appear.

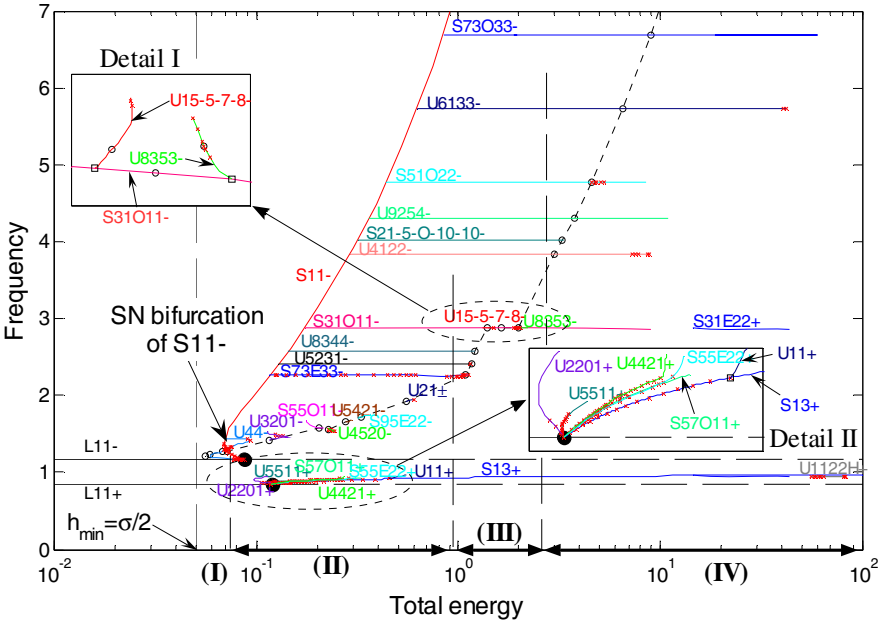

Fig. 2 The Hamiltonian FEP of the vibro-impacting system

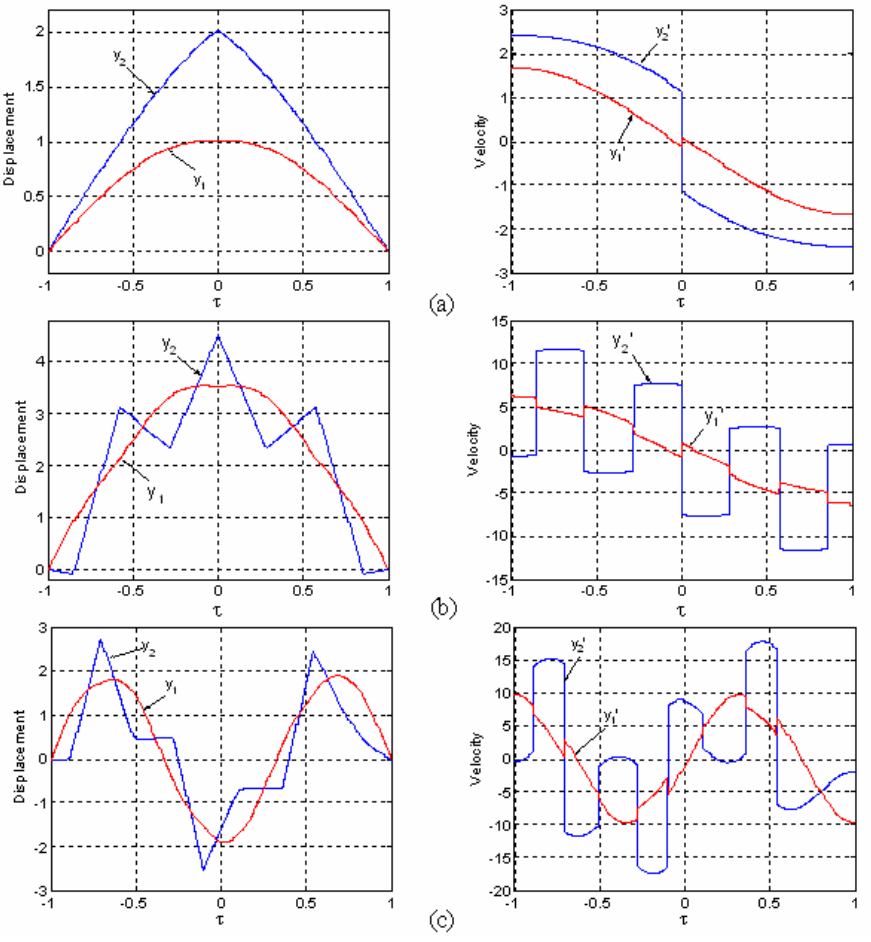

Fig. 3 Representative VI periodic orbits: (a) Symmetric orbit on the backbone $S13O00+ \equiv S13+$; (b) Symmetric VI orbit on $S73O33-$; (c) Unsymmetric orbit on $U8353-$

A different class of VI periodic solutions of the FEP lies on *subharmonic tongues (local branches);* these are multi-frequency periodic motions, possessing frequencies that are rational multiples of one of the linearized eigenfrequencies of the system. Each subharmonic tongue is defined over a finite energy range, and is composed of a pair of branches of in- and out-of-phase subharmonic oscillations. There exists a countable infinity of subharmonic tongues, corresponding to symmetric or unsymmetric VI subharmonic motions with different patterns of vibro-impacts during a cycle of the oscillation.

Finally, there exists a third class of VI motions in the FEP, *VI impulsive orbits (VI IOs).* These correspond to all initial conditions zero except for the initial velocity of the LO. A VI IO represents the response of the system at rest forced by a single impulse applied to the LO at time $t = 0+$. The importance of studying this

class of orbits stems from their essential role regarding passive TET from the linear oscillator to the NES (Lee et al., 2005; Kerschen et al. 2006).

It is interesting to note that the complexity of the FEP is solely due to the clearance δ that gives rise to vibro-impacts. *Indeed, in the limit of no clearance,* $\delta \to 0$*, the entire structure of VI orbits depicted in the FEP of Figure 2 collapses to two horizontal lines corresponding to the linear modes* $L11\pm$. We conclude that, due to the degeneracy of the VI dynamics, even a small clearance can generate significant complexity.

4 Concluding Remarks

The Hamiltonian FEP is a useful tool for studying the weakly dissipative transitions in system (1). As shown in (Vakakis et al., 2008; Lee et al., 2008) by superimposing the wavelet spectra of damped transient responses to the FEP we gain the capacity to identify transient resonance captures between the LO and the VI attachment, and targeted energy transfer from the LO to the attachment.

References

Babitsky, V.: Theory of Vibro-impact Systems. Springer, Berlin (1998)

Brogliato, B.: Non-smooth mechanics. Springer, Berlin (1999)

Georgiades, F., Vakakis, A., McFarland, D.M., Bergman, L.: Shock isolation through passive energy pumping caused by nonsmooth nonlinearities. J. Bif. Chaos 15(6), 1989–2001 (2005)

Georgiades, F.: Nonlinear localization and targeted energy transfer phenomena in vibrating systems with smooth and nonsmooth stiffness nonlinearities. PhD Thesis, National Technical University of Athens, Greece (2006)

Kerschen, G.Y., Lee, Y.S., Vakakis, A.F., McFarland, D.M., Bergman, L.A.: Irreversible passive energy transfer in coupled oscillators with essential nonlinearity. SIAM J. Appl. Math. 66(2), 648–679 (2006)

Lee, Y.S., Kerschen, G., Vakakis, A.F., Panagopoulos, P.N., Bergman, L.A., McFarland, D.M.: Complicated dynamics of a linear oscillator with an essentially nonlinear local attachment. Physica D 204, 41–69 (2005)

Lee, Y.S., Nucera, F., Vakakis, A., McFarland, D.M., Bergman, L.: Periodic orbits, damped transitions and targeted energy transfer in oscillators with vibro-impact attachments. Physica D (submitted, 2008)

Nucera, F., Vakakis, A., McFarland, D.M., Bergman, L., Kerschen, G.: Targeted energy transfers in vibro-impact oscillators for seismic mitigation. Nonlinear Dyn. 50(3), 651–677 (2007)

Nucera, F., LoIacono, F., McFarland, D.M., Bergman, L., Vakakis, A.: Application of broadband nonlinear targeted energy transfers for seismic mitigation of a shear frame: experimental results. J. Sound Vib. 313, 57–76 (2008)

Shaw, S., Rand, R.: The transition to chaos in a simple mechanical system. Int. J. Nonlinear Mech. 24, 41–56 (1989)

Vakakis, A.F., Gendelman, O., Bergman, L., McFarland, D.M., Kerschen, G., Lee, Y.S.: Passive Nonlinear Targeted Energy Transfer in Mechanical and Structural Systems: I and II. Springer, Berlin (in press, 2008)

Switching and Stick Motions in an Extended Fermi-Acceleration Oscillator

Albert C.J. Luo and Yu Guo

Abstract. The motion switching of the bouncing ball in a generalized Fermi oscillator is investigated through the theory of discontinuous dynamical systems. The analytical conditions of the motion switching are presented and illustration of periodic motions is given to show motion switching.

1 Introduction

The Fermi acceleration oscillator was first presented by Fermi in 1949, which was used to explain the mode of formation of cosmic ray. Since then, such an oscillator has been extensively investigated to interpret many physical and mechanical phenomena. In 1964, Zaslavskii and Chirikov [16] gave a comprehensive study of the Fermi acceleration mechanism in the one-dimensional case. In 1986, Jose and Cordery [2] studied the motion of the particle in a quantum Fermi-acceleration oscillator. In 1998, Saif et al [14] studied the dynamics of both classical and quantum Fermi accelerators and determined the dynamical localization of position and momentum for a modulation amplitude. In 2008, Leonel and Livorati [3] investigated the average effects of velocities of the particle in a dissipative Fermi acceleration oscillator through a scaling approach. Such an impact phenomenon exists extensively in engineering. In 1982, Holmes [1] assumed the mass of ball is much smaller than the one of table, and the ball and table always impact at the same position. In 1983, Shaw and Holmes [15] studied the harmonic, subharmonic and chaotic motions of a single-degree of freedom, non-linear oscillator. In 1996, Luo and Han [10] presented a reasonable model to investigate the dynamical behaviors of a bouncing ball with a sinusoidally vibrating table. In 2002, Luo [4] studied the stability and bifurcation for the unsymmetrical periodic motion of a horizontal impact oscillator with a periodic excitation. In 2005, Luo [5] presented the mapping dynamics of periodic motions in a non-smooth piecewise

Albert C J Luo
Southern Illinois University Edwardsville, Edwardsville, IL62026-1805, USA
aluo@siue.edu

Yu Guo
Southern Illinois University Edwardsville, Edwardsville, IL62026-1805, USA
yguo@siue.edu

R.A. Ibrahim et al. (Eds.): Vibro-Impact Dynamics of Ocean Systems, LNACM 44, pp. 179–189.
springerlink.com

system, and Luo [6] developed a theory for non-smooth dynamical systems on connectable and accessible sub-domains. Luo and Chen [8] used such a theory to investigate the grazing bifurcations and periodic motions in an idealized gear transmission system with impacts. In 2006, Luo and Gegg [9] used the non-smooth dynamical system theory to develop the force criteria of stick and non-stick motion in a harmonically forced, friction-induced oscillator. In 2007, Luo and O'Connor [11,12] discussed the dynamics mechanism of impact chatters and possible stick motions in a gear transmission system. Luo and Rapp [13] discussed the switching bifurcations of flows from a domain into its adjacent domain in a periodically driven, discontinuous dynamical system.

2 Mechanical Model

The Fermi accelerator model consists of a bouncing ball moving vertically between a fixed wall and the piston in a vibrating oscillator. The piston of mass m_2 is connected with a spring of constant k and a damper with coefficient c. Both of them are set on a periodically oscillating base, as shown in Fig. 1. The mass of ball is m_1 and the restitution coefficients of impact are e_1 and e_2 for the wall and piston, respectively. The gap between the fixed wall and the equilibrium piston is h. The oscillating displacement of the base is $D(t) = Q\cos\Omega t$.

Fig. 1 Mechanical model

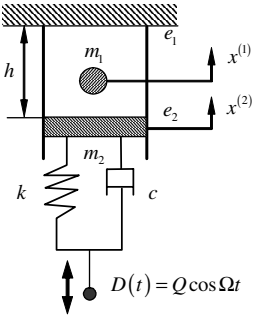

The equations of non-stick motion of the ball and piston are

$$\left.\begin{aligned} &\ddot{x}^{(1)} = -g, \\ &\ddot{x}^{(2)} + 2d\dot{x}^{(2)} + \omega^2 x^{(2)} = \omega^2 Q\cos\Omega t - 2dQ\Omega\sin\Omega t \end{aligned}\right\} \tag{1}$$

where $d = \frac{r}{2m_2}$ and $\omega = \sqrt{\frac{k}{m_2}}$. The impact relation between the ball and the fixed wall is

$$\left.\begin{aligned} &x_+^{(1)} = x_-^{(1)} = h,\ \dot{x}_+^{(1)} = -e_1\dot{x}_-^{(1)} \\ &x_+^{(2)} = x_-^{(2)},\ \dot{x}_+^{(2)} = \dot{x}_-^{(2)} \end{aligned}\right\} \tag{2}$$

where (+) and (-) represent after and before impact. The impact relation between the ball and the vibrating piston is

$$
\begin{aligned}
x_+^{(1)} &= x_+^{(2)} = x_-^{(1)} = x_-^{(2)}, \\
\dot{x}_+^{(1)} &= \frac{m_1\dot{x}_-^{(1)} + m_2\dot{x}_-^{(2)} - m_2 e_2(\dot{x}_-^{(1)} - \dot{x}_-^{(2)})}{m_1 + m_2}, \\
\dot{x}_+^{(2)} &= \frac{m_1\dot{x}_-^{(1)} + m_2\dot{x}_-^{(2)} + m_1 e_2(\dot{x}_-^{(1)} - \dot{x}_-^{(2)})}{m_1 + m_2}.
\end{aligned} \tag{3}
$$

For stick motion, there is a relation ($x^{(1)} = x^{(2)}$ and $\dot{x}^{(1)} = \dot{x}^{(2)}$) and the corresponding equation of motion becomes

$$
\ddot{x}^{(i)} + 2d_0\dot{x}^{(i)} + (\omega_0)^2 x^{(i)} = (\omega_0)^2 Q\cos\Omega t - 2d_0 Q\Omega\sin\Omega t \tag{4}
$$

where $d_0 = \frac{r}{2(m_1+m_2)}$ and $\omega_0 = \sqrt{\frac{k}{m_1+m_2}}$.

3 Discontinuous Dynamical Systems

The domains and boundaries in the absolute coordinate are sketched in Fig. 2. The origin of the absolute coordinate is set at the equilibrium point. The absolute domains $\Omega_1^{(1)}$ and $\Omega_1^{(2)}$ for the ball and piston without stick are defined as

$$
\left.
\begin{aligned}
\Omega_1^{(1)} &= \{(x^{(1)}, \dot{x}^{(1)}) \mid x^{(1)} \in (x^{(2)}, h)\}, \\
\Omega_1^{(2)} &= \{(x^{(2)}, \dot{x}^{(2)}) \mid x^{(2)} \in (-\infty, x^{(1)})\}.
\end{aligned}
\right\} \tag{5}
$$

The corresponding absolute boundaries are defined as

$$
\left.
\begin{aligned}
\partial\Omega_{1(+\infty)}^{(i)} &= \{(x^{(i)}, \dot{x}^{(i)}) \,\big|\, \varphi_{1(+\infty)}^{(1)} \equiv x^{(1)} - h = 0, \dot{x}^{(1)} \neq 0\}, \\
\partial\Omega_{1(-\infty)}^{(i)} &= \{(x^{(i)}, \dot{x}^{(i)}) \,\big|\, \varphi_{1(-\infty)}^{(i)} \equiv x^{(i)} - x^{(\bar{i})} = 0, \dot{x}^{(i)} \neq \dot{x}^{(\bar{i})}\}.
\end{aligned}
\right\} \tag{6}
$$

The absolute domains $\Omega_0^{(i)}$ and $\Omega_1^{(i)}$ ($i = 1, 2$) for the ball and piston with stick are defined as

$$
\left.
\begin{aligned}
\Omega_0^{(1)} &= \{(x^{(1)}, \dot{x}^{(1)}) \mid x^{(1)} \in (-\infty, x_{cr}^{(2)}), \dot{x}^{(1)} = \dot{x}^{(2)}\}, \\
\Omega_0^{(2)} &= \{(x^{(2)}, \dot{x}^{(2)}) \mid x^{(2)} \in (x_{cr}^{(1)}, h,), \dot{x}^{(1)} = \dot{x}^{(2)}\}, \\
\Omega_1^{(1)} &= \{(x^{(1)}, \dot{x}^{(1)}) \mid x^{(1)} \in (x_{cr}^{(2)}, h), \dot{x}^{(1)} \neq \dot{x}^{(2)}\}, \\
\Omega_1^{(2)} &= \{(x^{(2)}, \dot{x}^{(2)}) \mid x^{(2)} \in (-\infty, x_{cr}^{(1)}), \dot{x}^{(1)} \neq \dot{x}^{(2)}\}
\end{aligned}
\right\} \tag{7}
$$

where $x_{cr}^{(i)}$ is for appearance and vanishing of stick motion with $\dot{x}_{cr}^{(1)} = \dot{x}_{cr}^{(2)}$ and $x_{cr}^{(1)} = x_{cr}^{(2)}$. The domains of $\Omega_1^{(i)}$ and $\Omega_0^{(i)}$ are shown via the hatched and shaded regions in Fig. 3. The absolute boundaries depicted by dotted curves and lines are defined as

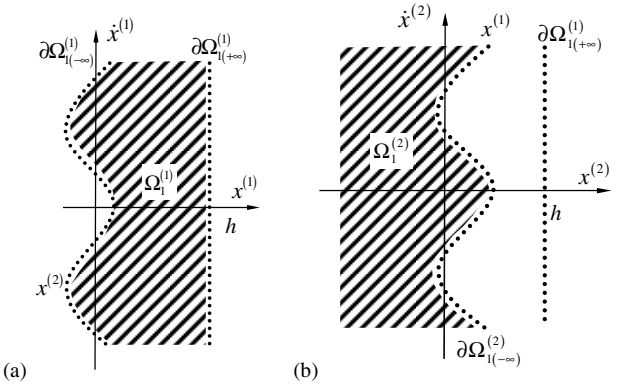

Fig. 2 Absolute domains and boundaries without stick: (a) ball and (b) piston

$$\left.\begin{aligned}\partial\Omega^{(i)}_{1(+\infty)} &= \{(x^{(i)},\dot{x}^{(i)})\,\big|\,\varphi^{(1)}_{1(+\infty)} \equiv x^{(1)} - h = 0, \dot{x}^{(1)} \neq 0\},\\ \partial\Omega^{(i)}_{10} &= \{(x^{(i)},\dot{x}^{(i)})\,\big|\,\varphi^{(i)}_{10} \equiv x^{(i)} - x^{(\bar{i})}_{cr} = 0, \dot{x}^{(i)} = \dot{x}^{(\bar{i})}_{cr}\}.\end{aligned}\right\} \tag{8}$$

From the domains, two vectors for absolute motions are introduced as

$$\mathbf{x}^{(i)}_{\lambda} = (x^{(i)}_{\lambda}, \dot{x}^{(i)}_{\lambda})^T, \mathbf{f}^{(i)}_{\lambda} = (\dot{x}^{(i)}_{\lambda}, F^{(i)}_{\lambda})^T \text{ for } i = 1,2 \text{ and } \lambda = 0,1 \tag{9}$$

where $\lambda = 0,1$ implies the corresponding domain. The state vector form for equations of absolute motion is

$$\dot{\mathbf{x}}^{(i)}_{\lambda} = \mathbf{f}^{(i)}_{\lambda}(\mathbf{x}^{(i)}_{\lambda}, t) \quad \text{for } i = 1,2 \text{ and } \lambda = 0,1 \tag{10}$$

where

$$\left.\begin{aligned}F^{(1)}_1(x^{(1)}_1, t) &= -g,\\ F^{(2)}_1(x^{(2)}_1, t) &= -2d\dot{x}^{(2)}_1 - \omega^2 x^{(2)}_1 + \omega^2 Q\cos\Omega t - 2dQ\Omega\sin\Omega t\end{aligned}\right\} \tag{11}$$

For the non-stick motion and with $i = 1$ and 2

$$F^{(i)}_1(x^{(i)}_0, t) = -2d_0\dot{x}^{(i)}_0 - (\omega_0)^2 x^{(i)}_0 + (\omega_0)^2 Q\cos\Omega t - 2d_0 Q\Omega\sin\Omega t \tag{12}$$

for the stick motion.

For convenience, the relative displacement, relative velocity and relative acceleration between the ball and the piston are $z^{(i)} = x^{(i)} - x^{(\bar{i})}$, $\dot{z}^{(i)} = \dot{x}^{(i)} - \dot{x}^{(\bar{i})}$ and $\ddot{z}^{(i)} = \ddot{x}^{(i)} - \ddot{x}^{(\bar{i})}$ where $i = 1$ and 2 represents the ball and piston, respectively. $\bar{i} = 1$ and 2 for $i = 2$ and 1, accordingly. The relative domains and boundaries for the ball and piston are sketched in Fig. 4. The stick domain and boundaries in the relative phase space become points, as shown in Fig. 4 (a) and (c). Therefore, the stick domain and boundaries in the space of relative velocity and acceleration

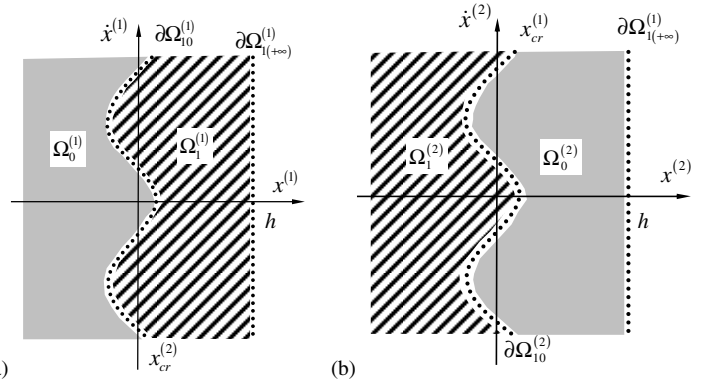

Fig. 3 Absolute domains and boundaries with stick: (a) ball and (b) piston

(i.e., $(\dot{z}^{(i)}, \ddot{z}^{(i)})$) are presented in Fig. 4 (b) and (d). The shaded and hatched domains are for stick and non-stick motions, respectively. The relative domains $\Omega_0^{(i)}$ and $\Omega_1^{(i)}$ for the ball and piston are defined as

$$\left.\begin{aligned}
&\Omega_0^{(i)} = \{(z^{(i)}, \dot{z}^{(i)}) \,\big|\, \dot{z}^{(i)} = 0, z^{(i)} = 0\} \text{ for } i = 1,2 \\
&\Omega_1^{(1)} = \{(z^{(1)}, \dot{z}^{(1)}) \,\big|\, z^{(1)} \in (0, h - x^{(2)})\}, \\
&\Omega_1^{(2)} = \{(z^{(2)}, \dot{z}^{(2)}) \,\big|\, z^{(2)} \in (-\infty, 0)\}.
\end{aligned}\right\} \tag{13}$$

The relative boundaries $\partial\Omega_{1(+\infty)}^{(i)}, \partial\Omega_{1(-\infty)}^{(i)}, \partial\Omega_{10}^{(i)}$ and $\partial\Omega_{01}^{(i)}$ for the ball and piston are defined as

$$\left.\begin{aligned}
&\partial\Omega_{1(+\infty)}^{(i)} = \{(z^{(1)}, \dot{z}^{(1)}) \,|\, \varphi_{1(+\infty)}^{(1)} \equiv z^{(1)} - h + x^{(2)} = 0\}, \\
&\partial\Omega_{1(-\infty)}^{(i)} = \{(z^{(i)}, \dot{z}^{(i)}) \,|\, \varphi_{1(-\infty)}^{(i)} \equiv z^{(i)} = 0\}, \\
&\partial\Omega_{10}^{(i)} = \partial\Omega_{01}^{(i)} = \{(z^{(i)}, \dot{z}^{(i)}) \,|\, \varphi_{10}^{(i)} \equiv \dot{z}_{cr}^{(i)} = 0, z_{cr}^{(i)} = 0\}
\end{aligned}\right\} \tag{14}$$

where $\partial\Omega_{1(-\infty)}^{(1)}$ is the impact chatter boundary for the ball, and the two stick boundaries for the ball are $\partial\Omega_{10}^{(1)}$ and $\partial\Omega_{01}^{(1)}$. Similarly, $\partial\Omega_{1(-\infty)}^{(2)}$ is the impact chatter boundary for the piston and the two stick boundaries for the piston are $\partial\Omega_{10}^{(2)}$ and $\partial\Omega_{01}^{(2)}$. The relative vectors are defined as

$$\mathbf{z}_\lambda^{(i)} = (z_\lambda^{(i)}, \dot{z}_\lambda^{(i)})^T, \mathbf{g}_\lambda^{(i)} = \dot{\mathbf{z}}_\lambda^{(i)} = (\dot{z}_\lambda^{(i)}, g_\lambda^{(i)})^T \tag{15}$$

The equation of relative motion is in the vector form of

$$\dot{\mathbf{z}}_\lambda^{(i)} = \mathbf{g}_\lambda^{(i)}(\mathbf{z}_\lambda^{(i)}, \mathbf{x}_\lambda^{(\bar{i})}, t) \text{ and } \dot{\mathbf{x}}_\lambda^{(\bar{i})} = \mathbf{f}_\lambda^{(\bar{i})}(\mathbf{x}_\lambda^{(\bar{i})}, t) \tag{16}$$

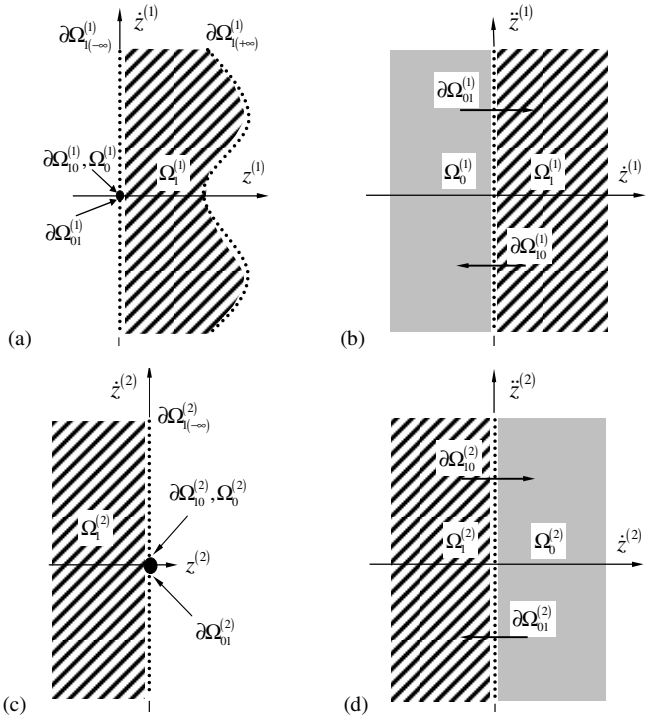

Fig. 4 Relative domains and boundaries in: (a) $(z,\dot{z})$ -plane for particle, (b) $(\dot{z},\ddot{z})$ -plane for particle, (c) $(z,\dot{z})$ -plane for piston and (d) $(\dot{z},\ddot{z})$ -plane for piston

where

$$\left.\begin{aligned} g_1^{(1)}(\mathbf{z}_1^{(1)},\mathbf{x}_1^{(2)},t) &= -g + 2d\dot{x}_1^{(2)} + \omega^2 x_1^{(2)} - \omega^2 Q\cos\Omega t + 2dQ\Omega\sin\Omega t,\\ g_1^{(2)}(\mathbf{z}_1^{(2)},\mathbf{x}_1^{(1)},t) &= -2d\dot{x}_1^{(2)} - \omega^2 x_1^{(2)} + \omega^2 Q\cos\Omega t - 2dQ\Omega\sin\Omega t + g \end{aligned}\right\} \tag{17}$$

for non-stick motion, and

$$\left.\begin{aligned} &\dot{z}_0^{(i)} = 0,\\ &g_0^{(i)}(\mathbf{z}_0^{(i)},\mathbf{x}_0^{(\bar{i})},t) = 0, \end{aligned}\right\} \text{ for } i = 1,2 \text{ with } \bar{i} = 2,1 \tag{18}$$

for stick motion.

4 Analytical Conditions

The analytical conditions of stick and grazing motions are developed using the non-smooth dynamical theory of Luo [7]. The normal vectors of the boundaries are

$$\left.\begin{aligned}\mathbf{n}_{\partial\Omega_{\alpha\beta}} &= \nabla\varphi_{\alpha\beta} = (\tfrac{\partial\varphi_{\alpha\beta}}{\partial z}, \tfrac{\partial\varphi_{\alpha\beta}}{\partial \dot{z}})^T \text{ for the relative frame,}\\ \mathbf{n}_{\partial\Omega_{\alpha\beta}} &= \nabla\varphi_{\alpha\beta} = (\tfrac{\partial\varphi_{\alpha\beta}}{\partial x}, \tfrac{\partial\varphi_{\alpha\beta}}{\partial \dot{x}})^T \text{ for the absolute frame}\end{aligned}\right\} \tag{19}$$

where $\nabla = (\frac{\partial}{\partial z}, \frac{\partial}{\partial \dot{z}})^T$. The normal vectors to the stick boundaries ($\mathbf{n}_{\partial\Omega_{10}^{(1)}}$ and $\mathbf{n}_{\partial\Omega_{01}^{(1)}}$) and impact boundary ($\mathbf{n}_{\partial\Omega_{1(+\infty)}^{(1)}}$ and $\mathbf{n}_{\partial\Omega_{1(-\infty)}^{(1)}}$) are given by

$$\begin{aligned}&\mathbf{n}_{\partial\Omega_{10}^{(1)}} = \mathbf{n}_{\partial\Omega_{01}^{(1)}} = (0,1)^T, \mathbf{n}_{\partial\Omega_{1(-\infty)}^{(1)}} = (1,0)^T \text{ in the relative frame,}\\ &\mathbf{n}_{\partial\Omega_{1(+\infty)}^{(1)}} = (1,0)^T \text{ in the absolute frame.}\end{aligned} \tag{20}$$

The zero-order and first-order G-functions in the relative frame are

$$\left.\begin{aligned}G^{(0,0)}_{\partial\Omega_{01}^{(i)}}(\mathbf{z}_0^{(i)}, t_{m\pm}) &= \mathbf{n}^T_{\partial\Omega_{01}^{(i)}} \bullet \mathbf{g}^{(i)}(\mathbf{z}_0^{(i)}, \mathbf{x}_0^{(\bar{i})}, t_{m\pm}),\\ G^{(0,1)}_{\partial\Omega_{10}^{(i)}}(\mathbf{z}_1^{(i)}, t_{m\pm}) &= \mathbf{n}^T_{\partial\Omega_{10}^{(i)}} \bullet \mathbf{g}^{(i)}(\mathbf{z}_1^{(i)}, \mathbf{x}_1^{(\bar{i})}, t_{m\pm}),\\ G^{(1,0)}_{\partial\Omega_{01}^{(i)}}(\mathbf{z}_0^{(i)}, t_{m\pm}) &= \mathbf{n}^T_{\partial\Omega_{01}^{(1)}} \bullet D\mathbf{g}^{(i)}(\mathbf{z}_0^{(i)}, \mathbf{x}_0^{(\bar{i})}, t_{m\pm}),\\ G^{(1,1)}_{\partial\Omega_{10}^{(i)}}(\mathbf{z}_1^{(i)}, t_{m\pm}) &= \mathbf{n}^T_{\partial\Omega_{10}^{(1)}} \bullet D\mathbf{g}^{(i)}(\mathbf{z}_1^{(i)}, \mathbf{x}_1^{(\bar{i})}, t_{m\pm}).\end{aligned}\right\} \tag{21}$$

The zero-order G-functions are the normal vector fields in the normal directions of the boundaries and the first order G-functions are the normal components of the change rate of vector fields. The G-functions for the impact boundaries are defined as

$$\left.\begin{aligned}G^{(0,1)}_{\partial\Omega_{1(+\infty)}^{(1)}}(\mathbf{x}_1^{(1)}, t_{m\pm}) &= \mathbf{n}^T_{\partial\Omega_{1(+\infty)}^{(1)}} \bullet \mathbf{f}^{(1)}(\mathbf{x}_1^{(1)}, t_{m\pm}),\\ G^{(1,1)}_{\partial\Omega_{1(+\infty)}^{(1)}}(\mathbf{x}_1^{(1)}, t_{m\pm}) &= \mathbf{n}^T_{\partial\Omega_{1(+\infty)}^{(1)}} \bullet D\mathbf{f}^{(1)}(\mathbf{x}_1^{(1)}, t_{m\pm}),\end{aligned}\right\} \text{ for } \partial\Omega_{1(+\infty)}^{(1)} \text{ in absolute frame,} \tag{22}$$

$$\left.\begin{aligned}G^{(0,1)}_{\partial\Omega_{1(-\infty)}^{(1)}}(\mathbf{z}_1^{(1)}, t_{m\pm}) &= \mathbf{n}^T_{\partial\Omega_{1(-\infty)}^{(1)}} \bullet \mathbf{g}^{(1)}(\mathbf{z}_1^{(1)}, \mathbf{x}_1^{(2)} t_{m\pm}),\\ G^{(1,1)}_{\partial\Omega_{1(-\infty)}^{(1)}}(\mathbf{z}_1^{(1)}, t_{m\pm}) &= \mathbf{n}^T_{\partial\Omega_{1(-\infty)}^{(1)}} \bullet D\mathbf{g}^{(1)}(\mathbf{z}_1^{(1)}, \mathbf{x}_1^{(2)} t_{m\pm}),\end{aligned}\right\} \text{ for } \partial\Omega_{1(-\infty)}^{(1)} \text{ in relative frame.} \tag{23}$$

From the normal vectors and G-functions, the analytical condition for stick motion is obtained from the passable flow from domain $\Omega_1^{(i)}$ to $\Omega_0^{(i)}$ in Luo [7], i.e.,

$$(-1)^i G^{(0,1)}_{\partial\Omega_{10}^{(i)}}(\mathbf{z}_1^{(i)}, t_{m-}) > 0 \text{ and } (-1)^i G^{(0,0)}_{\partial\Omega_{01}^{(i)}}(\mathbf{z}_0^{(i)}, t_{m+}) > 0. \tag{24}$$

Therefore, one obtains

$$(-1)^i g_1^{(i)}\left(\mathbf{z}_1^{(i)}, \mathbf{x}_1^{(\bar{i})}, t_{m-}\right) > 0 \text{ and } (-1)^i g_0^{(i)}\left(\mathbf{z}_0^{(i)}, \mathbf{x}_0^{(\bar{i})}, t_{m+}\right) > 0. \tag{25}$$

With the relative force per unit mass, equation (25) gives

$$\ddot{x}^{(2)}(t_{m\pm}) > \ddot{x}^{(1)}(t_{m\pm}) = -g. \tag{26}$$

From Eq.(26), the acceleration of the piston $\ddot{x}^{(2)}(t_{m\pm})$ is greater than $\ddot{x}^{(1)}(t_{m\pm}) = -g$. The criteria for vanishing of the stick motion at $\partial\Omega_{01}^{(i)}$ are given by

$$\left.\begin{aligned} &G^{(0,0)}_{\partial\Omega^{(1)}_{01}}\left(\mathbf{z}_0^{(i)}, t_{m-}\right) = 0 \text{ and } G^{(0,1)}_{\partial\Omega^{(1)}_{01}}\left(\mathbf{z}_1^{(i)}, t_{m+}\right) = 0, \\ &(-1)^i G^{(1,0)}_{\partial\Omega^{(i)}_{01}}\left(\mathbf{z}_0^{(i)}, t_{m-}\right) < 0 \text{ and } (-1)^i G^{(1,1)}_{\partial\Omega^{(i)}_{01}}\left(\mathbf{z}_1^{(i)}, t_{m+}\right) < 0. \end{aligned}\right\} \tag{27}$$

From Eq. (27) one obtains the relative force relations for $\partial\Omega_{01}^{(i)}$ as

$$\left.\begin{aligned} &g_0^{(i)}\left(\mathbf{z}_0^{(i)}, \mathbf{x}_0^{(\bar{i})}, t_{m-}\right) = 0 \text{ and } g_1^{(i)}\left(\mathbf{z}_1^{(i)}, \mathbf{x}_1^{(\bar{i})}, t_{m+}\right) = 0, \\ &(-1)^i \tfrac{d}{dt} g_0^{(i)}\left(\mathbf{z}_0^{(i)}, \mathbf{x}_0^{(\bar{i})}, t_{m-}\right) < 0 \text{ and } (-1)^i \tfrac{d}{dt} g_1^{(i)}\left(\mathbf{z}_1^{(i)}, \mathbf{x}_1^{(\bar{i})}, t_{m+}\right) < 0. \end{aligned}\right\} \tag{28}$$

From the relative acceleration and jerk, the above equation can be rewritten as

$$\ddot{x}^{(2)}(t_{m\pm}) = \ddot{x}^{(1)}(t_{m\pm}) = -g \text{ and } \dddot{x}^{(2)}_{m\pm} < \dddot{x}^{(1)}_{m\pm} = 0 \text{ for } \partial\Omega_{01}^{(i)}. \tag{29}$$

With the G-functions of a flow to boundaries, the conditions of grazing motions are

$$\left.\begin{aligned} &G^{(0,1)}_{\partial\Omega^{(1)}_{1(+\infty)}}\left(\mathbf{x}_1^{(1)}, t_{m\pm}\right) = 0 \text{ and } G^{(1,1)}_{\partial\Omega^{(1)}_{1(+\infty)}}\left(\mathbf{x}_1^{(1)}, t_{m\pm}\right) < 0 \quad \text{for } \partial\Omega^{(1)}_{1(+\infty)}, \\ &(-1)^i G^{(0,1)}_{\partial\Omega^{(i)}_{1(-\infty)}}\left(\mathbf{z}_1^{(i)}, t_{m\pm}\right) = 0 \text{ and } (-1)^i G^{(1,1)}_{\partial\Omega^{(i)}_{1(-\infty)}}\left(\mathbf{z}_1^{(i)}, t_{m\pm}\right) < 0 \quad \text{for } \partial\Omega^{(i)}_{1(-\infty)}. \end{aligned}\right\} \tag{30}$$

So one obtains the grazing conditions for the boundaries of non-stick motions, i.e.,

$$\left.\begin{aligned} &\dot{x}^{(1)} = 0 \text{ and } \ddot{x}^{(1)} = -g < 0 \quad \text{for } \partial\Omega^{(1)}_{1(+\infty)}, \\ &\dot{x}^{(1)} = \dot{x}^{(2)} \text{ and } \ddot{x}^{(2)} < \ddot{x}^{(1)} = -g \quad \text{for } \partial\Omega^{(i)}_{1(-\infty)}. \end{aligned}\right\} \tag{31}$$

In a similar fashion, the grazing conditions for the boundary of the stick motion is

$$\left.\begin{aligned} &G^{(0,1)}_{\partial\Omega^{(i)}_{10}}\left(\mathbf{z}_1^{(i)}, t_{m\pm}\right) = 0 \text{ and } (-1)^i G^{(1,1)}_{\partial\Omega^{(i)}_{10}}\left(\mathbf{z}_1^{(i)}, t_{m\pm}\right) < 0 \text{ for } \partial\Omega^{(i)}_{10}, \\ &G^{(0,0)}_{\partial\Omega^{(i)}_{01}}\left(\mathbf{z}_0^{(i)}, t_{m\pm}\right) = 0 \text{ and } (-1)^i G^{(1,0)}_{\partial\Omega^{(i)}_{01}}\left(\mathbf{z}_0^{(i)}, t_{m\pm}\right) > 0 \text{ for } \partial\Omega^{(i)}_{01}. \end{aligned}\right\} \tag{32}$$

With the acceleration and jerk, the conditions in Eq. (23) are given by

$$\left.\begin{aligned} &\ddot{x}^{(2)} = \ddot{x}^{(1)} = -g \text{ and } \dddot{x}^{(2)} < \dddot{x}^{(1)} = 0 \text{ for } \partial\Omega^{(i)}_{10}, \\ &\ddot{x}^{(2)} = \ddot{x}^{(1)} = -g \text{ and } \dddot{x}^{(2)} > \dddot{x}^{(1)} = 0 \text{ for } \partial\Omega^{(i)}_{01}. \end{aligned}\right\} \tag{33}$$

5 Illustrations

The analytical conditions for motion switching will be used in numerical simulations. The periodic motion without stick is presented in Fig. 5. In Fig. 5 (a) and

(b), the time-histories of displacement and velocity are plotted. The solid and dashed curves represent the motions of the bouncing ball and piston, respectively. The impacts between the bouncing ball and piston cause the discontinuity of velocity, which is observed in Fig. 5 (b). The trajectories of the bouncing ball and piston with the corresponding boundaries in phase space are given in Fig. 5 (c) and (d), respectively. The dashed curves give the moving boundary. In Fig. 5 (c) and (d), the dark point is the starting point for a motion of ball from the piston. Until the bouncing ball hits the fixed boundary, the motion is labeled by a mapping P_1. The impact between the ball and the fixed wall occurs because the velocity of ball is non-zero. After impact, the ball moves to the piston. Until the ball arrives to the oscillating piston, such a motion is labeled by a mapping P_2. Once the impact between the piston and ball occurs, the ball repeats such a motion process as described, and the bouncing ball returns back to the oscillating piston. After this impact, the bouncing ball cannot reach the fixed ball but it returns back to the piston and such motion is labeled by mapping P_3. Such a motion process forms a closed cycle in phase space, which is called a periodic motion. Such a periodic motion does not have any stick motion exist. The corresponding mapping structure of the periodic motion is given by $P_{3(21)^2} \equiv P_3 \circ P_2 \circ P_1 \circ P_2 \circ P_1$.

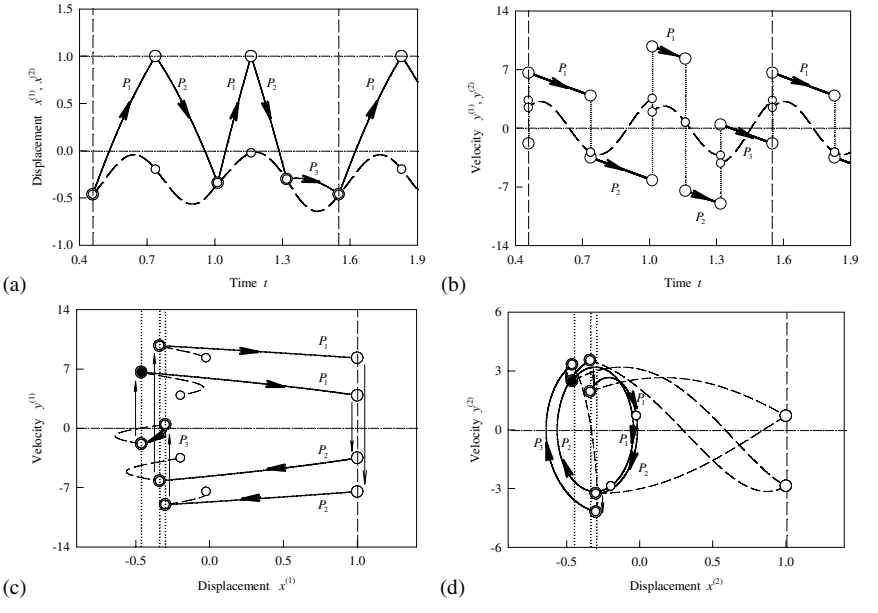

Fig. 5 Periodic motion of mapping $P_{3(21)^2}$: (a) displacement, (b) velocity, (c) phase plane (ball) and (d) phase plane (piston). ($m_1 = 0.1$, $m_2 = 1$, $k = 10$, $c = 8$, $e_1 = 0.9$, $e_2 = 0.8$, $h = 1$, $Q = 0.5$, $\Omega = 11.5$, $t_0 = 0.45824951$, $x_0^{(1)} = -0.46221559$, $\dot{x}_0^{(1)} = -1.83542559$, $x_0^{(2)} = -0.46221559$, $\dot{x}_0^{(2)} = 3.32981239$)

Consider a periodic motion with stick presented in Fig. 6. The time-histories of displacement and velocity are given in Fig. 6 (a) and (b), respectively. The trajectories of the bouncing ball and the piston with the corresponding boundaries in phase space also are plotted Fig. 6 (c) and (d), respectively. The starting point of the motion of ball is selected at the oscillating piston. The ball will not arrive to the fixed wall before the ball returns back to the oscillating piston. Such a motion is still labeled by a mapping P_3. After the ball touches the oscillating piston, both of them will stick together. Before the stick motion vanishes, the stick motion is labeled by a mapping P_0. Once the stick motion disappears, the ball will move toward the fixed wall. However, the ball cannot reach the fixed wall but it returns back to the oscillating piston with an impact. Repeating of the motion with the first mapping P_3 is obtained. Therefore, a periodic motion is formed with a mapping structure of $P_{303} \equiv P_3 \circ P_0 \circ P_3$. This periodic motion possesses a stick motion. The conditions for onset and vanishing of the stick motion in Eqs. (26) and (29) should be satisfied.

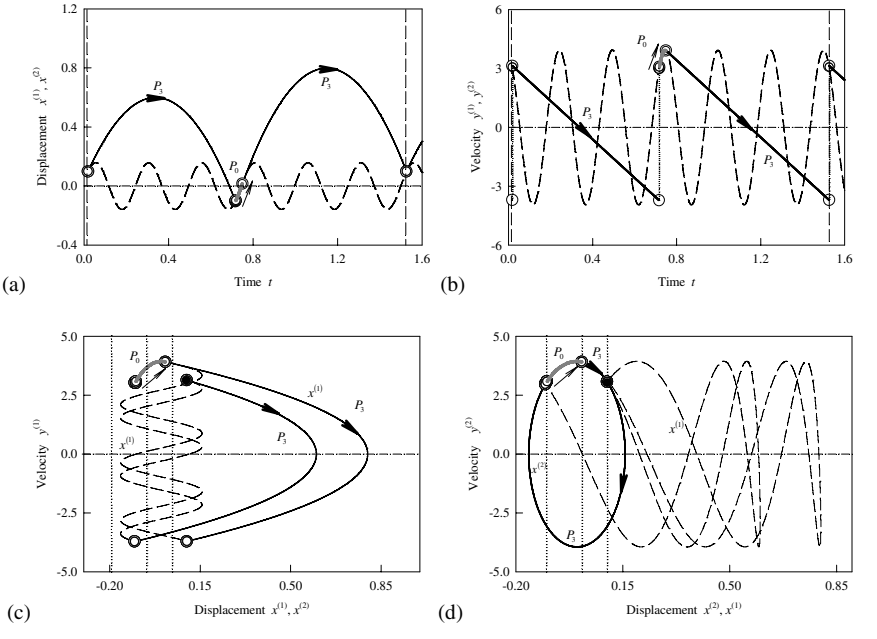

Fig. 6 Periodic motion with stick for mapping P_{303}. (a) displacement, (b) velocity, (c) phase plane (ball) and (d) phase plane (piston). ($m_1 = 0.001$, $m_2 = 1$, $k = 20$, $c = 8$, $e_1 = 0.9$, $e_2 = 0.01$, $h = 1$, $Q = 0.5$, $\Omega = 25$, $t_0 = 0.01825579$, $x_0^{(1)} = 0.098484094$, $\dot{x}_0^{(1)} = -3.704213264$, $x_0^{(2)} = 0.098484094$, $\dot{x}_0^{(2)} = 3.074054127$)

References

1. Holmes, P.J.: The dynamics of repeated impacts with a sinusoidally vibrating table. Journal of Sound and Vibration 84, 173–189 (1982)
2. Jose, J.V., Cordery, R.: Study of a quantum Fermi-acceleration model. Physical Review Letters 56(4), 290–293 (1986)
3. Leonel, E.D., Livorati, A.L.P.: Describing Fermi acceleration with a scaling approach: The Bouncer model revisited. Physica A 387, 1155–1160 (2008)
4. Luo, A.C.J.: An unsymmetrical motion in a horizontal impact oscillator. Journal of Vibration and Acoustics 124, 420–426 (2002)
5. Luo, A.C.J.: The mapping dynamics of periodic motions for a three-piecewise linear system under a periodic excitation. Journal of Sound and Vibration 283, 723–748 (2005)
6. Luo, A.C.J.: A theory for non-smooth dynamic systems on the connectable domains. Communications in Nonlinear Science and Numerical Simulation 10, 1–55 (2005)
7. Luo, A.C.J.: Global Transversality, Resonance and Chaotic Dynamics. World Scientific, Singapore (2008)
8. Luo, A.C.J., Chen, L.: Grazing bifurcation and periodic motion switching in a piecewise linear, impacting oscillator under a periodical excitation. In: ASME 2005 International Mechanical Engineering Congress and Exposition (IMECE 2005), Design Engineering, Parts A and B, pp. 913–924 (2005)
9. Luo, A.C.J., Gegg, B.C.: Stick and non-stick periodic motions in periodically forced oscillators with dry friction. Journal of Sound and Vibration 291, 132–168 (2006)
10. Luo, A.C.J., Han, R.P.S.: The dynamics of a bouncing ball with a sinusoidally vibrating table Revisited. Nonlinear Dynamics 10, 1–18 (1996)
11. Luo, A.C.J., O'Connor, D.: Nonlinear dynamics of a gear transmission system part I: Mechanism of impacting chatter with stick. In: Proceedings of the ASME 2007 International Design Engineering Technical Conference & Computers and Information in Engineering Conference, DETC2007-34881 (2007)
12. Luo, A.C.J., O'Connor, D.: Nonlinear dynamics of a gear transmission system part II: Periodic impacting chatter and stick. In: Proceedings of the ASME 2007 International Design Engineering Technical Conference & Computers and Information in Engineering Conference, DETC2007-43192 (2007)
13. Luo, A.C.J., Rapp, B.M.: Switching dynamics of a periodically forced discontinuous system with an inclined boundary. In: Proceeding of the ASME 2007 International Design Engineering Technical Conference & Computers and Information in Engineering Conference, DETC2007-34863 (2007)
14. Saif, F., Bialynicki-Birula, I., Fortunato, M., Schleich, W.P.: Fermi accelerator in atom optics. Physical Review A 58, 4779–4783 (1998)
15. Shaw, S.W., Holmes, P.J.: A periodically forced piecewise linear oscillator. Journal of Sound and Vibration 90, 129–155 (1983)
16. Zaslavskii, G.M., Chirikov, B.V.: Fermi acceleration mechanism in the one-dimensional case. Doklady Akademii Nauk SSSR 159, 306–309 (1964)

Vibro-Impact Models for Smooth Non-linear Systems

L.I. Manevitch

Abstract. Besides direct technical applications, vibro-impact models turn out to be powerful tool even for analysis of nonlinear systems strongly unlike those with impact interactions. Several examples of such analysis are presented. Firstly we propose a simple analytical description of transient vibrations of forced nonlinear oscillator. The concept of limiting phase trajectory (LPT) proposed by the author earlier is a key to solution of the problem. In this case LPT is of a special type solution corresponding to most intensive energy exchange between the oscillator and external source of energy. We show that two dynamical transitions occur in undamped system with change of nonlinearity and detuning parameters. First of them leads to qualitative change in temporal behavior of both amplitude of vibrations and phase shift and to formation of temporal amplitude dependence almost completely similar to that for vibro-impact vibrations. Further, we consider two weakly coupled nonlinear oscillators and weakly coupled oscillatory chains. It is shown that intensive energy exchange between oscillators can be adequately described by LPT via non-smooth functions of vibro-impact type in coordinates characterizing relationship between amplitudes of oscillators and phase shift between them.

1 Forced Nonlinear Oscillators

Let us suggest first that a harmonic force with small amplitude and frequency close to the resonance one acts on the nonlinear oscillator. This system is described by the following equation (in dimensionless form):

$$\frac{d^2u}{dt^2} + 2\gamma\varepsilon\frac{du}{dt} + u + 8\alpha\varepsilon u^3 = 2\varepsilon F\sin(1+s\varepsilon)t \tag{1.1}$$

with initial conditions

$$u(0) = \dot{u}(0) = 0$$

We introduce a change of variables [1]

$$\varphi = e^{-it}\left(\frac{du}{dt} + iu\right), \varphi^* = e^{it}\left(\frac{du}{dt} - iu\right). \tag{1.2}$$

L.I. Manevitch
Semenov Institute of Chemical Physics Russian Academy of Sciences,
4, Kosygina str., Moscow 119991 Russia
lmanev@chph.ras.ru

R.A. Ibrahim et al. (Eds.): Vibro-Impact Dynamics of Ocean Systems, LNACM 44, pp. 191–201.
springerlink.com

Using the multiple scale procedure, let us introduce the "slow" time $\tau_1 = \varepsilon t$ alongside with the "fast" time $\tau_0 = t$ and present $\varphi(\tau_0, \tau_1)$ as series

$$\varphi = \sum_n \varphi_n(\tau_0, \tau_1)\varepsilon^n . \tag{1.3}$$

As for differential operator in (1.1), it is changed by

$$\frac{\partial}{\partial \tau_0} + \varepsilon \frac{\partial}{\partial \tau_1}$$

The complex representation (1.2) allows combining displacement and velocity of oscillator in the single expression. It is especially convenient for formulation of initial conditions in the problem of energy exchange. Substituting (1.3) into (1.1) with taking into account (1.2) and equating the factors at each power of ε to zero we obtain from the term of ε^0-order

$$\frac{\partial \varphi_0}{\partial \tau_0} = 0 \tag{1.4}$$

from which one can find that $\varphi_0=\varphi_0(\tau_1)$ and for the term of ε-order

$$\begin{aligned} &\frac{\partial \varphi_0}{\partial \tau_1} + \frac{\partial \varphi_1}{\partial \tau_0} + \gamma\left(\varphi_0 + \varphi_0^* e^{-2i\tau_0}\right) \\ &+ i\alpha\left(\varphi_0^3 e^{2i\tau_0} - 3|\varphi_0|^2 \varphi_0 + 3|\varphi_0|^2 \varphi_0^* e^{-2i\tau_0} - \varphi_0^{*3} e^{-4i\tau_0}\right) \\ &= -iF\left(e^{is\tau_1} - e^{-i(2\tau_0 + s\tau_1)}\right). \end{aligned} \tag{1.5}$$

The condition of secular terms absence in the solution of Eq. (1.5) can be written as follows:

$$\frac{d\varphi_0}{d\tau_1} + \gamma\varphi_0 - 3i\alpha|\varphi_0|^2 \varphi_0 = -iFe^{is\tau_1}, \ .\varphi_0(0) = 0. \tag{1.6}$$

Let us use the polar representation $\varphi_0 = ae^{i\delta}$ where $a > 0$. Then Eq. (1.6) is equivalent to system of differential equations

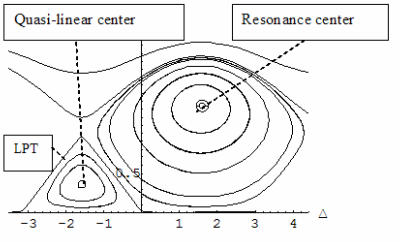

Fig. 1.1 Phase-plane portraits of the undamped nonlinear oscillator for s=0.4, F=0.13, α = 0.093

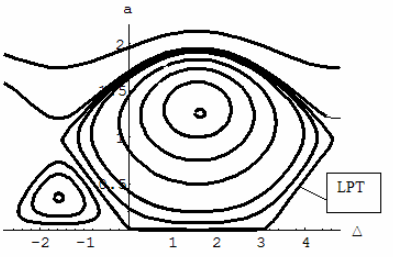

Fig. 1.2 Phase-plane portraits of the undamped nonlinear oscillator for s=0.4, F=0.13, $\alpha = 0.094$

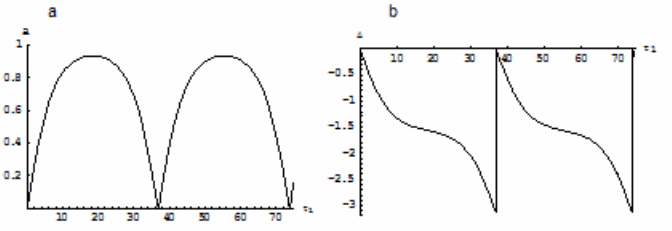

Fig. 1.3 Numerical solutions for the undamped nonlinear oscillator. F=0.13, s=0.4, α = 0.093. a. $a\,(\tau_1)$. b. $\Delta\,(\tau_1)$

$$\begin{aligned} &\frac{da}{d\tau_1} + \gamma a \;\; = F\cos\Delta, \\ &a\frac{d\Delta}{d\tau_1} + sa \;\; - 3\alpha a^3 = -F\sin\Delta, \end{aligned} \tag{1.7}$$

where $\Delta = \delta - (s\tau_1 - \pi/2)$.

If the damping is absent ($\gamma = 0$), system (1.7) has the integral of motion

$$H = sa^2 - \frac{3}{2}\alpha a^4 + 2aF\sin\Delta\,. \tag{1.8}$$

This is equation of phase trajectories on the plane (a, Δ). The stationary points, corresponding to steady state vibrations, satisfy the conditions

$$\frac{da}{d\tau_1} = 0, \qquad \frac{d\Delta}{d\tau_1} = 0. \tag{1.9}$$

Limiting phase trajectories (LPTs) satisfy the zeroth initial conditions (H = 0) [2]. They correspond to vibrations with the most intensive energy exchange between the oscillator and external source of energy. One can observe qualitative transformation of the phase plane portraits at

$$\alpha = \alpha_{cr} = \sqrt{\frac{2s}{9\alpha}} \tag{1.10}$$

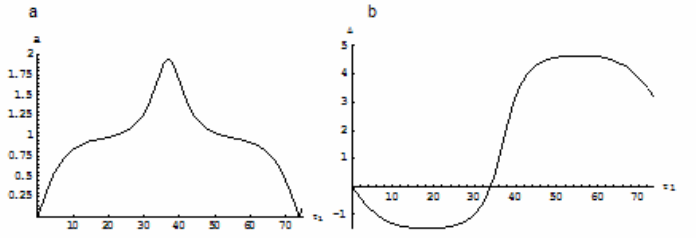

Fig. 1.4 Numerical solutions for the undamped nonlinear oscillator. F =0.13, s=0.4, α = 0.094. a. $a\,(\tau_1)$. b. $\Delta\,(\tau_1)$

This is the transformation of LPT from encircling the non-resonance "quasi-linear" center (Fig. 1.1) to encircling the "resonance" center (Fig. 1.2). We also observed the qualitative change in temporal behavior of both amplitude of vibrations a and phase shift Δ between the external force and oscillator (Fig. 1.3) and (Fig. 1.4). In these variables the transformation is a period-increasing transition [3], and temporal behaviour of amplitudes after it resembles vibro-impact oscillations (Fig. 1.4)

Let us note that the amplitude-phase diagrams show just pieces of actually periodic pictures. When $\alpha = 2\,\alpha_{cr}$ one can observe second topological transformation of the phase plane (Fig. 1.5) with further approach to saw-tooth form in temporal behaviour (Fig. 1.6). It allows us to consider a special non-smooth basis $\tau\,(\tau_1)$ and $e(\tau_1)$ similar to that introduced in [4] to study the vibrations close to vibro-impact ones and used in [2] for description of LPT in 2DoF system. Namely, $\tau\,(\tau_1)$ is saw-tooth function and $e\,(\tau_1)$ is its derivative in the sense of the Theory of distributions.

Therefore the functions $\tau(\tau_1)$ and $\Delta(\tau_1)$ tend to the following form

$$a\,(\tau_1) \to k\,\tau(\tau_1) = \left|\frac{2}{\pi}\arcsin\left(\sin\frac{\pi\tau_1}{2}\right)\right|,\ \Delta(\tau_1) \to \arccos\left[-\frac{k}{F}e(\tau_1)\right] \qquad (1.11)$$

with rise of nonlinearity parameter.

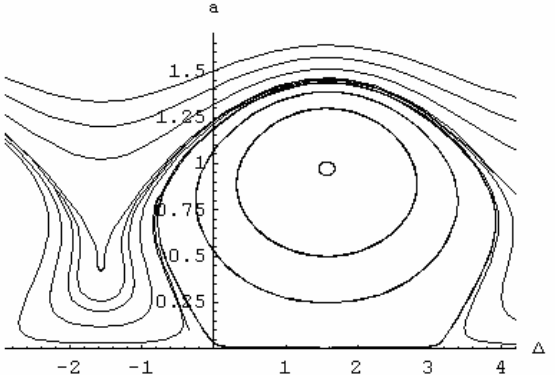

Fig. 1.5 Phase-plane portraits of the undamped nonlinear oscillator for s=0.4, F=0.13, α = 0.187

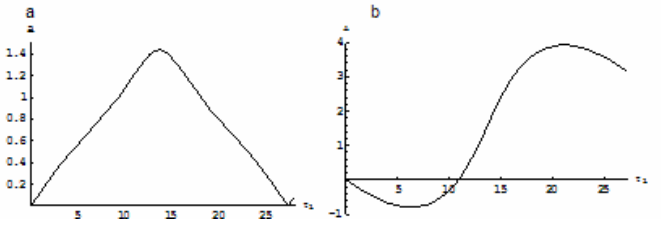

Fig. 1.6 Numerical solutions for the undamped nonlinear oscillator. F=0.13, s=0.4, α = 0.187. a. $a\,(\tau_1)$. b. $\Delta\,(\tau_1)$

To clarify the reason of the presented transformation of the solution corresponding to LPT let us consider more general case when elastic force is odd function of (2n-1)-order and s = 0 (for n=2 one has the cubic nonlinearity):

$$\frac{d^2a}{d\tau_1^2}+9\frac{n\alpha^2}{(n+1)^2}a^{2n-1}=0,\quad a\geq 0\,, \tag{1.12}$$

where the elastic term may be formally considered as a smooth approximation of vibroimpact interaction.

In general case ($s \neq 0$) analogous equation will be

$$\frac{d^2a}{d\tau_1^2}+9\frac{n\alpha^2}{(n+1)^2}a^{2n-1}-\frac{3}{2}\alpha s a^n+\frac{s^2}{4}a=0,\quad a\geq 0\,. \tag{1.13}$$

It is seen that besides the limiting case s = 0 there is other one, corresponding to linear system (α = 0) when the solution has a view

$$a=a_0\left|\sin\frac{s\tau}{2}\right| \tag{1.14}$$

The modulus operation reflects positivity of the amplitude a. Sine-like and saw-tooth functions determine two extreme types of LPT.

Let us consider now the damped nonlinear oscillator supposing that its starting phase trajectory corresponds to LPT.

Introducing the change of variable

$$\varphi_0=f_0e^{is\tau} \tag{1.15}$$

in Eq. 1.6 leads to description of damped and forced nonlinear oscillator by the following equation

$$\frac{\partial f_0}{\partial\tau_1}+(\gamma+is)f_0-3i\alpha\left|f_0\right|^2f_0=-iF\,. \tag{1.16}$$

Combining this equation with conjugated one after multiplication on f_0^* and f_0 respectively, one can find

$$\frac{\partial|f_0|^2}{\partial\tau_1}+2\gamma|f_0|^2=iF\left(f_0-f_0^*\right). \tag{1.17}$$

We consider Eq. (1.17) as a linear differential equation with respect to $N=|f_0|^2$. Then the solution of Eq. (1.17) $f_0(0)=0$ has a view

$$N=iF\int_0^{\tau_1}e^{-2\gamma(\tau_1-\xi)}\left[f_0(\xi)-f_0^*(\xi)\right]d\xi\,. \tag{1.18}$$

This solution can be presented in explicit form if to expand the function $\tilde{f}=f_0-f_0^*$ into power series

$$\tilde{f}=f_0+f_0^*=\sum_{n=0}^{\infty}\frac{1}{n!}\frac{\partial^n\tilde{f}}{\partial\xi^n}(0)\cdot\xi^n \tag{1.19}$$

and to calculate corresponding integrals.

From initial condition $f_0(\tau_1)=0$. Then the values $\dfrac{\partial^n f(0)}{\partial\tau_1^n}$ are determined from (Eq. 1.16) and its derivatives with taking into account the initial magnitudes of $f_0(\tau_1)$ and f_0^* which are equal to zero.

The temporal behaviour of the system has to be changed drastically with growth of time. If this behaviour resembles initially that of vibro-impact type, it becomes similar to steady state quasi-harmonic vibrations when approaching to attractor corresponding to stationary point at phase plane (a, Δ).

2 Two Weakly Coupled Nonlinear Oscillators

Let us consider the nonlinear problem of energy transfer in two weakly coupled nonlinear oscillators with cubic restoring forces (Fig.2.1). This problem can be described by the following system of two nonlinear equations (in dimensionless form):

$$\begin{aligned}\frac{d^2U_1}{d\tau_1^2}+U_1+2\beta\varepsilon(U_1-U_2)+8\alpha\varepsilon U_1^3=0,\\ \frac{d^2U_2}{d\tau_1^2}+U_2+2\beta\varepsilon(U_2-U_1)+8\alpha\varepsilon U_2^3=0,\end{aligned} \tag{2.1}$$

where

$$U_j=\frac{u_{j0}}{L_0},\ \tau_1=\sqrt{\frac{c_1}{m}},\ 8\alpha\varepsilon=\frac{c_3L_0^2}{c_1},\ 2\beta\varepsilon=\frac{c_{12}}{c_1}, \tag{2.2}$$

c_1 and c_3 are the linear and nonlinear stiffnesses of the first and second oscillators, respectively, and c_{12} is the stiffness of the coupling spring. Introducing the complex variables:

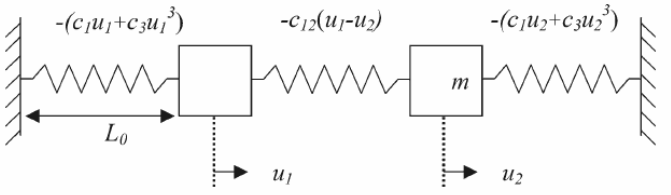

Fig. 2.1 The system under consideration

$$\varphi_1 = e^{-i\tau_1}\left(\frac{dU_1}{d\tau_1} + iU_1\right),\ \varphi_1^* = e^{i\tau_1}\left(\frac{dU_1}{d\tau_1} - iU_1\right),$$
$$\varphi_2 = e^{-i\tau_1}\left(\frac{dU_2}{d\tau_1} + iU_2\right),\ \varphi_2^* = e^{i\tau_1}\left(\frac{dU_2}{d\tau_1} - iU_2\right) \tag{2.3}$$

and slow time $\tau_2=\varepsilon\tau_1$ (along with the fast time τ_1), one can use the following two-scale expansions

$$\varphi_j(\tau_1,\tau_2) = \sum_n \varphi_{j,n}(\tau_1,\tau_2)\varepsilon^n,\ \ j=1,2. \tag{2.4}$$

After corresponding calculations taking into account Eqs. (2.1) - (2.4) we arrive at the equations of the principal asymptotic approach

$$\frac{df_1}{d\tau_2} + i\beta f_2 - 3i\alpha\left|f_1^2\right|f_1 = 0,$$
$$\frac{df_2}{d\tau_2} + i\beta f_1 - 3i\alpha\left|f_2^2\right|f_2 = 0, \tag{2.5}$$
$$\varphi_j = e^{i\beta\tau_2} f_j,\ \ j=1,2$$

This system (Eq. 2.5) is integrable and has two integrals:

$$H = \beta\left(f_2 f_1^* + f_1 f_2^*\right) - \frac{3}{2}\alpha\left(\left|f_1\right|^4 + \left|f_2\right|^4\right), \tag{2.6}$$

$$N = \left|f_1\right|^2 + \left|f_2\right|^2 \tag{2.7}$$

The best way to address this is to use Eq. (2.7) and the coordinates θ and Δ, where

$$f_1 = \sqrt{N}\cos\theta e^{i\delta_1},\ f_2 = \sqrt{N}\cos\theta e^{i\delta_2},\ \Delta = \delta_1 - \delta_2, \tag{2.8}$$

$$\frac{d\theta}{d\tau_2} = \beta\sin\Delta,\ \ \sin 2\theta\frac{d\Delta}{d\tau_2} = 2\beta\cos 2\theta\cos\Delta + \frac{3}{2}\alpha N\sin 4\theta. \tag{2.9}$$

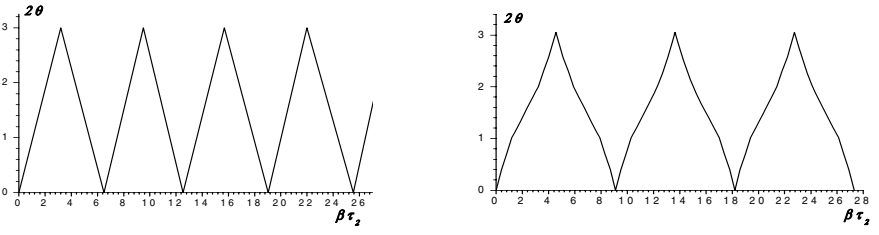

a b

Fig. 2.2 The function $2\theta = \left|am(2\tau_2, k)\right|$ for k=0.5 (a) and for k=0.9 (b)

The integral of Eq. (2.9) has the form following from expression Eq. (2.6)

$$H_0 = \sin 2\theta\left(\cos\Delta + k\sin 2\theta\right) - 2k \text{ , where } k = \frac{3\alpha N}{4\beta}, \alpha > 0 \tag{2.10}$$

We can consider the LPT corresponding to $H = 0$ as a fundamental solution (similarly to NNMs) whose behavior determines the second dynamic transition in the behavior of the oscillatory system. The LPT, which is far from the stationary points, can then be used as a generating solution to construct close trajectories with strong energy transfer [2].

Plots of $\theta\,(2\,\beta\tau_2)$ for two values of parameter k are presented in Figs. 2.2. The value $k = 0.5$ corresponds exactly to the first dynamic transition. However, the solution for the LPT (Fig. 2.2 - a) is still close to that for the linear case (saw-tooth function), except for a small change of period. Only for values of k that are close to unit the deflections from an exact saw-tooth profile and the change of period become noticeable.

The second dynamic transition occurs when k =1. In this case one can find a simple analytical solution corresponding to the LPT:

$$2\beta\tau_2 = \int_0^{2\theta} \frac{d(2\theta)}{\cos 2\theta}, \ \theta = \frac{1}{2}\arcsin\frac{1-e^{-2\beta\tau_2}}{1+e^{-2\beta\tau_2}}, \tag{2.11}$$

The LPT coincides with separatrix if $k \longrightarrow 1$: $\theta \to \pi/4$ when $\tau_2 \to \infty$.

As well as in the case of forced nonlinear oscillator one can use non-smooth basic functions $\tau\,(\tau_2)$, $e(\tau_2)$.

We would like to show that the natural area for application of these non-smooth basic functions is the description of beats (using the variables θ and Δ) and close trajectories with strong energy transfer. Actually, in the case $k = 0$ (the linearized system) the solution (2.8) can be rewritten in the form $\theta = (\pi/2)\ \tau$, $\Delta = (\pi/2)e$, $\tau = \tau\,(\tau_2/a)$, $e = e\,(\tau_2/a)$, where $a = \pi/2\beta$ (exactly as in a vibro-impact process with velocity $\Delta = \pi/2$). After introducing the basic functions $\tau\,(\tau_2/a)$, $e\,(\tau_2/a)$, we can present the solution as [5]

$$\theta = X_1(\tau) + Y_1(\tau)e, \ \Delta = X_2(\tau) + Y_2(\tau)e\,, \tag{2.12}$$

where the smooth functions $X_i(\tau)$, $Y_i(\tau)$ satisfy Eqs. (2.8):

$$\frac{\partial}{\partial\tau}\begin{Bmatrix}X_1\\Y_1\end{Bmatrix}=\frac{1}{2}a\beta[\sin(X_2+Y_2)\mp\sin(X_2-Y_2)]$$

$$\frac{\partial}{\partial\tau}\begin{Bmatrix}X_2\\Y_2\end{Bmatrix}=a\beta[ctg\ \ 2(X_1+Y_1)\cos(X_2+Y_2)\mp ctg\ \ 2(X_1-Y_1)\cos(X_2-Y_2)] \quad (2.13)$$

$$+\frac{3a}{2}\alpha N[\cos\ \ 2(X_1+Y_1)\mp\cos\ \ 2(X_1-Y_1)]$$

Despite some difference of expressions (1.11) from those used in [4,5], the representation (2.12), is still valid. Then, we can search for the solution of Eq. (2.13) in the form of power expansions in the independent variable τ:

$$X_i=\sum_{l=0}^{\infty}X_{i,l}\tau^l,\ Y_i=\sum_{l=0}^{\infty}Y_{i,l}\tau^l,\ i=1,2 \quad (2.14)$$

where the generating solution is the linear beat: $X_{1,0} = 0$, $X_{1,1} = \pi/2$, $Y_{1,0} = 0$, $X_{2,0} = 0$, $Y_{2,0} = \pi/2$, satisfying exactly the θ - Δ equations for the case of the strongest beat. It can be proved that the presentation (2.12), taking into account Eq. (2.14), recovers the exact solution of the nonlinear problem for the most intensive energy transfer between the oscillators. As this takes place, the expansions (2.14) restore the exact local representation of the corresponding elliptic function (near $\tau = 0$), but the expressions (2.12) allow the prediction of the exact global behavior of the system. It is important to note that, even for large enough values of k, the solution appears close to that of linear beats; the only change is the barely seen curvature of the lines that are straight for linear beats, and a change of the period.

One can find corresponding corrections by considering the next order of approximations, namely, $X_{1,0} = 0$, $X_{1,0} = \alpha\beta$, $X_{1,3} = -(2/3)\ (\alpha\ \beta)^3\ k^2$, $Y_{2,0} = \pi/2$, $Y_{2,1} = 2\ \alpha\beta k$, $Y_{2,3} = 4/3(\alpha\ \beta)^3$,. . ..

3 Two Weakly Coupled Oscillatory Chains

Let us consider a system of two weakly coupled Fermi-Pasta-Ulam (FPU) chains with potential energy containing the terms of fourth order alongside with parabolic ones. The respective Hamilton function is:

$$H=\sum_n\left\{\sum_{j=1,2}\left[\left(\frac{dq_{n,j}}{dt}\right)^2+\frac{c^2}{2}\left(q_{n+1,j}-q_{n,j}\right)^2+\frac{\beta}{4}\left(q_{n+1,j}-q_{n,j}\right)^4\right]+\varepsilon\frac{\gamma}{2}(q_{n,1}-q_{n,2})^2\right\} \quad (3.1)$$

where $q_{n,j}$ is dimensionless displacement of "n"-th particle in "j"-th chain; c, β, and γ are dimensionless parameters of interaction and $\varepsilon_2{}^{\gamma}$ is a small coefficient of interchain coupling. It is easy to show that considering a modulation of particle displacements at the right edge of spectrum of linearized system ($u_{n,j}=(-1)^n q_{n,j}$) one has the following continuum equations for envelope functions u_j:

$$\frac{\partial^2 u_j}{\partial \tau^2}+\frac{\partial^2 u_j}{\partial x^2}+u_j+16\beta {u_j}^3-\varepsilon\gamma u_{3-j}=0,\quad i=1,2$$
$$\tau=\omega t,\ \omega^2=4c^2+\varepsilon\gamma. \tag{3.2}$$

It is convenient again to use the complex variables:

$$\Psi_j=\frac{1}{\sqrt{2}}\left(\frac{\partial u_j}{\partial \tau}+iu_j\right),\quad \Psi_j^*=\frac{1}{\sqrt{2}}\left(\frac{\partial u_j}{\partial \tau}-iu_j\right). \tag{3.3}$$

The equations of motion (3.2) are converted to form:

$$i\frac{\partial}{\partial \tau}\Psi_j+\Psi_j+\frac{1}{2}\frac{\partial^2}{\partial x^2}(\Psi_j-\Psi_j^*)-4\beta(\Psi_j-\Psi_j^*)^3-\varepsilon\frac{\gamma}{2}(\Psi_{3-j}-\Psi_{3-j}^*)=0 \tag{3.4}$$

Now we will use following multiple-scale expansion:

$$\Psi_j=\sqrt{\varepsilon}(\psi_j+\varepsilon\psi_{j,1}+\varepsilon^2\psi_{j,2}+\ldots)$$
$$\tau_0=\tau,\quad \tau_1=\varepsilon\tau,\quad \tau_2=\varepsilon^2\tau \tag{3.5}$$
$$\xi=\sqrt{\varepsilon}x$$

which leads in main asymptotic approximation to two coupled equations in "slow" time:

$$i\frac{\partial}{\partial \tau_1}\chi_j+\frac{1}{2}\frac{\partial^2}{\partial \xi^2}\chi_j-\frac{\gamma}{2}\chi_{3-j}+12\beta|\chi_j|^2\chi_j=0,$$
$$j=1,2;\ \chi_j=\Psi_j e^{-i\tau_0} \tag{3.6}$$

Eqs. (3.6) allow solutions like anharmonic planar waves.

$$\chi_j=a_j X_j(\tau_2)\exp(ik\xi), \tag{3.7}$$

were $X_i(\tau_2)$ satisfy equations

$$i\frac{\partial X_j}{\partial \tau_1}-\frac{k^2}{2}X_j-\frac{\gamma}{2}\frac{a_{3-j}}{a_j}X_{3-j}+12\beta {a_j}^2|X_j|^2X_j=0. \tag{3.8}$$

These equations are similar to those for the system of two coupled oscillators (2.5). Therefore the saw-tooth type presentations of the phase variables in the case of intensive energy transfer are valid also.

So, the vibro-impact models turn out to be natural and efficient for dynamical systems with smooth potentials, if they are described in appropriate phase variables. In particular, it relates to classical models of forced nonlinear oscillator, coupled nonlinear oscillators and oscillatory chains.

Acknowledgments. This work was supposed by RFBR (grants No. 08-03-00420, 08-04-91118), CRDF (grants CGP No. 2920), RAN (program 4/OX-08).

References

1. Manevitch, L.I.: The description of localized normal modes in a chain of nonlinear coupled oscillators using complex variables. Nonlinear Dynamics 25, 95–109 (2001)
2. Manevitch, L.I.: New approach to beating phenomenon in coupled nonlinear oscillatory chains. Arch. Appl. Mech. 77(5), 301–312 (2007)
3. Manevitch, L.I., Musienko, A.I.: Transient forced vibrations of duffing oscillator. In: International Conference Nonlinear Phenomena in Polymer Solids and Low-dimensional Systems, Moscow, Russia, July 7-10, 2008, pp. 114–127. IChPh RAN (2008)
4. Pilipchuk, V.N.: A transformation for vibrating system based on a non-smooth pair of functions. Doklady AN Ukr, SSR, ser. A 4, 37–40 (1988) (in Russian)
5. Vakakis, A.F., Manevitch, L.I., Mikhlin, Y.V., Pilipchuk, V.N., Zevin, A.A.: Normal Modes and Localization in Nonlinear Systems, p. 550. Wiley, New York (1996)

Low Frequency Noise and Vibration Analysis of Boat Based on Experiment-Based Substructure Modeling and Synthesis

Masaaki Okuma

Abstract. This paper is to present a promising method of experiment-based substructure modeling and synthesis and a case study for low frequency noise and vibration analysis using a basic specimen of small boat consisting of a boat-hull, a single-cylinder-outboard-engine and its suspension-mechanism. Any machine generally consists of substructures and sub-machines. Cruiser is an example. Various combinations can be possible in choice of hulls, engines, engine-mounts or suspension-mechanisms. Noise and vibration characteristics are much dependent on the combinations. Therefore, it is desired to develop simple and speedy methods that are available to use for engineering design development and techno-business discussion with customers.

1 Introduction

In general, any machine consists of some substructures and sub-machines. The most of individual substructures and sub-machines are even complex so that it is not always possible to realize enough accurate modeling and analysis of them using only the finite element method(FEM in brief). Accurate FEM modeling will be very time-consuming and will not be always reliable without using model-updating process referring to experimental result. In addition, design improvement and modification are applied to a less number of substructures and sub-machines at a same time. Then, experiment-based approaches are still indispensable for practical modeling and analysis regarding noise and vibration engineering.

Many researches regarding such experiment-based approaches were reported in last decades. The modal analysis [1] and the building block approach [2] are the most fundamental theory and one of the methods in the linear modeling in the early days of the modern engineering of mechanical vibration and noise analysis. According to the theory of dynamics, both all independent rigid body motion modes and the natural vibration modes from the first order up to a certain high order have to be used to express the deflection of the substructures that become under free-free

Masaaki Okuma
Tokyo Institute of Technology, Department of Mechanical and Aerospace Engineering, 2-12-1-I3-15, O-okayama, Meguro-ku, Tokyo, 152-8552, Japan
mokuma@mech.titech.ac.jp

R.A. Ibrahim et al. (Eds.): Vibro-Impact Dynamics of Ocean Systems, LNACM 44, pp. 203–214.
springerlink.com

Fig. 1 The Boat-Hull and the Outboard-Engine with Its Suspension-Mechanism to Be Tested

boundary condition when they are detached from the entire machine system. Because the arbitrary displacement of such substructures in the vibratory displacement of the total machine system cannot be expressed mathematically by the linear combination using only their natural modes excluding the rigid body motion modes. Then, the identification of rigid body properties must be conducted as an additional other measurement besides the modal testing. The primitive and complex pendulum methods are generally conducted. However, they are very time-consuming and troublesome.

This paper presents a substructure synthesis method, SSM in brief, based on the experimental spatial matrix identification method [3, 4]. In this method, neither the pendulum testing nor swinging bench machines are necessary to conduct for obtaining the rigid body motion modes of individual substructures. Single-input and multiple-output FRFs(SIMO FRFs in brief) have only to be measured with respect to individual substructures under artificially-made free-free boundary condition. Therefore, it can make the substructure synthesis method much simpler than other conventional ones. The specimen of a small boat as shown in Fig. 1is analyzed regarding its low frequency noise and vibration characteristics as a case study. The boat-hull, the outboard-engine and the suspension mechanism are independently modeled regarding their dynamic characteristics in the form of spatial matrices by the experimental spatial matrix identification method.

2 Theory and Procedure

Let us call a structural system to be analyzed as *the entire structure*. *The entire structure* in the case study of this paper is the boat composed of the boat-hull, the outboard engine and its suspension mechanism with rubber mounts as shown in Fig.1. The entire structure should be decomposed into some number of structural parts for the analysis. Then, let us call the individual structural parts as *components*.The outline of the synthesis method is as follows.

The first step is to execute modal testing regarding each component for obtaining SIMO FRFs. In this research, hammering tests are conducted for the boat-hull, the outboard engine and the suspension mechanism under artificially-made free-free boundary condition. The dynamic stiffness of the rubber mounts in suspension-mechanism are estimated by the method in the literture [5].

The second step is to conduct the experimental spatial matrix identification regarding each component. Using the measured SIMO FRFs, their associated coherence functions and the coordinates of the FRF measument points set on the component, the dynamic characteristics of the each component are expressed in the form of spatial matrices. See the literatures [3, 4] for the algorithm. Note here that the method makes it possibile to identify a set of spatial matrices expressing all of the rigid body properties, feasible rigid body motion modes and elastically deformed natural modes since the coordinates of measurement points are essentially used for making a number of constraint equations with respect to the elements of spatial matrices. This is abstractly expressed mathematically using a few equations below.

Let us denote the degrees of freedom of the displacement regarding all the measurement points by the vector form of $\mathbf{x}(\omega)$, and a set of mass, viscous damping and stiffness matrix by $\mathbf{M}$, $\mathbf{C}$ and $\mathbf{K}$, respectively. Also let us denote the number of degrees of freedom of $\mathbf{x}(\omega)$ by n. Note that the vector $\mathbf{f}(\omega)$ is their associated force vector in which only one element corresponding to the driving point of vibration testing is substituted the value of 1 and all other elements are zeros. According to this the displacement vector $\mathbf{x}(\omega)$ SIMO FRFs are substituted into the left hand side of Eq.(1).

$$-\omega^2\mathbf{M}\mathbf{x}(\omega)+\mathbf{j}\omega\mathbf{C}\mathbf{x}(\omega)+\mathbf{K}\mathbf{x}(\omega)=\mathbf{f}(\omega) \tag{1}$$

Obtain the best values of the elements of the spatial matrices in Eq.(1) in order to make $\mathbf{x}(\omega)$ be fitting with experimental FRFs, subject to the following requirement of multi-objective optimization and the constraint equations between the elements of spatial matrices. The functions to be minimized are

$$\sum_{i=1}^{i=p}(\Omega_{i\_exp}-\Omega_{i\_mck})^2, \tag{2}$$

$$\sum_{i=1}^{i=p}(\tilde{\phi}_{i\_exp}-\tilde{\phi}_{i\_mck})^T(\phi_{i\_exp}-\phi_{i\_mck}) \tag{3}$$

and

$$\sum_{j=1}^{j=q}\{\tilde{\mathbf{x}}_{\mathbf{\_exp}}(\omega_{\mathbf{j}})-\tilde{\mathbf{x}}_{\mathbf{\_mck}}(\omega_{\mathbf{j}})\}^{\mathbf{T}}\{\mathbf{x}_{\mathbf{\_exp}}(\omega_{\mathbf{j}})-\mathbf{x}_{\mathbf{\_mck}}(\omega_{\mathbf{j}})\} \tag{4}$$

where Ω_{i_exp} and Ω_{i_mck} are the experimental natural frequencies and those to be derived from the identified spatial matrices in the frequency range of the identification, respectively. The top-positioned symbols such as on $\mathbf{x}_{\mathbf{i\_exp}}$ mean the conjugate of complex numbers. The parameter p is the number of the resonant peaks of FRFs in the frequency range of interest for the identification. The vector ϕ_i denotes the

i-th natural mode in the frequency range. The parameter q is the number of the sampling points of experimental FRFs in the frequency range of identification as well. $\mathbf{x_{mck}}(\omega_\mathbf{j})$ and $\mathbf{x_{exp}}(\omega_\mathbf{j})$ are the displacement vector obtained from Eq.1 and of the experimental FRFs, respectively.

The constraint equations are expressed below. First,

$$\mathbf{G_1^T M G_1} = \mathbf{M_{rigid}} \tag{5}$$

is those with respect to mass matrrix $\mathbf{M}$ to be identfied. The matrix $\mathbf{G_1} \in \mathbf{R^{(n\times 6)}}$ is the geometrical transformation matrix from six degrees of freedom of the motion of a point to the displacement of the measurement points under the assumption that the component behaves as a rigid body with small angular displacement. The geometrical transformation matrix can be easily obtained using the coordinates of the measurement points in vibration test. $\mathbf{M_{rigid}} \in \mathbf{R^{(6\times 6)}}$ is the rigid body mass matrix that has 6 degrees of freedom. The rigid body mass matrix always has a proper formation of elements as you can refer in the literatures [3, 8]. Next,

$$\mathbf{K G_1} = \mathbf{0} \tag{6}$$

and

$$\mathbf{C G_1} = \mathbf{0} \tag{7}$$

are those for the stiffness and the viscous damping matrix, respectively. These constraint equations mean that the component has neither stress nor strain all over the body when it moves as a rigid body.

The third step is to build up the spatial matrices of the entire structural system by the superposition of the spatial matrices of individual components obtained in the second step. The superposition can be conducted easily according to the connection configuration between all components in the entire structure. The superposition is a very simple mathematical operation.

The fourth step is to identify vibration excitation force generated in the outboard engine [6]. In this research, the force identification is conducted in two cases. The first case is the identification of force concentrated at the intersection between the axial center line of the crank-shaft and the longitudinal center line of the connecting-rod under the assumption that the cylinder-block behaves as a rigid body within the frequency range of interest for the convenience sake. Let us denote the intersectoin point by A. The second case is the identification of force distributed at measurement points of the cylinder-block without using the assumption. Note that it is very difficult to identify the real force precisely due to its complexity. This step consists of the following three sub-steps.

The first sub-step is to measure FRFs of the test outboard engine under mounting on a test bench. In the case study of this paper, hammering test is conducted to get FRFs at an appropriate number of measurement points on the test engine.

The second sub-step is to measure the vibration response of the engine being operated at a constant speed with constant load. The vibration response at the multi number of the measurement points should be measured simultaneously because the signals of measured vibration response in time domain should be transformed into the spectra with the phase information between the measurement points. Note that it is important to set an appropriate number of measurement points on the cylinder-block.

For the first case, the equation for the forced vibration can be written as

$$\mathbf{r}(\omega) = \mathbf{H}(\omega)\mathbf{G_2}\mathbf{f}(\omega) \tag{8}$$

where $\mathbf{r}(\omega)$, $\mathbf{H}(\omega)$, $\mathbf{G_2}$ and $\mathbf{f}(\omega)$ are the forced vibration response obtained in the second sub-step, the matrix of frequency response function obtained in the first sub-step, the geometrical transformation matrix between the six degrees of freedom of the motion of point A and the degrees of freedom of the actual measurement points on the cylinder-block, and the vibration excitation force vector to be obtained, respectively. Note that $\mathbf{G_2}$ is obtained as a constant matrix using the coordinates of these measurement points and point A.

The third sub-step is the computation to obtain the equivalent force. The least mean square method derived from Eq.(8) is conducted. That is,

$$\mathbf{f}(\omega) = \{\mathbf{G_2^T}\tilde{\mathbf{H}}^{\mathbf{T}}(\omega)\mathbf{H}(\omega)\mathbf{G_2})\}^{-1}\mathbf{G_2^T}\tilde{\mathbf{H}}^{\mathbf{T}}(\omega)\mathbf{r}(\omega). \tag{9}$$

The fifth step is the computation of vibration response of the entire boat system by substituting the excitation force obtained in the fifth step into the equations of motion of the entire boat system in the third step.

The sixth step is the acoustic analysis using a Boundary Element Method model (BE model in brief) regarding the surface of the entire boat system with the substitution of the vibration response computed in the sixth step onto the nodal points of the BE model [7].

3 Analysis of Boat

3.1 Modelling of Each Component

Fig. 2 shows a half part of the transam of the hull. With respect to the modeling of the hull, only the transam part is modeled. Because in the previous research work [7] it was made clear that the dominantly contributing part of the hull to low frequency noise radiation was the transam. The number of measurement points on the transam is 63, at each of which only the vibration perpendicular to the transam plane is measured. The experimental spatial matrix identification is conducted in the frequency

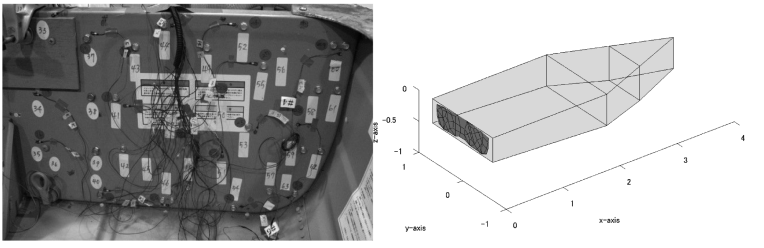

Fig. 2 View and Schematic of the Transam of the Boat-hull and of Its Measurement Point Location

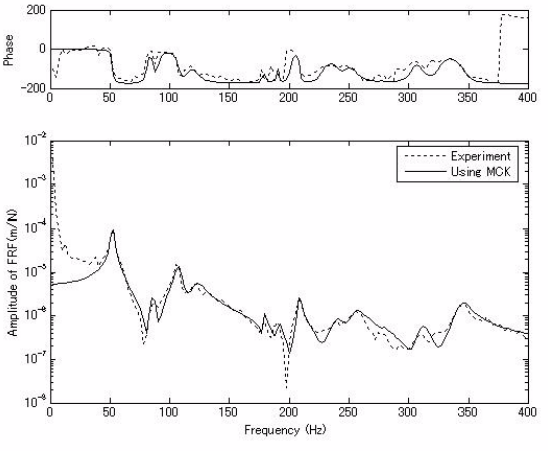

Fig. 3 Auto-FRF Fitting at a Hammering point in the Transam

range between 40 $\sim$ 400Hz. For example, the fitting of auto-FRF at a hammering point on the transam is shown in Fig. 3. The dotted and the solid line express its experimental FRF and the computational FRF derived from the set of spatial matrices identified by the method [3], respectively.

Fig. 4 shows the modeling of the outboard engine on which 24 measurement points are placed. Five points are located on the cylinder-block. For an example of verifying the spatial matrix identification, the auto-FRF fitting is shown in Fig.5. Fig.6 shows the suspension-mechanism on which 24 measurement points are placed. Fig. 7 shows the fitting of auto-FRF derived from the identified set of spatial matrices together with the experimental FRF. Fig. 8 shows one of two identical panels to be additionally attached to the transam part for this case study. Because the accuracy of the analysis by the method is to be investigated by observing the difference of the predictied dynamic behaviours of the hull in the two cases with and without the additional panels.

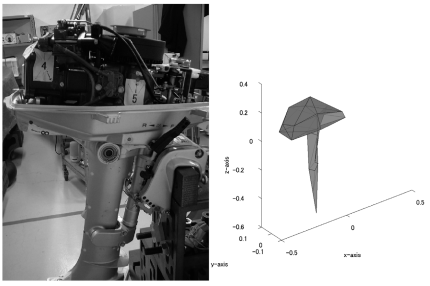

Fig. 4 View and Schematic of the Out-Board Engine and Its Measurement Point Location

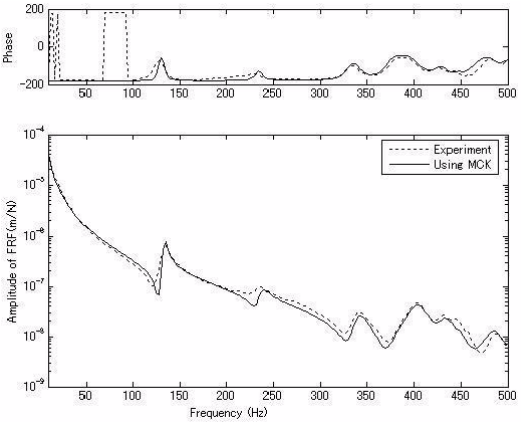

Fig. 5 Auto-FRF Fitting at a Hammering Point in the Engine

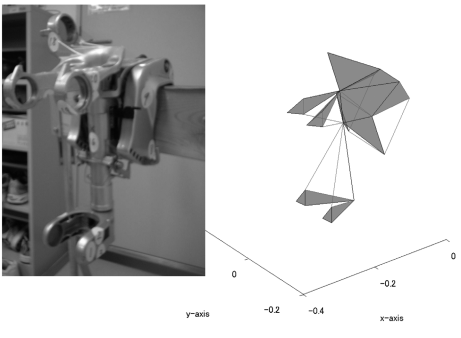

Fig. 6 View and Schematic of the Suspension-Mechanism and Its Measurement Point Location

3.2 Stiffness of Rubber-Mounts and Bolt-Joints

The rubber-mounts in the upper and the lower arms in the suspension mechanism for suspending the outboard engine are identified as a set of four identical springs in parallel for each rubber-mount. See the literature [5] reporting the detail of the identification technique. Table 1 lists the stiffness.

The equivalent stiffness of connecting points between the top-center part of the transam and the suspension-mechanism are assumed as moment-free perfect

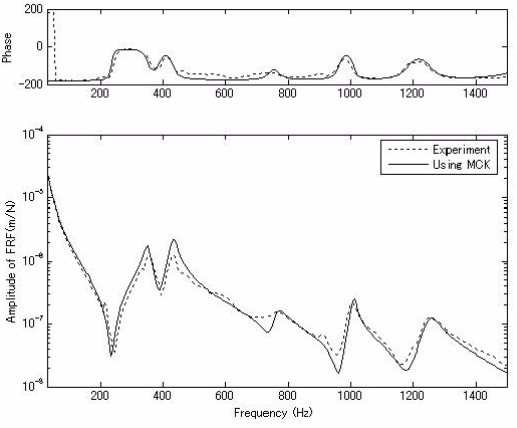

Fig. 7 Auto-FRF Fitting at a Hammering Point in the Suspension-Mechanism

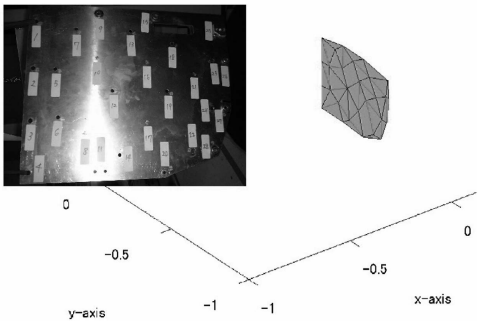

Fig. 8 View and Schematic of a Panel to Be Attached Additionally to the Transam and its Measurement Point Location

connection. The value of $3.0 \times 10^7 (N/m)$ is determined for convenience according to the averaged number of digits of the diagonal elements of the stiffness matrices identified for the outboard-engine and the transam.

The equivalent stiffness of connecting bolts, which are assumed to be all identical, between the transam and the additionally attached panels is determined as $3.5 \times 10^4 (N/m)$. The value is obtained by simply tuning from the initial value calculated using the bolt's specifications with respect to the dynamic charateristics of the system composed of only the hull and the two panels.

3.3 Force Identification

The vibration of the outboard-engine are measured and investigated at three different constant engine speeds. However, only the case of 4500rpm is reported in this paper due to allowable pages. The equivalent vibration forces are identified using the vibration data by the method on the fourth step in Section 2. As the result of the identification, Fig.9 shows the translational component into the transversal direction of the identified forces at 4500rpm (75Hz) for the two force model cases. The fine and the bold line denote the forces identified with and without the assumption that

Table 1 Stiffness of Rubber-Mounts in Upper and Lower Arms of Suspension-Mechanism

Mount Position	Stiffness Direction	Value of Stiffness(N/m)
Upper Arm	X-direct(longitudinal)	73,000x4
	Y-direct(transverse)	363,000x4
	Z-direct(vertical)	67,000x4
Lower Arm	X-direct(longitudinal)	54,000x4
	Y-direct(transverse)	261,000x4
	Z-direct(vertical)	49,000x4

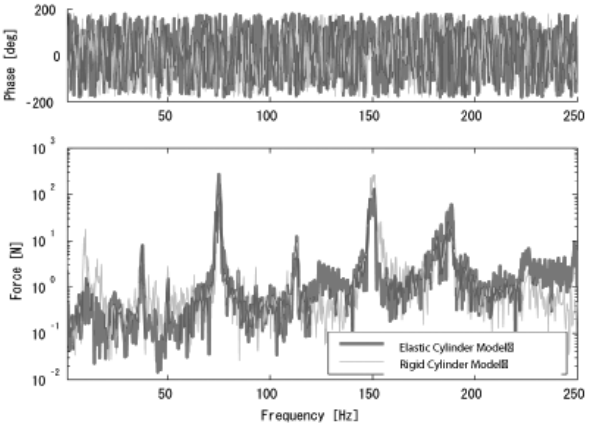

Fig. 9 Transverse Component of the Identified Force at 4500rpm Engine Speed

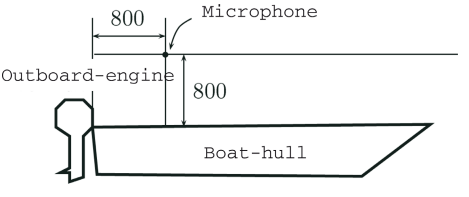

Fig. 10 Sound Pressure Measurement Position (Unit: mm)

the cylinder-block behaves as a rigid body in the frequency range of interest, respectively. Since the real force cannot be measured directly the force identification is verified by comparing the vibration response between experiment and simulation.

3.4 Vibration and Noise of Assembled Systems

Fig. 11 shows experimental and simulated auto-FRFs of a point on the transam of the boat-hull in the case that only two additional panels are attached to the boat-hull

using 56 bolts. With this result, it will be acceptable to use simple translational elastic modeling for the bolt-connection. However, see Fig.12 which is auto-FRF of a point on the cylinder-block of the outboard-engine in the case that all substructures are assembled. The dynamic characteristics of the entire system cannot be simulated with acceptable accuracy. It is found that the simple translational elastic modeling will not be appropriate enough for the connection between the transam and the engine-suspension-mechanism. This technical problem must be tackled in the future.

The vibration response at a measurement point on the entire structure of the boat system without two additional panels at constant engine speed of 4500rpm is shown in Fig. 13. Fig.10 shows the position of the microphone to measure the sound pressure level. The experimental and simulated sound pressure are shown in Fig. 14. The bold dotted line denotes experimental result. The scattered dots denotes the simulated result in the case that acutually measured vibration response data all over the entire boat system are substituted into the BE model. The spiky thin solid line denotes the simulated result in the case that the computed vibration response by the method are substituted into the BE model. The meaningful spectra of the first and

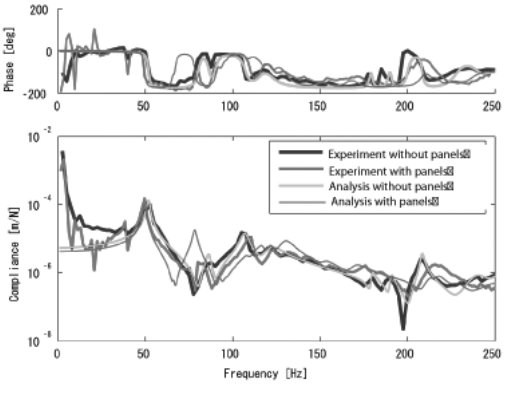

Fig. 11 An Auto-FRF of the Structure Composed of only Boat-hull and Two Additional Panels

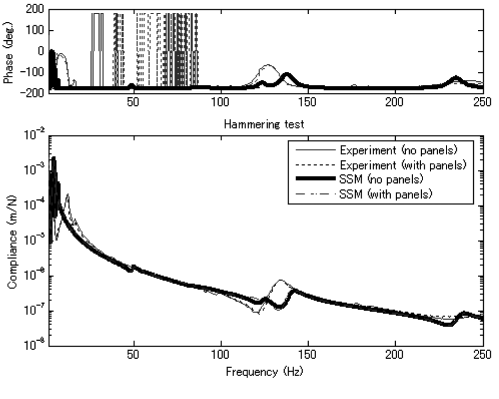

Fig. 12 An Auto-FRF of Entire Boat System Composed of Hull, Engine and Suspension-Mechanism

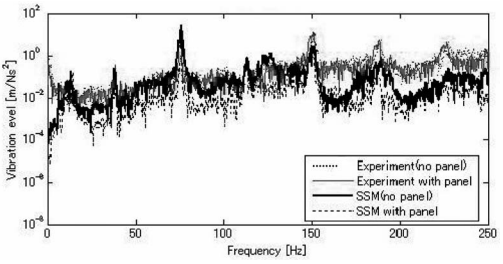

Fig. 13 Vibration of Entire Boat System at 4500rpm Constant Speed

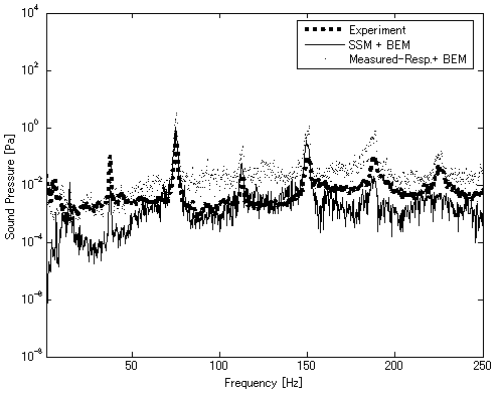

Fig. 14 Sound Pressure of Experiment and Simulation

the second harmonics of the engine revolution, 4500rpm(75Hz), are simulated about 10dB larger than the experimental result.

It is pointed out from the abovementioned case study that more practical modelings regarding the connections between the substructures will be able to improve the accuracy of the simulation.

4 Conclusions

In this research, the vibration and noise of a small boat system were simulated for three cases of constant engine speeds, 3700rpm, 4000rpm and 4500rpm using the methods of experiment-based substructure modeling and synthesis based on the experimental spatial matrix identificaiton and force identification. Then, in this paper, the case study of 4500rpm engine speed was presented. The simulated vibration and noise were compared with experiment. It is found that the modeling problem regarding connection between substructures should be still tackled in future work.

Acknowledgements. This research work was carried out under the cooperation with Mr. K. Shiomi, Mr. K. Okada and Mr. T. Ikeno of Power Products R&D Center, HONDA R&D Co., Ltd. Japan, and two graduate students of Tokyo Tech., Dr. T. Tomatsu and Miss N. Ishizuka. The author would appreciate their contribution.

References

1. Ewins, D.J.: Modal Testing: Theory and Practice. Research Study Press Ltd, Hertfordshire (1984)
2. Klosterman, A.L.: Building Bock Approach to Structural Dynamics, ASME Pub., VIBR-30 (1969)
3. Okuma, M., Shi, Q., Oho, T.: Development of Experimental Spatial Matrix Identification Method (Presentation of Current Theory and Basic Verification with a Frame Structure). J. of Sound & Vibration 219(1), 5–22 (1999)
4. Okuma, M., Heylen, W., Matsuoka, H., Sas, P.: Identification and Prediction of Frame Structure Dynamics by Spatial Matrix Identification Method. Trans. of ASME 123, 390–396 (2001)
5. Tomatsu, T., Okada, T., Ikeno, T., Shiomi, K., Okuma, M.: Identification of Engine Rubber Mount Dynamic Stiffness by Experimental Modal Analysis. Trans. of JSME (Part.C) 71-709, 2715–2722 (2005)
6. Otsuka, T., Okada, T., Ikeno, T., Shiomi, K., Okuma, M.: Force identification of an outboard engine by experimental means of linear structural modeling and equivalent force transformation. Journal of Sound & Vibration 308, 541–547 (2007)
7. Tomatsu, T., Otsuka, T., Okuma, M., Okada, T., Ikeno, T., Shiomi, K.: Sound-Radiation Analysis for Boat Hull Based on Hammering Test and BEM. In: Proc. DETC2005- 84628, 2005 ASME International Design Engineering Technical Conference & Computers and Information in Engineering Conference (2005) CD-ROM
8. Okuma, M.: Applied Mechanics. Suri-Kogaku-Sya Press Ltd. (Japanese publisher) (2005) (in Japanese)

Non Linear Dynamic Behaviour of an One-Sided Hertzian Contact Excited by an External Gaussian White Noise Normal Excitation

J. Perret-Liaudet and E. Rigaud

The system under study consists of a randomly excited single-degree-of-freedom non linear dynamic system. More precisely, we investigate the vibratory response of a moving mass preloaded by a normal force acting through a Hertzian contact. This study includes possible contact losses, and then vibroimpacts dynamic behaviour. The random excitation consists of an external Gaussian white noise normal force superimposed on the static one. Theoretical responses, in particular the spectral densities of the elastic restoring force, are obtained by using Monte Carlo simulations. In order to describe statistics of the stationary response, we have used the stationary Fokker-Planck equation. In order to validate theoretical results, we have also built an experimental test rig allowing us to simulate the studied non linear system. This test rig consists of a double sphere plane contact loaded by the weight of a rigid moving mass. Experimental results show a good agreement with experimental ones.

The contact loss non linearity appears to be rather strong compared with the Hertzian non linearity. It actually induces a large broadening of the spectral contacts of the response. This is of great importance in noise generation for many systems such as mechanisms using contacts to transform motions and forces. It can be also of great importance for tribologists preoccupied with preventing damage.

J. Perret-Liaudet and E. Rigaud
Laboratoire de Tribologie et Dynamique des Systèmes, UMR 5513
Ecole Centrale de Lyon
69134 Ecully cedex, France
joel.perret-liaudet@ec-lyon.fr
http://ltds.ec-lyon.fr/

R.A. Ibrahim et al. (Eds.): Vibro-Impact Dynamics of Ocean Systems, LNACM 44, pp. 215.
springerlink.com

On Impacts with Friction in Engineering Systems

Friedrich Pfeiffer

Abstract. For modeling contacts or more specifically impacts we have two possible concepts. Either we discretize the contact zone by applying some continuum mechanical approach, or we use a rigid body model, where the impact behavior follows from complementarity rules. It depends on the problem itself, which approach might be more convenient, more contact details in the first and more system aspects in the second case. In the following we shall consider the second method and apply it to large industrial problems.

1 Introduction

Impacts are contact processes of very short duration time, which generate in a small zone of the contact some typical deformations. Two arbitrarily approaching bodies with normal and tangential relative velocities produce normal and tangential impact forces, which deform the two bodies in normal and tangential directions and which include friction, though mainly in tangential direction. These deformations are accompanied by a partial conversion of the incoming kinetic energy into potential energy of the deformations, which act as a kind of spring on the bodies when moving apart again. The process generates energy losses by friction, which in special cases might be large enough to prevent a separation.

Modelling such processes requires the knowledge of the local stiffness around the point of contact. The corresponding forces put into the equations of motion usually lead to stiff differential equations. Such models make sense for problems, where we need to know the details of the impact deformations. For mechanical systems with many contacts the method results in very large computing times due to the elastic resolution of the individual impacts.

An alternative approach consists in rigid body models. We go from the above force/acceleration level of the equations of motion to an impulse/velocity level by

Friedrich Pfeiffer
Institute for Applied Mechanics, Technical University of Munich
Boltzmannstrasse 15, D-85747 Garching, Germany
pfeiffer@amm.mw.tum.de

R.A. Ibrahim et al. (Eds.): Vibro-Impact Dynamics of Ocean Systems, LNACM 44, pp. 217–230.
springerlink.com

integrating the equations of motion during the very small assumed duration time. Or better, we use the concept of measure differential equations instead of the classical equations of motion as suggested by Moreau. Working on an impulse-velocity-level instead on a force-acceleration-level turns out to be sufficient for a large variety of engineering problems, especially for large systems with many unilateral contacts.

The topic belongs to the more general field of non-smooth mechanics, which originally has been founded by J.J. Moreau [8], Montpellier, who not only established the mechanical but also the mathematical fundamentals of this new science, which represents a substantial extension of classical mechanics. As a matter of fact it is more than an extension, classical mechanics is in a sense a subset of non-smooth mechanics. Panagiotopoulos [9], Thessaloniki, Greece, completed the new theories by introducing inequalities with regard to non-convex features. Moreau and Panagiotopoulos both apply the idea of complementarity as one important and basic element for the theory. Most of their applications refer to problems of elastomechanics. Nevertheless and from the very beginning it was evident that the methods from Moreau and Panagiotopoulos could also be transfered to multibody dynamics. After long and fruitful discussions with Panagiotopoulos, who died much too early in 1998, the author's former Institute started about eighteen years ago to establish a theory for multibody systems with multiple unilateral contacts, which in the meantime has shown its reliability in many theoretical and practical tests ([11], [12], [10]).

2 Models

2.1 Classsical Approaches

With concern to classical theory we refer to [10] and [11]. For contacts we have the equations of motion together with the relative acceleration within the contact

$$\begin{aligned} &M\ddot{q} - h - [W_N + H_R,\, W_T] \begin{pmatrix} \lambda_N \\ \lambda_T \end{pmatrix} = 0 \quad \in \mathbb{R}^f \\ &\ddot{g}_N = W_N^T \ddot{q} + \overline{w}_N \quad \in \mathbb{R}^{n_N} \\ &\ddot{g}_T = W_T^T \ddot{q} + \overline{w}_T \quad \in \mathbb{R}^{n_T} \end{aligned} \tag{1}$$

and we have in addition the complementarity conditions in normal and tangential directions. In normal direction we get

$$\ddot{g}_N \geq 0, \;\; \lambda_N \geq 0, \;\; \ddot{g}_N^T \lambda_N = 0. \tag{2}$$

The conditions in tangential direction are

$$\begin{aligned} &|\lambda_{Ti}| < \mu_{0i}\lambda_{Ni} \quad \wedge \;\; \ddot{g}_{Ti} = 0 \quad (i \in I_T \;\; \text{sticking}) \\ &\lambda_{Ti} = +\mu_{0i}\lambda_{Ni} \quad \wedge \;\; \ddot{g}_{Ti} \leq 0 \quad (i \in I_N \backslash I_T \;\; \text{neg. sliding}) \\ &\lambda_{Ti} = -\mu_{0i}\lambda_{Ni} \quad \wedge \;\; \ddot{g}_{Ti} \leq 0 \quad (i \in I_N \backslash I_T \;\; \text{pos. sliding}) \end{aligned} \tag{3}$$

which also can be written in the form

$$y = Ax + b, \qquad y \geq 0, \quad x \geq 0, \quad y^T x = 0, \quad y, x \in \mathbb{R}^{n^*} \tag{4}$$

where $n^* = n_N + 4n_T$ in the case of decomposition into four and $n^* = n_N + 2n_T$ for a decomposition into two elementary corners, called "unilateral primitives" [6]. The magnitudes are: M mass matrix, q vector of generalized coordinates including the bilateral constraints, $W_{N,T}$ the constraint matrices due to contacts, H the sliding friction matrix, $\lambda_{N,T}$ the constraint forces, $\ddot{g}_{N,T}$ relative accelerations in the contact, μ_{0i} friction coefficients in Coulomb's law and the following index sets:

$$\begin{aligned} I_A &= \{1, 2, \ldots, n_A\} && \text{with } n_A \text{ elements,} \\ I_C(t) &= \{i \in I_A : g_{Ni} = 0\} && \text{with } n_C \text{ elements,} \\ I_N(t) &= \{i \in I_C(t) : \dot{g}_{Ni} = 0\} && \text{with } n_N \text{ elements,} \\ I_T(t) &= \{i \in I_N(t) : |\dot{g}_{Ti}| = 0\} && \text{with } n_T \text{ elements.} \end{aligned} \tag{5}$$

Considering impacts with friction we have to put these equations on a velocity level by integration over the impact time, which is as usual assumed to be infinitesimal small [5], [12]. Denoting the beginning of an impact, the end of compression and the end of expansion by the indices A, C, E, respectively, we get for $\Delta t = t_E - t_A$

$$\begin{aligned} M(\dot{q}_C - \dot{q}_A) - (W_N W_T) \begin{pmatrix} \Lambda_{NC} \\ \Lambda_{TC} \end{pmatrix} &= 0 \\ M(\dot{q}_E - \dot{q}_C) - (W_N W_T) \begin{pmatrix} \Lambda_{NE} \\ \Lambda_{TE} \end{pmatrix} &= 0 \end{aligned}$$

$$\text{with} \quad \Lambda_i = \lim_{t_E \to t_A} \int_{t_A}^{t_E} \lambda_i \mathrm{d}t \tag{6}$$

Here $\Lambda_{NC}, \Lambda_{TC}$ are the impulses in the normal and tangential direction which are transferred during compression, and Λ_{NE}, Λ_{TE} those of expansion. Defining $\dot{q}_A = \dot{q}(t_A)$, $\dot{q}_C = \dot{q}(t_C)$, $\dot{q}_E = \dot{q}(t_E)$ we express the relative velocities by [12]

$$\begin{aligned} \begin{pmatrix} \dot{g}_{NA} \\ \dot{g}_{TA} \end{pmatrix} &= \begin{pmatrix} W_N^T \\ W_T^T \end{pmatrix} \dot{q}_A + \begin{pmatrix} \tilde{w}_N \\ \tilde{w}_T \end{pmatrix}, \\ \begin{pmatrix} \dot{g}_{NE} \\ \dot{g}_{TE} \end{pmatrix} &= \begin{pmatrix} W_N^T \\ W_T^T \end{pmatrix} \dot{q}_E + \begin{pmatrix} \tilde{w}_N \\ \tilde{w}_T \end{pmatrix}, \\ \begin{pmatrix} \dot{g}_{NC} \\ \dot{g}_{TC} \end{pmatrix} &= \begin{pmatrix} W_N^T \\ W_T^T \end{pmatrix} \dot{q}_C + \begin{pmatrix} \tilde{w}_N \\ \tilde{w}_T \end{pmatrix}. \end{aligned} \tag{7}$$

The matrices W are the Jacobians from the constraints, they project the motion into the possible free directions. The vectors $\tilde{w}$ result from external excitations, whatsoever.

Considering in a first step the compression phase and combining the equations (6) and (7) we come out with

$$\begin{pmatrix} \dot{g}_{NC} \\ \dot{g}_{TC} \end{pmatrix} = \underbrace{\begin{pmatrix} W_N^T \\ W_T^T \end{pmatrix} M^{-1} \begin{pmatrix} W_N \\ W_T \end{pmatrix}^T}_{G} \cdot \begin{pmatrix} \Lambda_{NC} \\ \Lambda_{TC} \end{pmatrix} + \begin{pmatrix} \dot{g}_{NA} \\ \dot{g}_{TA} \end{pmatrix}, \tag{8}$$

where G is called the matrix of projected inertia. It consists of four blocks $G_{NN}, G_{NT}, G_{TN}, G_{TT}$. The mass projection matrix G is quadratic and symmetric, for the case with dependent constraints positive semi-definite, otherwise positive definite. The submatrices G_{NN}, G_{TT} possess the same properties as G and $G_{NT} = G_{TN}^T$ [2].

Equation (8) permits calculation of the relative velocities $\dot{g}_{NC}$ and $\dot{g}_{TC}$ at the end of the compression phase, depending from the velocities at the beginning of the impact $\dot{g}_{NA}$ and $\dot{g}_{TA}$ under the influence of the contact impulses Λ_{NC} and Λ_{TC}.

To evaluate these impulses two impact laws in normal and tangential direction are necessary. As already indicated magnitudes of relative kinematics and constraint forces (here impulses) are complementary quantities. In normal direction these are $\dot{g}_{NC}$ and Λ_{NC}. In tangential direction we have the relative tangential velocity vector $\dot{g}_{TC}$ and the friction saturation $[\Lambda_{TC} - (\mathrm{diag}\mu_{0i})\Lambda_{NC}]$. Decomposing the tangential behavior we obtain:

$$\begin{aligned} \Lambda_{TCV,i} &= \Lambda_{TC,i} + \mu_i \Lambda_{TN,i} \\ \dot{g}_{TC,i} &= \dot{g}_{TC,i}^{+} - \dot{g}_{TC,i}^{-} \\ \Lambda_{TCV,i}^{(+)} &= \Lambda_{TCV,i} \\ \Lambda_{TCV,i}^{(-)} &= -\Lambda_{TCV,i} + 2\mu_i \Lambda_{NC,i} \end{aligned} \tag{9}$$

Together with equation (8) this results in a Linear Complementary Problem (LCP) in standard form $y = Ax + b$ with $x \geq 0, \;\; y \geq 0$ and $x^T y = 0$:

$$\underbrace{\begin{pmatrix} \dot{g}_{NC} \\ \dot{g}_{TC}^{+} \\ \Lambda_{TCV}^{(-)} \end{pmatrix}}_{y} = \underbrace{\begin{pmatrix} G_{NN} - G_{NT}\mu & G_{NT} & 0 \\ G_{TN} - G_{TT}\mu & G_{TT} & E \\ 2\mu & -E & 0 \end{pmatrix}}_{A} \underbrace{\begin{pmatrix} \Lambda_{NC} \\ \Lambda_{TCV}^{(+)} \\ \dot{g}_{TC}^{-} \end{pmatrix}}_{x} + \underbrace{\begin{pmatrix} \dot{g}_{NA} \\ \dot{g}_{TA} \\ 0 \end{pmatrix}}_{b} \tag{10}$$

μ is a diagonal matrix, containing the friction coefficients of the contacts. The problem can be solved numerically. The velocities $\dot{g}_{NC}$, $\dot{g}_{TC}$ and the impulses Λ_{NC}, Λ_{TC} are either part of the result or can be obtained by the transformation (9) and by $\Lambda_{TC} = \Lambda_{TCV}^{(+)} - \mu\Lambda_{NC}$.

In the compression phase kinetic energy of the colliding bodies is stored as potential energy. During the expansion phase parts of this energy are released. This regaining process is governed by two coefficients of restitution in normal and tangential directions ε_N and ε_T respectively. They are empirical coefficients and must be measured.

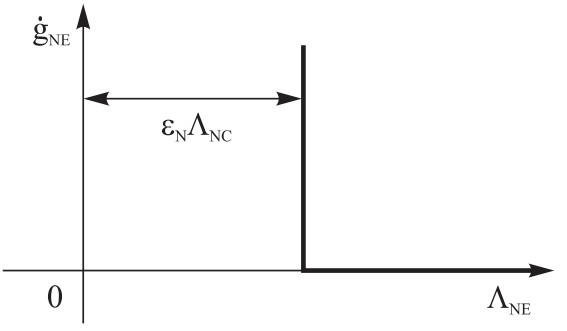

Fig. 1 Impact law for the phase of expansion in normal direction

In the case of multiple impacts Poisson's hypothesis does not guarantee impenetrability of the bodies. So the law is enhanced by an additional condition. The normal impulse during the phase of restitution Λ_{NE} is minimum with $\varepsilon_E\Lambda_{NC}$ in each contact, but can become arbitraryly large to avoid penetration. In this case the bodies remain in contact after the impact. This impact law with a complementary character is drawn in Figure 1.

In tangential direction the impact law is ruled by the following effects: at first a minimum impulse $[\varepsilon_N(\varepsilon_T\Lambda_{TC})]$ must be transfered. It is the impulse stored during compression reduced by losses due to Poisson's law, but as all contact actions in tangential direction are always connected with constraints in normal direction we have to consider also a loss due to ε_N. In addition the impulse must not exceed the friction limits. Between these limits a tangential relative velocity $\dot{g}_{TE0}$ appears, which is generated by an elastic effect: For tangential contacts we get an elastic compression of the local contact zone, which acts as a spring. The point of application of this tangential spring force is different from the contact point thus giving rise to a possible local tangential velocity. This velocity allows a restitution of the stored energy, if during the phase of restitution sticking occurs. The existence of $\dot{g}_{TE0}$ was detected by Beitelschmidt's measurements [2], it could be derived as a necessary correction. With

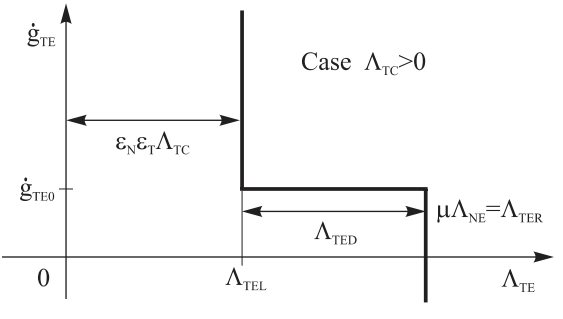

Fig. 2 Impact law for the phase of restitution in tangential direction

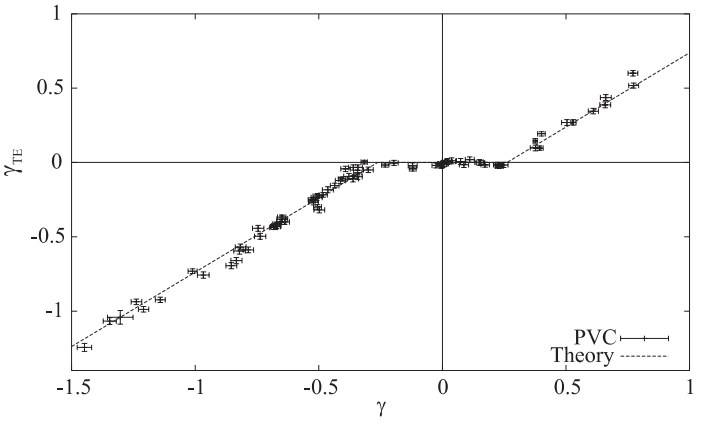

Fig. 3 Dimensionless tangential relative velocity after versus before the impact, measurements and theory, PVC-body, $\gamma = \frac{\dot{g}_{TA}}{-\dot{g}_{NA}}$, $\gamma_{TE} = \frac{\dot{g}_{TE}}{-\dot{g}_{NA}}$

$$\dot{g}_{TE0} = G_{TN}\varepsilon_N\Lambda_{NC} + G_{TT}\varepsilon_N\varepsilon_T\Lambda_{TC} \tag{11}$$

one can calculate $\dot{g}_{TE0}$ for all contacts and the tangential impact law looks like drawn in Figure 2. ε_N and ε_T are diagonal matrices containing the different coefficients for all contacts. To formulate the equation for the phase of restitution as a LCP similar to the compression phase the two matrices

$$\begin{aligned} S^+ &= \mathrm{diag}\left(\tfrac{1}{2}(1+\mathrm{sign}(\Lambda_{TC,i}))\right) \quad , \\ S^- &= \mathrm{diag}\left(\tfrac{1}{2}(1-\mathrm{sign}(\Lambda_{TC,i}))\right) \end{aligned} \tag{12}$$

are introduced. After some transformations similar to those of the compression phase the LCP writes

$$\begin{pmatrix} \dot{g}_{NE} \\ \dot{g}^+_{TEV} \\ \Lambda^{(-)}_{TEV} \end{pmatrix} = \begin{pmatrix} G_{NN} - G_{NT}S^-\mu & G_{NT} & 0 \\ G_{TN} - G_{TT}S^-\mu & G_{TT} & E \\ \mu & -E & 0 \end{pmatrix} \begin{pmatrix} \Lambda_{NP} \\ \Lambda^{(+)}_{TEV} \\ \dot{g}^-_{TEV} \end{pmatrix} + b \tag{13}$$

with

$$b = \begin{pmatrix} G_{NN}\varepsilon_N\Lambda_{NC} + G_{NT}S^+\varepsilon_N\varepsilon_T\Lambda_{TC} - G_{NT}S^-\mu\varepsilon_N\Lambda_{NC} + \dot{g}_{NC} \\ G_{TT}(S^+ - E)\varepsilon_N\varepsilon_T\Lambda_{TC} - G_{TT}S^-\mu\varepsilon_N\Lambda_{NC} + \dot{g}_{TC} \\ \mu\varepsilon_N\Lambda_{NC} - \varepsilon_N\varepsilon_T|\Lambda_{TC}| \end{pmatrix}. \tag{14}$$

After a corresponding solution the velocities $\dot{g}_{NC}, \dot{g}_{TC}$ and the impulses $\Lambda_{NC}, \Lambda_{TC}$ are either part of the result or can be obtained by the transformations:

$$\dot{g}_{TE} = \dot{g}^{+}_{TEV} - \dot{g}^{-}_{TEV} + \dot{g}_{TE0} \tag{15}$$

$$\Lambda_{NE} = \Lambda_{NP} + \varepsilon_N \Lambda_{NC}$$

$$\Lambda_{TE} = \Lambda^{(+)}_{TEV} + \Lambda_{TEL} = \Lambda^{(+)}_{TEV} + S^{+}\varepsilon_N \varepsilon_T \Lambda_{TC} - S^{-}\mu\Lambda_{NE} \tag{16}$$

If the impulses during the two phases of the impact are known, one can calculate the motion $\dot{q}_E$ of the multibody system at the end of the impact.

$$\dot{q}_E = \dot{q}_A M^{-1} \left(W_N(\Lambda_{NC} + \Lambda_{NE}) + W_T(\Lambda_{TC} + \Lambda_{TE})\right) \tag{17}$$

The above impact theory has been verified in [2]. More than 600 throwing measurements have been performed. Figure 3 depicts a typical result for a material pair PVC/PVC. The comparison with measurements is excellent, as in all other cases.

2.2 Recent Approaches

Moreau [8] suggested measure differential equations representing the equations of motion for systems with non-continuous phenomena. These equations contain a Lebesgue-measurable part for the continuous components and an atomic part based on a Dirac point measure for the impact parts (see also [6]). They write with $u = \dot{q}$

$$M(q,t)du - h(u,q,t)dt - W_N(q,t)d\Lambda_N - W_T(q,t)d\Lambda_T = 0\,. \tag{18}$$

The measure for the velocities $du = \dot{u}dt + (u^{+} - u^{-})d\eta$ is split in a Lebesgue-measurable part $\dot{u}dt$, which is continuous, and the atomic parts which occur at the discontinuity points with the left and right limits u^{+} and u^{-} and the Dirac point measure $d\eta$. Similarly, the measure for the impulses is defined as $d\Lambda = \lambda dt + \Lambda d\eta$.

In addition to this more general approach for the equations of motion we introduce a novel concept for the inequality constraints which originally comes from the linear programming field. It applies the proximal point idea from convex analysis [14] to develop the so-called "Augmented Lagrange Method" [1]. The proximal point of a convex set C to a point z is the closest point in C to z [7]

$$\mathrm{prox}_C(z) = \arg\min_{x^* \in C} |z - x^*|, \quad z \in \mathbb{R}^n, \tag{19}$$

which is illustrated in Figure 4. If we understand this convex set as the cut of a friction cone with different friction coefficients in the two contact directions, then every solution of the system falling outside the convex set is brought back to the boundary of the set. In the case of a complementarity in normal direction (contact/detachment-case) the set is just the half space with non-negative constraint forces λ_N. Therefore we get the relations

$$\lambda_N = \mathrm{prox}_{C_N}(\lambda_N - r g_N) \tag{20}$$

where C_N denotes the set of admissible normal contact forces

$$C_N(\lambda_N) = \{\lambda_N | \lambda_N \geq 0\}. \tag{21}$$

In the same manner we can put Coulomb's friction law (3) into the form

$$\lambda_T = \text{prox}_{C_T(\lambda_N)}(\lambda_T - r\dot{g}_T) \tag{22}$$

with C_T denoting the set of admissible tangential forces

$$C_T(\lambda_N) = \{\lambda_T | \quad |\lambda_{Ti}| \leq \mu_{0i}\lambda_{Ni}\}. \tag{23}$$

At this point we have to discuss the above expressions in more detail. We follow partly the very clear description of convex properties in the book of Leine [7]. He interprets the basic relationship for the constraints $[\lambda = \text{prox}_C(\lambda - rg)]$ as an "exact regularization", where r is the steepness parameter of this regularization. The above expression replaces the non-smooth contact laws by a prox-function, which is usually nonlinear, but which allows at the same time to reduce the whole system of the equations of motion together with the inequality constraints to a point mapping set. It can be treated by modern but well-known numerical methods.

Coming back to the expression $[\lambda = \text{prox}_C(\lambda - rg)]$ we see by a more heuristic consideration the following features: the relation can be satisfied only by left-hand and right-hand side expressions of equal sign or by left-hand and right-hand side expressions, which are zero. From this we may conclude the following results for a holonomic case (see [4] and [3])

$$[\lambda = \text{prox}_C(\lambda - rg)] \ \wedge \ [r > 0] \ \equiv$$

$$\equiv \begin{cases} \lambda = \lambda - rg & \text{if} \quad \lambda - rg \geq 0 \\ \lambda = 0 & \text{if} \quad \lambda - rg < 0 \end{cases} \tag{24}$$

The first case corresponds to an active contact with contact and no detachment, or it corresponds for the case $(g \ \rightarrow \ \dot{g})$ to an active tangential contact with stiction. The second case corresponds to a passive contact state. A more thourough consideration with respect to the equivalence of complementarities and the prox-representation may be found in [1] or [7].

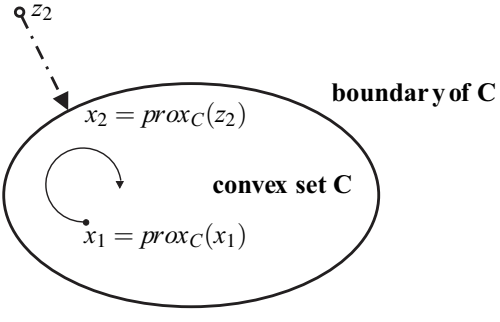

Fig. 4 The Proximal Point in Convex Analysis

Combining the contact laws (20) and (22) together with the equations of motion (18) we obtain a set of non-smooth continuous equations for the unknowns $\ddot{q}$, λ_N and λ_T

$$\begin{aligned} M(q,t)du - h(u,q,t)dt - W_N(q,t)d\Lambda_N - W_T(q,t)d\Lambda_T &= 0 \\ \lambda_N - \mathrm{prox}_{C_N}(\lambda_N - r\ddot{g}_N) &= 0 \\ \lambda_T - \mathrm{prox}_{C_T(\lambda_N)}(\lambda_T - r\ddot{g}_T) &= 0\,. \end{aligned} \tag{25}$$

which is a convenient form for applying the time stepping algorithm together with the Augmented Lagrange Idea for a numerical solution. It should be noted that the above equations contain the mechanics of general contacts and also the dynamics of impacts with friction.

3 Applications from Industry

A large body of industrial applications from power transmission to walking machines are presented in all details in [11]. In the following we shall focus on two typical examples, the vibration conveyor and the chimney damper.

3.1 Vibration Conveyor

Vibratory feeders are used in automatic assembly to feed small parts. They are capable to store, transport, orient and isolate the parts. An oscillating track with frequencies up to 100 Hz excites the transportation process, which is mainly based on impact and friction phenomena between the parts and the track. Vibratory feeders are applied for a wide variety of parts and for lots of different tasks. In the majority of cases, the parts are available as a sort of bulk material that is stored in a container. The transportation process, starting in this reservoir, is often combined with

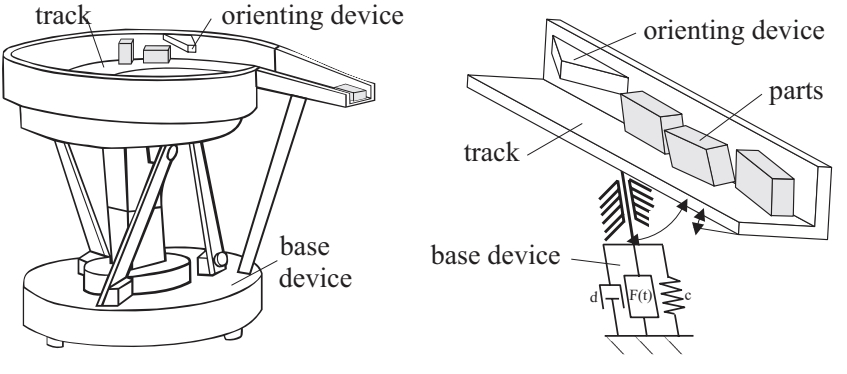

Fig. 5 Vibratory bowl feeder and mechanical model

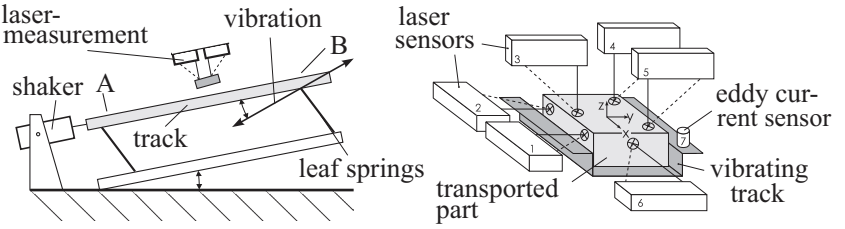

Fig. 6 Test setup and part measurement

orienting devices that orient parts, or select only these parts having already the right orientation (Figure 5 shows an example of a vibratory bowl feeder with an orienting device). Each kind of parts, with its special geometry and mechanical properties, requires an individual adaption of the feeder. This individual tuning comprises the development of suitable track and orienting device geometries and the adjustment of the excitation parameters frequency and amplitude. Due to the complex mechanics of the feeding process this design is usually done by trial and error without any theoretical background. A complete dynamical model of the transportation process allows a theoretical investigation and consequently an improvement of the feeder properties [15], [16].

Friction and impact phenomena between the parts and the track are the most important mechanical properties of transportation processes. Consequently, the required dynamical model has to deal with unilateral constraints, dry friction and multiple impacts. The mechanical model of the vibratory feeder can be split in two parts: the transportation process and the base device. The dissertation [15] focuses on modeling and simulation of the transportation process. The modeling of the base device can be done with well known standard technics for multibody systems.

For the verification of the developed model of the transportation process an experimental vibratory feeder was built, allowing different measurements concerning the impact model and the average transportation rates. Figure 6 shows the principle of the device. The track, fixed on leaf springs is excited with an electro magnetic shaker with a frequency about 50 Hz. The eigenfrequency of the system is at 52 Hz. The resulting vibration amplitude reaches a maximum value of about 2 mm. The track has an inclination angle $\alpha = 3^o$, the angle between the track and the direction

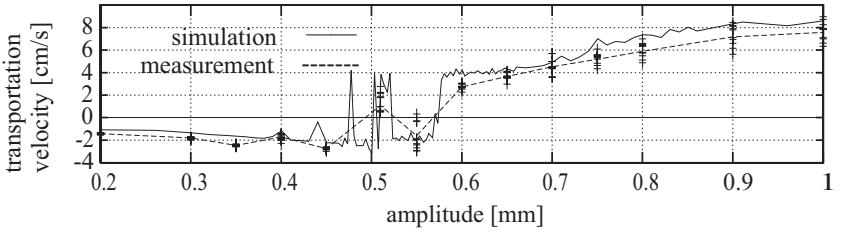

Fig. 7 Simulation and measurement of the average transportation rate

of the vibration is $\beta = 15^o$. For the accurate contactless measurement of the motion of the transported part six laser distance sensors were applied. For the vibration measurement of the track an eddy current sensor is used.

For a comparison of the theory and the measurements the averaged transportation rate was used. Figure 7 gives a result, which before the background of the complexity of the problem looks good. An interesting finding is the fact that the averaged transportation velocity does not depend very much on the number of parts and also not on the type of modeling, plane or spatial [15]. Therefore the design of vibration conveyors can be carried through considering one part only. For the layout of orienting devices we need of course a spatial theory.

3.2 Chimney Dampers

Towerlike structures like steel chimneys may be excited to vibrations by vortex streets. Such a mechanism becomes dangerous if the first eigenfrequency of the structure is small enough to be exited by not too large wind velocities which appear frequently. Oscillations of that type are damped significantly by a simple idea. A pendulum is attached to the chimney top. Its mass and length is tuned to the chimneys first eigenfrequency by classical analysis, and additionally optimal viscous damping is also evaluated by classical formulas, given for example by Den Hartog's method. In a second step the thus determined ideal damping behavior is not realized by viscous means but by a package of circular plates which are moved by the end of the pendulum rod through internal circular holes of the plates. The approximate realization of viscous damping by dry friction is accompanied by impacts of the pendulum rod in the plate holes and by stick-slip transitions between the plates. To achieve a best fit to the ideal viscous case an optimization of the complete

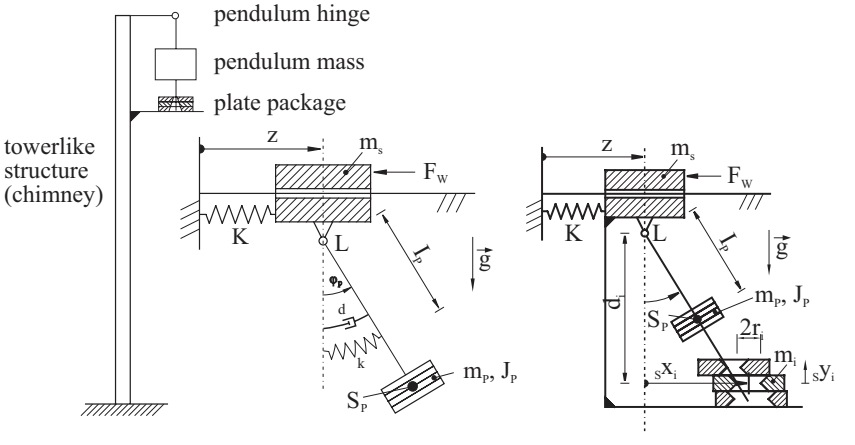

Fig. 8 Principal configuration, viscous and plate model

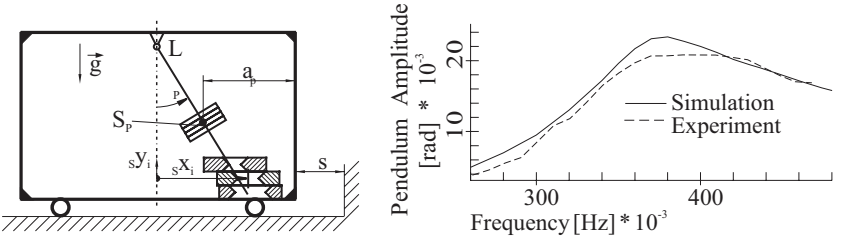

Fig. 9 Vibrating test-setup and a comparison theory/ measurements

pendulum-plate-system is carried through applying multibody theory with unilateral contacts [13].

Figure 8 illustrates the basic principle. At the top of the chimney a pendulum is arranged which damps the oscillations. To achieve best damping efficiency the damper is optimized in two steps. In a first step a classical damper is assumed working with viscous damping. For the resonance frequency area such a damper can be optimized with respect to length, mass and viscous damping of the pendulum. As damping will be realized by dry friction within a plate package, the plates must be selected in such a way that they perform a damping effect coming as nearest as possible to the optimal viscous damping. Therefore, in a second step the plate package will be optimized with respect to damping efficiency.

To verify the theory two types of experiments have been performed. In a first test a pendulum-plate-configuration has been arranged in a car-like frame with wheels, which could be excited periodically. Figure 9 depicts the results which compare well with theory.

A second test has been performed with a real steel chimney, which was bended by a steel rope. By releasing suddenly this rope the chimney starts to vibrate. This process has been measured and compared with the corresponding theory based on

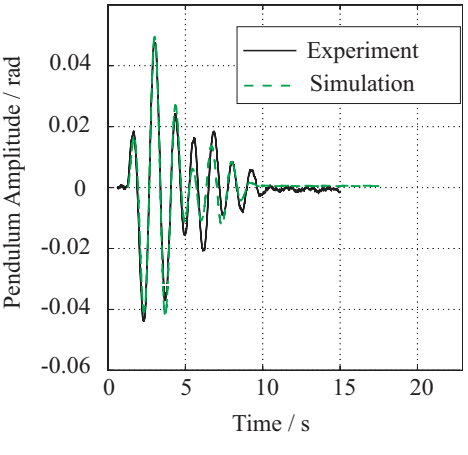

Fig. 10 Pendulum vibrations in a real chimney

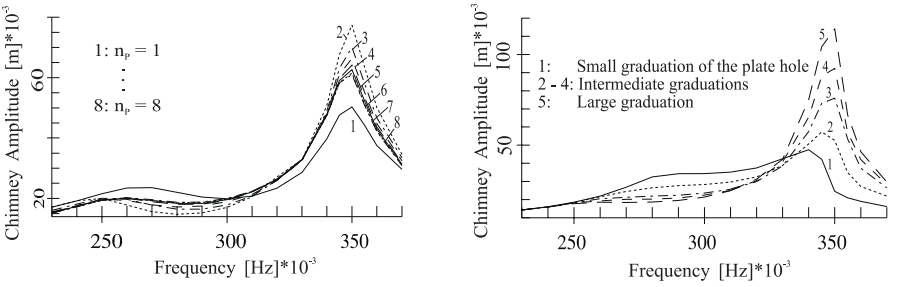

Fig. 11 Variation of plate number (left) and of graduation (right)

the equations of chapter 2. Figure 10 illustrates a comparison between experiment and simulation, which also confirms the methods presented.

If we approximate the optimal viscous system of Figure 8 (middle picture) by a package of plates, we can do that in a best way by optimizing the number of plates, their radii and thicknesses. We find that the number of plates affect the damping efficiency only partly. On the left side of Figure 11 the total mass of the plates is put constant, also the radius of the top at the ground damper plate. The number of plates is varied from one to eight. Doing so the distribution of the plate holes is kept linear. In the case of one plate the diameter of the plate hole is half as big as the largest one in all other cases.

Figure 11 shows that the damping mechanism works best with one plate and worst with two plates. The reason lies in the fact, that in the case of two plates only the upper one is moved effectively. The ground plate is ineffective and hence its damping is too small. As an important result it should be noticed, that the application of a large number of plates does not make sense. Obviously the damping characteristic cannot be improved by using more than five or six plates.

A further sensible parameter is the distribution of hole diameters over all plates, called graduation. The right graph of Figure 11 shows with number 1 the behavior of a system with small and with graph number 5 with a big graduation. The other curves belong to some intermediate graduations. Keeping the total mass of the plates constant an increasing graduation (from 1 to 5) leads to a decrease of damping and for the considered configuration to rising chimney displacements.

4 Summary

Impacts with friction in multibody systems with multiple contacts have been considered. A classical approach for modeling applies the complementarity idea for contacts and comes out with the necessary solution of linear or nonlinear complementarity problems. The second and more modern approach uses the concept of proximal functions to describe the contact and impact behavior. Both methods have to be treated numerically, where the second method offers a couple of advantages with respect to numerics.

The model has been applied to two industrial examples, a vibration vonveyor and a chimney damper, both systems possessing a rather large multibody structure. A comparison with measurements shows for both cases the reliability of the theory as presented.

References

[1] Alart, P.: CURNIER, A.: A Mixed Formulation for Frictional Contact Problems Prone to Newton-Like Solution Methods. Computer Methods in Applied Mechanics and Engineering 92, 353–375 (1991)

[2] Beitelschmidt, M.: Reibstösse in Mehrkörpersystemen. Fortschritt-Berichte VDI, Reihe 11, Nr. 275. VDI-Verlag Düsseldorf (1999)

[3] Foerg, M.: Mehrkörpersysteme mit mengenwertigen Kraftgesetzen - Theorie und Numerik. Fortschritt-Berichte VDI, Reihe 20, Nr. 411. VDI-Verlag Düsseldorf (2007)

[4] Foerg, M., Geier, T., Neumann, L., Ulbrich, H.: r-Factor Strategies for the Augmented Lagrangian Approach in Multi-Body Contact Mechanics. In: II European Conference on Computational Mechanics, Lisboa (2006)

[5] Glocker, C.: Dynamik von Starrkörpersystemen mit Reibung und Stössen. Fortschritt-Berichte VDI, Reihe 18, Nr.182. VDI-Verlag Düsseldorf (1995)

[6] Glocker, C.: Set-Valued Force Laws - Dynamics of Non-Smooth Systems. Springer, Heidelberg (2001)

[7] Leine, I., Nijmeijer, H.: Dynamics and Bifurcations of Non-Smooth Mechanical Systems. Springer, Heidelberg (2004)

[8] Moreau, J.J., Panagiotopoulos, P.D.: Unilateral Contact and Dry Friction in Finite Freedom Dynamics. Bd. 302. International Center of Mechanical Sciences (CISM), Courses and Lectures, Springer Wien (1988)

[9] Panagiotopoulos, P.D.: Hemivariational Inequalities. Springer, Heidelberg (1993)

[10] Pfeiffer, F.: Applications of unilateral multibody dynamics. Phil. Trans. R. Soc. Lond. A 359, 2609–2628 (2001)

[11] Pfeiffer, F.: Mechanical System Dynamics. Springer, Heidelberg (2008)

[12] Pfeiffer, F., Glocker, C.: Multibody Dynamics with Unilateral Contacts. John Wiley & Sons, Inc., New York (1996); Nayfeh, A. (ed.): Within the Wiley Series of Nonlinear Science

[13] Pfeiffer, F., Stiegelmeyr, A.: Damping Towerlike Structures by Dry Friction. In: Proc. of DETC 1997, ASME Design Eng. Techn. Conf. (1997)

[14] Rockafeller, R.T.: Convex Analysis. Princeton University Press, Princeton (1970)

[15] Wolfsteiner, P.: Dynamik von Vibrationsförderern. Fortschrittberichte VDI,Reihe 2, Nr. 511. VDI-Verlag Düsseldorf (1999)

[16] Wolfsteiner, P., Pfeiffer, F.: The Parts Transportation in a Vibratory Feeder. In: IUTAM Symposium on Unilateral Multibody Dynamics, München (1998)

Impact Mode Superpositions and Parameter Variations

V.N. Pilipchuk

Abstract. In this work, combinatorial impact modes are introduced as periodic motions of discrete linearly elastic systems with synchronous impacts of different particles with stiff constraints. Similarly to the idea of linear normal modes, these are still one-frequency vibrations admitting however multiple spatial shapes of the same temporal frequency. The number of such shapes depends on possible combinations of particles subjected to constraints and therefore can be much greater than the number of degrees of freedom. As the mode principal frequency moves above the upper boundary of the corresponding linear spectrum, the system energy is localizing on the particles interacting with constraints by absorbing the energy from the rest of the system. Using the triangular sine wave, as a new temporal variable, gives the corresponding exact closed form solutions. Based on such solutions, a parameter variation approach is suggested in order to describe non-periodic impact motions, for instance, - the evolution of local impact modes under damping conditions. The dynamic interaction of a dissipating impact and conservative linear oscillators is considered for illustration.

Keywords: Impact modes, Nonlinear localization, Nonsmooth temporal transformations.

1 Introduction

Vibration modes with impacts have been under study for several years [1], [2], [3], [4]. In practical terms, such studies deal with the dynamics of elastic structures whose amplitudes are limited by stiff constraints. These may be designed intentionally or occur due to a deterioration of joints. As a result, such kinds of dynamics are often accompanied by a rattling noise or dither during operating regimes of vehicles or machine tools. From the theoretical standpoint, the interest to such problems is

V.N. Pilipchuk
General Motors Technical Center, Warren, MI, USA

R.A. Ibrahim et al. (Eds.): Vibro-Impact Dynamics of Ocean Systems, LNACM 44, pp. 231–243.
springerlink.com

driven by the question what happens to linear normal modes as the energy of elastic vibrations becomes sufficient for reaching the constraints. Interestingly enough, some of the analytical approaches developed in the area recently found applications in molecular dynamics [5]. However, due to strong nonlinearities of the impact dynamics, most of the results relates to periodic particular solutions according to the idea of nonlinear normal modes [6]. Let us recall that the importance of linear normal modes is emphasized by the linear superposition principle as well as the parameter variation and averaging methods for weakly nonlinear cases. In this paper, a new parameter variation and averaging tools are introduced for impact modes. It is also shown that a specific combination of two impact modes gives another impact mode[1]. The corresponding manipulations with impact modes become possible due to the availability of closed form solutions derived through the triangular wave temporal substitution - the technique introduced first for smooth strongly nonlinear systems [7], [8] and then applied to impulsively loaded [9] and vibroimpact systems [3], [4]. In particular, it was shown that if the system between constraints is linear then the impact modes are described exactly in terms of closed form solutions. In contrast, approximate solutions for *smooth* nonlinear normal mode motions can be obtained in terms of polynomial expansions with respect to the triangular sine wave; see [6] and [10] for the related algorithms and applications.

The paper is organized as follows. First, Sections 2 and 3 illustrate a new parameter variation technique on one- and two degrees-of-freedom vibro-impact models, respectively. Then, Section 4 deals with the idea of superposition of impact modes in multiple degrees-of-freedom systems under multiple constraints conditions. Also, the high-energy asymptotic is considered which describes perfectly localized impact modes as a limit case of the infinitely large energy.

2 A One-Degree-of-Freedom Illustration

Let us consider a free harmonic oscillator under the constraint conditions as shown at the top of Fig. 1; this is one of the basic models considered in the theory of vibroimpact systems [11]. The constraints are assumed to be perfectly stiff and such that no energy loss happens when the oscillator strikes a constraint. Under the periodicity assumption, this model can be replaced by the free of constraints harmonic oscillator subjected to the periodic impulsive loading as shown at the bottom of Fig.1. Such an auxiliary model however is not a perfect equivalent of the original impact oscillator since it admits a broader class of solutions whose amplitudes may exceed Δ. Nevertheless, formal solutions and the corresponding impulses can be obtained in the form [4]

$$x = \Delta \frac{\sin[(\omega_0/\omega)\,\tau(\omega t + \alpha)]}{\sin(\omega_0/\omega)} \tag{1}$$

[1] Notice that the number of impact modes depends on the number of constraints and therefore can significantly exceed the number of degrees of freedom.

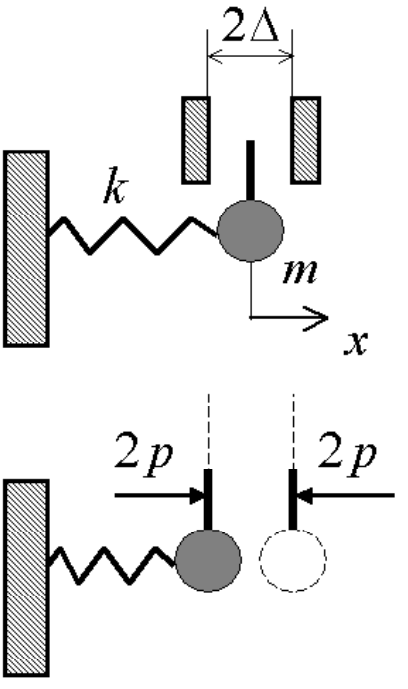

Fig. 1 The one-degree-of-freedom impact oscillator and its auxiliary model

$$p = \Delta\omega\omega_0 \cot(\omega_0/\omega) \tag{2}$$

where $\omega_0 = \sqrt{k/m}$ is an eigen frequency of the linear oscillator, the triangular sine wave function τ can be introduced in the closed form $\tau(\phi) = (2/\pi)\arcsin\sin(\pi\phi/2)$, and ω and α are arbitrary parameters determined by initial conditions.

Notice that the period of solution is $T = 4/\omega$ since the triangular wave' period is normalized to four in order to achieve the unit slope, $|\tau'(\phi)| = 1$; the corresponding sine-wave frequency is $\Omega = (\pi/2)\omega$. Further, assuming that $x(0) = 0$ and using solution (1), leads to expression

$$\frac{\omega_0}{\omega} = \pm\frac{1}{2}\arccos\left(1 - \frac{\omega_0^2\Delta^2}{E}\right) + k\pi; \qquad k = 0, 1, ... \tag{3}$$

where E is the total energy per unit mass.

If the total energy satisfies the condition $E \geq E_* = \omega_0^2\Delta^2/2$, and therefore the oscillator can reach the constraints, then the right-hand side of (3) is a sequence of real numbers. However, solution (1) describes a real motion of the impact oscillator only for the least root of the set (3), which insures that the oscillator remains within the region

$$|x| \leq \Delta \tag{4}$$

In order to illustrate the idea of parameter variations for solution (1), let us include the viscous damping into the model and represent the differential equations of motion between the constraints in the form

$$\begin{aligned} \dot{x} &= v \\ \dot{v} &= -2\zeta\omega_0 v - \omega_0^2 x \end{aligned} \tag{5}$$

where ζ is the damping ratio parameter.

In this case, the triangular wave frequency ω is not constant any more, although the amplitude of the vibration remains constant as long as the oscillator is in the impact regime. The corresponding parameter variation is implemented as a change of the state variables $\{x(t), v(t)\} \to \{\gamma(t), \phi(t)\}$, dictated by solution (1),

$$\begin{aligned} x &= \Delta\frac{\sin\gamma\tau}{\sin\gamma} \\ v &= \omega_0\Delta\frac{\cos\gamma\tau}{\sin\gamma}e \end{aligned} \tag{6}$$

where $\tau = \tau(\phi)$ and $e = \tau'(\phi)$ depend upon the fast phase $\phi = \phi(t)$, and $\gamma = \gamma(t)$ determines a relatively slow evolution of the temporal mode shape of the vibration.

Substituting (6) in (5), gives still exact equations

$$\begin{aligned} \dot{\gamma} &= 2\zeta\omega_0\cos^2\gamma\tau\tan\gamma \\ \dot{\phi} &= \frac{\omega_0}{\gamma}[1 + e\zeta(\sin 2\gamma\tau - 2\tau\cos^2\gamma\tau\tan\gamma)] \end{aligned} \tag{7}$$

Below, the first-order averaging procedure is applied. Notice that the right-hand side of equations (7) is periodic with respect to the phase ϕ. However, as proved in the attachment, the averaging can be conducted with respect to the variable τ over its interval $-1 \le \tau \le 1$. As a result, one obtains

$$\begin{aligned} \dot{\gamma} &= \zeta\omega_0\left(1 + \frac{1}{2\gamma}\sin 2\gamma\right)\tan\gamma \\ &= 2\zeta\omega_0\gamma + \frac{8}{45}\zeta\omega_0\gamma^5 + O(\gamma^6) \\ \dot{\phi} &= \frac{\omega_0}{\gamma} \end{aligned} \tag{8}$$

Keeping the leading-order term only on the right-hand side of the first equation in (8), gives solution

$$\begin{aligned} \gamma &= \gamma_0\exp(2\zeta\omega_0 t) \\ \phi &= \frac{1}{2\zeta\gamma_0}[1 - \exp(-2\zeta\omega_0 t)] \end{aligned} \tag{9}$$

A simple asymptotic analysis of expressions (6) and the remark after expression (3) give the parameter interval, $0 < \gamma < \pi/2$, within which the impact dynamics

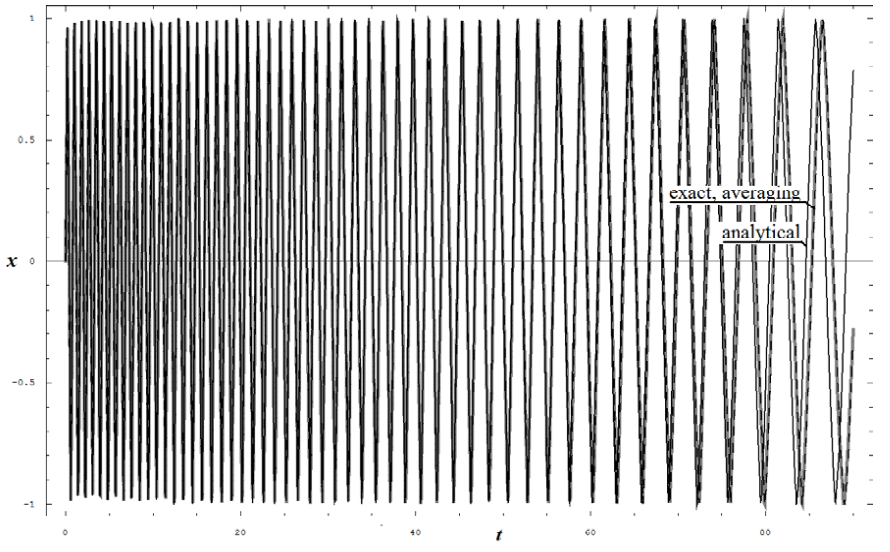

Fig. 2 The time history of the impact oscillator according to exact equations, those after the averaging, and the analytical closed form solution; the parameters are $\gamma_0 = 0.2$, $\zeta = 0.01$, $\omega_0 = 1.0$, and $\Delta = 1.0$.

takes place. The vibration mode shapes are close to the triangular wave near the left edge of the interval, but, as the energy dissipates and the parameter γ approaches $\pi/2$, vibrations become close to harmonic.

The total energy is expressed through the parameter γ in the form

$$E(t) = \frac{1}{2}\frac{\omega_0^2 \Delta^2}{\sin^2 \gamma(t)} \tag{10}$$

The duration of the impact stage of the dynamics is estimated via solution (9),

$$\gamma(t_{\max}) = \pi/2 \Longrightarrow t_{\max} = \frac{1}{2\zeta\omega_0} \ln\left(\frac{\pi}{2\gamma_0}\right) \tag{11}$$

where $\gamma_0 = \gamma(0)$.

As follows from Fig. 2, the above averaging procedure leads to practically no error of the time history record within the entire interval of validity of the approach. However, the analytical solution based on the reduced model gives some deviation from the exact curve at the end of the impact stage of the dynamics.

Notice that there is no impact interactions with the constraints for $t > t_{\max}$, where the model becomes harmonic oscillator whose amplitude exponentially decays due to the energy dissipation. At this stage, the transformation (6) is not valid any more nor there is any need in transformations. However, the question remains open about such solutions that would be capable of describing both impact and non-impact stages within the same unit-form expressions.

3 A Two-Degrees-of-Freedom Model

Let us consider the model shown in Fig. 3, where all the springs are linearly elastic. One-frequency motions with a predominant out-of-phase mode will be considered. It is known that such modes survive on high-energy levels with intensive impacts of the first mass with the constraints; see the next section for more details.

The differential equations of motion of the model can be represented in the form

$$\begin{aligned}\dot{x}_1 &= v_1\\ \dot{v}_1 &= -f_1(x_1,x_2,v_1,v_2)+pe'(\phi)\\ \dot{x}_2 &= v_2\\ \dot{v}_2 &= -f_2(x_1,x_2,v_1,v_2)\end{aligned} \tag{12}$$

where $pe'(\phi)=p\tau''(\phi)$ and

$$\begin{aligned}f_1(x_1,x_2,v_1,v_2) &= 2\zeta\Omega_1 v_1+\Omega_1^2 x_1+\beta(x_1-x_2)\\ f_2(x_1,x_2,v_1,v_2) &= \Omega_2^2 x_2-\beta(x_1-x_2)\end{aligned} \tag{13}$$

are impact and linear force components per unit mass, $\beta=k/m$ is the parameter of coupling, $\zeta=c/(2\Omega_1 m)$ is the damping ratio, and $\Omega_i=\sqrt{k_i/m}$ $(i=1,2)$.

The idea of parameter variations is implemented below as a change of the state variables, $\{x_1(t),v_1(t),x_2(t),v_2(t)\}\to\{\gamma(t),\phi(t),A(t),B(t)\}$:

$$\begin{aligned}x_1 &= \Delta\frac{\sin\gamma\tau}{\sin\gamma}\\ v_1 &= \Omega_1\Delta\frac{\cos\gamma\tau}{\sin\gamma}e\\ x_2 &= A\sin\frac{\pi\tau}{2}+B\cos\frac{\pi\tau}{2}e\\ v_2 &= -\Omega_1 B\sin\frac{\pi\tau}{2}+\Omega_1 A\cos\frac{\pi\tau}{2}e\end{aligned} \tag{14}$$

It is assumed in (14) that the principal frequency of the vibration, $\dot{\phi}(t)$, is dictated by the impact subcomponent rather then by a natural frequency of the corresponding linearized system. However, the scaling factor Ω_1 is still used in order to indicate the dominant oscillator of the dynamic process under consideration. Notice that $x_1$and $v_1$are transformed analogously to (6), whereas the transformation of x2 are v2 is based on the standard general solution of the harmonic oscillator represented however in the non-smooth temporal transformation form; see the attachments below for some details. Substituting (14) in (12) and taking into account remarks of the Attachment, gives

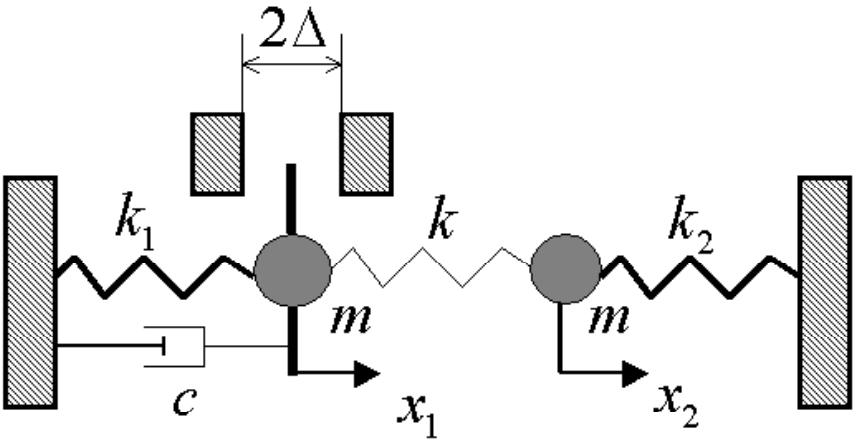

Fig. 3 The two-degrees-of-freedom model with viscous damping in the impact subcomponent

$$
\begin{aligned}
\dot{\gamma} &= \frac{e}{\Omega_1 \Delta}\cos\gamma\tau(f_1\sin\gamma - \Omega_1^2\Delta\sin\gamma\tau)\tan\gamma \\
\dot{\phi} &= \frac{1}{\gamma\Omega_1\Delta}[f_1\sin\gamma(\sin\gamma\tau - \tau\cos\gamma\tau\tan\gamma) \\
&\quad +\Omega_1^2\Delta\cos\gamma\tau(\cos\gamma\tau + \tau\sin\gamma\tau\tan\gamma)] \qquad (15)\\
\dot{A} &= -\frac{1}{2}\Omega_1 B(1-\cos\pi\tau) + \frac{1}{2}\pi B\dot{\phi} + (\frac{1}{2}\Omega_1 A\sin\pi\tau - \frac{1}{\Omega_1}f_2\cos\frac{\pi\tau}{2})e \\
\dot{B} &= \frac{1}{2}\Omega_1 A(1+\cos\pi\tau) - \frac{1}{2}\pi A\dot{\phi} - e\frac{1}{2}\Omega_1 B\sin\pi\tau + \frac{1}{\Omega_1}f_2\sin\frac{\pi\tau}{2}
\end{aligned}
$$

where the functions f_1 and f_2 are expressed through the new variables by substitution (14) in (13), and the impact term $pe'(\phi)$ has been eliminated by setting (compare with (2))

$$p = p(t) = \Delta\dot{\phi}(t)\Omega_1\cot\gamma(t) \qquad (16)$$

Further reduction of the system (15) includes two major steps, such as averaging with respect to the fast phase ϕ and applying the power series expansion with respect to the parameter γ. Since the periodic functions in equations (15) are expressed through the triangular sine wave $\tau(\phi)$ then the averaging can be implemented in terms of τ by using the rule of Lemma 1, which is proved in the Attachment. Then, keeping the leading-order terms of the power series expansions with respect to γ, gives

$$
\begin{aligned}
\dot{\gamma} &= 2\zeta\Omega_1\gamma \\
\dot{\phi} &= \frac{\Omega_1}{\gamma} \\
\dot{A} &= -B\left(\frac{\beta+\Omega_1^2+\Omega_2^2}{2\Omega_1} - \frac{\pi}{2}\dot{\phi}\right) \qquad (17)\\
\dot{B} &= A\left(\frac{\beta+\Omega_1^2+\Omega_2^2}{2\Omega_1} - \frac{\pi}{2}\dot{\phi}\right) - \frac{4\beta\Delta}{\pi^2\Omega_1}
\end{aligned}
$$

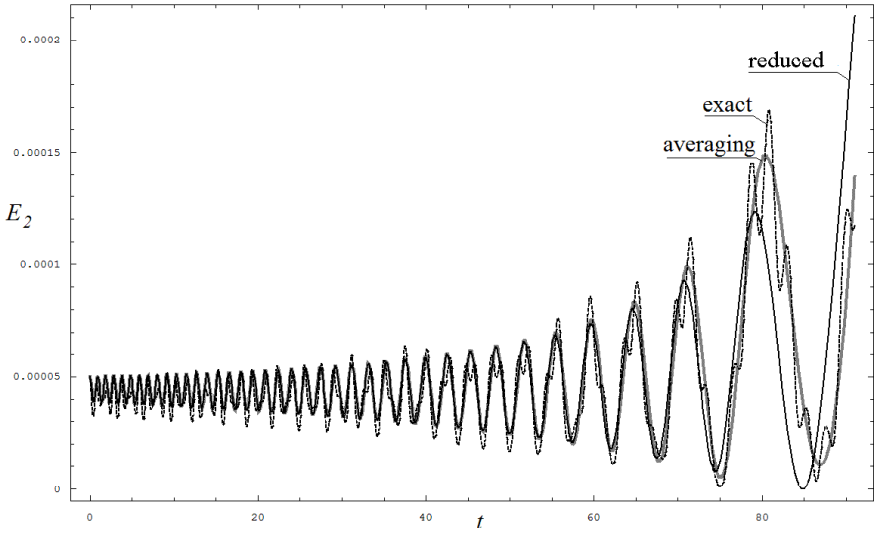

Fig. 4 The total energy of the second oscillator at relatively weak coupling, $\beta = 0.01$

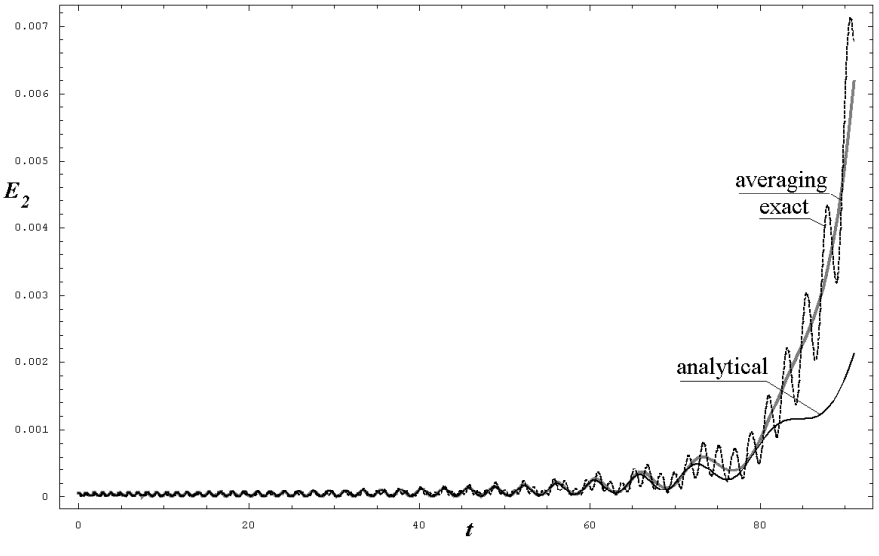

Fig. 5 The total energy of the second oscillator at stronger coupling, $\beta = 0.05$

Approximate equations (17) describe only one-way interaction between the oscillators so that the first two equations can be easily solved analytically by the analogy to the above one degree-of-freedom case. Then, substituting the result into the second two equations, gives a linear set of equations with variable coefficients for $A(t)$ and $B(t)$, which can also be considered analytically. Let us skip such kind of

analysis but illustrate the final result in Fig. 4 and Fig. 5 for two different strengths of the coupling β. The initial conditions and other parameters are selected as follows: $\gamma(0) = 0.2$, $\phi(0) = 0.0$, $A(0) = -0.01$, $B(0) = 0$, $\zeta = 0.01$, $\Omega_1 = \Omega_2 = 1.0$, $\Delta = 1.0$. The diagrams show the energy versus time of the second oscillator based on numerical solutions for three different equations, such as exact equations (15), the equations obtained by averaging (not described here), and the reduced set (17). The solutions are in quite a good match most of the time interval, however, the solution of truncated set (17) show some error near the end of the interval. This happens because the parameter γ is slowly approaching its limit magnitude $\pi/2$, at which the first oscillator stops interacting with the constraints and the entire system becomes linear. Remind that equations (17) were obtained by truncating the polynomial expansions in the neighborhood of $\gamma = 0$; as a result, the accuracy of the equations is low near the point $\gamma = \pi/2$. However, the precision can be improved significantly by keeping few more terms of the power series with respect to γ.

4 Impact Modes

Let us consider a mass-spring chain of N identical particles

$$\ddot{x}_n + \frac{k}{m}\left(-x_{n-1} + 2x_n - x_{n+1}\right) = 0 \tag{18}$$

$$n = 1, ..., N; \qquad x_0 = x_{N+1} = 0$$

under the constraint conditions; see Fig. 6, where k is the linear spring stiffness and m is the mass of each particle.

The constraint conditions are $|x_a| \le \Delta_a$ and $|x_b| \le \Delta_b$ or, in the vector form,

$$\left|\mathbf{I}_a^T \mathbf{x}\right| \le \Delta_a \text{ and } \left|\mathbf{I}_b^T \mathbf{x}\right| \le \Delta_b \tag{19}$$

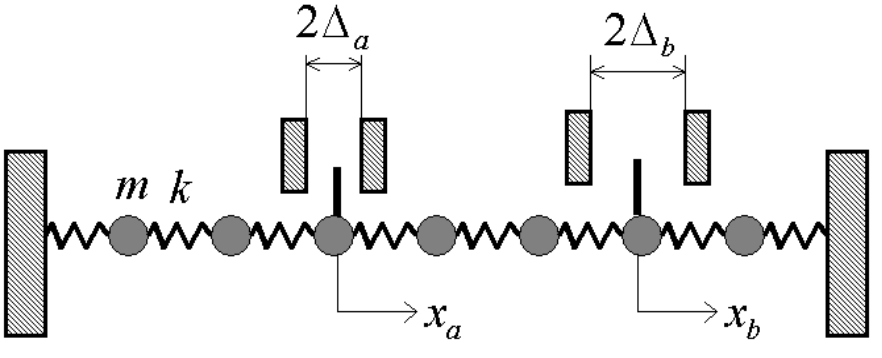

Fig. 6 The mass-spring chain with two masses under constraint conditions

where $\mathbf{x} = (x_1, ..., x_N)^T$ is the positional vector-function of time, and $\mathbf{I}_a = \left(0, ..., \underset{a}{1}, ..., 0\right)^T$.

Respectively, equations (18) take the vector form

$$\ddot{\mathbf{x}} + K\mathbf{x} = 0 \tag{20}$$

where K is a constant stiffness per unit mass matrix associated with equations (18).

If the vibration energy is low so that no constraints can be reached, then the system is linear and can be viewed as a finite element model of a continuous string. In this case, the jth mode vector and the related frequency are given by the expressions $K\mathbf{e}_j = \omega_j^2 \mathbf{e}_j$,

$$\mathbf{e}_j = \sqrt{\frac{2}{N+1}} \left(\sin\frac{\pi j}{N+1}, ..., \sin\frac{N\pi j}{N+1}\right)^T \tag{21}$$
$$\omega_j = \omega_{N+1} \sin\frac{\pi j}{2\,(N+1)}$$

where notation[2] $\omega_{N+1} = 2\sqrt{k/m}$ is introduced, and the basis vectors are normalized such that $\mathbf{e}_j^T \mathbf{e}_i = \delta_{ji}$.

In this case, the impulsive excitation on the right-hand side of auxiliary equation must act on the both ath and bth particles, so that the equation takes the form

$$\ddot{\mathbf{x}} + K\mathbf{x} = \omega^2 \left(P_a \mathbf{I}_a + P_b \mathbf{I}_b\right) \tau''(\omega t + \alpha) \tag{22}$$

where P_a and P_b are parameters to be determined.

The related solution of the period $T = 4/\omega$ includes terms related to P_a and P_b, and can be represented in the form

$$\mathbf{x} = \sum_{j=1}^{N} [P_a(\mathbf{e}_j^T \mathbf{I}_a)\mathbf{e}_j + P_b(\mathbf{e}_j^T \mathbf{I}_b)\mathbf{e}_j] \frac{\omega}{\omega_j} \frac{\sin(\omega_j \tau/\omega)}{\cos(\omega_j/\omega)} \tag{23}$$

Following the ideology of normal modes, let us assume that the impact mode periodic motion is accompanied by *synchronous* impact interactions with the constraints according to conditions

$$\mathbf{I}_a^T \mathbf{x} = \pm \Delta_a \text{ and } \mathbf{I}_b^T \mathbf{x} = \pm \Delta_b \text{ when } \tau = \pm 1 \tag{24}$$

Substitution (23) into (24) gives linear algebraic equations with respect to P_a and P_b in the form

$$\begin{aligned} K_{aa} P_a + K_{ab} P_b &= \Delta_a \\ K_{ba} P_a + K_{bb} P_b &= \Delta_b \end{aligned} \tag{25}$$

[2] Note that this is just a suitable notation since the $(N+1)$th frequency does not physically exist.

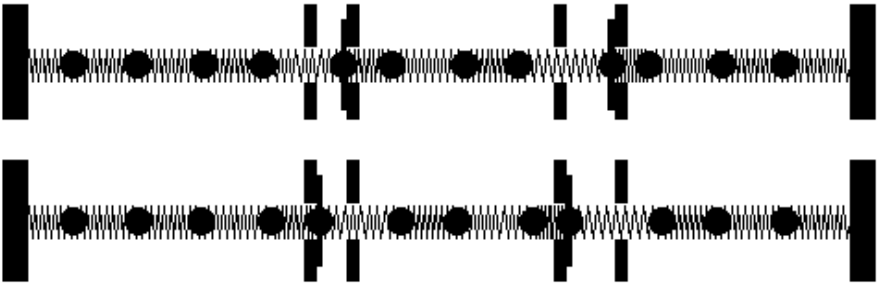

Fig. 7 Combined mode amplitude positions of the chain with two impacting particles

where

$$K_{ab} = \sum_{j=1}^{N} (\mathbf{e}_j^T \mathbf{I}_a)(\mathbf{e}_j^T \mathbf{I}_b) \frac{\omega}{\omega_j} \tan \frac{\omega_j}{\omega} \tag{26}$$

Expressions (23) and (25) give a formal impact mode solution, however the impact mode (23) exists for those frequencies ω at which the determinant of system (25) is non-zero, and also condition (19) holds.

Solution (23) can be viewed as a strongly non-linear superposition of the two impact modes, in which a single mass only can reach its constraints. The result of the superposition is shown in Fig. 7.

Let us consider the higher frequency domain $\omega >> (2/\pi)\omega_N$ within which $\tan(\omega_j/\omega) > 0$ for all $j = 1, ..., N$. In this case, the coefficients K_{ab} (26) create the Gram matrix with non-zero determinant [2] and therefore system (25) always has a solution; other cases are discussed in [4]. The asymptotic estimation below confirms this conclusion.

Indeed, for $\omega >> (2/\pi)\omega_N$ all the ratios ω_j/ω are small and thus the following estimate holds

$$\frac{\sin[(\omega_j/\omega)\tau]}{\cos(\omega_j/\omega)} = \frac{\omega_j \tau}{\omega} + \frac{1}{2}\left(\frac{\omega_j}{\omega}\right)^3 \left(\tau - \frac{\tau^3}{3}\right) + O\left(\omega^{-5}\right) \tag{27}$$

Substituting (27) in (23) and (26), gives asymptotic solution for an arbitrary cth particle in the form

$$x_c = (P_a \delta_{ac} + P_b \delta_{bc})\,\tau - \frac{1}{4}\left(\frac{\omega_{N+1}}{\omega}\right)^2 \left(\tau - \frac{\tau^3}{3}\right) \times \tag{28}$$
$$\times [P_a(\delta_{a,c-1} - 2\delta_{ac} + \delta_{a,c+1}) + P_b(\delta_{b,c-1} - 2\delta_{bc} + \delta_{b,c+1})] + O\left(\omega^{-4}\right)$$

where $x_c = \mathbf{x}^T \mathbf{I}_c$.

The impact intensity parameters, P_a and P_b, are given by the linear algebraic system (25) with the coefficients

$$K_{ab} = \delta_{ab} - \frac{1}{6}\left(\frac{\omega_{N+1}}{\omega}\right)^2 (\delta_{a,b-1} - 2\delta_{ab} + \delta_{a,b+1}) + O\left(\omega^{-4}\right) \tag{29}$$

Therefore, $K_{ab} \longrightarrow \delta_{ab}$ as $\omega \longrightarrow \infty$, and equations (25) give the solution $P_a = \Delta_a$ and $P_b = \Delta_b$. In this limit, the vibration energy becomes localized on the two particles oscillating between the barriers with the triangular sine wave temporal shape,

$$x_c \sim (\Delta_a \delta_{ac} + \Delta_b \delta_{bc})\, \tau(\omega t + \alpha)$$

whereas all other particles remain at rest.

5 Attachment

Lemma 1. *Let $x(t)$ be a general periodic function of the period $T = 4a$ so that the following presentation holds [8]*

$$x(t) = X(\tau(\phi)) + Y(\tau(\phi))e(\phi) \tag{30}$$

where $\phi = t/a$, $e(\phi) = \tau'(\phi)$ and

$$\begin{aligned} X(\tau) &= \frac{1}{2}\left[x(a\tau) + x(2a - a\tau)\right] \\ Y(\tau) &= \frac{1}{2}\left[x(a\tau) - x(2a - a\tau)\right] \end{aligned} \tag{31}$$

Then the mean value of $x(t)$ over its period is

$$\frac{1}{T}\int_0^T x(t)dt = \frac{1}{2}\int_{-1}^{1} X(\tau)d\tau \tag{32}$$

In other words, the 'imaginary' component Ye of the 'hyperbolic number' (30) gives zero contribution into the mean value.

Proof. With no loss of generality, let us assume that $a = 1$ and thus $T = 4$. Then, during one period $-1 < t < 3$,

$$\begin{aligned} \tau'(t) = e(t) = 1 \quad &\text{and} \quad dt = d\tau \quad \text{for} \quad -1 < t < 1 \\ \tau'(t) = e(t) = -1 \quad &\text{and} \quad dt = -d\tau \quad \text{for} \quad 1 < t < 3 \end{aligned}$$

Taking into account the above relationship and (30), gives

$$\frac{1}{T}\int_0^T x(t)dt = \frac{1}{4}\left[\int_{-1}^{1} x(t)dt + \int_1^3 x(t)dt\right]$$

$$= \frac{1}{4}\int_{-1}^{1}[X(\tau) + Y(\tau)]d\tau - \frac{1}{4}\int_{-1}^{1}[X(\tau) - Y(\tau)]d\tau = \frac{1}{2}\int_{-1}^{1} X(\tau)d\tau$$

Besides, the relationship $e^2 = 1$ holds almost everywhere and provides the combination (30) with a specific structure of hyperbolic complex numbers.

Example 1. Let $x(t)$ be a periodic function of the period T. Taking into account (30) and the above remark, gives

$$x^2 = (X + Ye)^2 = X^2 + Y^2 + 2XYe$$

Then, based on Lemma 1,

$$< x^2 > \equiv \frac{1}{T}\int_0^T x^2 dt = \frac{1}{2}\int_{-1}^{1}(X^2 + Y^2)d\tau \tag{33}$$

Example 2. Consider the case $x(t) = A\sin t + B\cos t$, where $T = 2\pi$ and $a = \pi/2$. In this case, relationships (31) give $X(\tau) = A\sin(\pi\tau/2)$ and $Y(\tau) = A\cos(\pi\tau/2)$. Therefore, (33) gives $< x^2 >= (A^2 + B^2)/2$.

References

1. Vedenova, E.G., Manevich, L.I., Pilipchuk, V.N.: Normal oscillations of a string with concentrated masses on nonlinearly elastic supports. Prikl. Mat. Mekh. 49(2), 203–211 (1985)
2. Zevin, A.A.: Localization of periodic oscillations in vibroimpact systems. In: XXXV Symposium Modeling in Mechanics, Gliwice, Poland, Politechnica Slaska, pp. 261–266 (1966)
3. Azeez, M.A.F., Vakakis, A.F., Manevitch, L.I.: Exact solutions of the problem of vibroimpact oscillations of a discrete system with two degrees of freedom. Prikl. Mat. Mekh. 63(4), 549–553 (1999)
4. Pilipchuk, V.N.: Impact modes in discrete vibrating systems with bilateral barriers. International Journal of Nonlinear Mechanics 36(6), 999–1012 (2001)
5. Gendelman, O.V., Manevitch, L.I.: Discrete breathers in vibroimpact chains: Analytic solutions. Physical Review E 78 (026609) (2008)
6. Vakakis, A.F., Manevitch, L.I., Mikhlin, Y.V., Pilipchuk, V.N., Zevin, A.A.: Normal modes and localization in nonlinear systems. Wiley, New York (1966)
7. Pilipchuk, V.N.: The calculation of strongly nonlinear systems close to vibroimpact systems. Journal of Applied Mathematics and Mechanics 49(5), 572–578 (1985)
8. Pilipchuk, V.N.: Transformation of oscillating systems by means of a pair of nonsmooth periodic functions. Dokl. Akad. Nauk Ukrain. SSR Ser. A (4), 37–40, 87 (1988)
9. Pilipchuk, V.N.: Application of special nonsmooth temporal transformations to linear and nonlinear systems under discontinuous and impulsive excitation. Nonlinear Dynam. 18(3), 203–234 (1999)
10. Ibrahim, R.: Liquid Sloshing Dynamics. Cambridge University Press, New York (2005)
11. Babitsky, V.I.: Theory of Vibroimpact Systems and Applications. Springer, Berlin (1998)

The Evolution of Analytical Treatments of Vibro-Impact Oscillators

Steven W. Shaw

Prior to 1980 vibro-impact systems had been studied, primarily in the context of impact dampers, by several researchers. The focus of those efforts was on the existence and stability of simple periodic responses, and their utility in vibration attenuation, generally using models with two degrees of freedom (DOF). The treatments of single DOF systems by Senator and two DOF systems by Masri and Caughey were the most sophisticated and thorough of these works. In the early 1980's, simulation studies by Thompson and Ghaffari showed that even the simplest single DOF vibro-impact model displayed a rich variety of previously unexpected responses, including chaos, and exhibited several interesting bifurcations relating these responses as system and/or excitation parameters were varied. Around the same time Holmes showed that a simple model for a ball bouncing on a vibrating table (a vibro-impact system with gravity as the restoring force) possessed Smale horseshoes, that is, the topology required for chaotic dynamics. Those works motivated my Ph.D. research on piecewise linear single DOF systems, including the limiting case of vibro-impact dynamics. We attempted to attack these problems by casting the traditional approaches used for analyzing periodic responses in these systems in the form of a more general Poincare map. This approach allowed for systematic local and bifurcation analyses, and provided the means to show that chaos, in the form of horseshoes were present in the system models. It was after completion of my Ph.D. in 1983 that I learned of the extensive, earlier work of Peterka on these systems, which included detailed observations about bifurcations and chaos using analog computer simulations. Also, around this time a number of people started to work on vibro-impact systems, focusing on the peculiarities that arise due to the non-smooth nature of the system dynamics. Most notable of these was the work by Nordmark, who developed systematic methods for investigating grazing dynamics and their attendant bifurcations, providing results which laid the foundation for many subsequent studies. In this paper I will briefly outline some of this history and show how these early studies of vibro-impact systems paved the way for several ongoing efforts in the area of piece-wise smooth systems. I will also show some very recent results by others on vibro-impact systems in some new application areas, including microsystems and turbomachinery.

Steven W. Shaw
Department of Mechanical Engineering
Michigan State University
East Lansing, MI 48824 USA

R.A. Ibrahim et al. (Eds.): Vibro-Impact Dynamics of Ocean Systems, LNACM 44, pp. 245.
springerlink.com

Analysis of Damage Propagation in Single Lap Joints in Impact Fatigue

George Tsigkourakos, Juan Pablo Casas-Rodriguez, and Vadim V. Silberschmidt

Abstract. Repetitive low-velocity impact loading can result in substantial damage in adhesively bonded joints after few impacts with low force levels compared to other types of loading. The main aim of this paper is to investigate the behavior of adhesive joints subjected to impact fatigue (IF) and standard fatigue (SF) as well as their combinations and compare their effect on damage in single lap joints (SLJs). Damage evolution in both SF and IF regimes is analyzed in terms of the deterioration of residual strength of joints after respective loading histories. Fractography analysis is implemented to correlate the residual stiffness reduction under IF and SF loading with the crack propagation behavior of SLJs.

1 Introduction

Last decades saw a continuous increase in the use of composites in naval structures. This development has been driven by improvements linked to the benefits of composite structures and components (due to their high strength-to-weight and stiffness-to-weight ratios, increased corrosion resistance etc.), improved stealth as well as the need to reduce the acquisition and maintenance costs of naval craft. Among the possible applications are, for instance, elements of superstructures, decks, advanced mast systems etc. There are also cases of introduction of complete composite structures for fast patrol boats, corvettes etc. These developments in naval architecture accelerate a transition to adhesive bonding as one of the main manufacturing techniques, and there is an obvious need for better information on performance of adhesive bonds in naval structures.

The latter are exposed to complicated loading histories that contain impact loads. This explains an increasing interest in the effect of impact fatigue (IF), i.e. repetitions of multiple low-energy impacts produced in components and structures [1], on damage and fracture in adhesive joints. The effects of IF are of considerable importance for structural integrity of components and structures because of the potential damage that can be generated after relatively few impacts at low force levels in comparison to SF loading [2].

George Tsigkourakos, Juan Pablo Casas-Rodriguez, and Vadim V. Silberschmidt
Wolfson School of Mechanical and Manufacturing Engineering
Loughborough University, Leicestershire LE11 3TU, UK

R.A. Ibrahim et al. (Eds.): Vibro-Impact Dynamics of Ocean Systems, LNACM 44, pp. 247–257.
springerlink.com

IF can have a detrimental impact on performance and reliability of components/structures, exacerbated by the fact that in many cases it is disguised (in loading histories) by non-impact loading cycles with higher amplitudes. Although IF is more dangerous than SF [3], it is less studied and explored. And though there is a broad understanding of the danger of high-energy single impacts, the studies of the effect of repetitive impacting on damage evolution has been usually reduced to very short series.

An extensive experimental program of impact fatigue tests has been implemented at Loughborough University (UK). Adhesive joints of aluminum and carbon-fiber reinforced laminates have been subjected to a controlled series of multiple tensile impacts using a fully instrumented specialized testing machine. This system allows force and deformation histories to be recorded with high precision for each loading cycle. Measurements of strains and a crack (delamination) growth have been accompanied by microstructural studies of fracture surfaces for both types of fatigue as well as for the case of quasi-static loading of composite joints.

Results of these studies of various aspects of impact fatigue of adhesive joints are presented elsewhere [1-4]. The main aim of this paper is to present some new results on the behavior of adhesive joints subjected to impact and standard fatigue and their effect on single lap joints.

2 Experimental Studies

The specimens used in this work in both IF and SF experiments are SLJs. They were manufactured using a clad 7075-T6 aluminum alloy and an adhesive/primer combination of FM-73M and BR 127 from Cytec Ltd (Figure 1). An electro-hydraulic fatigue testing machine with a digital controller was used in SF tests to generate constant-amplitude fatigue with the load ratio $R = 0.1$ and a loading frequency of 5 Hz. The average quasi-static failure force for specimens was 4.61 kN.

A program of IF tests was carried out using a modified CEAST RESIL impactor with a specimen being supported at one end in a vice and its opposite end struck repeatedly by a pendulum hammer, resulting in a dynamic uniaxial tensile loading mode. In the tests the pendulum hammer is released from a pre-selected initial angle in the range of 0º - 150º, which corresponds to a potential energy in the range of 0-4 J and velocity 0-3.7 m/s.

Three stages of experimental study were implemented. In Stage 1, after evaluating the quasi-static strength, SF tests were performed at 90%, 75% and 60% of that level until the specimen's failure to assess the fatigue lives of specimens in terms of respective numbers of cycles N_f^{SF}. IF tests were carried out at 0.5, 1, 2, 3 and 4 J until the failure and their corresponding fatigue lives (N_f^{IF}) were recorded.

With the known fatigue lives, Stage 2 of the experimental studies was implemented to investigate the damage accumulation resulting from two studied types of loading. So, undamaged specimens, similar to those used in Stage 1, were loaded under the same loading conditions but at this stage the number of cycles for each load corresponded to 80%, 60% and 40% of N_f^{SF}.

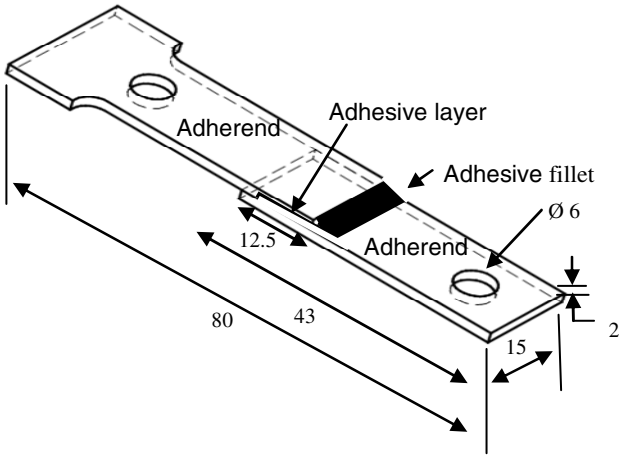

Fig. 1 Dimensions of single lap joint (in mm)

In a similar way, new IF tests were performed for the same energy levels with numbers of impacts equal to 80%, 60% and 40% of $N_{\mathrm{f}}^{\mathrm{IF}}$ that was obtained at Stage 1.

After described cyclic testing, both SF and IF specimens were subjected to quasi-static tensile tests until failure in order to determine their residual strength σ_{R}. The latter is used to analyze the process of mechanical deterioration of specimens due to damage caused by SF and IF loading.

The final stage of the experimental study – Stage 3 – was focused on the behavior of SLJs under combined IF and SF loading. The first group of experiments of this stage involved subjecting SLJs to SF followed by IF while the second group involved an inverse order of loading. Blocks of both SF and IF had different durations (in terms of numbers of cycles), shown in Table 1 as percentage of the respective fatigue lives – $N_{\mathrm{f}}^{\mathrm{SF}}$ and $N_{\mathrm{f}}^{\mathrm{IF}}$, respectively.

For SF, the force level in all the tests was 60% of the quasi-static strength, and for IF the energy level was 1 J.

Table 1 Various sub-cases of loading regimes at Stage 3

	Sub-case		
	a	b	c
Case 1	SF(16%) + IF(15%)	SF(8%) + IF(7.5%)	2 × [SF(4%) + IF(3.3%)]
Case 2	IF(15%) + SF(16%)	IF(7.5%) + SF(8%)	2 × [IF(3.3%) + SF(4%)]

3 Results and Discussion

Results of standard fatigue tests of Stage 1 are presented as a plot of the force amplitude, normalized with quasi-static strength *vs*. a number of cycles to failure N_f^{SF}, presented in semi-logarithmic coordinates in Fig. 2. It demonstrates a traditional, nearly linear decline in the area of high-cycle fatigue.

Since the controlled input parameter in the impact fatigue tests is the energy of the pendulum, linked to its initial angle, traditional Wöhler S-N diagrams are substituted with E-N ones ('E' is for energy). Figure 3 shows such a diagram that also demonstrates a nearly linear trend in semi-logarithmic coordinates presenting the increase in the fatigue life N_f^{IF} with declining impact energy E, thus confirming the previous experimental results [2].

When comparing IF and SF loading regimes, it can be seen that IF has a significantly greater detrimental effect on the fatigue life. It should be noted here that the maximum attained level of force in a single impact in IF with $E = 1$ J

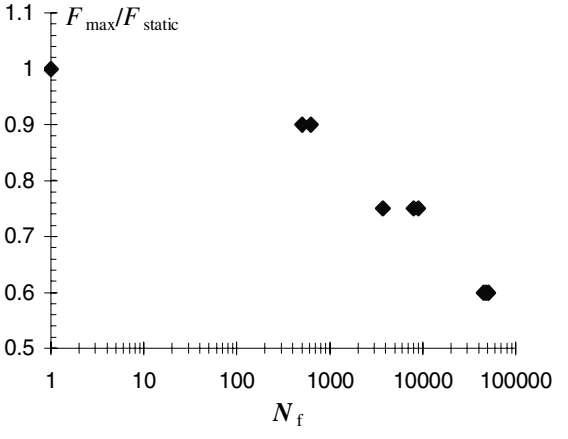

Fig. 2 Normalized S-N diagram for standard fatigue

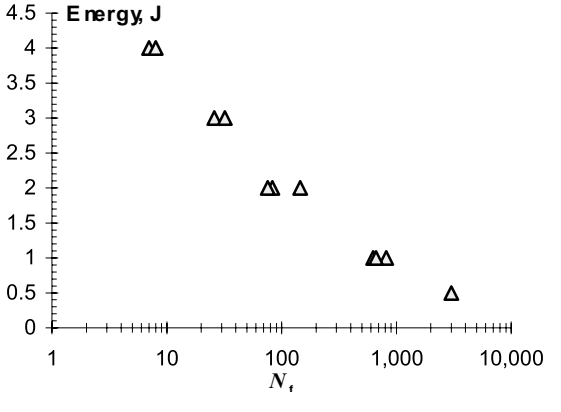

Fig. 3 E-N diagram for impact fatigue

corresponds to approx. 11% of the quasi-static strength of SLJs. Importantly, very low input energy levels still result in much shorter lives as compared to standard fatigue. It is worth noting here that the respective levels of maximum loads are well below the durability limit.

The scope of Stage 2 of the experimentation involved the comparison of SF and IF in terms of the decrease in residual strength with increasing number of cycles n - harmonic or impact – to which SLJs are exposed. This would provide useful information about the damage deterioration resulting from these two modes of loading.

At this stage, an extension of the Schaff and Davidson's model [5, 6] was used in order to predict this damage development in SLJs. This model is based on the prediction of residual strength $\sigma_{\mathrm{R}}(n)$ of a specimen under Variable Amplitude (VA) cyclic loading conditions. The model assumes that a residual strength for a block satisfies the following function;

$$\sigma_{\mathrm{R}}(n) = \sigma^{\mathrm{static}} - \left(\sigma^{\mathrm{static}} - \sigma_{\max}\right)\left(\frac{n}{N_{\mathrm{f}}}\right)^{\nu}, \tag{1}$$

where ν is the degradation parameter. This parameter was calculated for both IF and SF and was used together with Eq. (1) to predict the theoretical value of residual strength σ_{R}. Finally, experimental results and their approximations were compared, as shown in Figures 4 and 5 for SF and IF, respectively.

Damage accumulation under conditions of standard fatigue (Fig. 4) results in a sharp decline of residual strength only at the last stages of the specimens' lives. The Schaff and Davidson's model adequately describes only the lowest used force amplitude – 60% of quasi-static strength.

Nearly the same features are observed for impact fatigue (Fig. 5). Here, two cases corresponding to the lowest energy levels are fairly approximated by Eq. (1).

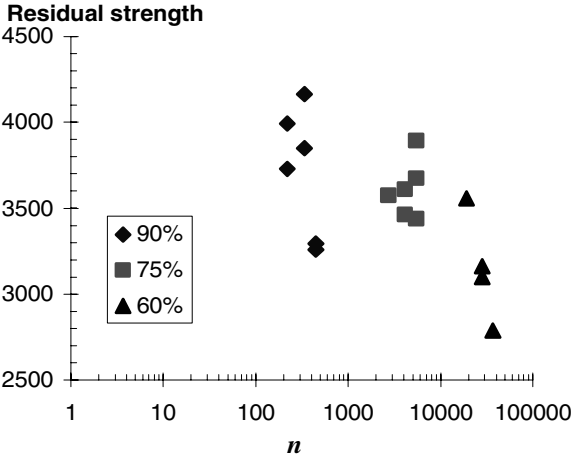

Fig. 4 Effect of the number of cycles in standard fatigue on residual strength (in N)

Obviously, only relatively short loading histories – significantly shorter than for standard fatigue – are required here to produce the same deterioration of mechanical properties. Large decreases in the σ_R value for all the energy levels (1-3 J) at numbers of cycles very close to failure – between 60% and 80% N_f^{IF} – are observed.

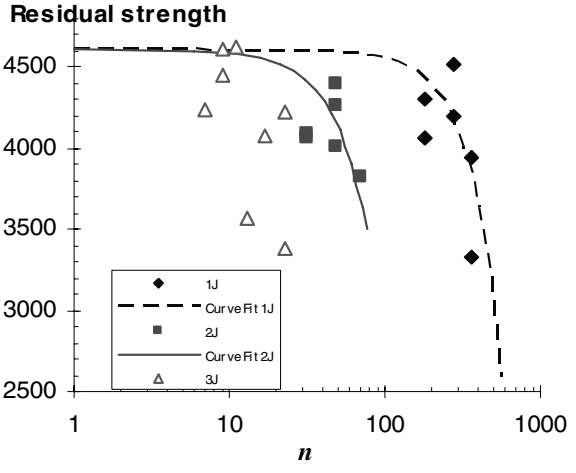

Fig. 5 Effect of the number of cycles in impact fatigue on residual strength (in N)

A significant scatter is noticeable in both IF and SF data, however it is more pronounced in IF. This can be attributed to the effects of microstructure that generally has a greater effect in IF than in SF [7].

It was shown above that the Schaff and Davidson's model can be used to describe the damage evolution in SLJs. This model can also be extended to multiple stress level loading [6]. In this section an investigation revealing whether this feature is true for combined IF and SF loading will be carried out.

The starting point involved defining the ways, in which the residual strength is decreasing in VA loading. It has been found [8] that the residual strength σ_R degrades by two different mechanisms:

a) Degradation due to cycles or impacts above the fatigue life or the energy threshold.
b) Degradation due to transitions from one load block to another having a higher value of mean stress $\Delta\sigma_{mn}$.

Assuming a linear damage accumulation, the residual strength degradation by each cycle can be defined as:

$$\sigma_R(n) = \frac{\sigma^{static} - \sigma_{max}}{N_f}.$$

So, Stage 3 of the research focuses on the effects of the specific parameters of the loading history that combines blocks of both standard and impact fatigue. The

chosen schemes, presented in Table 1, comprise blocks of varying durations as well as the order of their application: Case 1 starts with an SF block while Case 2 with an IF one. Since two types of blocks have different levels of maximum forces (stresses) this type of loading is similar to the varying amplitude fatigue. The obtained experimental results (Table 2) are rather inconsistent though some trends can be determined. Generally, when beginning with SF blocks, the residual strength tends to be higher than for the inversed order. This difference is small in sub-cases 1b and 2b.

A larger number of shorter blocks of loading cycles results in a more detrimental effect on residual strength. For instance, sub-cases c have the same number of SF cycles as sub-cases b (totaling 8% of $N_{\mathrm{f}}^{\mathrm{SF}}$) and a smaller number of impacts (6.7% of $N_{\mathrm{f}}^{\mathrm{IF}}$ instead of 7.5%) but in two blocks instead of one. And both Case 1c and Case 2c resulted in significantly reduced levels of stiffness.

One sub-case – not shown in Tables 1 and 2 – comprising a number of cycles equal in total to 32% of $N_{\mathrm{f}}^{\mathrm{SF}}$ and 22% of $N_{\mathrm{f}}^{\mathrm{IF}}$ (each in two blocks) – resulted in premature failures of all specimens of Case 2 and of a significant number of those of Case 1.

The inconsistency in experimental results for adhesively bonded joints is a well-known feature of cyclic loading histories, especially containing impacts [1-4]. This is explained by multiplicity of fracture/damage mechanisms, various realizations of which determine differences between specific fracture development scenarios.

Table 2 Results for average residual strength σ_{R} (in N) for combined SF and IF loading

Case 1a	Case 2a
3374	4055
Case 1b	Case 2b
4040	4097
Case 1c	Case 2c
2685	3302

4 Fractography

To better understand the fracture character in each case of cyclic loading, fracture surfaces of SLJs were studied. For the SLJ specimens tested in SF and IF until failure in Stage 1, fractographic analyses showed two main failure scenarios – cohesive failure and mixed-mechanism fracture paths. Cohesive fracture in SF was observed at force amplitudes equal to 90% and 75% of quasi-static strength (Fig. 6 a, b) while in IF at the energy level of 3 J (Fig. 7 a).

Mixed-mechanism fracture paths, combining cohesive fracture and delamination at the interface, were observed in SF specimens at lower amplitudes (60% of quasi-static strength) (Fig. 6c) while in IF in the energy range of 1-2 J (Fig. 7 b, c).

At the energy level of 2 J only a short interface fracture path is observed while at 1 J the fracture interface path is much greater.

Fractography data were obtained for damage propagation scenarios as well. For that reason four specimens were tested under SF conditions at 60% of quasi-static strength (3.6 kN) for 60% and 80% of $N_{\mathrm{f}}^{\mathrm{SF}}$. Similarly, four specimens were subjected to IF loading with impacts with energy of 1 J for 60% and 80% of $N_{\mathrm{f}}^{\mathrm{IF}}$.

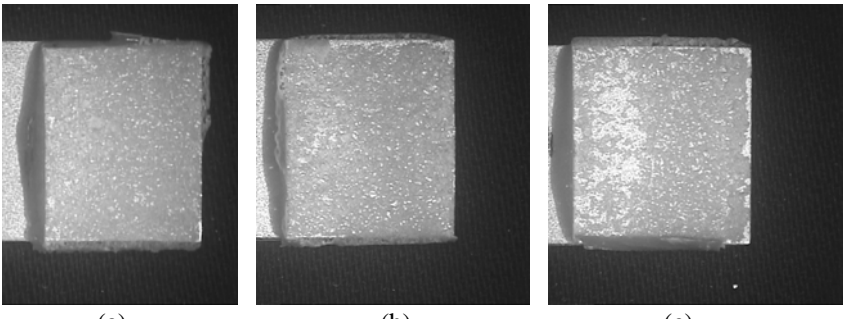

(a) (b) (c)

Fig. 6 Fractography of SLJs after SF with various the amplitudes: (a) 90%, (b) 75% and (c) 60% of quasi-static strength

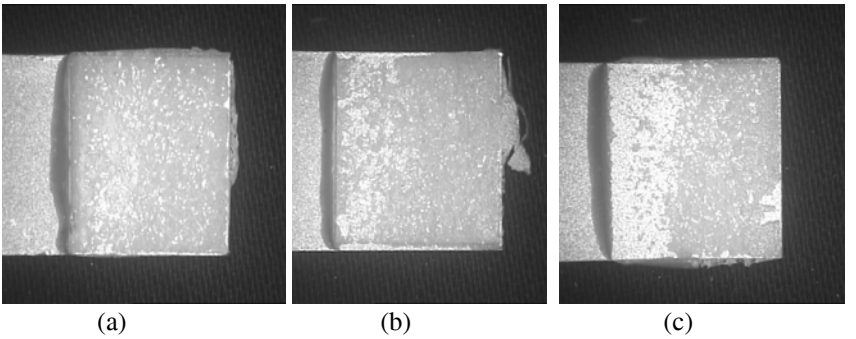

(a) (b) (c)

Fig. 7 Fractography of SLJs under IF for energy levels (a) 3 J, (b) 2 J and (c) 1 J

After testing, the eight specimens were sectioned across the x'-x axis (as shown in Fig. 8) and grinded with subsequently finer grit. The cracks in the prepared cross-sections were measured using an OLYMPUS BX60M microscope.

In Figures 9 and 10, obtained from examining the sectioned surfaces, the bright areas are the adherends and the dark ones belong to the adhesive in the fillet area. Positions of cracks are circled with white. The cracks are situated near the edges of adherends – areas with high stress concentration.

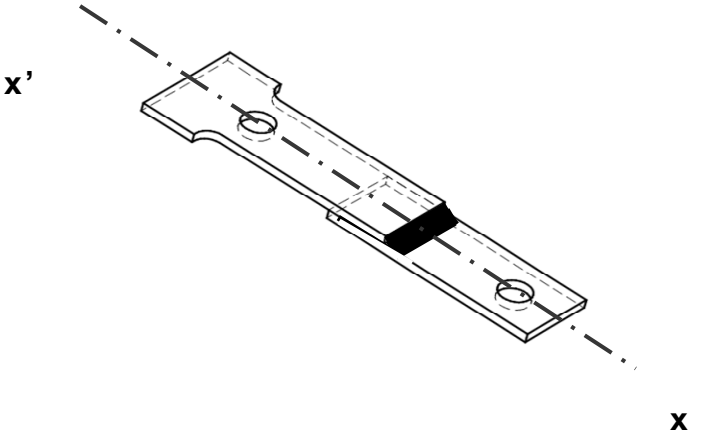

Fig. 8 Sectioning of SLJ

Fig. 9 Damage in SLJs exposed to to SF at (a) 60% Nf and (b) 80% of N_f

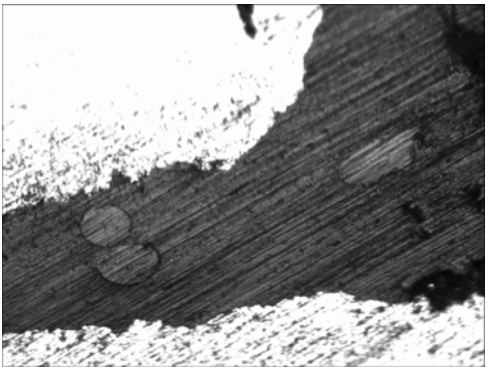

(a)

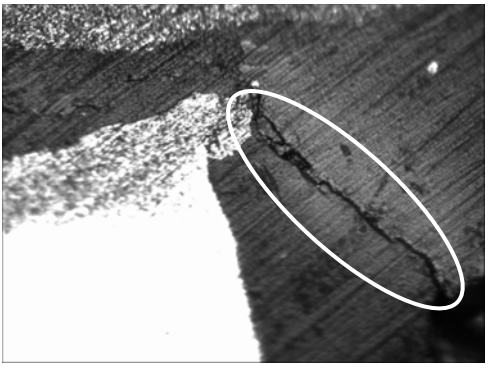

(b)

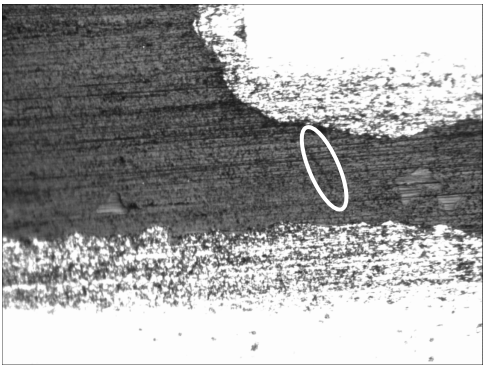

(a)

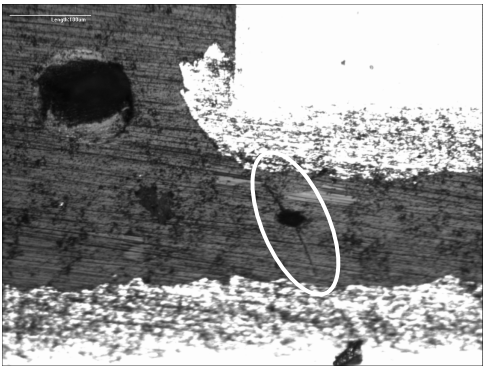

(b)

Fig. 10 Damage in SLJs exposed to to IF at (a) 60% N_f and (b) 80% of N_f

Generally, both in standard and impact fatigue the distributed damage begins accumulating between 40% and 60% of the fatigue life. Though there are no macroscopic cracks in the specimens their load-bearing capacity diminishes. Between 60% and 80% of N_f macro cracks are generated and start growing in the specimens; after 80% of N_f the crack propagation is rapid.

In IF, the crack propagation rate is higher than in SF manifested in a more sudden reduction in stiffness.

Small cracks were observed at 60% and 80% of the fatigue life for IF while for SF greater cracks occurred at 80% of N_f. The facts that IF cracks were smaller and that the reduction in stiffness is higher mean that crack growth rates in IF are higher than SF.

5 Conclusions

A detailed analysis of SF and IF of SLJs revealed that the latter loading regime has a far more detrimental effect on the fatigue life of joints. It was found that the

Schaff and Davidson's model is capable to describe damage evolution in adhesive bonds at some levels of external load; however, this model is inadequate for analysis of combined IF and SF loading. IF – as a single loading regime or as a part of a combined loading regime that includes also sinusoidal cycles – always results in a higher damage development in adhesive joints than SF. This type of loading results in an earlier transition to formation of the macroscopic crack; at advanced stages of the loading history it causes accelerated crack propagation. These differences are due to the changes in fracture mechanism (for more details see discussions in [2-4]).

Acknowledgement. The authors are very grateful for a partial financial support by the Royal Society within the framework of its International Joint Projects scheme.

References

[1] Casas-Rodriquez, J.P., Ashcroft, I.A., Silberschmidt, V.V.: Effect of impact-fatigue on damage in adhesive joints. Key Engng. Mater. 347, 653–658 (2007)

[2] Casas-Rodriquez, J.P., Ashcroft, I.A., Silberschmidt, V.V.: Damage evolution in adhesive joints subjected to impact fatigue. J. Sound Vibrat. 308, 467–478 (2007)

[3] Casas-Rodriquez, J.P., Ashcroft, I.A., Silberschmidt, V.V.: Delamination in adhesively bonded CFRP joints: Standard fatigue, impact-fatigue and intermittent impact. Compos. Sci. Technol. 68, 2401–2409 (2008)

[4] Casas-Rodriquez, J.P., Ashcroft, I.A., Silberschmidt, V.V.: Damage in adhesively bonded CFRP joints: Sinusoidal and impact-fatigue. Compos. Sci. Technol. 68, 2663–2670 (2008)

[5] Schaff, J.R., Davidson, B.D.: Life prediction methodology for composite structures. Part I-constant amplitude and two-stress level fatigue. J. Compos. Mater. 31, 128–157 (1997)

[6] Erpolat, S., Ashcroft, I.A., Crocombe, A.D., Abdel-Wahab, M.M.: Fatigue crack growth acceleration due to intermittent overstressing in adhesively bonded CFRP joints. Compos A 35, 1175–1183 (2004)

[7] Yu, J., Liaw, P.K., Huang, M.: The impact fatigue fracture of metallic materials. JOM 51, 15–18 (1999)

[8] Erpolat, S., Ashcroft, I.A., Crocombe, A.D., Abdel-Wahab, M.M.: A study of adhesively bonded joints subjected to constant and variable amplitude fatigue. Int. J. Fatigue 26, 1189–1196 (2004)

[9] Van Paepegem, W., Degrieck, J.: A new coupled approach of residual stiffness and strength for fatigue of fibre-reinforced composites. Int. J. Fatigue 24, 747–762 (2002)

Some Non-smooth Dynamical Systems in Offshore Mechanics

L.N. Virgin and R.H. Plaut

Abstract. Examples of vibro-impact mechanical and structural systems in the field of offshore engineering are not uncommon. Various buoyant systems incorporating mooring lines, tethers, rigid bodies, and risers are used for a wide spectrum of purposes, and they often exhibit non-smooth behavior when a characteristic changes abruptly, e.g., when a floating body contacts a rigid harbor, or a slack mooring line becomes taut. However, they present interesting challenges to the analyst and designer trying to predict both their static and dynamic behavior. The environmental conditions in a typical offshore situation naturally lead to stochastic effects, but even in a relatively simple deterministic context, the behavior can still be complicated and somewhat unpredictable. This paper considers two examples drawn from applications in offshore engineering in which a system characteristic (typically stiffness) undergoes a sudden change. They are the motion of a buoyant object restrained by cables, and the rocking of a container on a moving vessel. The primary focus of this paper is to consider relatively simple models, especially the subtle issue of accurately capturing the discrete change in stiffness, and to show the potential for complicated (highly erratic) dynamic behavior. Careful numerical simulation is the primary method of analysis.

1 Introduction

Mechanical systems with non-smooth characteristics occur commonly in practice, especially in the context of offshore engineering where the relatively harsh environment can lead to severe dynamic forcing of restrained dynamical systems. The need to tether or moor buoyant systems is commonplace, and it is the sudden change in a system characteristic (e.g., when a floating object comes into contact

L.N. Virgin
Department of Civil and Environmental Engineering
Duke University
Durham, North Carolina 27708
l.virgin@duke.edu

R.H. Plaut
Department of Civil and Environmental Engineering
Virginia Polytechnic Institute and State University
Blacksburg, Virginia 24061
rplaut@vt.edu

R.A. Ibrahim et al. (Eds.): Vibro-Impact Dynamics of Ocean Systems, LNACM 44, pp. 259–268.
springerlink.com

with a fixed body, or a mooring line becomes taut) that leads to the possibility of extremely complicated dynamic behavior.

By way of introduction, consider the situation shown schematically in Figure 1. There is a mass that can be considered to be free of external forces unless it either comes into contact with the rigid wall on the left-hand side, or a connected tether becomes taut and prevents the mass from moving beyond a certain point to the right. Hence we can associate these two conditions with the application of a suddenly applied restoring force. This is shown below in the plot of restoring force versus deflection (measured from an arbitrary position). There might typically be a small amount of stiffness rather than purely free motion for small deviations from the origin, and even after contact there might be a degree of compliance of the mass, wall, or tether such that the center of mass penetrates a little beyond the initiation of contact. The important modeling point is that the system is nonlinear, i.e., the stiffness is a function of position, even if it is constant over a range of deflections.

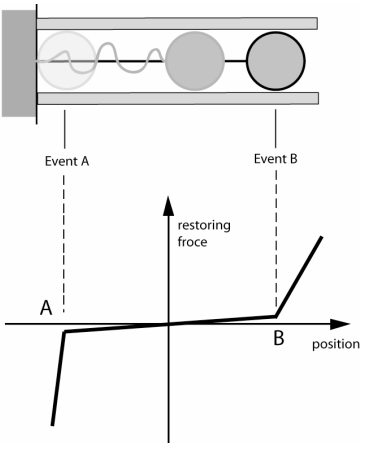

Fig. 1 A schematic showing abrupt changes in the stiffness characteristic

This type of nonlinearity can be considered as severe. That is, the behavior may be radically different according to whether the 'stiffer' regions of phase space are entered or not. A typical scenario might result in a situation in which the oscillations slowly grow until contact is encountered. This may cause a very different type of motion to result, in contrast to a linear system in which a small change to an input typically leads to a small change in the output, and even to many smooth nonlinear systems.

Two systems will receive focus in this paper. The first involves a tethered mass subject to sinusoidal forcing. The second considers a rigid block free-standing on a 'seesawing' foundation. Both of these systems exhibit behavior unique to dynamical systems with non-smooth characteristics.

2 A Tethered Object

A possible mechanism for mitigating the effects of wave action causing beach erosion or other storm damage is the concept of suspending buoyant cylinders

beneath the water surface. The buoyant cylinders are attached to the seabed via chains, and extract or repel energy from incoming waves. The motion of the cylinders consists of phases in which only buoyancy forces are acting and the cylinder would naturally float to the surface, and phases in which the tethered chains are stretched taut (or some are taut and some are slack). When a chain becomes taut, effectively an elastic rebound occurs, and the cylinder experiences a sudden change in direction of motion (Niedzwecki and Thampi, 1991; Huang and Vassalos, 1993). The oscillation process continues as the system is excited by wave action.

This situation is shown in Figure 2(a). The left-hand diagram illustrates the buoyant mass in equilibrium. The middle diagram shows the mass constrained by one of the chains with the other chain slack, and the right-hand diagram illustrates the mass with both chains slack. This situation can be viewed as a two-dimensional analog of the system described in Figure 1.

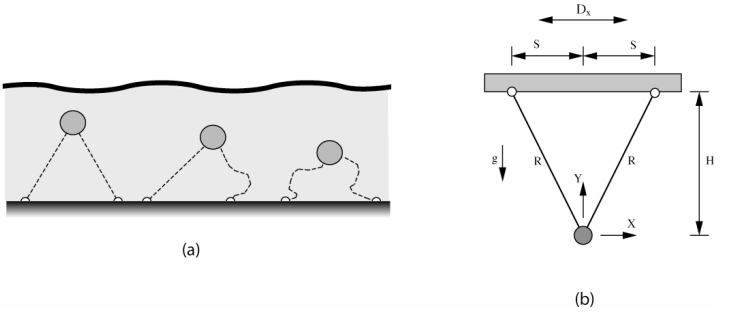

Fig. 2 (a) Submerged cylinders tethered to the seabed by chains; (b) A schematic of a hanging mass in a gravitational field

If we assume that the buoyancy is twice the weight of the mass, then this system is equivalent to a mass *m* that hangs under the influence of gravity (Onu et al., 1995; Plaut and Farmer, 2000). Such a system is shown schematically in Figure 2(b). In the original motivation for this model, the forcing (due to wave action) can be thought of as acting elliptically, and thus having components $F_x(T)$ and $F_y(T)$ in the x and y directions, respectively, where T is time. We consider the following nondimensional quantities (where X, Y, R, and H are shown in Figure 2(b)):

$$x = \frac{X}{S}, y = \frac{Y}{S}, r = \frac{R}{S}, h = \frac{H}{S}, t = T\sqrt{\frac{g}{S}}, f_x = \frac{F_x}{mg}, f_y = \frac{F_y}{mg}, \qquad (1)$$

with $r > 1$ and $h = (r^2 - 1)^{1/2}$.

A key modeling issue occurs when either of the cables becomes taut. These constraints correspond to circular arcs given by $g_1 = 0$ and $g_2 = 0$, where

$$g_1 = (1-x)^2 + (h-y)^2 - r^2, g_2 = (1+x)^2 + (h-y)^2 - r^2. \qquad (2)$$

If g_1 and g_2 are both less than zero, the equations of motion are particularly simple and are given by

$$\ddot{x} = f_x, \ddot{y} = f_y - 1, \tag{3}$$

where a typical forcing might be given by

$$f_x(t) = f_0 \cos \Omega t, f_y(t) = 0.5 f_0 \sin \Omega t. \tag{4}$$

The solution procedure then consists of numerically integrating equation (3) and monitoring the constraint conditions associated with equations (2). When g_1 or g_2 increases to zero, one of the cables becomes taut, and effectively an impact condition occurs. In the analysis, this involves reversing the sign of the normal velocity (in the axial direction of the cable). A coefficient of restitution can be incorporated. More modeling details are given in Farmer (1999) and Plaut and Farmer (2000).

Figure 3(a) shows a sample free response over a finite period of time. The coefficient of restitution $e = 0.9$. The mass is released from a certain xy location I with a given velocity (Plaut and Farmer, 2000). After a brief period of free-flight (under constant acceleration), one of the cables becomes taut and the system suddenly bounces back. These phases of free-flight and impact continue, and eventually the mass would approach a state of rest (equilibrium) at the origin (with both cables taut). Figure 3(b) demonstrates the case with the same initial conditions but $e = 1$. The motion simulation ends at point A with $y = h$, but since energy is conserved the motion would continue in an erratic manner.

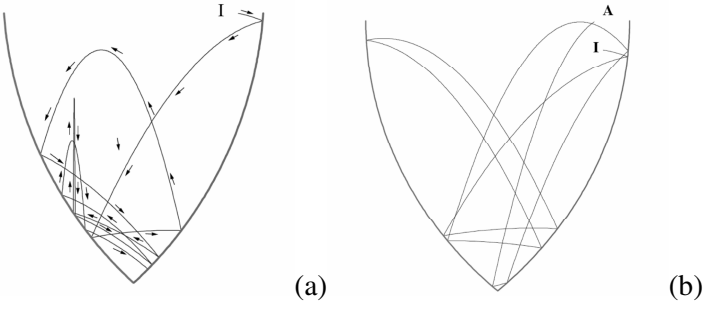

Fig. 3 Free motion of the mass; (a) e = 0.9, (b) e = 1

In the forced case it is possible to obtain a periodic motion in which the mass effectively bounces back as either cable becomes taut. Figure 4(a) shows an example, but it should be mentioned that maintaining a periodic solution in terms of numerical stability is an issue. Figure 4(b) shows another typical forced response. Here, $e = 0.9$, the magnitude of forcing $f_0 = 0.5$, the forcing frequency $\Omega = 0.9$, and $r = 2.5$. An erratic, possibly chaotic, response results (Plaut and Farmer, 2000).

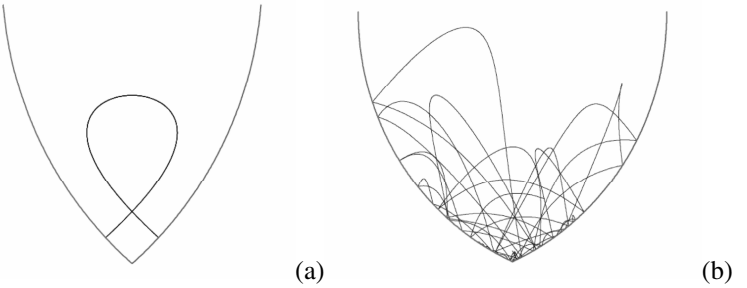

Fig. 4 Typical forced responses; (a) periodic behavior, (b) chaotic behavior

In order to gain some experimental insight into this type of system, we briefly focus attention on a purely horizontal excitation acting on the supports of the hanging mass (Figure 2(b)), operating in a regular gravitational field. In this case we introduce an additional nondimensional term $d_x = D_x/S$ and apply a displacement excitation $d_x = d_0 \sin \Omega t$. Adding a little continuous linear viscous damping with coefficient C results in the equations of motion

$$\begin{aligned} \ddot{x} &= -c\dot{x} \\ \ddot{y} &= -1 - c\dot{y}, \end{aligned} \tag{5}$$

where $c = (C/m)\sqrt{S/g}$. We note that here a relative value of x is used ($x_{rel} = x - d_0 \sin \Omega t$) since the support is being shaken in that direction. In the numerical simulation of equations (5) it is important to accurately capture the instantaneous taut condition; otherwise, numerical errors can accumulate.

A typical numerical result is shown in Figure 5 (Virgin et al., 2001). Here the parameters are set at $d_0 = 1.5$, $\Omega = 1.8$, and $r = 2$. The erratic nature of the response is readily apparent in the configuration space of Figure 5(a), even allowing for the decay of any induced transients starting from the prescribed initial conditions. Figure 5(b) uses the same data and plots the horizontal component for a range of time. This figure also exhibits vertical line segments at the discrete instants of time when either one of the cables becomes taut. Other types of behavior (e.g., periodic and quasi-periodic motion) are possible for other values of the system parameters (including weak forcing that is insufficient to initiate any relative motion).

A brief experimental study is described in Virgin et al. (2001). Without going into details, a small mass, able to freely slide on an inclined plane, was attached to angled cables and shaken. The subsequent bouncing of the mass as the cables alternated between being slack and taut was then captured by a strain gage attached to one end of a cable. Thus, although continuous data (e.g., the xy position of the mass) was not acquired, a discrete map was extracted, and it reflects the periodic (or otherwise) nature of the dynamic response.

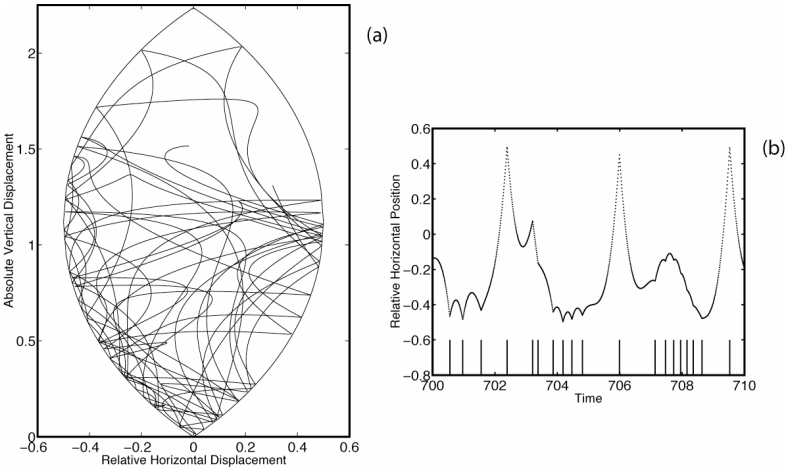

Fig. 5 (a) A typical numerical response under strong excitation; (b) the x-component of a portion of the motion from part (a) together with a discrete mapping of the time instants when either cable becomes taut

3 A Rigid Block on a Rolling Foundation

There are many situations in ocean engineering systems in which a floating platform exhibits dynamic behavior. In some cases, the focus of concern is the possibility of capsize (Virgin, 1987), but we may also have the case of a rigid block (or stacked blocks) resting on the deck of a floating ship or platform. Clearly, one

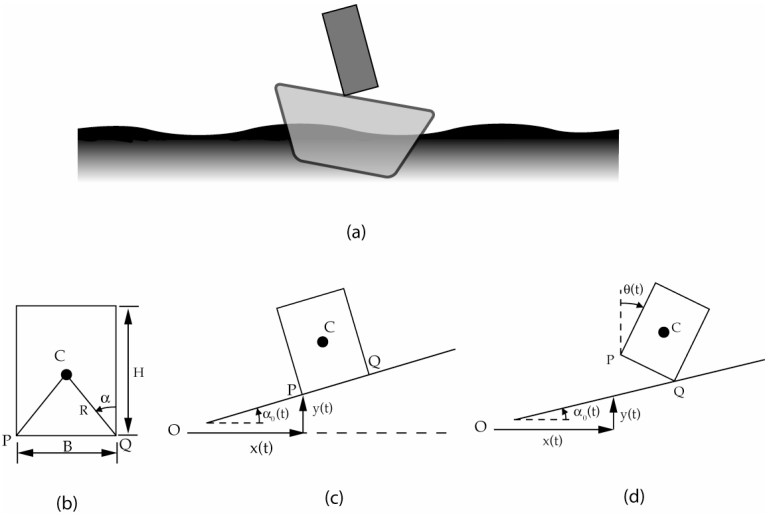

Fig. 6 (a) Schematic and (b)-(d) geometry of a rigid block rocking on a rolling deck

possibility is sliding. However, if the block is slender and there is a high coefficient of friction between the block and the deck, then the possibility of rocking is present, and even overturning (Yim and Lin, 1991; Plaut et al., 1996; Virgin et al., 1996).

Consider the situation shown schematically in Figure 6(a). The motion of the block is described by a single angle (relative to the angle of the deck). We shall consider a homogeneous rectangular block with center of mass at *C*, mass *M*, base *B*, and height *H*. Figures 6(b) to 6(d) show the other parameters of interest, and the goal here is to establish regimes of the forcing parameters (the magnitude and frequency of $\alpha_o(t)$) that lead to toppling of the block. We assume that the seesawing deck rotation is harmonic and of the form $\alpha_0(t) = \psi \sin \omega t$, where t is dimensional time, and thus we are especially interested in how the block responds as a function of ψ and ω.

We again present a brief overview of the important modeling equations. The nondimensional equation of motion is given by (Virgin et al., 1996)

$$\begin{aligned} &\frac{d^2\theta}{d\tau^2} - D\psi\Omega^2 \sin\alpha \sin\Omega\tau \sin(\alpha - S\theta - S\psi \sin\Omega\tau) \\ &-SD\psi^2\Omega^2 \sin\alpha \cos^2\Omega\tau \cos(\alpha - S\theta - S\psi \sin\Omega\tau) \\ &+S\sin(\alpha - S\theta) = 0 \end{aligned} \tag{6}$$

where $\Omega = \omega\left[I/(MgR)\right]^{1/2}$, $\tau = t\left[MgR/I\right]^{1/2}$, $I = (4/3)MR^2$, $D = MR^2/I = 3/4$ and S is the signum function, i.e., $S = +1$ for $\theta + \alpha_o > 0$ and S = –1 for $\theta + \alpha_o < 0$. The initial conditions are $\theta(0) = 0, \quad \theta'(0) = -\alpha_0'(0) = -\psi\Omega$ where a prime denotes differentiation with respect to τ. After 15 forcing cycles, ψ is set equal to zero in equation (6). We also introduce a new angle $\Theta(\tau) = \theta(\tau) + \alpha_o(\tau)$, i.e., a relative measure of the angle between the bottom of the block and the supporting deck.

As with the cable-mass system studied earlier, it is important to accurately model the impact condition when the block switches from rocking about one corner to the other (i.e., numerical capture of the $\Theta = 0$ condition). We shall present results for a block with a height-to-base ratio $H/B = 4$ and a coefficient of restitution of 0.912 in terms of the relative velocity $d\Theta/d\tau$.

Two sets of time series are shown in Figure 7 (Virgin et al., 1996). The left column shows 15 cycles of forcing on the bottom panel as well as plots of both absolute and relative angle and velocity. Free rocking motion ensues once the forcing has ceased, but during the period when the external forcing is acting the block does not topple over. The right panel shows a case in which the block overturns after about 8 forcing cycles.

It is most instructive to map out the combinations of forcing parameters ψ and Ω that lead to overturning (or not). Figure 8 presents results for the range $0 < \psi <$ 0.30 and $0 < \Omega < 7$ (Virgin et al., 1996). Below the dotted line, the block does not move relative to the foundation. The colors are associated with the number of impacts that occur before the block overturns, as described in the caption.

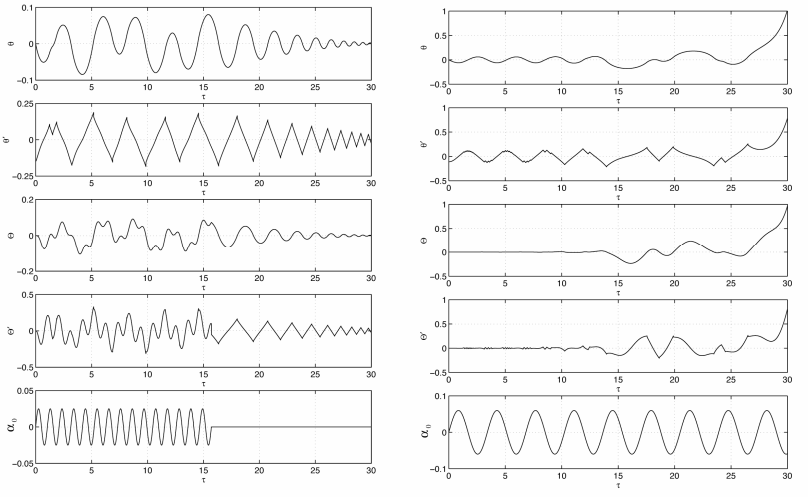

Fig. 7 Time series of the response. The forcing function is plotted in the lower panel. (a) $\psi = 0.025$, $\Omega = 6.0$; (b) $\psi = 0.06$, $\Omega = 1.84$

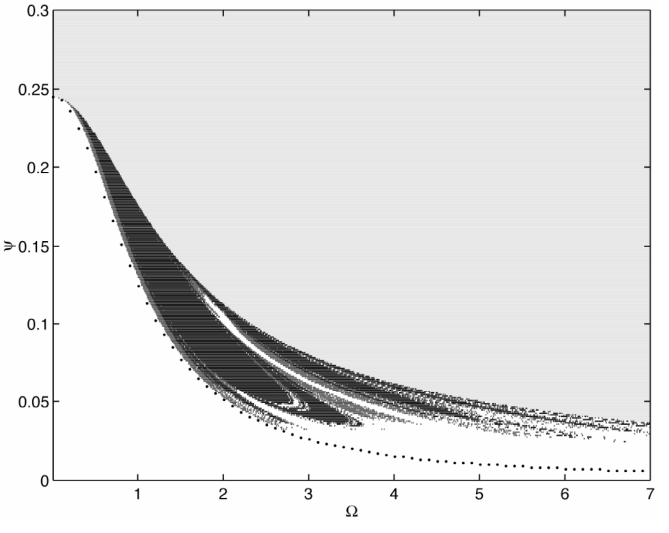

Fig. 8 Overturning of the block as a function of forcing parameters. The shading scheme corresponds to the number of impacts prior to overturning: light gray – no impacts; medium gray – 1-4 impacts; dark gray – at least 5 impacts; white – no overturning

A close-up view is provided in Figure 9 for $0.026 < \psi < 0.10$ and $2 < \Omega < 4$. In order to generate Figures 8 and 9, the forcing parameters were divided into a fine grid, and 210,700 numerical simulations were conducted to determine the overturning characteristics. It is interesting to note that there is the possibility of energy being imparted to the block, depending on the direction of the block

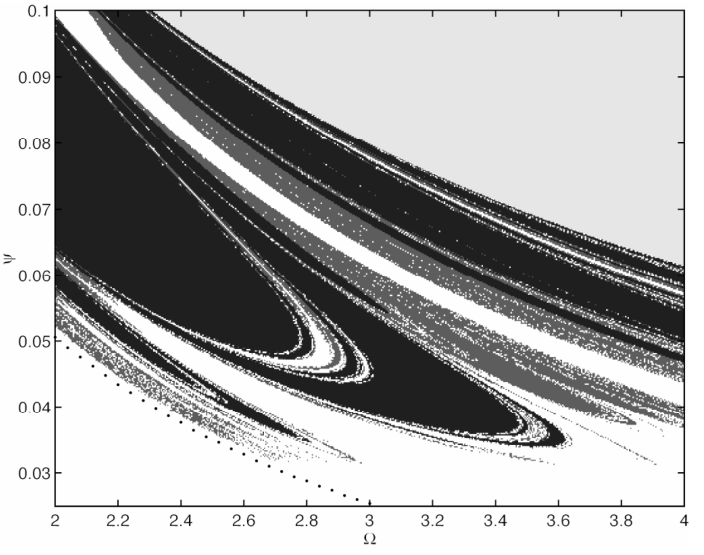

Fig. 9 A close-up view of the overturning of the block as a function of forcing parameters. See the caption of Figure 8 for details

motion relative to the base, and in this sense the problem bears some similarity with the cable-suspended-mass of the previous section. The boundary between overturning and not overturning is far from smooth, and exhibits certain fractal characteristics.

4 Concluding Remarks

This paper briefly describes two systems that have relevance to important problems in ocean engineering. They both involve a sudden change in a system characteristic tantamount to an impact condition. The first problem involves a mass suspended by cables. The behavior of the mass may be highly erratic, even in a deterministic description, as the cables alternately become slack and taut. In the second problem, a free-standing rigid block rests on a deck or foundation that rotates harmonically. The behavior of the block may also be highly erratic depending on the forcing, with overturning a possibility.

References

Farmer, A.L.: Investigation into Snap Loading of Cables used in Moored Breakwaters, M.S. Thesis, Virginia Polytechnic Institute and State University, Blacksburg, VA (1999), http://scholar.lib.vt.edu/theses/available/etd-112999-093701

Huang, S., Vassalos, D.: A numerical method for predicting snap loading of marine cables. Applied Ocean Research 15, 235–242 (1993)

Niedzwecki, J.M., Thampi, S.K.: Snap loading of marine cable systems. Applied Ocean Research 13, 2–11 (1991)

Onu, D., Hernried, A., Magana, M.: Robust control of a nonlinear two-cable suspended concentrated-mass system. In: Sture, S. (ed.) Engineering Mechanics (Proceedings of the 10th Conference), ASCE, NY, vol. 2, pp. 107–110 (1995)

Plaut, R.H., Farmer, A.L.: Large motions of a moored floating breakwater modeled as an impact oscillator. Nonlinear Dynamics 23, 319–334 (2000)

Plaut, R.H., Fielder, W.T., Virgin, L.N.: Fractal behavior of an asymmetric rigid block overturning due to harmonic motion of a tilted foundation. Chaos, Solitons & Fractals 7, 177–196 (1996)

Virgin, L.N.: The nonlinear rolling response of a vessel including chaotic motions leading to capsize in regular seas. Applied Ocean Research 9, 89–95 (1987)

Virgin, L.N., Fielder, W.T., Plaut, R.H.: Transient motion and overturning of a rocking block on a seesawing foundation. Journal of Sound and Vibration 191, 177–187 (1996)

Virgin, L.N., Nichols, J.M., Simmons, W.N., Plaut, R.H.: On the response of a shaken cable-suspended mass. ASME DETC2001/VIB-21552 (2001)

Yim, S.C.S., Lin, H.: Nonlinear impact and chaotic response of slender rocking objects. Journal of Engineering Mechanics 117, 2079–2100 (1991)

Effect of More Accurate Hydrodynamic Modeling on Calculating Critical Nonlinear Ship Rolling Response

Srinivas Vishnubhotla and Jeffrey Falzarano

Abstract. It is well known in the marine hydrodynamics field that the radiated wave force is frequency dependent. However, much work in the nonlinear marine dynamical systems field has assumed frequency independence or a constant coefficients approximation. Assuming constant coefficients may be a reasonable approximation for single frequency steady state motion and even the transient response of a nonlinear system with a single frequency excitation but clearly not for multiple frequency excitation. In this work we will assess the effect of approximating the radiated wave force by constant coefficients versus the more accurate impulse response function modeling. We will apply these two types of hydrodynamic force modeling to calculate critical dynamics of ship rolling motion in regular and irregular waves. The critical dynamics are directly determined using a unique calculation method (Vishnubhotla, Falzarano, Vakakis, 2000). This method directly calculates motions on either the stable and unstable manifolds. Since the stable manifolds form the basin boundaries, the safe basin can be defined. Moreover, this method can be used as an alternative to the so-called Melnikov method by directly calculating the distance between the stable and unstable manifolds. This method is potentially more powerful than Melnikov methods since is it not dependent upon the so-called "Melnikov trick" which practically limits the Melnikov method to first order. This paper will contain results of constant coefficients (for various constant frequencies) versus impulse response function for regular wave excitation and various spectra.

1 Physical System Modeling

In this work we study the single degree of freedom roll equation of motion with roll uncoupled from the other five degrees of freedom. The single degree roll equation of motion is as follows:

$$(I_{44} + A_{44}(\omega))\ddot{\varphi} + B_{44}(\omega)\dot{\varphi} + B_{44q}(\omega)\dot{\varphi}|\dot{\varphi}| + \Delta GZ(\varphi) = F_4(t)$$

Srinivas Vishnubhotla
Det Norske Veritas (U.S.A) Inc, Houston Texas

Jeffrey Falzarano
Ocean Engineering, Texas A&M University, College Station, Texas

R.A. Ibrahim et al. (Eds.): Vibro-Impact Dynamics of Ocean Systems, LNACM 44, pp. 269–274.
springerlink.com

In the above equation it can be seen that the added mass A_{44} and the radiated wave damping B_{44} are functions of frequency and are constants only if the external excitation is harmonic. Due to the softening nonlinearity of the roll restoring moment, the roll motion may be stable and bounded or unstable and unbounded. The focus of this work is to determine the basin boundary curve which separates these two types of motions. The so-called safe basin is the region in the phase space where initial conditions located in this region will remain bounded while initial conditions outside this safe region will not remain bounded. An alternative representation of the above equation which considers the frequency dependence of the hydrodynamic reaction force (see e.g., Cummins, 1962) is as follows:

$$(I_{44} + A_{44}(\infty))\ddot{\phi} + \int_{-\infty}^{t} K_{44}(t-\tau)\dot{\phi}(\tau)\,d\tau$$

$$+ B_{44q}(\omega)\dot{\phi}\,|\dot{\phi}| + \Delta GZ(\phi) = F_4(t)$$

In the above equation, the integral is the so-called convolution integral and represents the hydrodynamic force due to an arbitrary excitation. If the external excitation and response is not harmonic then a more accurate modeling of the linear radiated wave force is needed. In this paper we analyze the critical motion response or basin boundaries as they are affected by the more accurate hydrodynamic modeling represented by the impulse response function. In this study we consider the external excitation to be a multi-frequency summation or realistic representation of random sea waves and we study how the basin boundary is affected by this approximation.

2 Dynamics Solution Technique

It is well known in the nonlinear dynamics field that the safe basin boundary is simple when the excitation is small relative to the system's damping. However, as the excitation increases beyond a critical value the basin boundary or stable manifold may intersect the unstable manifold. This intersection results in a complicated fractal structure of the basin boundary. This critical amount of forcing can be approximately predicted using Melnikov methods (Falzarano, Shaw and Troesch, 1992). Although Melnikov methods are quite general (Zhang and Falzarano, 1994) and capable of analyzing e.g., multiple degrees of freedom system, they are practically limited to first order due to their use of the so-called "Melnikov trick." The Melnikov trick significantly simplifies the determination of the manifold separation since it only requires evaluation of the perturbed (with forcing and damping) differential equation along the unperturbed solution trajectory which is without forcing or damping. If the unperturbed equation is simple the solution may be known explicitly. Over the last several years we have been developing an alternative to Melnikov methods for analyzing nonlinear ship rolling motion which is based upon the theory of differential equations and was originally developed by Vakakis (1994). The method involves calculating solutions along the stable or

unstable manifold (see e.g., Figure 1). Recently, we have compared our results with those obtained numerically and those obtained using Melnikov methods and found that we obtained comparable results for harmonic excitation. Specifically the numerical results differed somewhat but the Melnikov results were exactly the same. In addition we have also applied this method to consider pseudo-random excitation and in this work we investigate the effect of including a more accurate hydrodynamic model.

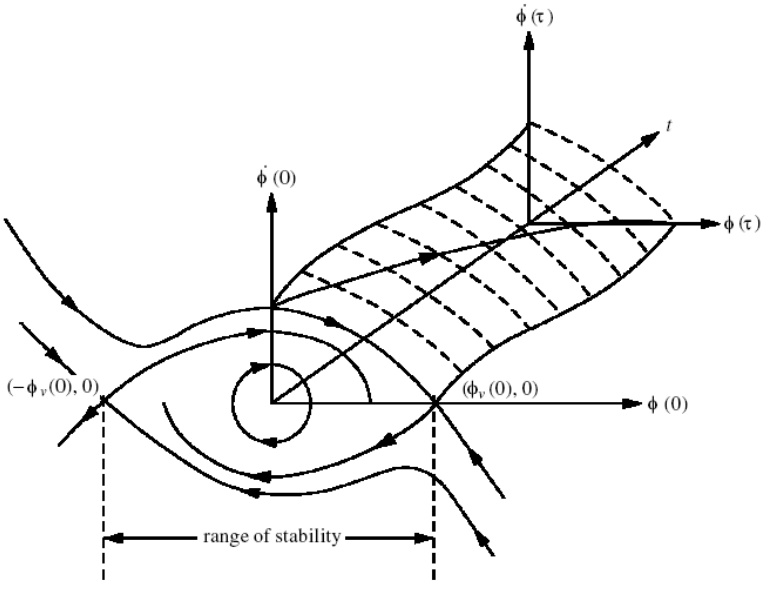

Fig. 1 Determination of Solution on Stable Manifold

The dynamics solution technique can basically be summarized as follows. First determine solution to unperturbed equation without damping or forcing. For example

$$\ddot{x} + x - k\,x^3 = 0$$

gives the unperturbed solutions as follows

$$x(\tau) = \frac{1}{\sqrt{k}} \tanh\left(\frac{\tau - \tau_0}{\sqrt{2}}\right),$$

$$\dot{x}(\tau) = \frac{1}{\sqrt{2k}} Sech^2\left(\frac{\tau - \tau_0}{\sqrt{2}}\right)$$

Next express scaled equation of motion as sum of an unperturbed and an additional perturbation, i.e.,

$$\ddot{x} + x - k x^3 = \varepsilon(-\gamma \dot{x} - \gamma_q \dot{x}|\dot{x}| + F(\eta))$$

Next express the unknown solution with the additional perturbation as a series, i.e.,

$$x(\eta) = x_0(\eta) + \varepsilon x_1(\eta) + ...$$

Using known zeroth order solution from above, one can obtain easily the first and possibly higher order terms in the series.

$$\ddot{x} + x - 3k x_1 x_0^2 = \hat{G}(x_0, \eta, \tau_0)$$

More details of this method in general are contained in Vakakis (1994) and this method applied to this specific problem in Vishnubhotla, Falzarano, and Vakakis (2000). We have since applied this method to more general perturbations including impulse response function modeling of the hydrodynamic reaction forces and pseudo-random external forcing and those results are the focus of this paper.

3 Results

Currently, the US Navy is involved in the design and construction of a new generation of destroyer hull forms, the so-called DDG-1000 Zumwalt class. This innovative hull is radically different from previous and existing destroyer hull forms, most notably in that it has tumble home sides, a wave piercer bow and a broad flat stern. The ship is designed to minimize signature not unlike the stealth aircraft. Unfortunately, due to this hull form's unique features the vessel's motion response is dramatically different from existing hull forms. In an effort to gain a better understanding of this new vessels motion unique motion response, we study the response of the US Navy's currently existing destroyer hull form a so-called traditional hull form. The traditional hull form is similar to the US Navy's Burke class DDG hull form although an earlier version of the hull. The physical characteristics of this vessel are summarized in Table 1.

In this paper we analyze the critical roll motion response of the traditional hull as affected by improved hydrodynamic modeling. The key result of this analysis is the comparison of the critical safe basin boundaries using the two different hydrodynamic modeling. The results are for the traditional US Navy destroyer hull-form in a pseudo-random seaway. The seaway is represented by two-parameter seaway with intensity Sea State 2, and significant wave height of 2.9 feet and a peak period of 7.5 seconds. The constant coefficients added mass and damping are calculated at the vessel's linear natural frequency. Since roll is lightly damped and highly tuned one would expect the constant coefficients and impulse response function results to be quite close. However, since the roll restoring moment curve for this vessel is highly nonlinear, the magnification curve is

Table 1 Physical Characteristics of Traditional Hull-form

Parameter	Units	Dimensional Value
Length of the vessel, L	ft	466.00
Displacement, Δ	lb	18900000.00
Linear restoring arm, C_1	ft	6.570
Nonlinear restoring arm, C_3	ft	3.120
Wave amplitude, ζ	ft	5.70
Forcing frequency, ω	rad/s	0.90
Linear natural frequency, ω_n	rad/s	0.572
Hydrodynamic mass, $(I_{44} + A_{44}(\omega))$	slug-ft^2	380000000.00
Linear damping, $B_{44}(\omega)$	slug-ft^2-s^{-1}	1810000.00
Nonlinear damping, B_{44q}	slug-ft^2	18400000.00
Total wave force, $F_{44}(\omega)$	lb-ft^{-1}	4125000.00

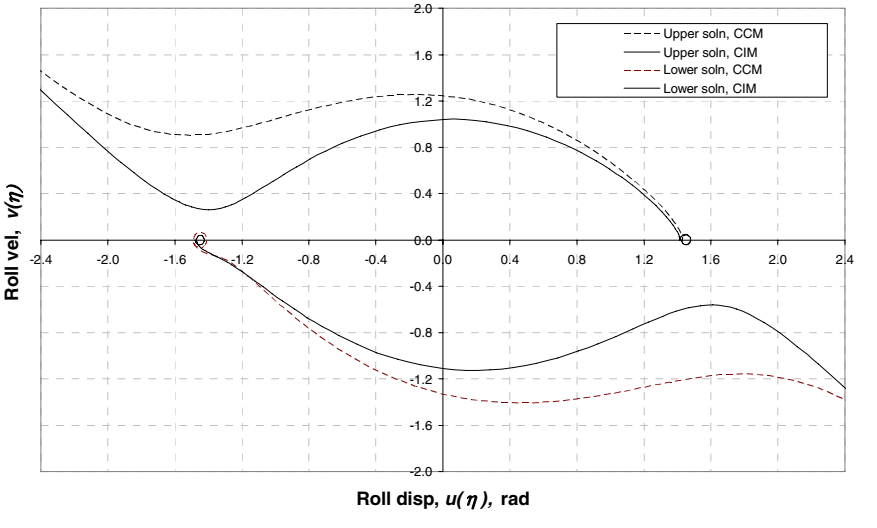

Fig. 2 Comparison of Critical Roll Response CCM vs. IRF

significantly bent to lower frequencies and the linear roll natural frequency is not indicative of the response. For a description of this phenomenon for the general see, Falzarano, Esparza and Taz Ul Mulk, (1994) and for this particular hull see Juckett, Falzarano, Vishnubholtha (2006).

One can see from Figure 2 that the effect of the more accurate impulse response function hydrodynamic modeling can be significant.

4 Conclusion

The ultimate goal of this research is to predict when a vessel is likely to capsize in random seas over its lifetime. This research described in this paper provides a tool to answers only part of that question and much more work is needed. However, we hope that this is a valuable contribution in this area and may eventually make it possible for vessel designers to assess the safety of a proposed innovative vessel design which may be dramatically different from existing vessel designs.

Acknowledgments. The authors would like to acknowledge the support of the Wayne State University Low Temperature Naval Research Center with Director Professor Raouf Ibrahim and Government Program Manager Kelly Cooper. The second author would also like to acknowledge the direct support of the Office of Naval Research Grant #N000140711067 ONR with Government Program manager Kelly Cooper.

References

Vishnubhotla, S., Falzarano, J., Vakakis, A.: A New Method to Predict Critical Vessel/Platform Dynamics in a Realistic Seaway. Philosophical Transactions of the Royal Society, Theme issue on Nonlinear Dynamics of Ships, June 15 (2000)

Falzarano, J., Shaw, S., Troesch, A.: Application of Global Methods for Analyzing Dynamical Systems to Ship Rolling Motion and Capsizing. International Journal of Bifurcation and Chaos in Applied Sciences and Engineering 2(1), 101–115 (1992)

Zhang, F., Falzarano, J.: Multiple Degree of Freedom Global Analysis of Transient Ship Rolling Motion. In: ASME Winter Annual Meeting, Symposium on Nonlinear Dynamics of Marine Vehicles, pp. 57–72 (November 1993)

Cummins, W.E.: The Impulse Response Function and Ship Motions. In: Symposium on Ship Motions at the Institute fur Schiffbau der Universitat Hamburg, January 25-27 (1962)

Vakakis, A.: Exponentially Small Splitting of manifolds in a Rapidly Forced Duffing System. Journal of Sound and Vibration 179(1) (1994)

Falzarano, J., Esparza, I., Taz Ul Mulk, M.: A Combined Steady State and Transient Method to Study Nonlinear Ship Rolling Motion. SNAME Journal of Ship Research (1995)

Juckett, S., Falzarano, J., Vishnubhotla, S.: Comparison of the Relative Response of a Traditional Versus an Advanced Naval Hull in Survival Seas. In: 10th International Conference on Hydrodynamics (ICHD), October 2006, ISCHIA (2006)

Discontinuity Mapping for Near-Grazing Dynamics in Vibro-Impact Oscillators

Xiaopeng Zhao

Abstract. Vibro-impact oscillators may undergo zero-velocity impacts, also known as grazing contacts. Near-grazing dynamics refer to low-velocity impacts. The conventional technique of local stability analysis suffers singularity when applied to grazing dynamics. Discontinuity mapping conceived by Nordmark provides a powerful tool to analyze and predict the plethora of complex phenomena due to grazing. This article intends to help beginners in vibro-impact dynamics better understand the concept of discontinuity mapping through a lucid derivation of the discontinuity mapping. The fundamental approach consists of three steps. First, a Poincaré map is introduced for the oscillatory dynamics without impacts. Second, impact dynamics near a grazing contact point are approximated using a series expansion to generate the so-called discontinuity mapping. Finally, the overall oscillations involving low-velocity impacts are analyzed using a combination of the Poincaré map and the discontinuity mapping derived in the previous two steps. We first present a transparent derivation of the discontinuity mapping for a generic one-degree-of-freedom vibro-impact oscillator. Then, the approach is applied to a linear mass spring oscillator whose vibrations are restricted by a rigid wall.

1 Introduction

Vibro-impact oscillators have an oscillating mass whose vibration amplitude is restricted by a fixed boundary. Although the dynamics in between impacts may be smooth or even linear, contacts of the oscillating mass with the boundary lead to discontinuous changes in the system's properties, resulting highly nonlinear and nonsmooth dynamics. Vibro-impact oscillators have found many applications in engineering [1].

Xiaopeng Zhao
Mechanical, Aerospace, and Biomedical Engineering Department
University of Tennessee Knoxville TN 37996
xzhao9@utk.edu

R.A. Ibrahim et al. (Eds.): Vibro-Impact Dynamics of Ocean Systems, LNACM 44, pp. 275–285.
springerlink.com

An oscillator whose dynamics is smooth can be analyzed using classical techniques such as the variational equations [11]. On the other hand, impacts introduce jumps into the system's state, rendering the system's dynamics discontinuous. According to the impact velocities, vibro-impact dynamics shall be tackled using two different approaches. High-velocity impacts, in which impact velocities are sufficiently high such that all nearby trajectories have impacts, can be analyzed by introducing a modification to the standard variation equations [1, 10, 15]. Conversely, low-velocity impact problems impose great challenges because nearby trajectories may or may not have impacts. In particular, the conventional technique of local stability analysis becomes singular for zero-velocity impacts, the so-called grazing impacts. This singularity can be handled using the so-called discontinuity mapping approach, which was first conceived by Nordmark [12] and later extended by various authors [13, 4, 8, 5, 17, 9].

Nordmark derived a mapping for a one-degree-of-freedom vibro-impact oscillator [12]. A particular form of this mapping was named the Nordmark mapping and studied in detail by Chin et al. [2, 3]. Here, we use a different yet more transparent approach to rederive the Nordmark mapping to illustrate the concept of discontinuity mapping. We first derive the discontinuity mapping for a general one-degree-of-freedom oscillator with a unilateral boundary. Then, we apply the approach to a linear mass-spring oscillator whose movement is limited by a rigid wall. For discontinuity mapping of more general nonsmooth dynamical systems, see the work of di Bernardo et al. [8, 9]. Alternatively, another approach based on the implicit function theorem can be found in [5, 17].

2 Discontintuity Mapping for a General Vibro-Impact Oscillator

Consider a one-degree-of-freedom forced oscillator

$$\ddot{x} + g(x, \dot{x}) = f(t), \tag{1}$$

where x is the displacement, overhead dots represent derivatives with respective to time t, g represents the resultant force related to $\dot{x}$ and x (e.g. the summation of damping force and restoring force for a mass-spring oscillator), and $f(t)$ represents a periodic external force. We consider the case when the movement of the oscillator is limited by a rigid wall placed at $x = \delta > 0$. We assume impacts between the oscillator and the wall can be modeled using the coefficient of restitution [1] such that $\dot{x}^+ = -e\dot{x}^-$, where $\dot{x}^-$ is the velocity of the mass immediately before impact and $\dot{x}^+$ is the velocity immediately after impact. We first render the nonautonomous governing equation (1) autonomous by introducing a new variable θ such that $\dot{\theta} = 1$. Thus, θ represents the phase of the oscillator. We further denote the velocity of the oscillator by v and the acceleration by a. We further assume a periodic oscillatory solution grazes the wall, that is, impacts the wall at zero velocity. Then, we denote the displacement, velocity, acceleration, and phase at the grazing contact point by

x_*, v_*, a_*, and θ_*, respectively. Since the grazing contact occurs at the maximum displacement on a periodic trajectory, it follows that $x_* = \delta$, $v_* = 0$, and $a_* < 0$. Next, we will derive a mapping to describe dynamics in a neighborhood of the grazing periodic solution.

2.1 Vibration in the Absence of the Wall

We begin the analysis by temporarily neglecting the existence of the rigid wall, that is, we consider the dynamics of Eqn. (1) in the absence of the unilateral constraint at $x = \delta$. This vibration problem can be analyzed using the Poincaré map approach [11]. We choose the Poincaré section [11] to be the surface defined by $v = 0$ in the direction of decreasing v. Then, the Poincaré mapping $\mathbf{P}$ can be defined as the flow of dynamics that starts from an arbitrary point in the state space and ends on the Poincaré section.

Let us introduce a state vector $\mathbf{x} = \{x, v, \theta\}^T$. Then, the equation of motion of the oscillator can be written in a vector form:

$$\dot{\mathbf{x}} = \mathbf{f}(\mathbf{x}), \tag{2}$$

where $\mathbf{f}(\mathbf{x}) = \{v, f(\theta) - g(x,v), 1\}^T$. Let us denote the solution of Eqn. (2) by the flow function $\boldsymbol{\Phi}(t, \mathbf{x})$. It follows that

$$\frac{\partial}{\partial t}\boldsymbol{\Phi}(t, \mathbf{x}) = \mathbf{f}(\boldsymbol{\Phi}(t, \mathbf{x})). \tag{3}$$

We represent the Poincaré section by the zero-level surface of a function $h^P(\mathbf{x}) \equiv v$. Then, the Poincaré map can be defined as $\mathbf{P}(\mathbf{x}) = \boldsymbol{\Phi}(\tau(\mathbf{x}), \mathbf{x})$ such that $h^P(\mathbf{P}(\mathbf{x})) = 0$, where $\tau(\mathbf{x})$ is the time of flight from $\mathbf{x}$ to the Poincaré section. Under this definition, the grazing contact point, $\mathbf{x}_* = \{x_*, v_*, \theta_*\}^T$, is a fixed point of $\mathbf{P}$, that is $\mathbf{P}(\mathbf{x}_*) = \boldsymbol{\Phi}(\tau(\mathbf{x}_*), \mathbf{x}_*) = \mathbf{x}_*$. And $\tau(\mathbf{x}_*)$ is the period of the periodic orbit, which we denote by T for later convenience.

As shown in details in [15], the Jacobian of $\mathbf{P}$ can be computed as follows

$$\mathbf{P}_{\mathbf{x}}(\mathbf{x}_*) = \left(\mathbf{I} - \frac{\mathbf{f}(\mathbf{x}_*) \cdot h_{\mathbf{x}}(\mathbf{x}_*)}{h_{\mathbf{x}}(\mathbf{x}_*) \cdot \mathbf{f}(\mathbf{x}_*)}\right) \boldsymbol{\Phi}_{\mathbf{x}}(T, \mathbf{x}_*). \tag{4}$$

Let us further denote the Jacobian of $\mathbf{P}$ by

$$\mathbf{P}_{\mathbf{x}} = \begin{bmatrix} P_{11} & P_{12} & P_{13} \\ P_{21} & P_{22} & P_{23} \\ P_{31} & P_{32} & P_{33} \end{bmatrix}. \tag{5}$$

Since Eqn. (2) is an autonomous system, one can show that [11]

$$\boldsymbol{\Phi}_{\mathbf{x}}(T, \mathbf{x}_*) \cdot \mathbf{f}(\mathbf{x}_*) = \mathbf{f}(\mathbf{x}_*). \tag{6}$$

Applying the above relation to Eqn. (4) yields

$$\mathbf{P}_{\mathbf{x}}(\mathbf{x}_*) \cdot \mathbf{f}(\mathbf{x}_*) = \mathbf{0}. \tag{7}$$

Moreover, recall that the map $\mathbf{P}$ projects any point to the Poincaré section $v = 0$. In other words, the second row of $\mathbf{P}(\mathbf{x})$ equals zero for any given $\mathbf{x}$. Therefore, it follows that $P_{21} = P_{22} = P_{23} = 0$.

If the wall did not exist, local stability of a periodic orbit can be determined through evaluating the eigenvalues of $\mathbf{P}_{\mathbf{x}}$. In the presence of the wall, orbits that come close to the wall may lose stability by disturbances that cause intermittent contacts with the wall. Thus, behavior of oscillation near a rigid wall is not solely determined by $\mathbf{P}_{\mathbf{x}}$. Rather, it may be significantly influenced by the impact dynamics.

2.2 *Vibro-Impact Dynamics Near Grazing*

We will extend the work in the previous section to consider vibro-impact dynamics near a grazing orbit. As manifested above, a nonimpacting trajectory near the grazing periodic orbit will transversally cross the Poincaré section at a point at the left of but near the grazing contact point. Conversely, an impacting trajectory dose not intersect the Poincaré section but jump across the section. For example, Figure 1 shows a trajectory that starts at point A, impacts the wall at point X, then jumps to point Y, and finally ends at point B. To utilize the Poincaré section, we temporally ignore the existence of the wall and extend the trajectory A-X forward in time until it intersects the Poincaré section. Apparently, this virtual intersection point is at the right of the grazing contact point.

Denote an arbitrary point on the Poincaré section and near the grazing contact point by (x, θ). From the above analysis, we can conclude that if $x < 0$ then it is an intersection of a nonimpacting trajectory; conversely, if $x > 0$ then it results from the virtual intersection of an impacting trajectory. Starting from an arbitrary intersection or virtual intersection (x_n, θ_n) and following the subsequent dynamics will result in another intersection or virtual intersection on the Poincaré section, which we denote by (x_{n+1}, θ_{n+1}).

If $x_n < 0$, (x_{n+1}, θ_{n+1}) can be obtained by directly applied $\mathbf{P}$ to (x_n, θ_n). In linear form, this is

$$x_{n+1} = P_{11}x_n + P_{13}\theta_n, \tag{8}$$

$$\theta_{n+1} = P_{31}x_n + P_{33}\theta_n. \tag{9}$$

If $x_n > 0$, we can not directly apply $\mathbf{P}$ to (x_n, θ_n). In terms of the impacting trajectory in Fig. 1, the subsequent dynamics following the virtual intersection point N can not be obtained by directly applying $\mathbf{P}$ to N. Thus, we need to find a "correction" to

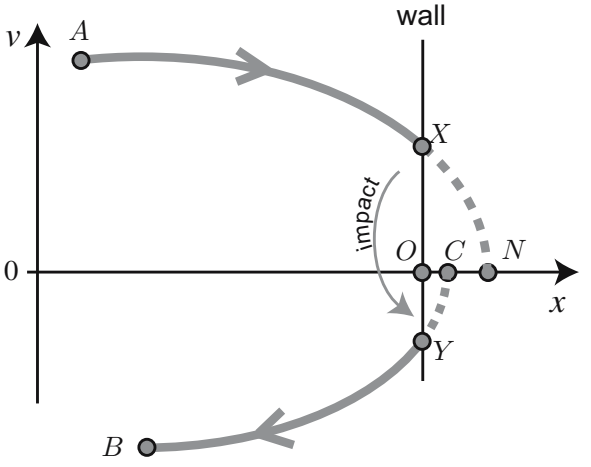

Fig. 1 Sketch of a trajectory with a low-velocity impact. The trajectory sequentially consists of points A, X, Y, and B. Impact maps Point X to Point Y, leading to discontinuity in the system's velocity.

point N on the Poincaré section such that the subsequent dynamics can be obtained by applying to $\mathbf{P}$ to this correction. Again, we temporally ignore the wall and extend the trajectory B-Y backward in time until it intersects the Poincaré section at point C. As shown in Fig. 1, point C is a correction to point N. We denote the coordinate of N by (x_n, θ_n) and the coordinate of C by (x_c, θ_c). It is obvious that x_c and θ_c are functions of x_n and θ_n. Then, the subsequent intersection or virtual intersection on the Poincaré section can be obtained by applying $\mathbf{P}$ to (x_c, θ_c):

$$x_{n+1} = P_{11} x_c(x_n, \theta_n) + P_{13} \theta_c(x_n, \theta_n), \tag{10}$$

$$\theta_{n+1} = P_{31} x_c(x_n, \theta_n) + P_{33} \theta_c(x_n, \theta_n). \tag{11}$$

Next, we need to solve x_c and θ_c in terms of x_n and θ_n. As shown in Figure 1, the correction from N to C consists of the following pieces: flow from N to X, jump from X to Y, and finally flow from Y to C.

Since we consider low-velocity impacts, points X, Y, N, and C are all close to the grazing contact point O. Then, the flow from N to C can be solved using local dynamical analysis. To this end, we consider a trajectory starting from a point with state x, v, θ, and flying for a short time interval τ. Using Taylor Series Expansion, we write the final state on the trajectory as: $x + v\tau + \frac{1}{2}a\tau^2$, $v + a\tau$, and $\theta + \tau$. Since we dynamics in the neighborhood of the grazing contact point, we replace a by the acceleration at the grazing point a_*.

i). Flow from N to X. We assume the time of flight from N to X is $-\tau_1$ and note that $v_n = 0$. It follows that the displacement, velocity, and phase at point X can be written in terms of those at point N as follows:

$$x_X = x_n + \frac{1}{2} a_* \tau_1^2 \tag{12}$$

$$v_X = -a_* \tau_1 \tag{13}$$

$$\theta_X = \theta_n - \tau_1 \tag{14}$$

Since $x_X = 0$, one can show that $\tau_1 = \sqrt{-2x_n/a_*}$.

ii). Jump from X to Y. Applying the coefficient of restitution law, we get the state at point Y:

$$x_Y = x_X = 0, \tag{15}$$

$$v_Y = -e\, v_X = e\, a_* \tau_1, \tag{16}$$

$$\theta_Y = \theta_X = \theta_n - \tau_1. \tag{17}$$

iii). Flow from Y to C. Assuming the time of flight from Y to C is $-\tau_2$, we can write the state at point C in terms of the state at point Y:

$$x_C = -v_Y \tau_2 + \frac{1}{2} a_* \tau_2^2 = -e\, a_* \tau_1 \tau_2 + \frac{1}{2} a_* \tau_2^2, \tag{18}$$

$$v_C = v_Y - a_* \tau_2 = e\, a_* \tau_1 - a_* \tau_2, \tag{19}$$

$$\theta_C = \theta_Y - \tau_2 = \theta_n - \tau_1 - \tau_2. \tag{20}$$

Since $v_C = 0$, one can show that $\tau_2 = e\tau_1 = e\sqrt{-2x_n/a_*}$. It then follows that

$$x_C = -\frac{1}{2} e^2 a_* \tau_1^2 = e^2 x_n, \tag{21}$$

$$\theta_C = \theta_n - (1+e)\,\tau_1. \tag{22}$$

Substituting Eqns. (21,22) into (10,11) yields the mapping for $x_n > 0$

$$x_{n+1} = P_{11} e^2 x_n + P_{13}\left(\theta_n - (1+e)\,\tau_1\right), \tag{23}$$

$$\theta_{n+1} = P_{31} e^2 x_n + P_{33}\left(\theta_n - (1+e)\,\tau_1\right). \tag{24}$$

Then, near-grazing dynamics can be studied by iteration of the mapping (8,9) and (23,24). To put this mapping in the form of the Nordmark mapping, we introduce the following transformation: $x_n = c_1 \chi_n$, $\theta_n = c_2 \chi_n + c_3 \psi_n$, where

$$c_1 = -\frac{2}{a_*}(1+e)^2 P_{13}^2, \tag{25}$$

$$c_2 = -\frac{2}{a_*}(1+e)^2 P_{13} P_{33}, \tag{26}$$

$$c_3 = -\frac{2}{a_*}(1+e)^2 P_{13}. \tag{27}$$

Substituting (25-27) into (8,9) and (23,24) yields a discontinuity mapping in a form similar to the Nordmark mapping:

$$\chi_{n+1} = \alpha\,\chi_n + \psi_n, \tag{28}$$

$$\psi_{n+1} = -\gamma\,\chi_n, \tag{29}$$

when $\chi_n \le 0$ and

$$\chi_{n+1} = -\text{sign}\,(P_{13})\,\sqrt{\chi_n} + \left(\alpha - \left(1-e^2\right)P_{11}\right)\chi_n + \psi_n, \tag{30}$$

$$\psi_{n+1} = -\gamma e^2 \chi_n \tag{31}$$

when $\chi_n > 0$. Here, the coefficients $\alpha = P_{11} + P_{33}$ and $\gamma = P_{11}P_{33} - P_{13}P_{31}$.

When $P_{13} > 0$, if we neglect the second term at the right hand side of Eqn. (30), we will recover the original Nordmark mapping as shown in [12]. However, as shown by Molenaar et al. [14], a full consideration of Eqn. (30) is essential for certain situations.

Thus, the near-grazing dynamics of a general vibro-impact oscillator as defined in Eqn. (1) can be fully described by Eqns. (28-31). Since the coefficients of these equations are solely determined by the elements of the Jacobian of the map $\mathbf{P}$, characteristics of the near-grazing dynamics depend on the properties of the grazing periodic orbit.

3 Discontintuity Mapping for a Linear Mass-Spring Oscillator

Once coefficients of the Jacobian of $\mathbf{P}$ in Eqn. (5) are known, one can compute the discontinuity mapping following Eqns. (28-31). For a general vibro-impact oscillator, the Jacobian $\mathbf{P_x}$ often needs to be calculated numerically. In this section, we consider a special example, whose solution can be analytically obtained.

We apply the discontinuity mapping approach to a mass-spring oscillator governed by the following equation.

$$\ddot{x} + 2\zeta\omega\dot{x} + \omega^2 x = f\cos(\theta), \tag{32}$$

where θ represents the phase of the oscillator and is determined by the following equation:

$$\dot{\theta} = \Omega. \tag{33}$$

To derive the discontinuity mapping, the key is to find the Poincaré map corresponding to the grazing periodic orbit. To this end, we first solve the flow function Φ and then compute the Jacobian of $\mathbf{P}$ using Eqn. (4). Assume the initial conditions of the oscillator are $x(0) = x_0$, $v(0) = v_0$, and $\theta(0) = \theta_0$. Let the state variable $\mathbf{x} = \{x, v, \theta\}^T$ and denote $\mathbf{x}_0 = \{x_0, v_0, \theta_0\}^T$. The flow function can be written as

$$\Phi(t, \mathbf{x}_0) = \left\{\begin{array}{c} x(t) \\ v(t) \\ \theta(t) \end{array}\right\} = \left\{\begin{array}{c} c_1 e^{s_1 t} + c_2 e^{s_2 t} + Q(\theta) \\ c_1 s_1 e^{s_1 t} + c_2 s_2 e^{s_2 t} + \Omega Q'(\theta) \\ \Omega t + \theta_0 \end{array}\right\}, \tag{34}$$

where s_1 and s_2 are solutions of the characteristic equation

$$\lambda^2 + 2\zeta\omega\lambda + \omega^2 = 0 \tag{35}$$

and $Q(\theta)$ represents the steady state solution of Eqn. (32). Specifically, $s_{1,2} = -\zeta\omega \pm \omega\sqrt{\zeta^2 - 1}$.

It follows from Eqn. (34) that

$$\frac{\partial}{\partial \mathbf{x}_0}\boldsymbol{\Phi}(t, \mathbf{x}_0) = \begin{bmatrix} \frac{\partial x(t)}{\partial x_0} & \frac{\partial x(t)}{\partial v_0} & \frac{\partial x(t)}{\partial \theta_0} \\ \frac{\partial v(t)}{\partial x_0} & \frac{\partial v(t)}{\partial v_0} & \frac{\partial v(t)}{\partial \theta_0} \\ 0 & 0 & 1 \end{bmatrix} \tag{36}$$

Applying the initial condition to Eqn. (34) yields

$$x_0 = c_1 + c_2 + Q(\theta_0), \tag{37}$$

$$v_0 = c_1 s_1 + c_2 s_2 + \Omega Q'(\theta_0). \tag{38}$$

It follows that

$$\begin{pmatrix} c_1 \\ c_2 \end{pmatrix} = \mathbf{S}^{-1} \begin{pmatrix} x_0 - Q(\theta_0) \\ v_0 - \Omega Q'(\theta_0) \end{pmatrix}, \tag{39}$$

where

$$\mathbf{S} = \begin{bmatrix} 1 & 1 \\ s_1 & s_2 \end{bmatrix}. \tag{40}$$

Substituting Eqn. (39) into Eqn. (34) yields

$$\begin{pmatrix} x(t) \\ v(t) \end{pmatrix} = \mathbf{E}\mathbf{S}^{-1} \begin{pmatrix} x_0 - Q(\theta_0) \\ v_0 - \Omega Q'(\theta_0) \end{pmatrix} + \begin{pmatrix} Q(\theta) \\ \Omega Q'(\theta) \end{pmatrix}, \tag{41}$$

where

$$\mathbf{E} = \begin{bmatrix} e^{s_1 t} & e^{s_2 t} \\ s_1 e^{s_1 t} & s_2 e^{s_2 t} \end{bmatrix}. \tag{42}$$

Then, it follows from Eqn. (41) that

$$\begin{bmatrix} \frac{\partial x(t)}{\partial x_0} & \frac{\partial x(t)}{\partial v_0} \\ \frac{\partial v(t)}{\partial x_0} & \frac{\partial v(t)}{\partial v_0} \end{bmatrix} = \mathbf{E}\mathbf{S}^{-1} = \frac{1}{s_1 - s_2} \begin{bmatrix} s_1 e^{s_2 t} - s_2 e^{s_1 t} & e^{s_1 t} - e^{s_2 t} \\ s_1 s_2 \left(e^{s_2 t} - e^{s_1 t}\right) & s_1 e^{s_1 t} - s_2 e^{s_2 t} \end{bmatrix} \tag{43}$$

As shown in the previous section, the grazing contact point can be denoted as $\mathbf{x}_* = \{\delta, 0, \theta_*\}$. And the period of the grazing orbit is $T = 2\pi/\Omega$. The corresponding vector field is $\mathbf{f}(\mathbf{x}_*) = \{0, a_*, \Omega\}^T$. Substituting the expression of $\mathbf{f}(\mathbf{x}_*)$ into Eqn. (6) yields two nontrivial conditions

$$\phi_{12} a_* + \phi_{13}\Omega = 0, \tag{44}$$

$$\phi_{22} a_* + \phi_{23}\Omega = a_*. \tag{45}$$

It thus follows that $\phi_{13} = -\phi_{12} a_* / \Omega$ and $\phi_{23} = a_* (1 - \phi_{22}) / \Omega$. Now, we can write down $\Phi_{\mathbf{x}} (T, \mathbf{x}_*)$ by combining Eqns. (36) and (43) as well as the conditions for ϕ_{13} and ϕ_{23}:

$$\Phi_{\mathbf{x}} (T, \mathbf{x}_*) = \begin{bmatrix} \frac{s_1 e^{s_2 T} - s_2 e^{s_1 T}}{s_1 - s_2} & \frac{e^{s_1 T} - e^{s_2 T}}{s_1 - s_2} & -\frac{a_*}{\Omega} \frac{e^{s_1 T} - e^{s_2 T}}{s_1 - s_2} \\ \frac{s_1 s_2 \left(e^{s_2 T} - e^{s_1 T} \right)}{s_1 - s_2} & \frac{s_1 e^{s_1 T} - s_2 e^{s_2 T}}{s_1 - s_2} & \frac{a_*}{\Omega} \left(1 - \frac{s_1 e^{s_1 T} - s_2 e^{s_2 T}}{s_1 - s_2} \right) \\ 0 & 0 & 1 \end{bmatrix}. \tag{46}$$

Recall that $h(\mathbf{x}) = v$. It follows that $h_{\mathbf{x}} (\mathbf{x}_*) = (0, 1, 0)$. Then, we can compute the Jacobian of $\mathbf{P}$ using Eqn. (4)

$$\mathbf{P}_{\mathbf{x}} (\mathbf{x}_*) = \begin{bmatrix} \frac{s_1 e^{s_2 T} - s_2 e^{s_1 T}}{s_1 - s_2} & \frac{e^{s_1 T} - e^{s_2 T}}{s_1 - s_2} & -\frac{a_*}{\Omega} \frac{e^{s_1 T} - e^{s_2 T}}{s_1 - s_2} \\ 0 & 0 & 0 \\ -\frac{\Omega}{a_*} \frac{s_1 s_2 \left(e^{s_2 T} - e^{s_1 T} \right)}{s_1 - s_2} & -\frac{\Omega}{a_*} \frac{s_1 e^{s_1 T} - s_2 e^{s_2 T}}{s_1 - s_2} & \frac{s_1 e^{s_1 T} - s_2 e^{s_2 T}}{s_1 - s_2} \end{bmatrix}. \tag{47}$$

It then follows that

$$\alpha = P_{11} + P_{33} = e^{s_1 T} + e^{s_2 T} \tag{48}$$

$$= 2 e^{-2\pi \zeta \omega / \Omega} \cosh \left(2\pi \sqrt{\zeta^2 - 1} \omega / \Omega \right) \tag{49}$$

and

$$\begin{aligned} \gamma &= P_{11} P_{33} - P_{13} P_{31} \\ &= \frac{1}{(s_1 - s_2)^2} \left(\left(s_1 e^{s_2 T} - s_2 e^{s_1 T} \right) \left(s_1 e^{s_1 T} - s_2 e^{s_2 T} \right) - s_1 s_2 \left(e^{s_2 T} - e^{s_1 T} \right) \left(e^{s_1 T} - e^{s_2 T} \right) \right) \\ &= \frac{1}{(s_1 - s_2)^2} \left(\left(s_1^2 + s_2^2 \right) e^{(s_1 + s_2) T} - s_1 s_2 \left(e^{2 s_2 T} + e^{2 s_1 T} \right) + s_1 s_2 \left(e^{2 s_1 T} + e^{2 s_2 T} - 2 e^{(s_1 + s_2) T} \right) \right) \\ &= e^{(s_1 + s_2) T} \\ &= e^{-4\pi \zeta \omega / \Omega}. \end{aligned}$$

Since $P_{13} = -\frac{a_*}{\Omega} \frac{e^{s_1 T} - e^{s_2 T}}{s_1 - s_2}$ and $a_* < 0$, one can show that

$$\begin{aligned} sign(P_{13}) &= sign \left(\frac{e^{s_1 T} - e^{s_2 T}}{s_1 - s_2} \right) \\ &= sign \left(\frac{\sinh \left(\omega T \sqrt{\zeta^2 - 1} \right)}{\sqrt{\zeta^2 - 1}} \right). \end{aligned} \tag{50}$$

When $\zeta > 1$, one can show that $P_{13} > 0$ and $sign(P_{13}) = 1$. On the other hand, when $\zeta < 1$, $sign(P_{13}) = sign \left(\sin \left(2\sqrt{1 - \zeta^2} \omega / \Omega \right) \right)$. It follows that the sign of P_{13} varies as Ω changes. In particular, when $\Omega = 2\sqrt{1 - \zeta^2} \omega / (n\pi)$, $P_{13} = 0$, which corresponds to co-dimension-two grazing bifurcations [5, 17].

Note that the expressions of α and γ are consistent with those obtained by Chin et al. [2, 3]. However, Chin et al. did not show how to derive the mapping for impacting dynamics (i.e. Eqns. (30,31)) and how to relate the corresponding coefficients to physical parameters.

4 Summary and Discussion

In this article, we have illustrated a detailed derivation of the discontinuity mapping for one-degree-of-freedom vibro-impact oscillators. Moreover, we have demonstrated for a linear-mass-spring oscillator based on vibro-impact how the discontinuity mapping is related to the physical parameters of the system. The mapping system (28-31) yields a plethora of complex phenomena corresponding to different choices of parameters. A comprehensive study of the discontinuity-induced bifurcations in this mapping system has been presented in the work of Chin et al. [2, 3] and de Weger et al. [6, 7]. We note that discontinuity mapping for high degree-of-freedom vibro-impact oscillators and for more general nonsmooth problems can be derived using a similar approach. The discontinuity mapping approach has been used by various authors to understand grazing bifurcations in various engineering systems [8] and in design and control nonsmooth dynamics [5, 18].

References

1. Brogliato, B.: Nonsmooth Mechanics. Springer, New York (1999)
2. Chin, W., Ott, E., Nusse, H.E., Grebogi, C.: Grazing Bifurcation in Impact Oscillators. Physical Review E 50, 4427–4444 (1994)
3. Chin, W., Ott, E., Nusse, H.E., Grebogi, C.: Universal Behavior of Impact Oscillators near Grazing Incidence. Physics Letters A 201, 197–204 (1995)
4. Dankowicz, H., Nordmark, A.B.: On the Origin and Bifurcations of Stick-Slip Oscillations. Physica D 136, 280–302 (1999)
5. Dankowicz, H., Zhao, X.: Local Analysis of Co-dimension-one and Co-dimension-two grazing bifurcations in Impact Microatuators. Physica D 202, 238–257 (2005)
6. de Weger, J., Binks, D., Molenaar, J., van de Water, W.: Generic Behavior of Grazing Impact Oscillators. Physical Review Letters 76, 3951–3954 (1996)
7. de Weger, J., van de Water, W., Molenaar, J.: Grazing Impact Oscillators. Physical Review E 62, 2030–2041 (2000)
8. di Bernardo, M., Budd, C.J., Champneys, A.R.: Normal form maps for grazing bifurcations in *n*-dimensional piecewise-smooth dynamical systems. Physica D 160, 222–254 (2000)
9. di Bernardo, M., Budd, C.J., Champneys, A.R., Kowalczyk, P.: Piecewise-smooth dynamical systems: theory and applications. Applied Mathematics series no. 163. Springer, Heidelberg (2007)
10. Leine, R.I., Van Campen, D.H., Van de Vrande, B.L.: Bifurcations in nonsmooth discontinuous systems. Nonlinear Dynamics 23, 105–164 (2000)
11. Nayfeh, A.H., Balachandran, B.: Applied Nonlinear Dynamics: Analytical, Computational, and Experimental Methods. Wiley, New York (1995)

12. Nordmark, A.B.: Non-periodic motion caused by grazing incidence in an impact oscillator. Journal of Sound and Vibration 145, 279–297 (1991)
13. Nordmark, A.B.: Universal limit mapping in grazing bifurcations. Physical Review E 55(1), 266–270 (1997)
14. Molenaar, J., de Weger, J.G., van de Walter, W.: Mappings of Grazing-Impact Oscillators. Nonlinearity 14, 301–321 (2001)
15. Zhao, X., Dankowicz, H., Reddy, C.K., Nayfeh, A.H.: Modeling and Simulation Methodology for Impact Microactuators. Journal of Micromechanics and Microengineering 14, 775–784 (2004)
16. Zhao, X.: Modeling and Simulation of MEMS Devices, Ph.D. Thesis, Virginia Tech. (2004)
17. Zhao, X., Dankowicz, H.: Unfolding Degenerate Grazing Dynamics in Impact Actuators. Nonlinearity 19, 399–418 (2006)
18. Zhao, X., Dankowicz, H.: Control of Impact Microactuators for Precise Positioning. ASME Journal of Computational and Nonlinear Dynamics 1, 65–70 (2006)

Author Index